Imaging Physiological and Pathological Activity in the Brain using Electric Impedance Tomography

Anna Vongerichten

28th November 2014

Submitted for the degree of Doctor of Philosophy
Department of Medical Physics and Bioengineering
University College London

Declaration

I, Anna Nastasia Vongerichten, confirm that the work presented in this thesis is my own. I confirm that information, which has been derived from other sources is indicated in the thesis.

Signature

Date

Acknowledgements

I am deeply grateful for the support that I received from a my colleagues at UCL. I would like to thank my supervisors, Prof. David Holder and Mr Andrew McEvoy for the opportunity to work on this exciting project and for their realism and encouragement. I would also like to thank Prof. Jem Hebden for his support and foresight throughout the project.

My research could not have been possible without my colleagues support. I am especially grateful to Dr Gustavo Sato dos Santos and Dr Kirill Aristovich, who were both tremendously supportive of my projects. Both contributed in all aspects of this work, Dr Aristovich particulary in the calculation of the forward solutions and Dr Santos in the image reconstruction. Additionally, I would like thank Tom Dowrick, for design and construction of the custom made current source, as well as technical advice throughout the projects; James Avery and Hwan Koo, for his technical support, and Dr Brett Packham for his advice on the animal experiments. I am grateful to Mohamed Koronfel and Elliot Magee for the design and production of the microelectrodes. Prof. Matthew Walker kindly advised me on the epilepsy models and the assessment of the epilepsy data. Finally, I want to thank my husband for his support and understanding throughout the project.

Abstract

Electric Impedance Tomography (EIT) is a promising medical imaging technique that reconstructs the internal conductivity of an object from boundary measurements. EIT is currently being used to monitor the lung during ventilation clinically. Amongst other suggested uses for imaging it can also be used to image neuronal function. There are different ways on how EIT can image neuronal function and two of these are tested in this thesis. The overall aim of our work was to advance imaging of physiological and pathological neuronal activity using EIT and assess its potential for future clinical use. In Chapter 1, a general introduction into brain imaging techniques and EIT is given. In Chapter 2, the effect of different anaesthetics on the neuronal signal was assessed to prepare for EIT recordings under anaesthesia. In Chapter 3, we assessed the validity of two biophysical models regarding the behaviour of the impedance in response to alterations in the carrier frequency experimentally. This allowed an assessment of the ideal carrier frequency to image physiological neuronal activity. In Chapter 4, the source of the fast neural signal in EIT is discussed further. In Chapter 5, the possibility of imaging physiological neuronal activity throughout the brain is tested and its limitations are discussed. In Chapter 6, the impedance response to epileptiform activity is characterized and the potential use of EIT in imaging epileptic foci in epilepsy patients is discussed. In Chapter 7, imaging of epileptic foci in subcortical structures is tested using two different ways of imaging with EIT.

Publications and Presentations

Refereed Papers

Vongerichten, A., Aristovich, K., Dos Santos, G. S., McEvoy, A. W., & Holder, D. S. (2014). Design for a three-dimensional printed laryngoscope blade for the intubation of rats. Lab Animal, 43(4), 140–2. doi:10.1038/laban.463

Conference Talks

Vongerichten, A., Santos, G., Aristovich, K., Walker, M., McEvoy, A., Holder, D.S. Imaging Epileptic Seizures in a Rat Model using Electric Impedance Tomography and its Clinical Implications. 15th International Conference on Biomedical Applications of Electrical Impedance Tomography, Gananoque, Canada, April 2014
Vongerichten, A., Sato dos Santos, G., Aristovich, K., Holder, D.S. Impedance changes during evoked responses in the rat cortex in the 225–1575 Hz frequency range. 14th International Conference on Electrical Impedance Tomography (EIT), Heilbad Heiligenstadt, Germany April 2013.
Koronfel M., Avery, J., **Vongerichten**, A., Packham, B. and Holder, D.S. A flexible polyimide epicortical electrode array for imaging fast neural activity in the rat cortex using EIT. XVth International Conference of Electrical Bioimpedance and XIVth Conference on Electrical Impedance Tomography, Heiligenstadt, Germany, April 2013.
Sato dos Santos G., Aristovich K., **Vongerichten A**., Holder D.S. (2013) Forward and inverse modelling for EIT imaging of fast neural activity in the rat brain. 14th International Conference on Electrical Impedance Tomography (EIT), Heilbad Heiligenstadt, Germany April 2013.
Magee, E., **Vongericthen, A.**, Packham, B., Aristovich, K., Vanhoestenberghe, A. and Holder, D.S. Design, production and use of stainless steel microelectrode arrays for the collection of epicortical fast neural electrical impedance tomography data. IMAPS-UK Annual Conference "MicroTech", Cambridge, United Kingdom, March 2013.

Posters

Vongerichten A, Santos G, Aristovich K, Walker M, McEvoy A, Holder DS. Electrical Impedance Tomography (EIT) of epileptic seizures in rat models– a potential new tool for diagnosis of seizures. 30th International Congress of Clinical Neurophysiology (ICCN) of the IFCN, Berlin, Germany 2014

Contents

List of Figures

List of Tables

1. Introduction to Electric Impedance Tomography

1.1. Introduction

1.2. Imaging fast neural activity of the brain

Human beings have desired greater understanding of brain function for over a century. Damage or disease of the neural system profoundly interferes with our lives, which fuels our interest in its function. In order to better understand our brain and the diseases which afflict it we would like to image brain activity and use this information to understand circuitry and function. The ideal imaging method would be non-invasive, include the entire volume of the brain, and have very high temporal and spatial resolution. And while there are a multitude of well-established functional neural imaging methods, each with their advantages and disadvantages, the ideal imaging method for many purposes does not currently exist. For example, there is a void of the ideal method to image the abnormal neuronal activation in epilepsy, a common neurological disorder with a prevalence of 4.5-5/1000 in Europe (Forsgren et al. [2005]). Epilepsy is characterized by spells of hyper-synchronous neuronal activity, the epileptic seizures. The seizures of 60-70% of patients with epilepsy can be controlled by medication, while surgery is an option for some of the remaining patients (Schuele and Lüders [2008]). In order to successfully cure or control the seizures of a patient with refractory epilepsy a focus from where their epilepsy starts has to be found. To localize this epileptogenic focus, a vast range of imaging techniques are employed, in addition to neuropsychology, videotelemetry, and non-invasive as well as invasive neurophysiological monitoring with electroencephalograms (EEG). The invasive neurophysiological monitoring includes the implantation of electrodes directly on the surface of the brain as well as the insertion of depth electrodes. There is often a nescessity to insert electrodes into the cortex, risking damage, bleeding, and infection. This reflects how unsatisfactory the existing functional imaging methods are to image the epileptic seizures. The imaging methods used to find the epileptogenic focus include structural magnet resonance imaging (MRI) to look for any suspicious lesions, positron emissions tomography (PET) to look for interictally hypometabolic areas, and functional MRI (fMRI) to assess whether the suspected epileptogenic area is close to eloquent areas such as motor function and speech (Schuele and Lüders [2008]). The use of fMRI maps which are correlated to EEG voltage maps of epilepsy are currently being investigated (Grouiller et al. [2011]). Epilepsy patients usually receive invasive and/or non-invasive long-term EEG monitoring whilst being under video surveillance in an attempt to map the electrophysiological result to the clinical picture (Schuele and Lüders [2008]). These EEG recordings are sometimes used to do EEG source modelling, but this has its intrinsic problems which will be discussed in 1.4. If a patient is considered for surgery they often also receive a CT scan of their head to set intra-operative neuro-navigation systems up. None of these elaborate and well established neuro-imaging methods can provide us with a clear image of the propagation of the epileptic activity of the brain, the advantages and disadvantages

of each of the functional neuro-imaging methods will be discussed in 1.4. The main problem with most of these imaging techniques is that they use secondary effects of neuronal activity to image active areas of the brain. Hence they cannot provide the temporal resolution necessary as neuronal activity can propagate at speeds of up to 100 ms^{-1}(Hursh [1939]). High temporal resolution functional imaging would be of great value in diseases such as epilepsy as the epileptic focus will be the first activation point in operable epilepsy. In order to distinguish the focus from secondary activated areas a method that provides a temporal resolution in the range of milliseconds whilst showing the propagating activity in a three-dimensional space would be needed. The effect of a clearer determination of epileptic foci would be two-fold: surgery is only considered in patients where the surgeons and physicians are reasonably sure that an operation would cure or control their epilepsy therefore more patients could undergo this life-changing procedure; the clearer we can determine which area of the brain causes the epilepsy the smaller an area could be removed which would likely improve the postoperative cognitive function in these patients. EIT is an imaging method that has the potential to fill this gap and the goal of this PhD project is to develop 3D EIT and test its usefulness for clinical imaging.

1.3. Relevant Physiology of Neuronal Systems

1.3.1. Anatomy of the Neural Cell

A neuron is a specialized cell whose defining feature is excitability and the presence of synapses. A typical neuron is formed of the cell body called the soma, dendrites, and axon (see figure 1.1). The dendrites are filaments arising from the soma and offer surface area for axodentritic synapses coming from other neurons as well as giving stability for the micro-structure of neuronal tissue. The axon arises from the axon hillock of the soma and is a long filament on which electrical impulses can travel to reach other neurons. The axon branches on its end and connects to other neurons via button-like endings called synapses to communicate information from cell to cell. Some axons will be surrounded by an insulating layer, the myelin sheath, which is formed by oligodendrocytes in the central nervous system and schwann cells in the peripheral nervous system (Kandel et al. [2000]).

1.3.2. Anatomy of the Neuronal Cell Wall

Like all cells of the human body, the cell wall of a neural cell consists of a phospholipid bilayer with a number of large proteins embedded in and attached to it. Phospholipid molecules are esthers of glycerol and contain two long-chain fatty acids, the fatty acid chains are hydrophobic while the 'head' of the molecule is hydrophilic. Membrane proteins can act as pathways to transport substances from one side of the membrane to the other, either in the form of active energy dependent pumps, as transporters, or as channels that contain trans-membrane aqueous pores

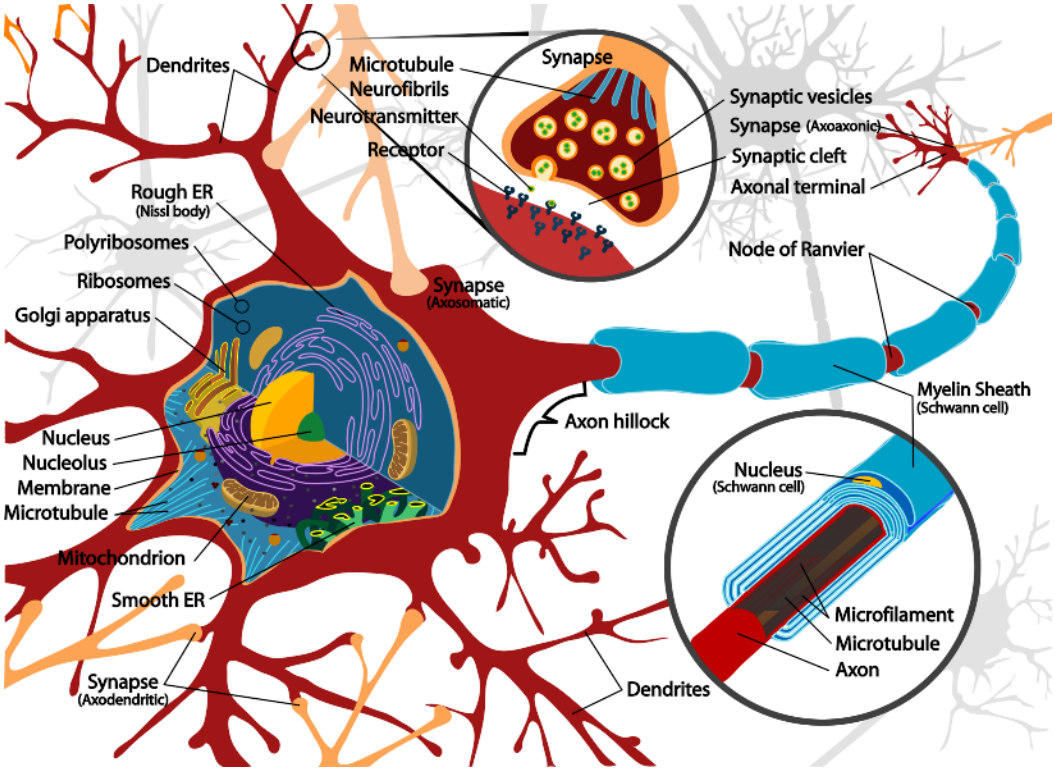

Figure 1.1.: Diagram of a typical myelinated neuron (source: http://en.wikipedia.org).

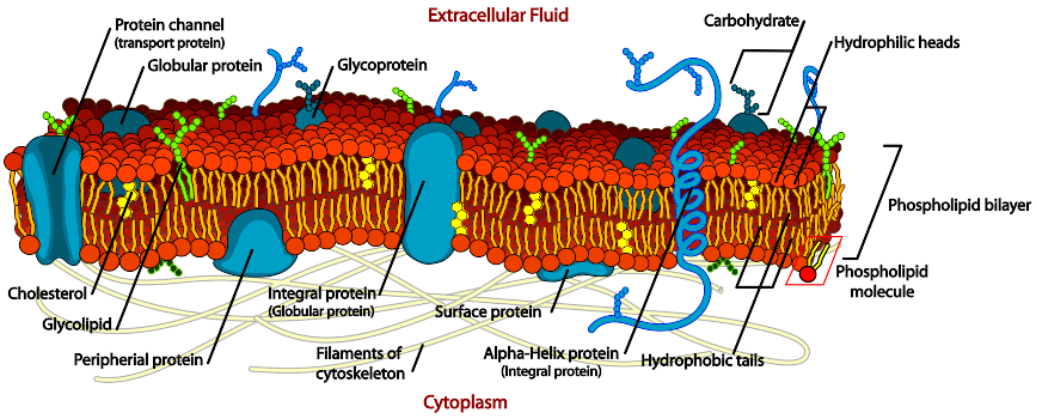

Figure 1.2.: Phospholipid bilayer of cell membranes with its hydropilic outside ('heads') and hydrophobic inside ('tails') (source: http://en.wikipedia.org).

which can allow water or ion to flow down their concentration gradient. The cell wall is approximately 8-10 nm thick and electrically it acts as a combined resistor and capacitor in parallel. Cell walls have a very high intrinsic electrical resistivity as they contain lipids so that most conductance in cell walls is due to the alternative pathways across membrane proteins, the ion channels. The resistivity of neural tissue therefore depends on whether the ion channels within the membrane are in a closed or open state (Aidley [1998]).

1.3.3. Neural Membrane at rest

Excitable cells maintain a constant membrane potential during rest. This membrane potential is generated by ion channels that are selective to certain ions and specific ion pumps. Membrane potentials can generally be created when two compartments containing fluids with different salt concentrations are separated by a semi-permeable membrane that, for example, only lets one type of kation through. The difference in salt concentration in cells is achieved by a constantly working ATP-dependent pump that exchanges 3 sodium ions for 2 potassium ions . The action of this pump, the $\frac{3Na+}{2K+}$-ATPase, leads to high concentrations of extracellular sodium and high potassium intracellular. The cell membrane at rest is mainly permeable for potassium ions so that the potassium ions flow will follow the diffusion gradient. In the cell there is about 30 times as much potassium inside the cell compared to outside so that there will be chemical force that drives the potassium ions to the extracellular space. As the anions cannot follow the potassium there will be a negative charge on the inside of the cell (Klinke and Silbernagel [2003], Aidley [1998]). David Goldman developed the constant field theory in 1943 which assumes that (1) ions move in the membrane under the influence of electric fields and con-

centration gradients just as they do in free solution, (2) that the concentration of ions in the membrane at its edges are proportional to those in the aqueous solutions in contact with it, and (3) that the electric potential gradient across the membrane is constant (Goldman [1943], Aidley [1998]). From this assumption the equation to calculate cell membrane potential when there is no current flowing was derived and first systematically applied by Hodgkin and Katz in 1949 (Hodgkin and Katz [1949]). The normal resting potential on the membrane of a neuron is between -70 and -80 mV.

1.3.4. The Action Potential

Information is transmitted by changes in the membrane potential of neuronal cells. This change of membrane potential is termed action potential. Action potentials have three phases (1) the fast depolarization and reversal of the membrane potential, (2) slower repolarization and (3) hyperpolarization. To start an action potential voltage-gated sodium channels as well as voltage-gated potassium channels open, the presence of voltage gated ion channels in the cell wall of neuronal cells allows neurons to be excitable. There is a big driving force for sodium ions to enter the cell following their chemical gradient which leads to a transient reversal in polarity (reaching a membrane potential of +20 mV). These voltage-gated sodium channels progress into an inactive state after opening and the repolarization is started. Due to the simultaneous activation of voltage-gated potassium channels the repolarization is sped up and there will be a short period of hyperpolarization. Action potentials follow the so-called all-or-nothing law. This means they will either be elicited with unchanged amplitude when a depolarization above the threshold opens voltage-gated sodium channels or nothing will happen. Information in the neural system must therefore be coded by frequency of action potentials rather than changes in the amplitude of action potential (Klinke and Silbernagel [2003], Aidley [1998]).

1.3.5. Propagation of the Action Potential

A depolarization on the neuron will propagate down the axon to reach other neurons. The areas of the membrane next to the depolarized section will also depolarize due to opening of their voltage gated channels. The action potential only travels down the neuron in one direction because the sodium channels have a refractory period during which they are unable to pass current after an action potential. The axons of some neurons will be myelinized in order to speed up conduction. Myelin increases membrane resistance and reduces capacitance. The myelin sheath is arranged in an interrupted fashion with unmyelinated segments called nodes of Ranvier between them. An arriving action potential will depolarize the unmyelinated membrane only so that the movement of the action potential can commence in a saltatory fashion which increases the conduction velocity. The arriving depolarization will then be transmitted by synapses to excite or inhibit other neurons. These synapses can either be chemical or electric. In electric synapses, which for example connect

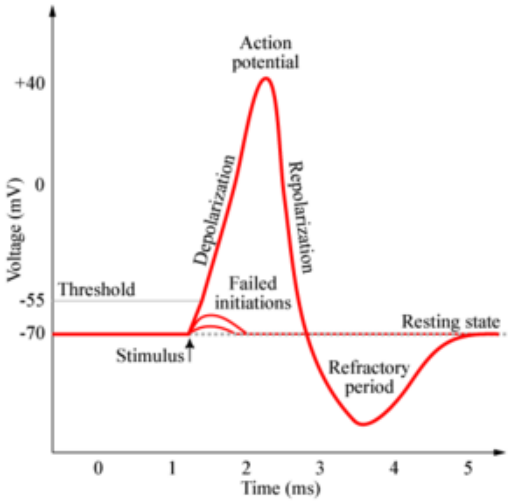

Figure 1.3.: Action potential showing the fast depolarization according to the all-or-nothing law, the slower repolarization and the refractory period (source: http://en.wikipedia.org).

neurons of the thalamus to each other, the synapse is directly connected to the membrane of the next neuron via channels termed gap junctions. The electric potential can then directly travel from the neuron to the next cell (Hestrin [2011]). In chemical synapses a neurotransmitter is excreted from the synapse in response to an incoming action potential. This neurotransmitter is stored in the nerve ending in vesicles which fused with the presynaptic cell wall to release their contents into the synaptic cleft in response to the influx of Ca^{2+}ions. The influx of Ca^{2+}ions is achieved by voltage gated calcium channels which open when in response to the incoming action potential. The neurotransmitter will diffuse across the synaptic cleft to bind and activate receptors on the postsynaptic membrane, and can either have an excitation or inhibitory effect onto the next neuron. The temporary depolarization of the postsynaptic membrane is termed excitation postsynaptic potential (EPSP) and the temporal or spatial summation of EPSP's can lead to an action potential. The temporary hyperpolarization of the postsynaptic membrane due to inhibitory neurotransmitters is called an inhibitory postsynaptic potential (IPSP) and it makes the occurrence of an action potential less likely (Kandel et al. [2000]).

1.4. Neuro-imaging methods

Electric Impedance Tomography as a neuro-imaging method will be discussed separately in 1.7. EIT can image both the neuronal activity directly as well as metabolic changes associated with neuronal activity, but does not provide a structural image of the brain.

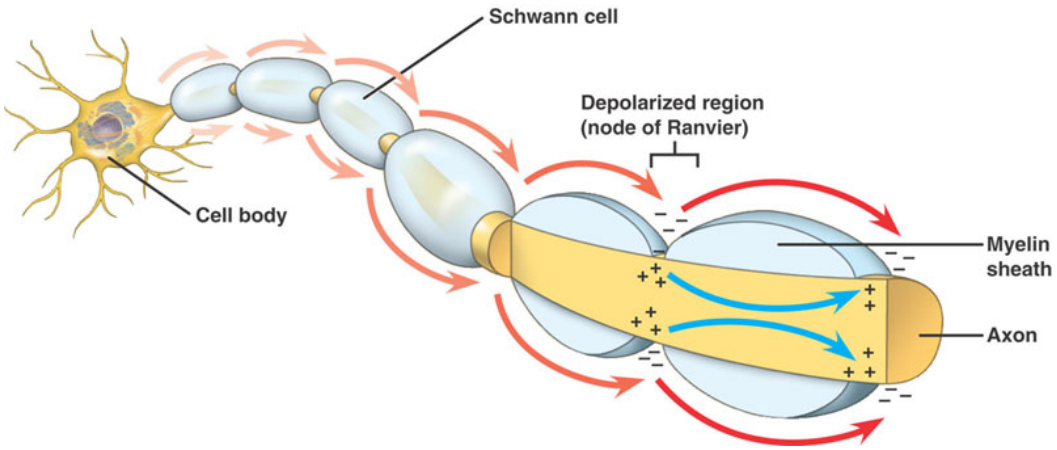

Figure 1.4.: Saltatory conduction of the action potential on an axon showing the 'jumping' depolarization along the axon (source: http://en.wikipedia.org).

1.4.1. Structural imaging methods

The currently most commonly used structural neuro-imaging methods are CT and MRI. CT uses x-rays and hence has the disadvantage that ionizing radiation is needed for a scan. It has the advantage of a very accurate imaging of the bony structures, blood and a reasonable contrast in the soft tissues especially when contrast agents are used (Kretschmann and Weinrich [2004]). It is furthermore a very fast technique and it can usually be performed with monitoring equipment for the patient in place which makes an invaluable clinical tool for strokes or imaging in acute medical settings. MRI is an imaging method that makes use of the nuclear magnetic resonance of atoms and can provide good contrast between soft tissues. It is the best method to obtain a structural image of the brain and can be further enhanced with contrast agents (Kretschmann and Weinrich [2004]). It has the advantage of not using any ionizing radiation, but is expensive and the scans take much longer than CT scans. Also, most standard monitoring equipment can not be brought into the MRI scanner which makes a MRI scan of intensive care patients difficult.

1.4.2. Imaging the metabolic changes associated with neuronal activity

Several imaging methods use the physiological increase in blood flow and metabolism caused by neuronal activity. Functional MRI, PET, functional ultrasound, and most optical imaging methods all make use of either changes in blood flow directly or their oxygen and glucose contents. The currently most commonly used functional imaging method is fMRI, in which the changes in blood supply of active areas are

used for mapping. In fMRI the different effect of oxygenated and deoxygenated haemoglobin in the blood on a magnetic field is used. If an area in the brain is activated its metabolic demands rise and more blood is directed to this area. The increase in blood flow leads to a higher oxygen content in active vs inactive areas of the brain, this effect is called the blood-oxygenation level dependent (BOLD) response (Logothetis [2008]). fMRI has a good spatial resolution of about 2mm (Hopfinger et al. [2000]), but it's temporal resolution is intrinsically limited to the time it takes for the blood flow to respond to neural activity which makes it not useful to image the spread of neuronal activity. PET imaging of neuronal activity also makes use of the metabolic demands of activated neuronal tissue. To image neural activity a radionuclide, such as oxygen-15 or fluorodeoxyglucose, is injected and its emitted positrons are indirectly measured (Wieler et al. [1986]). Often a CT scan is performed on the same patient in the same machine to aid 3D imaging by co-registering the images. Ultrasound is another method that has recently been used for functional neuroimaging based on the changes in bloodflow for research purposes. To image with ultrasound (US) high frequency pulses are sent into the tissue and their echos are recorded. The pulses are scattered by the different tissues and their echoes can be used for image reconstruction. Moving blood can specifically imaged by the characteristic change it causes to the emitted pulses in the tissue by making use of the Doppler effect. New developments in ultrasound have allowed researchers to record changes in local blood flow in response to neuronal activity (Macé et al. [2011], van Raaij et al. [2011]). Some have enhanced this effect with an injectable contrast agent (van Raaij et al. [2012]). Further to the methods discussed, there are several optical imaging methods that have been applied to image neuronal function, mainly in research settings. Diffuse optical imaging uses the different spectra of oxyhaemoglobin and deoxyhaemoglobin while intrinsic optical imaging measures the absorption spectra of blood (Gibson et al. [2005], Franceschini et al. [2003]). Both of these methods have a good temporal resolutions but can only be used to image on directly underlying cortex, which limits its clinical usefulness.

1.4.3. Imaging the neuronal activity directly

EEG and MEG record a surface map of the electric and electromagnetic fields that neural activity produces, respectively. Both have a temporal resolution of milliseconds and both can be used for source modelling (Barkley and Baumgartner [2003], Jousmäki [2000]). However the inverse solution of EEG is not unique and no travelling activity can be imaged unless it is occurring directly on the cortical surface on which EEG electrodes are placed. Unfortunately, no 3D imaging of the travelling neural activity is possible with either EEG or MEG. Another way of imaging the neuronal activity directly are voltage sensitive dyes or calcium sensitive dyes, which can be used to image changes in neuronal cell wall due to activity or change in intracellular calcium concentration, respectively. These methods are used for research purposes, they provide excellent temporal and spatial resolution for surface recordings, however they require exposed brain and they are neurotoxic

which limits their clinical usefulness (Hillman [2007]).

1.5. Introduction to Electric Impedance Tomography (EIT)

Electrical impedance tomography is an emerging method that could potentially be used for imaging neural activity as well as some pathological changes in the brain e.g. in stroke or epilepsy (Oh et al. [2011a], Liston et al. [2012], Holder [1987]). The company Draeger has recently marketed an EIT-system that adjusts ventilator settings according to their recordings on ventilated patients in intensive care. The use of bio-impedance for breast tumour detection has also been suggested (Holder [2005], Costa et al. [2009]). Electrical impedance is a measure of the opposition a tissue or other substance has to current (Kennely [1893]). Information in the neural systems is transmitted by electrical changes on neurons, this change in membrane potential is due to changes in the conductivity of the membrane to sodium and potassium ions via ion channels. The resistance of the neuron changes with the opening and closing of ion channels that allow more or less ions to pass through the cell membrane. As electrical current passes through biological tissues via the ions within the substance, changes in the ion concentration in the different compartments of the cell will change the electrical conductivity of biological tissue (Aidley [1998]). The idea of using electrical impedance to measure neuronal activity is not new in itself - in fact in the 1930's several researchers used measurements of changes in impedance to substantiate the then-assumption that the membrane potentials and action potentials were due to opening and closing of ion channels (Cole and Curtis [1939], Lullies [1930], Cole and Curtis [1938]). Electric impedance measurements make use of some of the basic electric properties of neurons and its use for imaging neuronal function therefore seems favourable. There are several technical difficulties to overcome but electric impedance tomography has the potential to provide functional images with a very high temporal resolution. The speed in which information is transmitted in the brain makes the temporal resolution of any functional brain-imaging method crucial. Most other imaging methods (e.g. fMRI and PET) are measuring secondary effects of neuronal activation and therefore have an intrinsic limit to temporal resolution. Electric impedance however would have the potential to measure the slow secondary changes due to neuronal activation as well as the primary fast electric component of neural activity.

1.6. Bio-impedance of neural tissues

Bio-impedance is a measure of the opposition of a biological system to current flow which depends on the resistive and capacitive properties of the tissues. Mathematically, impedance is measured in ohms and is represented by a complex number with a real part - the resistance (R) - and an imaginary part - the reactance (X).

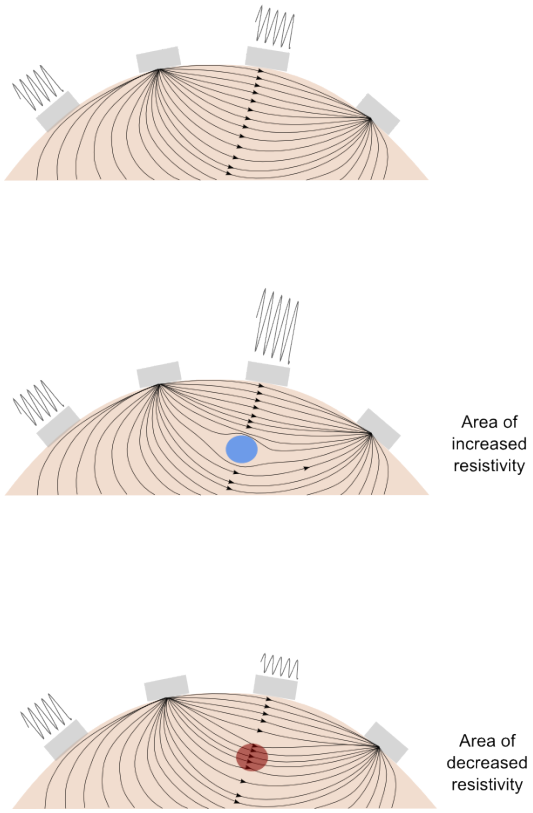

Figure 1.5.: Principle of EIT represented on a semicicular body with electrodes on the surface. Current is passed between a pair of the electrodes and the remaining electrodes are used to record the resulting voltages. The flow of current and hence the recorded voltages change if the resistivity of the cortex is temporarily altered. The top figure shows the current pattern at rest, the middle figure shows the alteration in voltage if the resistivity is temporarily increased and the bottom figure shows the alteration in voltage if the resisitvity is temporarily decreased.

Reactance is the opposition of a circuit element to a change of electric current or voltage, due to that element's capacitance (the ability of a body to store an electrical charge), as a built-up electric field resists the change of voltage on the element. As discussed above, the opening of ion channels during action potentials or post-synaptic potentials causes the electrical resistance of neuronal cell membranes to decrease. As a consequence, the resistance of a neural tissue is expected decrease by 0.06-1.7% during local neuronal activity, as predicted by biophysical modelling based on cable theory (Liston et al. [2012]). In contrast, the capacitance of cell membranes does not change substantially with the opening of the ion channels, and therefore the effect of neuronal activity on the reactance of the neural tissue is most likely negligible (Cole and Curtis [1939]). For this reason, in the present thesis I will consider only the resistance - and not the reactance - of neural tissues and its modulation during neuronal activity.

1.7. Electrical Impedance Tomography of Brain function

Electrical Impedance Tomography (EIT) is a novel method employed for the imaging of neural activity. EIT uses electrodes for the injection of electric current into an object and for the measurement of electric potential over its surface. One or more pairs of electrodes are then used to inject a defined current and the remaining electrodes record the resulting voltage maps on the surface of the object. EIT has the potential to image fast neuronal activity in the brain by treating it as a network of resistors and reconstructing changes in the resistance of neural tissue due to activity. Resistive changes in the brain can be detected as voltage changes on its surface, and because the injected current is known, these resistive changes can be reconstructed by mathematical modelling.

1.7.1. The sine wave method in EIT

Oh et al. developed a method to measure impedance changes due to the fast neural in the cortex of a rat (Oh et al. [2011a]). The experimental set-up they used is illustrated in figure 1.6 and it included a 29-channel electrode grid being implanted on the part of the primary sensory cortex (S1) that represents the forepaw in a rat. The electrode was connected to a current source and EEG recording system via a multiplexer. The multiplexer would address two electrodes on the electrode grid for current injection and the remaining electrodes recorded the resulting voltage map. They used a carrier frequency of 225 Hz for the injected current and reported peak impedance decreases of -0.07% in response to an electric stimulus at 2 Hz. The injected constant current sine wave was locked to forepaw stimulus which was applied at 2 Hz. The frequency of the carrier frequency was odd (225 Hz), which resulted in the first of each pair of evoked stimuli being in phase while the second is in antiphase. The activation of neurons due to the forepaw stimulation will produce a voltage itself that can be recorded with surface electrodes. This voltage due to

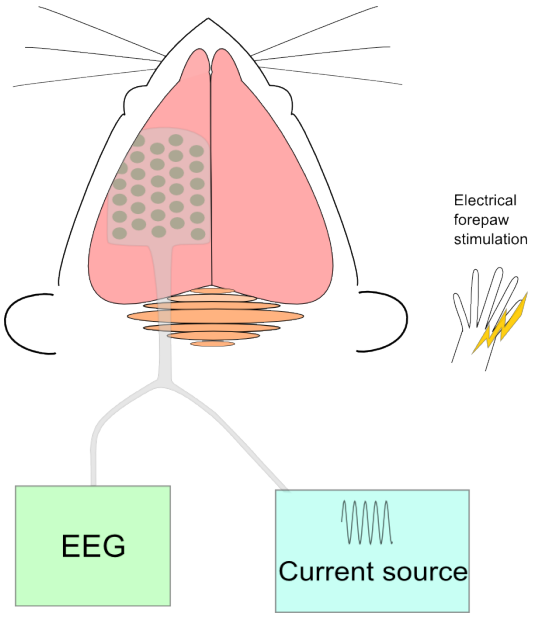

Figure 1.6.: Experimental set-up for EIT recordings of the fast neural response to electric stimuli to the forepaw of a rat. Two of the contacts on the electrode grid are used for current injection and the rest is recording the voltages. The recorded voltages contain the EEG with the voltages added due to the current injection.

neuronal activation is called evoked potential (EP) and will be discussed in detail in 2.1.2.2. When EIT recordings are conducted with the set-up described by Oh et al. the injected current will cause a voltage that can be measured on the surface of the brain which is altered by the changing resistivity (or its inverse the change in conductivity ($\Delta\sigma$)) of the tissue due to neuronal activity and has the EP of the neurons themselves added to it. In order to extract the evoked potential two consecutive segments can be added together. The carrier frequency will be cancelled out as the segment with the first evoked stimuli will be in phase while the second one will be in anti-phase. When two consecutive segments of evoked activity are subtracted from each other the evoked potential will mostly cancel out. The change in conductivity ($\Delta\sigma$) is a good measure of the change in impedance (ΔZ) as it is mainly the conductivity changing (the phase angle of nervous tissue is less than 10° up to 1 kHz (Oh et al. [2011b]). The $\Delta\sigma$ can be extracted by band pass filtering and demodulating the evoked potential free segment and is used as a measure of the change in impedance (ΔZ)(Oh et al. [2011a]).

1.7.2. Image reconstruction process

In order to calculate the change in conductivity $\Delta\sigma$ (the inverse of resistivity) in the brain, the flow of current is modelled in a 3D model of the head. The boundary voltages (BV) which should result from a known injected current with this estimated $\Delta\sigma$ is calculated for every element of the 3D model (also called the mesh). The calculated results are then matched to the recorded BV's and the process repeated with a different estimate of $\Delta\sigma$ should they not match. This iterative process is called inverse modelling. It is easy to understand that this is an intensely time consuming process and therefore most EIT recordings are reconstructed using a sensitivity matrix. A sensitivity matrix (also known as the Jacobian matrix) is a matrix which is defined by the mesh, the electrode positions, the current injection and the measurement protocol. The sensitivity matrix allows the mapping of the measured Δv to $\Delta\sigma$:

$$\Delta v = A\Delta\sigma \tag{1.1}$$

where A is the sensitivity matrix. $\Delta\sigma$ can then be calculated as:

$$\Delta\sigma = A\,\dagger\,\Delta v \tag{1.2}$$

where $A\dagger$ is the pseudo-inverse of the sensitivity matrix. The multiple $\Delta\sigma$'s can then be used to reconstruct an EIT-image. When using a sensitivity matrix we use a linear approximation of the forward model, so treat the change in conductivity as linear, when in fact it is not. This approximation can be used as Δv changes in a nearly linear fashion provided that $\Delta\sigma$ is small (less than 20% (Holder and Khan [1994])) which is the case in imaging fast neural activity with a $\Delta\sigma$ of approximately 1%. Our Mesh requires a large number of elements to provide accurate forward modelling (calculating the expected flow of current). However, we have substantially fewer independent measurements (voltage measurements on elec-

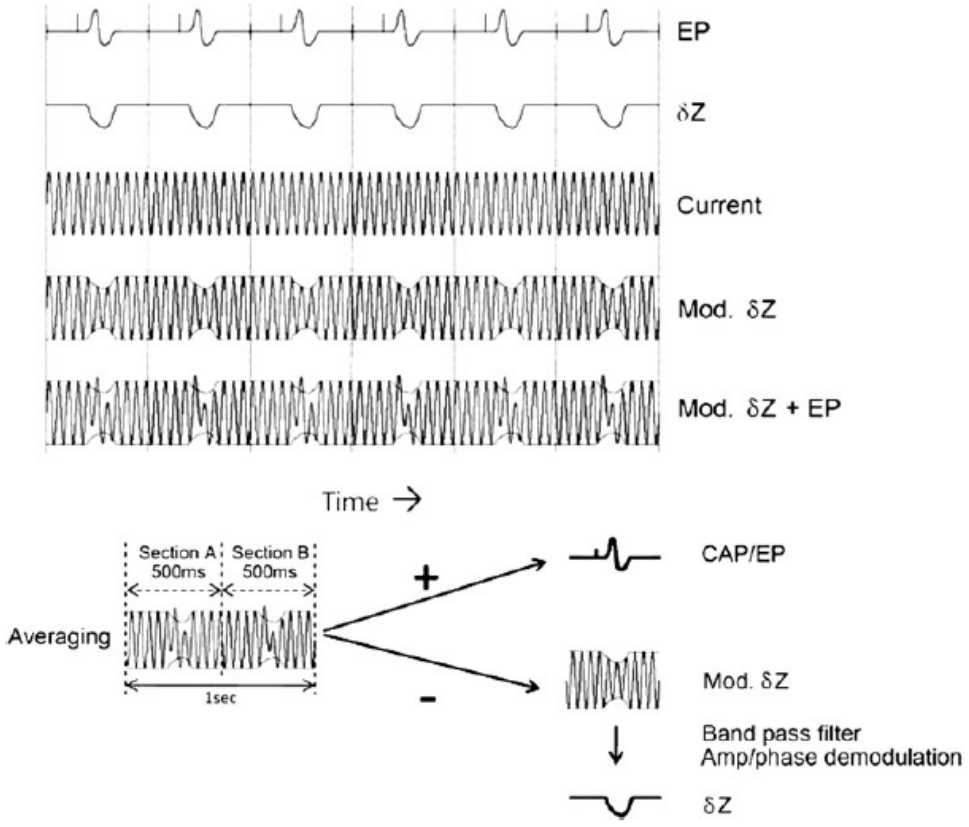

Figure 1.7.: Illustration of extraction of ΔZ Oh et al. [2011a], with permission. By adding to segements in anti-phase the evoked potential is extracted. By subtracting them the EP is removed mostly from the data and the remaining voltages can be band-pass filtered to obtain the ΔZ .

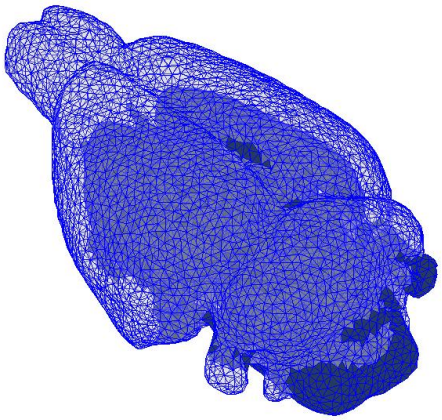

Figure 1.8.: Finite element mesh used as a 3D model to calculate the flow of current.

trodes) than unknowns (elements in the mesh) in the domain. Mathematically this means that the problem is under-determined (we have more unknowns than explanatory measurements) and therefore regularization assumptions (adding assumptious information) are needed for the inverse modelling.

1.7.3. Instrumentation

A recording system for EIT as used by Oh et al. has the following components (Oh et al. [2011a]):

- A current source for current injection
- A multiplexer, to switch between pairs of injecting electrodes
- A recording system to record voltage maps; a clinical EEG head-box is usually sufficient
- A personal computer for control of the components and data storage

1.8. Purpose and Design

The goal of this thesis is to develop EIT as a neuroimaging method and to test its potential usefulness in clinical settings. In order to be useful for the clinical setting it ideally would supply us with a 3D image of the neuronal activity in the entire volume of the brain or the area of the brain that is covered by electrode grids as mesial structures are involved in a substantial number of operable epilepsy

forms. As a first step it was necessary to improve the method Oh et al. described (Oh et al. [2011a]). This was accomplished by improving the rat, testing which which carrier frequency to use, and testing two competing assumptions from the biophysical modelling. An attempt to image physiological function in 3D has then been made and its limitations are discussed. I then focus on epilepsy, where the pathophysiology allows using EIT to image more than just one process and I make an assessment of EIT's potential for clinical use.

2. Anaesthetic considerations for EIT measurements

2.1. Introduction

2.1.1. Orienting statement

EIT recordings of sensory stimuli in anaesthetised animals are planned and should the effect that the anaesthetic might have on the recordings should therefore considered. There is no data available that describes the effects of anaesthetic drugs on EIT recordings, but it is highly likely that the effects anaesthetics have on the sensory evoked potential (SEP) in EEG will correlate with the effects it has on the EIT signal. Evoked potentials (EP's) in EEG represent a population of neurons that are similarly orientated and fire simultaneously such that a large change in impedance is expected with large EP's in the EEG. A review of the available literature on the effect of anaesthetics on SEPs in EEG has therefore been undertaken. It is well described in the literature that anaesthetics, to varying degrees, cause a decrease in the amplitude and an increase in the latencies of evoked potentials. The decrease in amplitude of evoked potentials - especially auditory evoked potentials - is even used to monitor anaesthesia depth (Mantzaridis and Kenny [1997], Kurita et al. [2001], Davies et al. [1996]). Apart from minimizing the depressing effect of anaesthetics on our recordings other considerations should be taken into account. The anaesthetic regime chosen for these experiments should be well controllable, in order to keep the rat in a stable state for prolonged recordings, and have as little systemic and autonomic effect as possible. Additionally, the depth of anaesthesia should be as stable and as easily adjustable as possible as there is a different depth of anaesthesia necessary for surgery compared to the recordings.

Four general anaesthetics were chosen and their effects on evoked potentials tested; these comprised anaesthetics that have been reported to have minimal depressing effects on EPs and one anaesthetic for which no data is available at present.

2.1.2. Background

2.1.2.1. Previous work

The previous anaesthetic protocol within our group was developed by Oh et al. to conduct their EIT measurements on the rat's cortex. The anaesthetic protocol for this study comprised induction with 4% halothane and maintenance with 1-2% halothane with a 70/30% mix of O_2 and N_2O. The animals were tracheotomized and the blood pressure was constantly monitored (Oh et al. [2011a]). These experiments were terminal. The previous group achieved an average EP amplitude of $655 \pm 212 \mu V$ (mean±SD) with this protocol. The intra-individual variability was substantial: one standard deviation of the intra-individual measurements was typically one third of the mean value.

2.1.2.2. Evoked Potentials

Somatosensory evoked potentials are pre− and postsynaptic responses recorded over parts of the nervous system following stimulation of a peripheral nerve, the visual or the auditory system (Daube [2002]). Evoked potentials can also be elicited by physiologic stimuli to the peripheral nerves (e.g. tendon stretch, finger tap), but only electric stimulation produces amplitudes big enough to make the EP sufficiently reliable for clinical use (Daube [2002]). EP's are most commonly recorded in electroencephalograms (EEG) in clinical use but are also measured with magnetencephalography (MEG) for research purposes. Evoked potentials are generally rather small, with amplitudes of up to several microvolts in human scalp recordings, compared to the background EEG fluctuations, which are tens of microvolts in human scalp recordings. Evoked potentials have to be repeated and averaged over time in order to be recorded reliably. There are generally 500-2000 repetitions needed to record somatosensory EPs from the scalp of a human (Daube [2002]).

Somatosensory Evoked Potentials SEP's in humans are usually recorded over the limbs, spine, and scalp following the stimulation of peripheral nerve trunks and cutaneous nerves. The most commonly used peripheral nerves are median or ulnar on the upper limb, and tibial or peroneal nerve on the lower limb (Daube [2002]). Factors that affect the amplitude of the evoked response are muscle artefact and electrical artefact, which includes stimulus artefact and 50 Hz mains hum. The convention for naming the deflection is N for upward (negative) and P for downward (positive) deflections when recording with the grid-1 negative-up convention (Daube [2002]). The first cortical positive deflection is often termed P1, and the first negative deflection is termed N1. Alternatively a description of the positive and negative peaks according to their latency in milliseconds can be found in the literature e.g. P_{10} for a positive peak occurring at 10 ms. P1 is generally more consistent in size than N1 in median nerve evoked potentials and is therefore preferably used in this review (Daube [2002]).

Humans The average peak-to-peak (P-N) amplitude of human scalp recordings of median nerve EPs is 1-5 μV (Colon and Visser [1990], Peterson et al. [1986]). The amplitude, but not so much the latency, of EPs shows great intra - and inter-individual variability and is often distributed in a non-Gaussian fashion (Colon and Visser [1990]). Allison et al., following median nerve stimulation, recorded intracranial SEPs with amplitudes of 195.3 ± 60.9 µV for recordings without general anaesthesia and 79.8 ± 21.0µV with various general anaesthetics; however, this was a study with a wide range of surgical patients and the anaesthetic protocols for the group was not uniform (Allison et al. [1989]).

Rats There was no data for median nerve stimulation in the awake rat found in the literature review undertaken; however the evoked response to various noxious

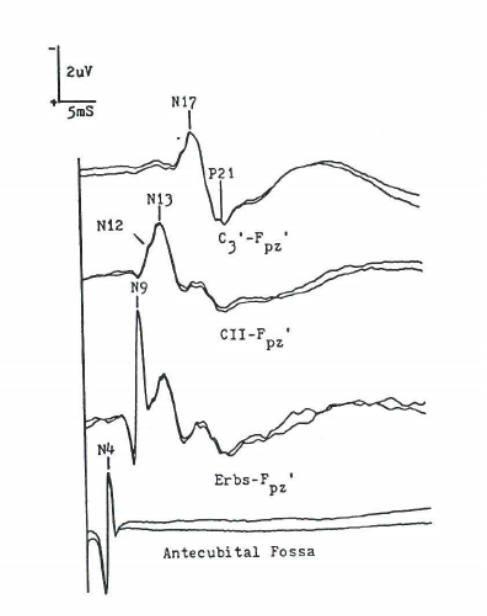

Figure 2.1.: Standard EP recorded on a human scalp after stimulation of the median nerve. Source: DeLisa et al. (1994), with permission.

stimuli in the awake animal has been reported. The reported EPs were recorded epidurally and P1 amplitudes of 25 μV and 240 μV were recorded in response to noxious stimuli to the tail and the whisker pad (Stienen et al. [2003]). In contrast to the limited data on awake recordings, there are several groups that reported the size of EPs in their paradigms under a multitude of anaesthetics. These studies are differentiated into intra- and extra-cranial recordings to allow for comparison of EP amplitudes. In extra-cranial recordings the authors either used sub-dermal needle electrodes or attached the recording electrode to the skull. With subdermal needle electrodes P1 amplitudes of $17 \pm 7.8 \mu V$ have been reported under pentobarbital anaesthesia (Freeman and Sohmer [1996]). Another group that used subdermal needle electrodes did a comparison of EP amplitudes under different anaesthetics and reported P1 amplitudes of 8.21 μV (SD 4.99) under ketamine, 7.52 μV (SD 3.54) under medetomidine, 5.41 μV (SD 2.64), and 6.29 μV (SD 2.64) under fentanyl/fluanisone/midazolam anaesthesia (Hayton et al. [1999]). In a set-up where the recording electrodes were directly fixed to the skull, P1 amplitudes of 200 μV have been reported under $\alpha-$chloralose anaesthesia. In intracranial extradural recordings of P1 amplitudes of 400 μV under pentobarbital anaesthesia have been reported (Desk et al. [1990]). Under anaesthesia with $\alpha-$chloralose and urethane mean P1 amplitudes of 520 μV and 500 μV were reported from epidural recordings, dependent on the frequency of the forepaw stimulation of 1 Hz or 2 Hz respectively (Ngai et al. [1999]). No data for subdural extra-cerebral recordings of

EPs of forepaw stimuli could be found for this literature review. In summary the largest reported EPs were recorded from epidural electrodes under $\alpha-$chloralose anaesthesia. A comparison however remains difficult since different types of electrodes and locations of recordings have been used in the reviewed studies.

2.2. Anaesthetics

Anaesthetics can be differentiated according to the route of administration: volatile (or inhalational), intravenous, intraperitoneal, subcutaneous, or intramuscular anaesthetics. I will not further discuss intraperitoneal, subcutaneous and intramuscular drugs as they are difficult to control over longer periods of time. Most general anaesthetics interact with neurotransmitter receptors, most commonly with the γ-aminobutyric acid (GABA-) system. They act on different subunits of the GABA-receptors and some of these receptors are specific for different areas of the brain (Katzung and Trevor [2009]).

2.2.1. Volatile anaesthetics

Volatile anaesthetics include nitrous oxide, halothane (a fluorinated alkane) and the halogenated methyl ethers, e.g. isoflurane or sevoflurane. Nitrous oxide is an incomplete anaesthetic, but is often added to veterinary anaesthetic protocols for its analgesic value; its mode of action is complex and not fully understood (Travis [2004]). It is assumed that volatile anaesthetics influence $GABA_A$-receptors but mice with altered subunits of their $GABA_A$-receptors only showed an obtunded response to volatile anaesthetics while the effect of injectable anaesthetics such as propofol or etomidate was entirely abolished (Jurd et al. [2003]). Volatile anaesthetics decrease the brain metabolism, but increase cerebral blood flow due to a mild vasodilatory effect (Waelbers et al. [2010]). Halothane has been reported to interrupt the functional-metabolic coupling of the brain in surgical dosages (Ueki et al. [1992]). All of the described volatile anaesthetics cause dose dependent respiratory depression and depress the normal ventilatory response to carbon dioxide, even at sub-anaesthetic concentrations (Schüttler and Schwilden [2008]). Isoflurane is currently the volatile anaesthetic of choice for anaesthesia of rats as it suppresses the cardiopulmonary system less than halothane and is less expensive than sevoflurane (Wolfensohn and Lloyd [2010], Schüttler and Schwilden [2008]). Halothane is being taken off the market in the UK for veterinary use due to its liver toxicity as there is concern for staff health and safety (Njoku et al. [2002], Elliott and Strunin [1993]). Using volatile anaesthetics in humans that require EP recordings during surgery is generally not recommended as they suppress the SEPs to a larger degree than injectable anaesthetics (Sloan and Heyer [2002], Hans and Bonhomme [2006], Sloan [1998]). Hayton et al. compared the effect of isoflurane on SEPs to a range of injectable agents in rats, and found a significantly larger suppression of the EP with isoflurane than with the injectable agents (Hayton et al. [1999]). All of the

currently used volatile anaesthetics decrease the amplitude and increase the latency of cortical SEPs but the effect is dose dependent. In a study that compared the effects of inhaled anaesthetic agents onto EPs in humans it was shown that halothane reduces the N1-P1 amplitude down to 0.54±0.34 μV on a MAC of 1.5 with 60% N_2 O and 0.90± 0.39 μV without N_2O compared to 2.67±1.21 μV before induction. Isoflurane reduced the N1-P1 amplitude to 0.14±0.26 μV on a MAC of 1.5 with N_2O and to 0.28±0.33 μV without N_2O down from 2.80±2.02 μV (Peterson et al. [1986]).

2.2.1.1. Alfaxalone

Alfaxalone is an anaesthetic steroid; anaesthetic steroids modulate $GABA_A$-receptors in a way that increases the effect of $GABA_A$on these receptors. They were taken off the market in the mid-80's as the soluble agent it was distributed in caused allergic reactions, however, no such reactions have occurred since it was reintroduced with an improved soluble agent (Whittem et al. [2008]). A single dose of alfaxalone will provide short term anaesthesia, but it can be used for long-term surgery if a continuous infusion is given Wolfensohn and Lloyd [2010]. Alfaxalone is easily adjustable, has a linear anaesthetic effect, and minimal effect on blood pressure (Wolfensohn and Lloyd [2010]). The effect on EEG as tested in dogs was a shift in the dominant frequency band from beta to delta and occasional burst suppression. At some frequencies EEG power increased soon after the start of alfaxalone infusion, then decreased below baseline later (biphasic pattern) (Ambrisko et al. [2011]). The literature review undertaken did not find any study examining the effect of alfaxalone on EPs.

2.2.1.2. α-chloralose

Chloralose is a chloral derivate of pentose or hexose sugars. Chloraloses cause sedation and anaesthesia, but also has a stimulant action manifested by spontaneous myoclonic movements and clonic convulsions following sudden peripheral stimulation (chloralose hyper-excitability) (Balis and Monroe [1964], Wang et al. [2008]). They most likely interact with $GABA_A$-receptors, but the exact mode of action remains unknown (Hayton et al. [1999], Riviere and Papich [2009]). $\alpha-$chloralose activates the EEG in general as well as activating abnormalities in epileptic and brain lesion patients, but rarely ever causes actual seizures in non-epileptic patients (Balis and Monroe [1964], Monroe et al. [1956]). $\alpha-$chloralose also sets off psychotic episodes in patients that have a history of psychosis (MONROE and MICKLE [1967]). It causes minimal cardiovascular depression, little change in blood pressure and no change or only a small reduction in heart rate (Wang et al. [2008]). $\alpha-$chloralose preserves functional-metabolic coupling even at surgical dosages and is especially suited for studies that rely on this coupling process such as fMRI studies under anaesthesia in animals. It produces very light sedation and, as a sole agent, it should only be used for non-painful procedures (Flecknell [2009]). $\alpha-$chloralose should be

used for terminal experiments only due to its toxicity Flecknell [2009]. It has been suggested that $\alpha-$chloralose makes it easier to elicit epileptic seizures by electric stimulation in animal epilepsy models (Rosenblueth and Cannon [1941]).

2.2.1.3. Medetomidine

Medetomidine is a selective full agonist of central and peripheral α_2-adrenoreceptors, it inhibits noradrenergic neurons in the locus coerulus and causes a complete disruption of the signal from the ventrobasal thalamus to the cortex (Angel [1993]). This makes it undesirable for future EIT 3D-imaging projects of deeper structures. It has both analgesic and anaesthetic effects. In a study on the effects of anaesthesia on EPs it reduced the EPs to a larger extent than other injectable agents (see 2.1.2.2 for comparison) (Hayton et al. [1999]).

2.2.1.4. Propofol

Propofol is a short-acting hypnotic, it has a very short half-life and is therefore easy to adjust when given as a continuous infusion. It may cause an initial drop in blood pressure and apnoea. Its effect is mainly due to potentiation of $GABA_A$-receptor activity, and also works as a sodium channel blocker and may affect the endocarbinoid system. It is the favoured anaesthetic by many neuro-anaethetists for anaesthesia involving craniotomies as it has ICP-lowering and oedema-reducing properties (Hans and Bonhomme [2006]). EPs elicited under propofol anaesthesia had significantly larger amplitudes when compared to those under isoflurane anaesthesia and sevoflurane anaesthesia (Clapcich et al. [2004], Boisseau and Madany [2002]).

2.2.1.5. Barbiturates

Barbiturates facilitate the actions of GABA at multiple sites in the central nervous system and appear to increase the duration of GABA-gated chloride channel opening. They also might be GABA-mimetic at high concentrations (Katzung and Trevor [2009]). Commonly used barbiturates in veterinary practice are pentobarbitone, thiopentone, and methohexidone. Pentobarbitone has been shown to decrease the amplitude of SEPs and prolong their latencies to a larger degree than ketamine (Goss-Sampson and Kriss [1991]). All benzodiazepines cause severe respiratory depression (Flecknell [2009]). Pentobarbitol has a very small security margin and accidental overdoses are common (Wolfensohn and Lloyd [2010]). They also lead to functional-metabolic decoupling (Ueki et al. [1992]).

2.2.1.6. Benzodiazepines

Benzodiazepines − in contrast to barbiturates − enhance GABA effects allosterically without interacting with the GABA-receptor (Katzung and Trevor [2009]). Benzodiazepines produce frontal $\beta-$activity with a decrease in $\alpha-$activity at low

doses (Sloan [1998]). Midazolam in doses consistent with anaesthesia induction produces mild depression of cortical SSEPs and minimal effect on subcortical and peripheral evoked potentials (Sloan [1998]). Diazepam does not alter the SEP at all when used alone in humans (**?**). All negative effects of benzodiazepines to the EEG are dose dependent, but their effect is less marked than the effect of volatile anaesthetics (Cottrell and Smith [2001], Sloan [1998]).

2.2.1.7. Opioids

Opioids act on the μ-, κ- and δ-opioid receptors. They are commonly used in combination anaesthesia protocols as they act synergistically with volatile and injectable anaesthetics (Cottrell and Smith [2001], Schüttler and Schwilden [2008]). Opioids produce a dose related decrease in frequency of the EEG until the delta-range, while exhibiting almost no effect on the EEG amplitude (Sloan [1998]). As a result of this property they are frequently used in epilepsy surgery (Sloan [1998]). A study on humans showed no significant change in SEP's when fentanyl was given (**?**). However, used alone they are not sufficient as an anaesthetic agent. There have been concerns that opioids may raise intracranial pressure, but this view is no longer supported and opioids are regularly given to patients with raised intracranial pressure (Lauer et al. [1997]).

2.2.1.8. Ketamine

Ketamine acts on N-Methyl-D-Aspartate (NMDA)-, opioid-, muscarinic- and different voltage-gated-receptors. It has analgesic and sedative properties, and appropriate doses of it lead to a lack of apparent awareness termed dissociative anaesthesia (Schüttler and Schwilden [2008]). Ketamine produces high theta activity in EEG with an accompanying increase in beta activity that appears to represent activation of thalamic and limbic structures (Sloan [1998]). It provokes seizure activity in epileptic subjects, but not in normal subjects. It provides excellent analgesia and hypnosis but may increase ICP in patients with intracranial abnormalities (Sloan [1998]). It increases cortical SEP's and increases muscle tone, even spontaneous movements may occur and should it should thus be used in combination with a benzodiazepine (Flecknell [2009]).

2.3. Rationale for the study

The main purpose of this study is to find an anaesthetic regime that allows us to maintain stable surgical anaesthesia over 10 hours or more and decreases the EP amplitude as little as possible. In order to determine the favourable anaesthetic I report on observations specific to each anaesthetic used, such as blood pressure problems or difficulties in maintaining anaesthesia, as well as the mean amplitude reached with each anaesthetic and a comparison between the groups.

2.4. Experimental design

The same anaesthetic protocol as Oh et al. was used to measure impedance and different anaesthetic protocols were tested against their protocol (Oh et al. [2011a]). EPs show a large intra- and inter-individual variability and testing of the anaesthetics regime on large groups of animals was avoided by recording forelimb SEP's under halothane and then a switched to the anaesthetics under investigation. Because this method provided a within-subject comparison, fewer animals were used. The effects of propofol, ketamine, $\alpha-$chloralose and alfaxalone were examined. Propofol was chosen, as it is a commonly used anaesthetic in cranial neurosurgery and it has been previously shown that it allows larger EP-amplitudes than sevoflurane and isoflurane (Clapcich et al. [2004], Boisseau and Madany [2002]). In a study that compared the effect of different anaesthetics on EPs ketamine produced the largest EP-amplitudes and therefore it was included in this study (Hayton et al. [1999]). $\alpha-$chloralose has been chosen as it allows significantly larger BOLD responses in fMRI compared to halothane, but no direct comparison of EP-amplitude under halothane and $\alpha-$chloralose anaesthesia is available in the literature (Austin et al. [2005]). Alfaxalone was chosen as there is no data available on its effect on EPs. The different anaesthetics were tested in a random order to avoid effects of a user dependent learning curve. All anaesthetics were dosed according to the individual need of the animal used; the dosage ranges are given in table 2.1.

2.5. Methods

2.5.1. Animals

10 female Sprague-Dawley rats, 5 to 8 months old and weighed between 280 and 400g were used. They were clinically healthy and were housed in cages in groups of up to three with a 12 hour light/dark cycle and food and water ad libitum. All work done with the rats was approved under UK Home Office regulations and was carried out in accordance with the Animals (Scientific Procedures) Act 1986 regulations and the European Directive 2010/63/EU on the protection of animals used for scientific purposes, project license number 70/7450.

2.5.2. Anaesthetic Protocols

All protocols were tested against a halothane protocol which has been our previous standard (Oh et al. [2011a]). For all protocols adrenaline, labetolol, and mannitol were used if needed for blood pressure and intracranial pressure control. All animals received rimadyl subcutaneously, which is long-acting non-steroidal analgesic for pain control. The animals were relaxated with pancuronium as soon as anaesthesia was sufficient, but only if mechanical ventilation could not be achieved without it. All animals were ventilated via a tracheostoma. Body-temperature of all animals

was monitored with a rectal probe and maintained by the use of a heating blanket attached to a feed-back system. All of our experiments were terminal.

2.5.2.1. Protocol 1: Propofol

- Induce with halothane and nitrous oxide (50%)
- Give s.c. rimadyl
- Perform craniotomy under halothane and record forelimb SEP's with EEG and EIT
- Switch to propofol and await the end of the detection of halothane in the exhaled air by the anaesthetic monitor (and a minimum of 30 min)
- Record forelimb SEP's with EEG and EIT under propofol

2.5.2.2. Protocol 2: $\alpha-$chloralose

- Induce with halothane and nitrous oxide (50%)
- Give s.c. rimadyl
- Perform craniotomy under halothane and record forelimb SEP's with EEG and EIT
- Switch to i.v. $\alpha-$chloralose and await the end of the detection of halothane in the exhaled air by the anaesthetic monitor (and a minimum of 30 min)
- Record forelimb SEP's with EEG and EIT under $\alpha-$chloralose

2.5.2.3. Protocol 3: Alfaxalone

- Induce with halothane and nitrous oxide (50%)
- Give s.c. rimadyl
- Perform craniotomy under halothane and record forelimb SEP's with EEG and EIT
- Switch to i.v. alfaxalone and await the end of the detection of halothane in the exhaled air by the anaesthetic monitor (and a minimum of 30 min)
- Record forelimb SEP's with EEG and EIT under alfaxalone

	Propfol	Alphachloralose	Alfaxalone	Ketamine/ Diazepam
Induction Dose	10-30mg/kg	80mg/kg	N/A	30mg/kg Ketamine
Maintenance Dose	10-50 mg/kg/h	25-35 mg/kg/h	12 mg/kg/h	50-90 mg/kg/h
Source	Flecknell (2009)	Brinker et al. (1999); Ueki et al. (1992); Storer et al. 1997	personal communication Dr Mocho, vetinary surgeon	Flecknell (2009)

Table 2.1.: Doses ranges of the intravenous anaesthetics, all anaesthetic doses were adapted the individual animal requirements to maintain surgical anaesthesia.

2.5.2.4. Protocol 4: Ketamine and Diazepam

- Induce with halothane and nitrous oxide (50%)
- Give s.c. rimadyl
- Perform craniotomy under halothane and record forelimb SEP's with EEG and EIT
- Switch to i.v. ketamine and diazepam and await the end of the detection of halothane in the exhaled air by the anaesthetic monitor (and a minimum of 30 min)
- Record forelimb SEP's with EEG and EIT under ketamine and diazepam

2.5.3. Anaesthetic and surgical procedure

The rat was induced in a perspex box into which a mixture of 2 l/min O_2, 2 l/min N_2O and halothane at 4% was introduced. A nose cone was applied as soon as they lost consciousness and halothane reduced to 2% or less depending on their respiratory effort, and O_2 and N_2O were reduced to 1 l respectively. Mechanical ventilation was started, after a tracheostomy was performed, with a Harvard Apparatus Inspira Ventilator (Harvard Apparatus, Ltd, UK). A veterinary dosing catheter (Size: 8fg, Vet Tech Solutions Ltd., UK) was cut to size and used as a tracheostomy tube. The respiratory rate and tidal volume was calculated automatically by the ventilator based upon the weight of the rat. The rat was initially ventilated in assisted volume mode and then switched to volume mode once the ventilator detected weakening of the breathing reflex ("assist alarm"). The total input of gas was reduced

to 0.3 l/min with a 50/50 ratio of O_2 and N_2O once the mechanical ventilation was started. The blood pressure was monitored via a 24 G cannula (BD Insyte/Vialon, Becton, Dickinson U.K. Ltd.) in the femoral artery with a clinical blood pressure transducer (TruWave, Edwards Lifescience Ltd.) attached to an anaesthetic monitor (Cardiocap 5, Datex Ohmeda). The same anaesthetic monitor also recorded the exhaled gases (CO_2, N_2O and halothane) during the procedure as well as the ECG via adapted standard monitor ECG leads. The femoral vein was also cannulated using a 24 G cannula to allow intravenous access. Anaesthesia depth was monitored throughout the procedure by assessment of withdraw response to painful stimuli (toe pinch) and corneal reflexes. The anaesthetics were adjusted according to the reflex monitoring and absence of increase in blood pressure during painful procedures and evoked potentials, aiming to use as little of any given anaesthetic as possible. Minimal corneal reflexes were tolerated during EP recording, but not during surgery. The mean arterial pressure (MAP, calculated as diastolic blood pressure $+\frac{1}{3}$ systolic blood pressure) was kept between 90 and 110 mm Hg using labetolol and adrenaline as necessary. An increase in MAP to painful stimuli was taken as a sign of inadequate anaesthesia depth and the drug dose was adjusted accordingly. The body temperature of the rat was controlled with a homoeothermic heating unit comprising a heating blanket in which the rat was wrapped and a rectal probe which provided temperature feedback to the system (Harvard Apparatus, Kent, UK) The rat was fixed in a stereotactic frame in the prone position using earbars. The rat's head was then shaved and the skin incised using a scalpel. The bone was then freed from periosteum and the suture lines identified. The insertion of the temporal muscle on the left side was cauterized using a bipolar cauterization system (Malis CMC 2, Codman, USA). The insertion line was then incised with a scalpel and the muscle bluntly dissected off the bone using a cotton bud until the zygomatic arch came into view. A craniotomy reaching para-medial from 2 to 3mm rostral to the bregma to just rostral of the lamda suture in a triangular fashion with the tip of the triangle reaching down laterally to 1 mm above the level of the junction of zygoma to temporal bone (see figure 2.2). A veterinary bone drill was used for the craniotomy (Ideal Micro-Drill ^{TM}). The bone flap was then lifted and the dura incised with micro scissors in a crescent shape and deflected over the mid-line to avoid damage to the superior saggital sinus. The electrode grid (see Appendix A for description) was then placed over the primary sensory cortex. The brain was kept moist with warm (38°C) 0.9% Na Cl solution. The electrode was weighed down with wet cotton wool and covered with cling film to avoid drying the brain out during recordings. A 1.5 x 1.5 cm silver/silver chloride reference electrode plate was placed under the skin of the right side of the skull, opposing the electrode grid. Silver needle electrodes where placed in the right forepaw for stimulation.

2.5.4. Hardware

The system used to record the EPs was a 32-channel EEG acquisition system (ActiveTwo AD-box, Biosemi, Netherlands) with low-noise DC coupled amplifiers, 2 V dy-

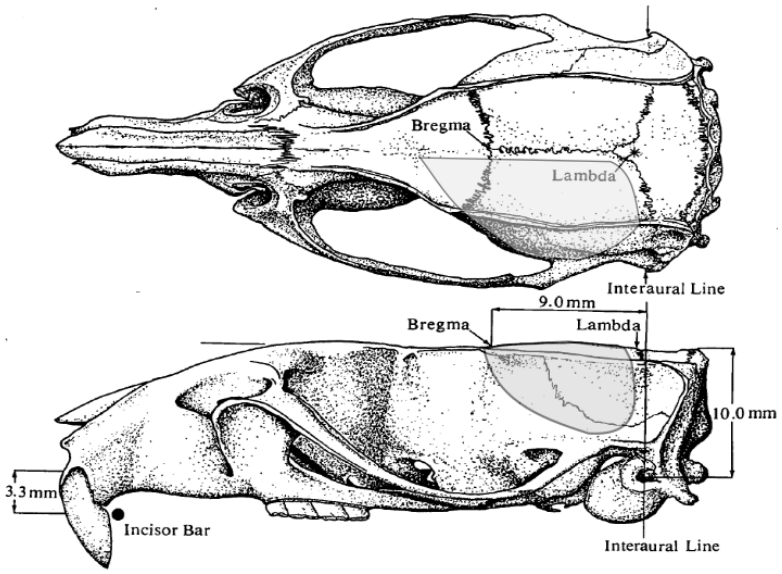

Figure 2.2.: Craniotomy margins shown on an anatomical drawing of the skull.

namic range, and 24-bit output on each channel. Sampling was performed at 16,384 Hz with hardware anti-aliasing filter at 3 kHz. An isolated stimulator (NL800A, Digitimer, UK) was employed to produce somatosensory stimulation. The entire system was optically isolated and controlled by a Windows PC (Fig. 3.6). Some of the EPs were extracted from EIT recordings. For the EIT recordings, an ultra low noise programmable constant current source was used to inject current. It can produce a sinusoidal waveform from 1 Hz to 2 kHz with an amplitude of 0.1–100 μA; the output impedance was over 1 MΩ (UCL-CS2 current source; details in Oh et al. [2011a]). The current source could address any pair of the 29 electrodes in the electrode array. In the EIT measurements voltages were recorded using the EEG system mentioned above. Sampling was performed at 16,384 Hz with hardware anti-aliasing filter at 3 kHz. A more detailed description of the EIT hardware set-up can be found in Chapter 3 under 3.2.3. A diagram of the experimental set-up is shown in chapter 1 under 1.6. The recording electrode grid is described in detail in Appendix A; the design has been published by Schuettler et al. (Schuettler et al. [2008]).

2.5.5. Measurement of evoked Potentials

A 10 mA electrical stimulus to the forepaw at 2 Hz was used to evoke the EPs and these were averaged over 1.5 min. The measurements were recorded with an ActiveTwo AD-box EEG system (Biosemi, Netherlands) and 29 of the 128 available channels used. The sampling frequency was 16 384 Hz, the low pass filter was set to 3 kHz. A current of 50μA at a frequency of 225 Hz was injected using the CS2

in the cases were the EPs were extracted from EIT recordings. The EPs of the EIT recordings were subtracted out so that their values could be used for the calculation of the mean amplitude of the EPs for each protocol as well; this provided EPs averaged over 30 min. The method to extract the EPs from the EIT was the same as used by Oh et al. and is described in detail in 1.7.1. The EEG data sets were read into Matlab (Matlab R2011a) for processing. The reference electrode was a 1.5 x 1.5 cm silver/silver chloride plate which was placed into the skin opposite the recording electrode grid.

2.5.6. Statistical comparison between the groups

The difference between the mean of the EPs with the injectable anaesthetic and the baseline with halothane was used as a variable in each rat. A single sample t-test was used to compare the difference between injectable anaesthetics and baseline. A single-factor ANOVA was used to test for differences between the groups. Post hoc two-sample t-tests with a pooled variance were performed to compare between the groups in pairs. A significance level of $p<0.05$ was set.

2.6. Results

2.6.1. Technical issues

The main technical difficulty during the experiments was ventilator failure, which occurred in four experiments. Subsequently two experiments did not produce usable data. On one occasion the ventilator failed at the end of the experiment.

2.6.2. Anaesthesia dependent observations

2.6.2.1. Propofol

In two of the three subjects that received propofol there was an episode of high blood pressure up to 160/120 mmHg lasting for approximately 30 min. This occurred despite absent blink reflexes and toe-pinch reflex. Another observation worth mentioning is that after 3-5 hours the required dose of continuously injected propofol drops off sharply. In all three cases only half of the initial dose was needed after 5 hours of continuous propofol injection.

2.6.2.2. $\alpha-$chloralose

Animals under $\alpha-$chloralose anaesthesia showed spontaneous movements despite absent blink reflex and toe-pinch reflexes. Two of the three tested subjects had spontaneous whisker movements and one of the subjects moved the forepaw spontaneously.

Group 1: Propofol		
	Halothane (mV)	Propofol (mV)
Rat 1	0.17±0.1	0.31±0.07
Rat 2	0.77±0.002	1.31±0.1
Rat 3	0.59±0.31	0.73±0.1
Rat 4	0.41±0.03	0.42±0.04
Rat 5	0.91±0.12	1.71±0.12

Group 2: $\alpha-$ Chloralose			Group 3: Alfaxalone		
	Halothane (mV)	$\alpha-$ Chloralose (mV)		Halothane	Alfaxalone
Rat 1	0.73±0.27	1.42±0.88	Rat 1	0.63±0.23	0.68±0.22
Rat 2	0.56±0.14	1.4±0.28	Rat 2	0.31±0.02	0.68±0.33
Rat 3	0.49±0.08	1.29±0.18	Rat 3	1.08±0.31	0.54±0.12

Table 2.2.: Summary of results of the evoked potentials in the three groups used for further evaluation.

2.6.2.3. Alfaxalone

There was one run of spikes on the EEG lasting for approximately 20 seconds during anaesthesia with alfaxalone which unfortunately could not be recorded on time. There were no other anaesthetic difficulties under alfaxalone anaesthesia.

2.6.2.4. Ketamine

Prolonged and significant blood pressure drops occurred in both animals in which ketamine was used. The ketamine group was removed from further analysis for this reason.

2.6.3. Comparison of EP amplitudes

The evoked potentials recorded under halothane anaesthesia differed significantly from those recorded under the injectable anaesthesia ($p<0.05$). The ANOVA revealed a significant difference between the propofol, $\alpha-$chloralose and alfaxalone groups ($p<0.05$). The post-hoc t-tests showed no significant difference between the propofol and $\alpha-$chloralose group ($p>0.05$) but a significant difference between

the $\alpha-$chloralose group and the alfaxalone group ($p<0.05$). However, no difference between the propofol and the alfaxalone group could be shown ($p>0.05$).

2.6.4. Shape of the Evoked Potentials

Figures 2.3,2.7,2.4,2.6, and 2.5 shows examples of typical EPs under the respective anaesthetics. It is noteworthy that EPs under halothane anaesthesia are broadened while the shape of propofol is the most natural when compared with a standard EP as seen in figure 2.1.

2.7. Discussion

Our analysis confirmed the notion from the literature that injectable anaesthetics generally produce larger amplitudes for EPs than inhalational anaesthetics (Sloan [1998]). Ketamine was removed from the analysis as the switch from halothane to ketamine led to prolonged blood pressure drops, which might have caused brain damage and would have made any assessment unreliable. These blood pressure drops could well be due to the interaction of the metabolites of ketamine with halothane which has been described in the past (White et al. [1973]). It is expected that similar problems would occur if isoflurane was used for induction instead of halothane, because ketamine interacts with the metabolites of isoflurane as well (Hollmann et al. [2001]). EPs elicited under$\alpha-$chloralose anaesthesia had significantly larger amplitudes than those elicited under alfaxalone, while the amplitudes were not significantly larger compared to propofol anaesthesia. It was, however, difficult to maintain stable surgical anaesthesia with $\alpha-$chloralose, and the long half life of the drug makes dose titration difficult. The most irritating feature of anaesthesia with $\alpha-$chloralose in rats was spontaneous movements that made assessment of anaesthesia depth difficult and may cause movement artefacts. Spontaneous movements under $\alpha-$chloralose have been previously described in the literature and occurred in our experiments while both blink reflex as well as the paw withdraw reflex where absent (Balis and Monroe [1964]). There was no significant difference between propofol and $\alpha-$chloralose or propofol and alfaxalone. There was however a significant difference between $\alpha-$chloralose and alfaxalone. It appears that propofol stands in the middle of these two agents regarding the amplitude of the EPs. Propofol was especially easy to handle and to adjust allowing long periods of stable anaesthesia. Furthermore propofol decreases intracranial pressure, which helps to avoid both injury to the brain during surgery as well as secondary damage to the brain during the recording. Another observation was that the shape of the EPs under propofol anaesthesia are the closest to the natural shape (compare figure 2.1 with 2.7, note that in our recordings, in contrary to the quoted example, positive changes are shown as an upward deflection). EPs evoked alfaxalone anaesthesia were significantly smaller than those evoked under $\alpha-$chloralose which makes it appear the least favourable choice of injectable anaesthetics for recording of evoked

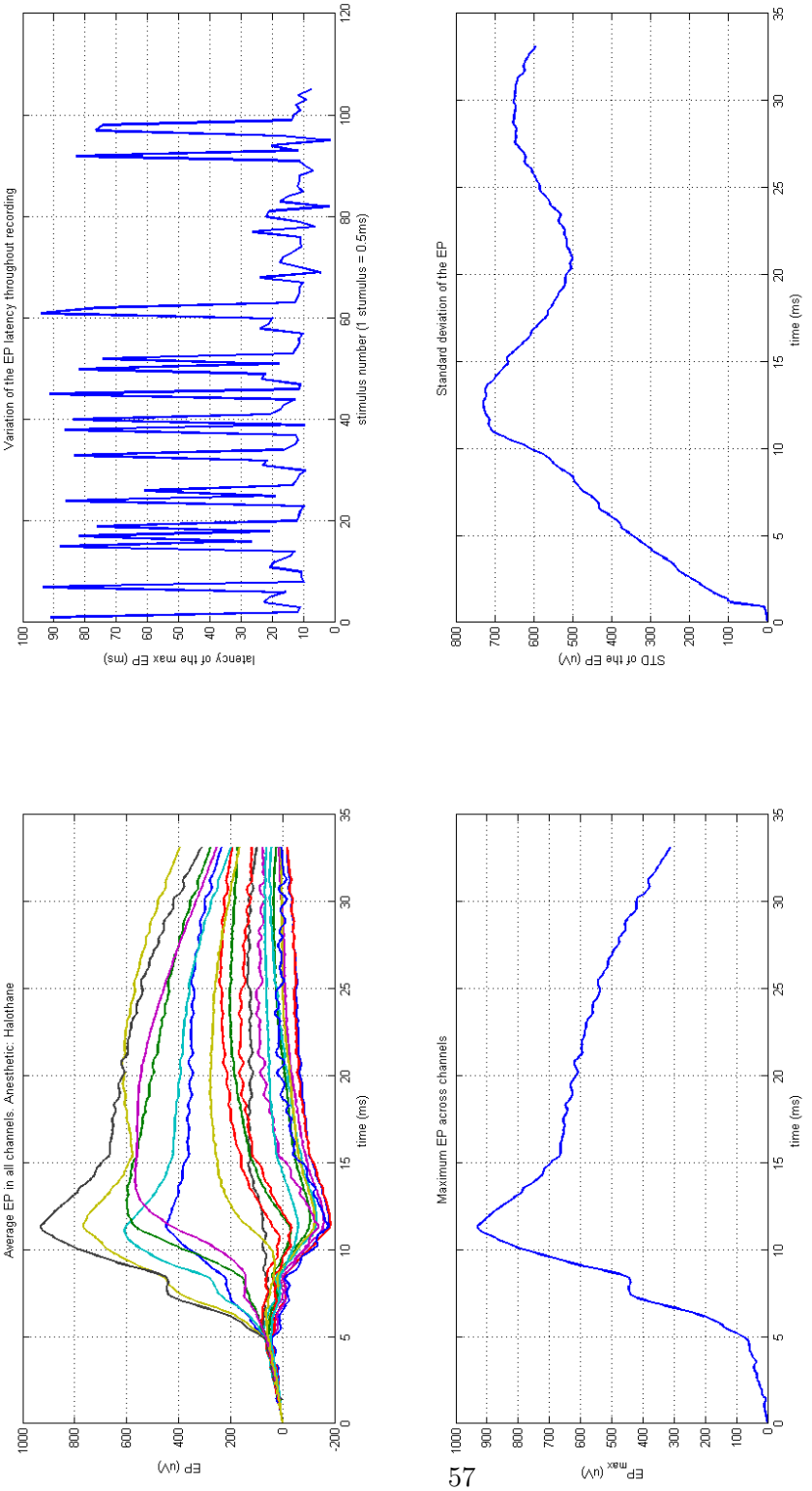

Figure 2.3.: Typical averaged evoked potential under halothane anaesthesia. The top right panel shows the average EP measured in all channels, the

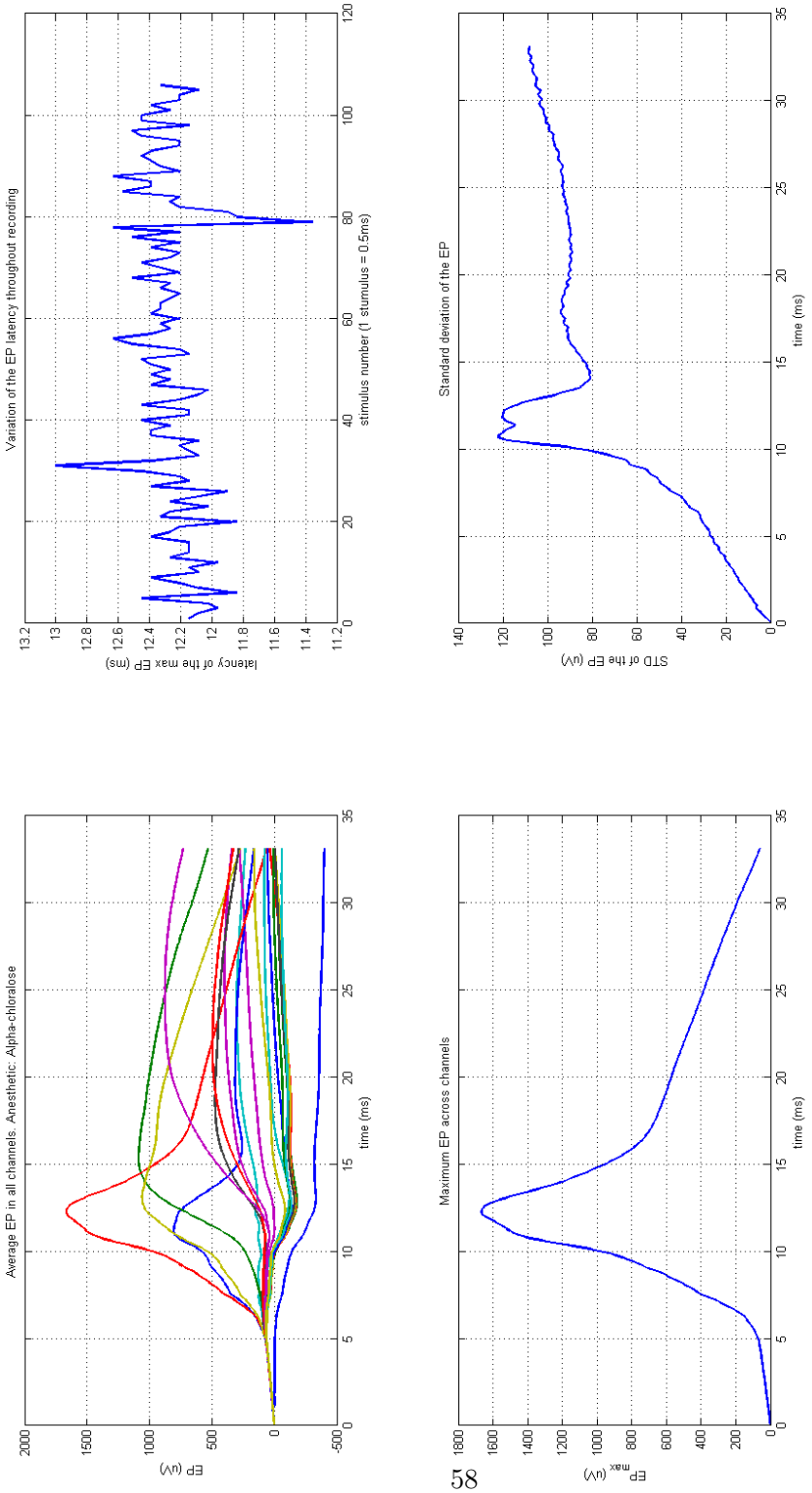

Figure 2.4.: Typical evoked potential under $\alpha-$chloralose anaesthesia. The top right panel shows the average EP measured in all channels, the bottom right

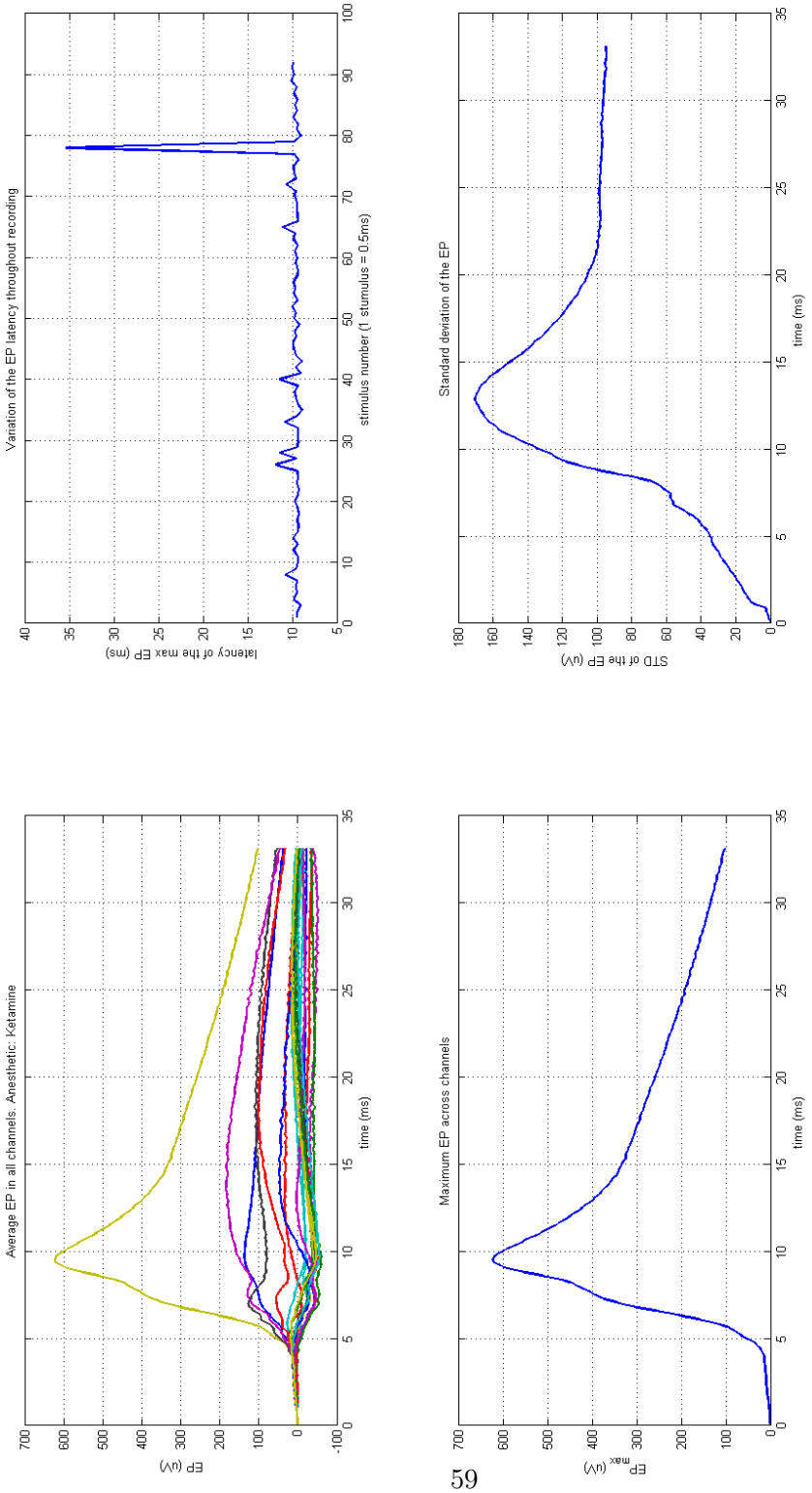

Figure 2.5.: Typical averaged evoked potential under Ketamine anaesthesia. The top right panel shows the average EP measured in all channels, the

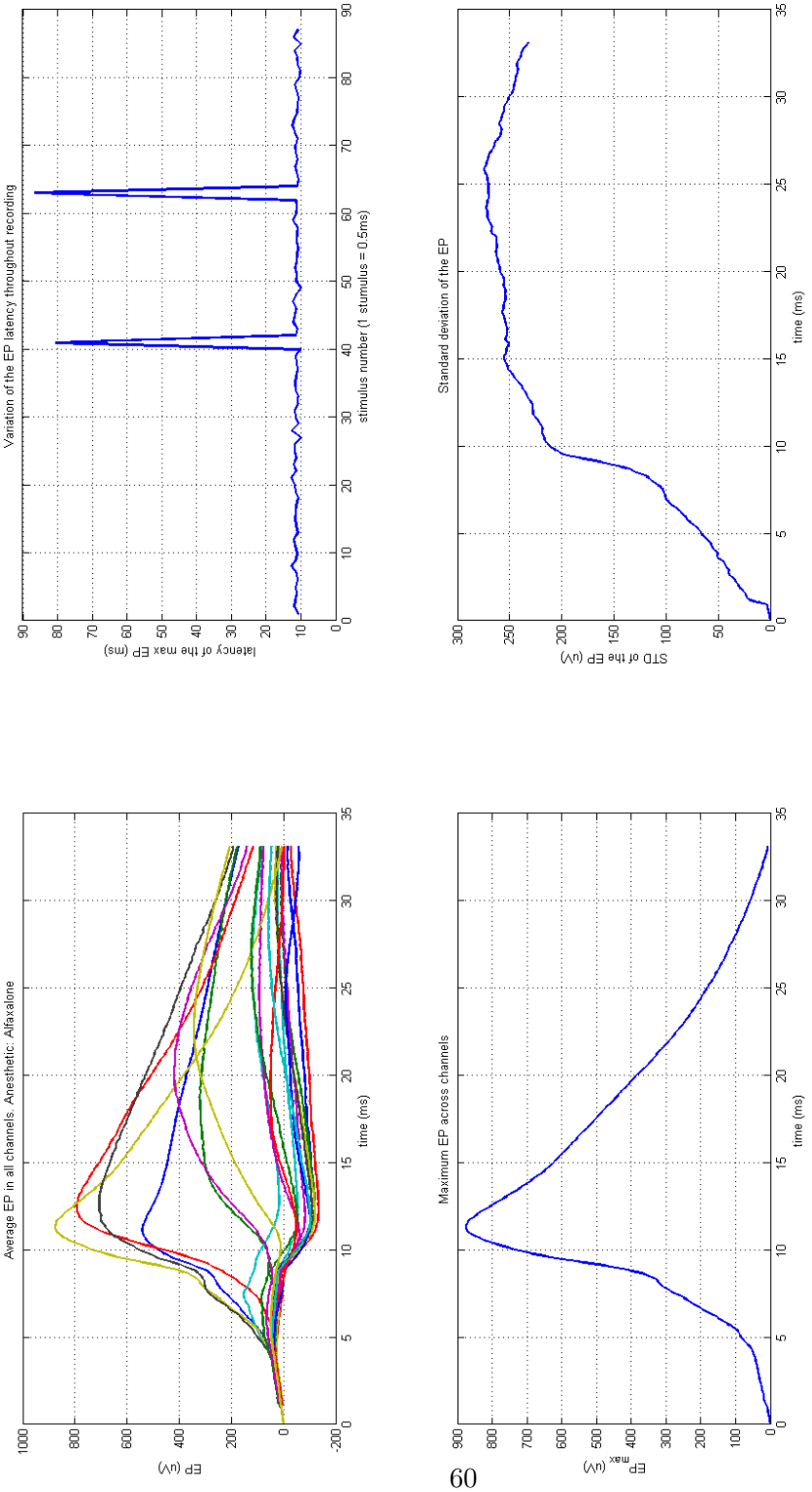

Figure 2.6.: Typical averaged evoked potential under Alfaxalone. The top right panel shows the average EP measured in all channels, the bottom right

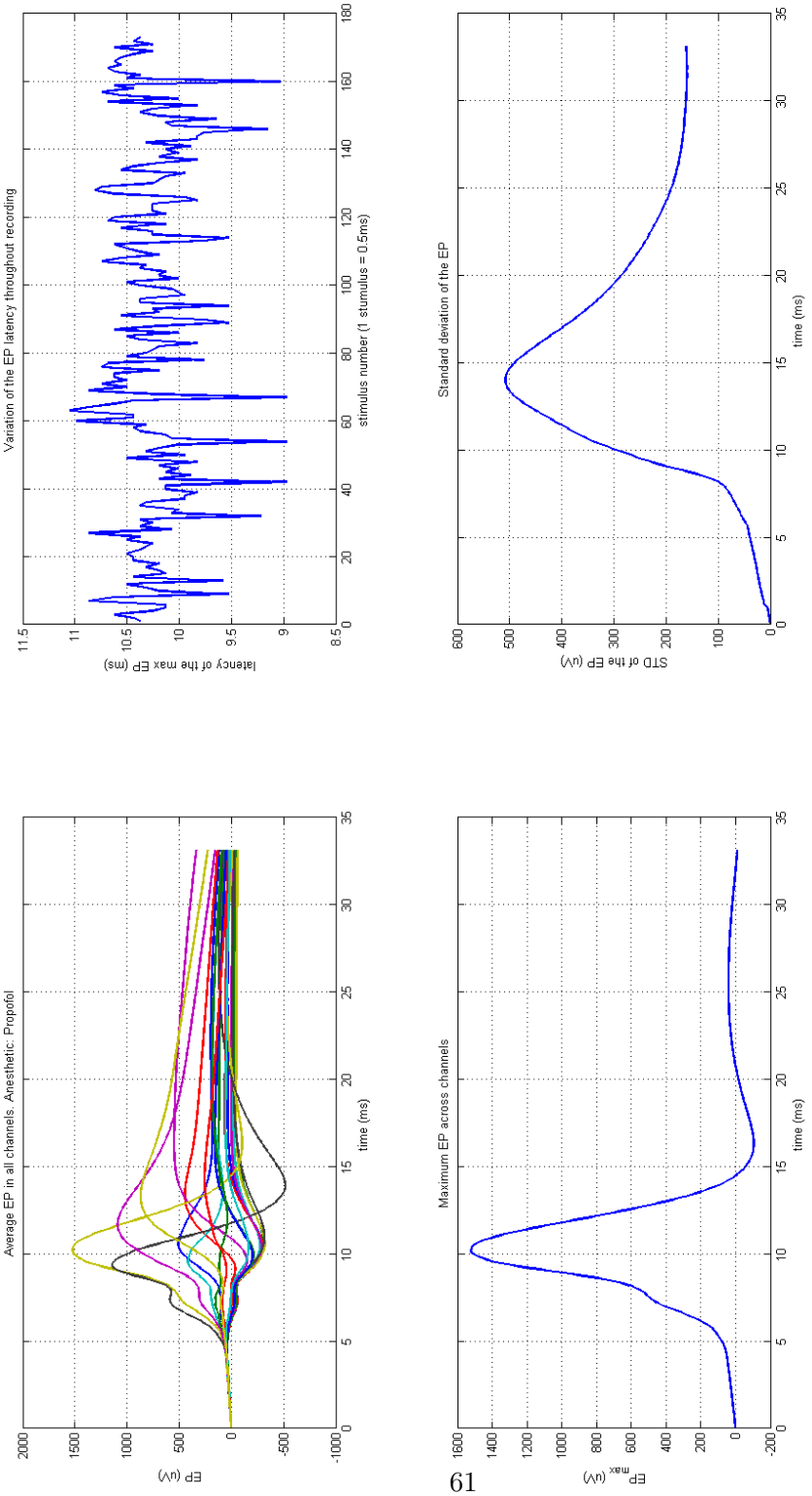

Figure 2.7.: Typical averaged evoked potential under propofol anaesthesia. The top right panel shows the average EP measured in all channels, the

potentials. It is appreciated that a small number of animals have been used in this study. However, the results are in agreement with the literature as far as it is available. No direct comparison of the anaesthetics used were available, but the literature review predicted an improvement of the EP-amplitudes with all of the chosen agents except for alfaxalone over halothane, where no data was available. The larger EP-amplitudes with propofol compared to halothane is in accordance with the results of Clapcich et al., and the comparison of $\alpha-$chloralose to halothane mirrors the fMRI results of Austin et al. which showed a larger bold signal with $\alpha-$chloralose (Hayton et al. [1999], Austin et al. [2005], Clapcich et al. [2004]).

2.8. Conclusion

Propofol will be used as a main agent for future EIT recordings as it produces stable EPs which are larger in amplitude than halothane and it produces stable, easily adjustable, surgical anaesthesia. No significant difference to $\alpha-$chloralose was detected, however it is appreciated that $\alpha-$chloralose may produce larger EPs than propofol, but the spontaneous movements and difficulty of assessing anaesthesia depth make the drug unfavourable. I am planning to use isoflurane as the induction agent for future experiments and hence am avoiding ketamine due to its interactions with isoflurane and its associated difficulties. Because halothane is no longer available on the UK market, future experiments will be performed with isoflurane as the induction agent. Induction with a volatile agent has the advantage that it does not stress the animal, furthermore, propofol is given intravenously which makes a separate agent for induction necessary until cannulation is achieved.

3. Impedance changes during evoked responses in the rat cortex in the 225-1975 Hz frequency range

3.1. Introduction

3.1.1. Orienting paragraph

The ideal functional neuroimaging method will generate images with sufficiently high spatial and temporal resolution such that the propagation of neuronal activity is clearly observable. Sine-wave EIT can potentially achieve this goal: it has the capability to image neural activity with sub-millisecond time resolution and spatial resolution in the few hundreds of micrometers within the region of interest. The temporal resolution of sine-wave EIT is limited by the frequency of the sinusoidal current (the carrier) injected for the impedance measurement. For example, the resolution is at most 1 millisecond with a 1-kHz carrier, or 500 microseconds with a 2-kHz carrier. This is due to the maximum width possible for the bandpass filter. In this chapter I will examine the possibility of increasing the time resolution of EIT by recording evoked responses from the rat cortex using higher carrier frequencies. The temporal resolution of the sine-wave EIT method will be determined based on the signal-to-noise ratio (SNR) of the impedance measurements at higher frequencies.

3.1.2. Background

3.1.2.1. Previous work within our group

Biophysical modelling

The principle by which EIT could image neuronal activity rests on the application of low-frequency currents which remain in the extracellular space under resting conditions because they cannot enter significantly into the intracellular space across the capacitative cell membrane. During the action potential or neuronal depolarization, the membrane resistance diminishes by about 80x (Cole and Curtis [1939]) so that the applied current enters the intracellular space as well. Over a population of neurones, this will lead to a net decrease in the resistance during coherent neuronal activity, such as cortical evoked responses, as the intracellular space will provide additional conductive ions. The magnitude of such fast changes was previously modelled in our group for the unmyelinated crab nerve. The biophysical modelling was based on cable theory to predict the behaviour of currents on passive dendrites by modelling them as cylinders composed of segments with capacitances and resistances combined in parallel. The local resistivity changes were predicted to be maximal at DC and to decrease quickly at higher frequencies; at 1 kHz, the changes were predicted to be 1000x smaller than at DC (Liston et al. [2012]). These predictions were in agreement with empirical measurements on the crab nerve (Gilad et al. [2009]). Oh et al. assumed that the cortex would behave in a similar fashion to the crab nerve, based on Liston et al.s prediction and on empirical quantification of noise, they assessed that the signal-to-noise ratio (SNR) of the impedance changes on the cortex would peak around 250 Hz, as the predicted decrease in the impedance signal would be offset by a steeper decrease in the noise level (Fig. 3.1,

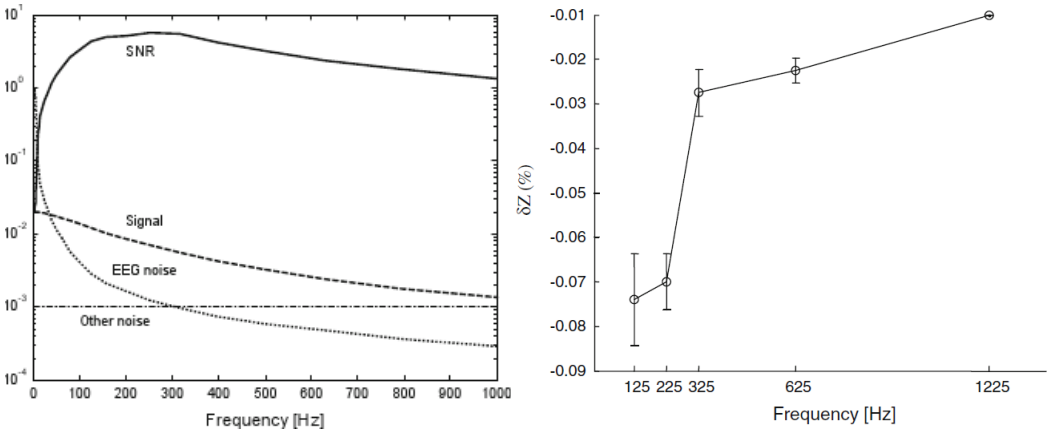

Figure 3.1.: Left: Diagrammatic illustration of relative amplitudes of resistance change during fast neural activity, EEG noise amplitude, and the resulting SNR over frequency. The signal and EEG noise are normalised and shown in arbitrary units. The EEG amplitude was recorded from rat cortex during anaesthesia with halothane, resistance change is from biophysical modelling for the crab nerve (Liston et al. [2012]), and 'other noise' is instrumentation noise scaled to the EEG. Right: Amplitude of impedance decreases during evoked responses in rat cortex with varying carrier frequency. Figures from Oh et al. [2011a], reproduced with permission.

Oh et al. [2011a]).

Recordings in the rat cortex

Oh et al. measured impedance changes during evoked responses in the cortex of anaesthetised rats using the sine-wave EIT method (Oh et al. [2011a]). Their instrumentation was the same as the one used by us, described in section 3.2.3 below, with the exception of the acquisition system. They used a 32-channel system with 22-bit sampling at 2 kHz per channel and hardware filters of 0.15–570 Hz (SD32R system, Micromed, Italy). Oh et al. recorded activity related impedance decreases of -0.07±0.0006% with a signal-to-noise ratio of >50 (after averaging) with this set-up. They achieved a time resolution of 8 ms using a 225-Hz carrier.

Oh et al. also made single-channel impedance measurements in the rat cortex at higher frequencies: 325, 625 and 1225 Hz, which were not published. For these measurements, they replaced the Micromed system with a 1-channel system comprised of a Neurolog pre-amplifier (NL106, Digitimer, UK) and filter unit (NL125, Digitimer, UK). The gain was set to 50 and the bandpass filter was set from DC to 10 kHz. (NL106, common mode rejection ratio >68dB @ 50Hz and input impedance >1 MΩ). The data were sampled at 16 kHz by a National Instruments 16-bit

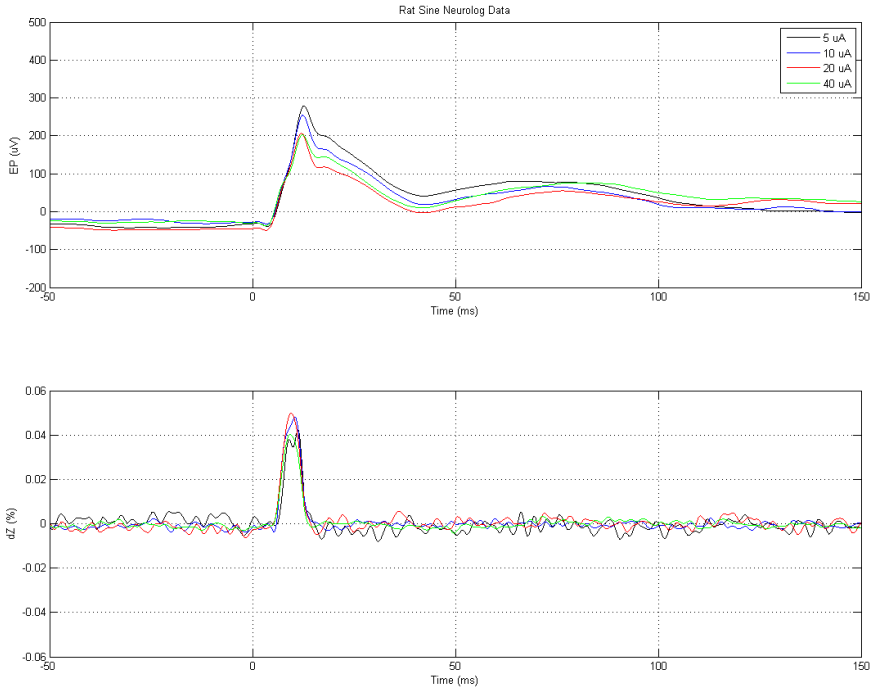

Figure 3.2.: Unpublished recordings of the impedance response of cortical tissue to forepaw stimulation using the Neurolog system with a carrier frequency of 625 Hz and current amplitudes from 5 to 40 μA. The top row shows the evoked EEG response and the bottom row shows the relative change in tissue impedance due to activity. The relative change in impedance stays constant irrespective of the current amplitude used.

data acquisition system set to oversample and provide 18-bit resolution (NI USB 6259, National Instruments, USA). They conducted measurements in 6 rats at 625 Hz; instead of an impedance decrease, they obtained an impedance increase at this frequency (see figure 3.2). This positive impedance change was assumed to be an artefact.

3.1.2.2. Other impedance measurements of brain function

Probably the most relevant functional impedance study for our purposes, apart from Oh et al. is the work of Klivington and Galambos (Klivington, K Galambos [1967]). They used wire depth electrodes to record impedance changes on the exposed cortex of a cat with a Wheatstone bridge and carrier frequencies ranging from 1 kHz to 100 kHz; an auditory stimulus was used to elicit evoked responses. They recorded impedance decreases of approximately 0.03 Ω (measured at 10 kHz carrier frequency,

the baseline impedance of the cortex was not stated), followed by an increase in response to the stimulus and reported a modest signal decrease at higher carrier frequencies. This study is particularly interesting to us because they used 1 kHz as the minimum frequency, which according to the modelling of Liston et al. would have produced an almost negligible signal in the crab nerve (Liston et al. [2012]). Their findings encouraged us to test higher carrier frequencies for EIT imaging of fast neural activity.

Impedance measurements have also been used in other neurophysiological studies. For example, Tsukahara et al. and Smith et al. both used impedance recordings of activity in neurons in the red nucleus and spinal motorneurons of cats, respectively (Tsukahara and Fuller [1969], Smith et al. [1967]). Both studies reported that inhibitory postsynaptic potentials (IPSPs) were easily recordable in their intracellular recordings, but excitatory postsynaptic potentials (EPSPs) were not. They reached the conclusion that EPSPs are mainly elicited from synapses at the dendrites of neurons while IPSPs are mainly elicited from synapses at the soma of neurons based on their data.

More recent studies tried to collect tomographic impedance images from human subjects. Tidswell et al. used scalp electrodes placed around the head in a circular fashion Tidswell et al. [2001a]. They used a 50 kHz injection frequency to image the changes in blood flow due to neuronal activity in response to visual stimuli. Unfortunately, they only detected impedance changes in ˜20% of electrode measurements. The measured changes were in the correct anatomical location. Peak increases in the impedance recordings were 0.4±0.1% and decreases were -0.5±0.1% for visual paradigms, while the peak increases for a somatosensory paradigm were 0.18±0.07% and peak decreases were -0.07±0.03%. Gilad et al. made tomographic impedance measurements to attempt to image fast neural activity in response to visual stimuli (Gilad and Holder [2009]). They used scalp electrodes distributed over the head and selected a (DC) square wave as a carrier. They were unable to image the activity even though they could measure significant impedance changes (0.0010±0.0005) as the signal-to-noise ratio (SNR) was too low (2:1).

3.1.2.3. Other modelling

Seoane et al. modelled the frequency dependence of the transencephalic impedance change during cerebral hypoxia, which causes a decrease in extracellular change due to cell swelling. They modelled the brain tissue as a suspension of spherical cells using an equation from Cole (Cole [1928], Seoane et al. [2005]); in contrast, Liston et al. had modelled the cortex as a suspension of randomly oriented cables (Liston et al. [2012]). Seoane et al.'s model predicted a flat impedance spectrum from DC to 20 kHz (i.e., most of the current is extracellular) followed by a gradual decrease in impedance up to 750 kHz; these predictions were validated with measurements in anaesthetised piglets (Seoane et al. [2005]). Logothetis et al. conducted impedance measurements on the cortex of macaque monkeys over frequencies from 10 Hz to 5 kHz, and showed that the impedance of the cortex was independent of frequency,

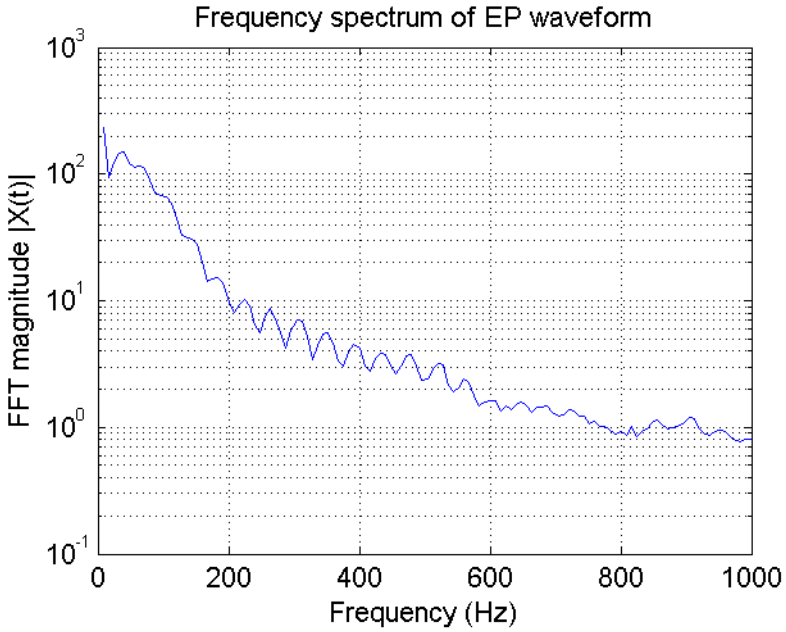

Figure 3.3.: Frequency spectrum of the EP waveform. FFT = fast fourier transform, calculated from the average of 100 SEPs in a rat by stimulating the contralateral forepaw. The EP-only recording was obtained between impedance recordings.

homogeneous and tangentially isotropic within the grey matter. They concluded that the cortex can be modelled as a pure-resistive conductor for theoretical predictions of impedance behaviour over frequencies from 10 Hz to 5 kHz (Logothetis et al. [2007]). Ranck measured the cortical impedance over frequency in the anaesthetised rabbit and reported a flat response from zero to 100 kHz with a maximum phase shift of 7°at 50 to 100 Hz (Ranck [1963]).

3.1.2.4. Potential artefacts

Artefact due to Evoked Potentials (EPs) One of the possible sources of artefact is the cortical evoked potential. If the EP coheres with the injected carrier current, it can cause artefactual modulation of the signal if its removal is incomplete. The frequency band of the evoked potential drops rapidly at higher frequencies ($\frac{1}{10}$ at 200 Hz compared to 1 Hz and $\frac{1}{100}$ at 600 Hz compared to 1 Hz), which means that, the higher the carrier frequencies, the less likely are any artefactual changes from the EP (compare figure 3.3).

A related artefact may occur if the shape or timing of the EP waveform are altered by the injected current used to measure the impedance. If this occurs, then the EP will differ during the phase and antiphase segments so that, after subtraction, there will be a residual voltage which will appear as an apparent change in impedance.

Artefacts due to problems in the instrumentation The hardware can cause artefacts due either to the current source or the recording system. If the current source does not output a constant current then it would appear as a change in the measured impedance. On the recording side there could be an artefact caused by poor linearity of the EEG system; however, such an artefact would be random and not consistent across channels or recordings since it would depend on the DC component of each channel. Therefore, there is a negligible chance of having a consistent artefact due to instrumentation.

3.1.3. Experimental Design

3.1.3.1. Statement of purpose

The purpose of this work was to measure fast-neural impedance changes of the rat brain at higher carrier frequencies, and determine the optimal carrier frequency for EIT recordings with respect to SNR and temporal resolution. To come to a conclusion on what frequency to use, the dZ signal at higher frequencies needs to be characterized. This would permit us to image with higher temporal resolution. It was tested whether the cortex is mainly resistive to frequencies up to 50 kHz, as measured by Ranck, Seoane et al. and Logothetis et al., or whether the signal amplitude (and consequently SNR) decrease as fast as predicted by the biophysical model of Liston et al. for the crab nerve. The characteristics of the reconstructed images at higher frequencies were assessed for the spatial measures of the reconstructed centre of neuronal activity.

3.1.3.2. Rat experiments

The change in impedance of the rat brain in response to a sensory stimulus to the forepaw was recorded; a subdural electrode grid comprising 29 contacts was used for the recordings. To assess the characteristics of the impedance signal over frequencies, current was injected from 175 to 1975 Hz in steps of 50 Hz. The current was injected using one pair of the contacts and the remaining contacts of the electrode were used to record a voltage map. Furthermore images of evoked activity were recorded at a variety of carrier frequencies to assess image quality. Carrier frequencies of 225 Hz, 625 Hz, 1025 Hz, 1525 Hz and 1925 Hz were used for the imaging recordings.

3.1.3.3. Rationale for controls

To ensure that the recorded changes were technically sound, a number of control recordings were conducted. These control recordings were designed to address the different potential sources of artefacts: the hardware (i.e., the current source, EEG headbox, or stimulator), the software (e.g., the demodulation algorithm), or from possible neuronal stimulation due to the injected current.

Hardware controls included:

- testing the constant current output by simultaneously recording the voltage drop across a known series resistor during an experiment, to ensure that the current output was stable and to determine the capacitive component of the signal.
- using an ipsilateral forepaw/no stimulation paradigm to ensure that the stimulator did not cause any artefact in the impedance recordings.

Software controls included:

- a simulation analysis to test whether the algorithm was effective in separating the impedance signals from the EPs;
- recordings with varying current amplitude levels, since an added artefact from imperfectly subtracted EPs or alterations in the EP-waveform due to the injected current would not be proportional to the current amplitude.

The variable current-level control was also used to test whether the neuronal activity was changed, since the impedance signal may behave in a non-linear fashion with respect to current if neuronal activity was being stimulated at higher current amplitudes.

3.2. Methods

3.2.1. Alternative modelling

As an alternative to Liston et al.'s model, the cortex was modelled as a suspension of spherical cells with passive cell membranes (see figure 3.4). Cole's equation for the electric impedance of suspensions of spheres (Cole [1928]) was used:

$$Z = r_e \frac{(1-f)r_e + (2+f)(r_i + \frac{Z_m}{a})}{(1+2f)r_e + 2(1-f)(r_i + \frac{Z_m}{a})}$$

where Z is the specific impedance of the tissue in Ωcm^2 , r_e is the resistivity of extracellular fluid in Ωcm, r_i is the resistivity of the cytoplasm in Ωcm , $Z_m$is the surface membrane impedivity in Ωcm^2 (r_m being the resistive component, and C_m the capacitive component), a is the cell radius in cm and f is the volume factor of concentration of cells. The same values Liston et al.'s were used in this model: $r_e = 60\Omega cm$, $r_i = 70\Omega cm$, $r_m = 2,500\Omega cm^2$, $C_m = 2\mu F/cm^2$, $a = 17\mu m$, and $f = 0.55$ (Liston et al. [2012]). To model the effect of neuronal depolarisation on the bulk impedance of the tissue, the membrane resistivity was decreased from 2,500 Ωcm^2 to 1 Ωcm^2.

3.2.2. Animals, anaesthetic and surgical procedure

Female Sprague-Dawley adult rats were used for the experiments and were surgically prepared as described in Chapter 22.5.3. They were induced with 4% isoflurane in

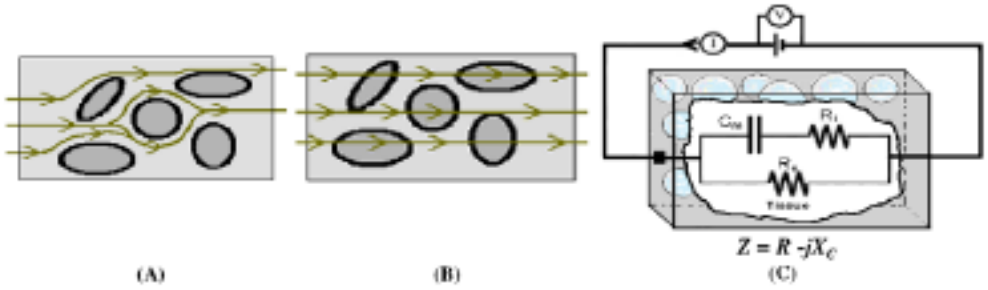

Figure 3.4.: (A) and (B) show the pathways of the electrical current through biological tissue; (A) low frequency, (B) high frequency. (C) shows the electrical circuit model used for the neuronal membranes. Picture from Seoane et al. (Seoane et al. [2005]), with permission.

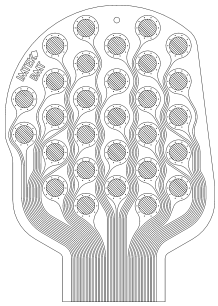

Figure 3.5.: Subdural electrode array, reproduced from Schuettler et al., with permission (Schuettler et al. [2008]).

30% oxygen and 70% air and maintained with 2% isoflurane on the nose-cone until intravenous access was established. The anaesthesia was then continued with a constant infusion of propofol, as described in Chapter 2. All work was conducted with permission of the UK Home Office.

A craniotomy was performed to expose one cerebral hemisphere widely. The dura was resected and recordings were made with a custom designed electrode array, 8 x 8 mm placed on exposed cortex. This was constructed of platinum foil on a silicone rubber backing which had been laser cut to provide 29 circular electrodes, 0.6 mm in diameter, hexagonally arranged with a centre-to-centre distance of 1.2 mm. The electrodes were platinised to reduce contact impedance and noise from the electrode–electrolyte interface (Schuettler et al. [2008]).

3.2.3. Hardware

The instrumentation comprised an ultra low noise programmable constant current source which could produce a sinusoidal waveform from 1 Hz to 2 kHz with an

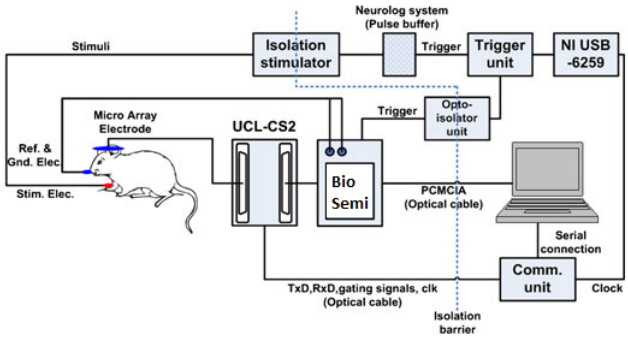

Figure 3.6.: Instrumentation set-up for recordings on rat cerebral cortex (adapted from Oh et al. [2011a], with permission)

amplitude of 0.1–100 μA; the output impedance was over 1 MΩ (UCL-CS2 current source). This current source was constructed from a FPGA (EP1K50, Altera, USA), programmed as a main controller and digital waveform generator. It received commands from a PC and produced timing and control signals to the acquisition system. The sine waveform was digitally generated in a ROM which contained 2,000 samples of sine waveform data which were read by the FPGA and able to generate frequencies from 1 Hz to 2 kHz. The DC component and high frequency clock noise were rejected by a band pass filter (10 Hz– 10 kHz). There were two independent current sources to supply 0.1–10 μA or 10–100 μA. These comprised a floating Howland current source which contained digitally controlled potentiometers (DS1267-010 and DS1267-050, Dallas, USA) to provide equal resistance ratios. Power was supplied from two 6 V batteries and was stabilised with isolated 6W DC-DC converter modules with regulated output (TMR-6, Traco Electronic GmbH, Germany). The current source could address any pair of the 29 electrodes in the electrode array. Voltages were recorded with 32 channels of the 128-channel EEG acquisition system (ActiveTwo AD-box, Biosemi, Netherlands) which has low-noise DC coupled amplifiers, 2 V dynamic range, less than 0.1% distortion, and 24-bit output on each channel. Sampling was performed at 16,384 Hz with hardware anti-aliasing filter at 3.6 kHz. The EEG system and the current source were floating independently. An isolated stimulator (NL800A, Digitimer, UK) was employed to produce somatosensory stimulation. The entire system was optically isolated and controlled by a Windows PC (Fig. 3.6).

3.2.4. EP and impedance recordings

Somatosensory evoked responses were produced by stimulation of the contralateral forepaw via needle electrodes at 2 Hz with pulses 100 μs in duration and 10 mA peak amplitude in all subjects. Cortical EPs were first recorded by averaging 120 responses. The electrode array was repositioned if needed so that the maximum response was near the centre of the array. Impedance was then recorded either as frequency-sweep recordings or as full recordings, as described below. All measurements were made with respect to the reference electrode contralateral to the electrode array. The reference electrode was a 1.5 x 1.5 cm silver/silver chloride plate which was placed into the skin opposite the recording electrode grid. The data processing and analysis to estimate the change in dZ is described in detail in 3.2.6.2.

3.2.4.1. Frequency-sweep recordings

These were short recordings which allowed measurement of impedance with a large number of carrier frequencies in order to compare the effect of frequency on the dZ signal. Impedance changes were recorded from the non-injecting electrodes during evoked responses in 6 rats, using the same stimulation settings as in the EP recordings. The injecting electrodes were chosen so that one electrode was on the region of maximum evoked response and the other was at any of the edges of the array, this meant that they were two to three electrode contacts apart (2.4 to 3.6 mm). The frequency of the injected current ranged from 175 Hz to 1525 Hz in 3 rats and was extended to 1975 Hz in another 3 rats, all conducted in steps of 50 Hz. Unless otherwise stated, the carrier current was 60 μA rms amplitude. No carrier frequencies were left out in any of the recordings.

3.2.4.2. Image recordings

These recordings were performed with multiple injection pairs in order to reconstruct images of the conductivity changes occurring in the cortex during evoked responses. In a similar fashion to the frequency-sweep recordings, impedance was recorded during contralateral forepaw stimulation at 2 Hz over 1 minute for each injection pair. The injected current was 50 μA peak amplitude and had its frequency set at 225 Hz, 625 Hz, 1025 Hz, 1525 Hz or 1925 Hz. Each recording set had 25-30 injection pairs; the injection protocol was optimized to provide large dZ signals and maximum distinguishability between layers, as predicted by forward simulations (fig. 3.7). The protocol was adapted to each experiment according to the location of the largest EP signals.

Recording type	Number of rats	Number of recordings
Image recording at 225 Hz	5	5
Image recording at 625 Hz	8	8
Image recording at 1025 Hz	7	7
Image recording at 1525 Hz	2	2
Image recording at 1925 Hz	3	3
Total image recordings	8	24
Frequency sweep up to 1525	3	6
Frequency sweep up to 1975	3	4

Table 3.1.: Overview of numbers of recordings. The numbers per recording are due to the length of time required for each full recording, it was therefore not always possible to collect a full set of images at all frequencies. Imaging at higher frequencies was only made possible by reprogramming the current source so that the initial frequency sweeps and images went up to 1525 Hz but later ones went up to 1925 Hz. There are therefore more data points for the frequencies below 1525 than there are for the frequencies above.

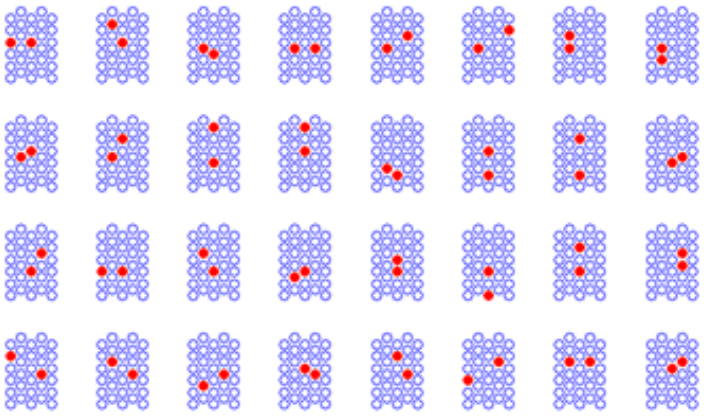

Figure 3.7.: Example of electrode addressing protocol, the electrode contacts marked in red represent the source/sink.

Control type	Number of rats	Number of recordings
Ipsilateral/No stimulation	2	3
Current level control	2	4
Current output control	1	2

Table 3.2.: Overview of numbers of controls

3.2.5. Experimental controls

3.2.5.1. Ipsilateral/no stimulation

Impedance recordings during (1) ipsilateral forepaw stimulation or (2) no stimulation. These controls were performed to verify whether the impedance signal may have been artefactual and caused by the electrical stimulation or a hardware problem. Impedance was measured with a carrier set at 625 Hz and 60 μA peak amplitude.

3.2.5.2. Current level control

Impedance recordings with different current amplitudes were conducted to verify whether the proportional impedance changes remained constant over a range of current levels. This can detect the presence of an additive artefact in the impedance signal, which by definition would not be proportional to the carrier amplitude. Furthermore, this control can also detect whether the injected current is stimulating or inhibiting the neural activity and thus modifying the impedance changes. The frequency of the carrier was set at 1025 Hz, and the peak amplitude of the carrier was varied from 12 μA to 60 μA in steps of 6 μA. The same injection pair as for the frequency sweep recordings was used for the current control recordings in each rat. The Pearson correlation was used to test whether the absolute dZ value was proportional to current amplitude. Neuronal stimulation was checked for by testing the effect of current amplitude on the size of the EPs, also using Pearson correlation test.

3.2.5.3. Current output control

The current source was tested during the experiments as follows. A 1-kΩ resistor was placed in-series with the current-injecting channel, and the voltage drop across the resistor was recorded during the impedance recordings in one rat. The measured current was analysed in the same way as dZ signals (explained in Section 3.2.6.2); Student's t-test was used to detect significant fluctuations in the injected current around the time of the observed impedance changes (i.e., 5-20 ms after the forepaw stimulation). These recordings were also used to estimate the phase angle of the impedance signals.

3.2.5.4. Reconstruction of full recordings with variable bandpass filtering

To ensure that the bandpass filtering had no effect on the image reconstruction, one recording at 1925 Hz carrier frequency was reconstructed with varying bandpass filters. This should only change the temporal resolution but not the localisation of the reconstructed activity. The bandpass filter for this control was 120 Hz, 300 Hz and 1 kHz.

3.2.6. Data processing and analysis

3.2.6.1. Recovery of the EPs during impedance measurements

During impedance recordings, the voltage measurements at each electrode contained three superimposed components: (1) the spontaneous EEG activity; (2) the evoked potentials elicited by the forepaw stimulation; and (3) the boundary voltage due to the current injection modulated by the changing conductivity ($\Delta\sigma$) of the tissue (e.g., during neuronal activity). Evoked potentials were produced every 500 ms and the frequency of the carrier frequency was odd, which resulted in the first EP of each segment pair being in phase with the carrier and the second being anti-phase. Therefore, in order to cancel out the carrier signal and extract the evoked potentials, two consecutive segments were simply added together (see Fig. 1.7).

3.2.6.2. Estimation of change in impedance (dZ)

The impedance changes (i.e., dZ signal) were estimated by the following five-step procedure on each paired segment (see Fig. 1.7): (1) subtraction of the paired segments to cancel out the EPs (in reality, it is not possible to remove EPs perfectly; section 3.2.6.5 describes the analysis done to test whether the leftover EP signal was a potential source of noise); (2) band-pass filtering the resulting signal around the carrier frequency (details below); (3) demodulation using the Hilbert transform (details below); (4) subtraction of the baseline (i.e., the segment average) to obtain impedance changes; and (5) normalisation by the baseline, so that the impedance changes are expressed as percentage of the baseline. The baseline was subtracted at each 1-second segment, which removed any slow drifts due to battery depletion (the drift during each segment was negligible).

Band pass filtering The band-pass filter applied was set as wide as possible up to a bandwidth of 300 Hz around the carrier frequency but above 105 Hz in order to avoid the EEG band. The 300-Hz bandwidth limit was used to make the impedance signal amplitudes comparable at higher frequencies. The bandwidth (temporal resolution) was as follows for the different carrier frequencies: 70 Hz (14.3 ms) for the 175-Hz carrier, 120 Hz (8.3 ms) for the 225 Hz carrier, 170 Hz (5.9 ms) for the 275 Hz carrier, 220 Hz (4.5 ms) for the 325 Hz carrier, 270 Hz (3.7 ms) for the 375 Hz carrier, and 300 Hz (3.3 ms) for all other carrier frequencies: 425-1975 Hz.

Demodulation Following the band-pass filtering, the carrier signal was demodulated by calculating the absolute values and phases on an analytic version of the signal computed using the Hilbert transform. The modulus of the analytic signal was taken to be the real component, as the phase angle of nervous tissue was previously measured as being less than 10° at frequencies up to 2 kHz (Oh et al. [2011a]), so that the modulus could be assumed to be negligibly close to the real component. This assumption was validated in two recordings during which the phase of the current was recorded, and the impedance signal was decomposed into resistive and reactive components (see Section 3.2.5.3).

Normalisation For comparison of the impedance changes in the frequency sweep, the recordings were normalised as follows. The channel with the largest impedance changes was identified for each rat, and the dZ signals from this channel were weighted by their maximum amplitude over all carrier frequencies. Then, the normalized dZ signals were averaged over all recordings.

3.2.6.3. Statistics

The recording period for each injection pair was generally set to 1 minute, yielding 60 dZ signal samples which were independently processed as described above. Samples with changes greater than 200 μV were considered to be outliers and removed from further analysis; these outliers were later confirmed by visual inspection to be due to noisy measurements (a typical recording session had fewer than 10% of the samples removed due to noise). Following outlier removal, the average and standard deviation of the dZ signal samples were computed at each time point. The average was used as the best estimate of the dZ signal, and the SNR was estimated as the ratio between the average and standard deviation of the dZ signal samples at each time point. Significant impedance changes were detected by computing the t-statistic of the dZ signal at each time point, with the significance level set at $p<0.001$ (two-sided). Finally, to compute population statistics over all frequency sweep recordings, the channel with the largest impedance changes was first identified in each recording and was normalised by its maximum amplitude over all frequencies. Then the normalised dZ signals were averaged across recordings, and the t-statistic was computed at each time point to detect significant changes in the population-level impedance signal (significance level was set at $p<0.01$). All results are given as mean±SE.

3.2.6.4. Reconstruction of conductivity changes in the cortex

A 2.3-million element cylindrical mesh was used to model the rat cortex. A cylindrical mesh instead of an anatomical correct brain mesh was used, because simulations comparing the anatomical correct mesh and the cylindrical mesh showed no significant difference in the reconstruction. The mesh dimensions were 8 mm radius and 5 mm in height, and the electrodes were placed in the middle of the

top flat surface. The resolution of the mesh near the electrodes was very fine (80 μm) and gradually became coarser in depth, as the distance from the electrodes increased. A complete electrode model was used for the forward modelling, assuming 1 kΩ contact impedance for all electrodes and 0.3 S/m baseline conductivity in the cortex. The baseline boundary voltages predicted by the finite element model closely matched those recorded during the experiments (from visual inspection). The forward model was used to estimate a sensitivity (Jacobian) matrix for the current injection protocol used in each experiment. Conductivity changes were estimated from the recorded dZ signals using the sensitivity matrix and applying first-order Tikhonov regularization (Holder [2005]). The regularization parameter was optimised by the cross-validation method (Abascal et al. [2008]) as follows: for each parameter value in the search space, the cross-validated error was computed by 'leaving out' an injection pair from the reconstruction procedure, and then using the estimated conductivity changes to 'predict' the data for the injection pair that had been left out. This procedure was repeated for every injection pair to obtain an unbiased estimate of the model's generalisation error. Finally, the parameter value associated with the lowest cross-validated error was chosen and used to estimate the conductivity changes using all the data.

3.2.6.5. Simulation analysis of dZ signal estimation

A simulation analysis was performed to verify whether the signal processing algorithm was effective in removing the EPs from the impedance signals in similar conditions to those found in actual recordings. A constant sine wave was added to individual traces of EPs recorded immediately prior to impedance recordings (120 EP traces of 1 min each, the recordings with the largest EPs were chosen; n = 6 rats). The frequency, amplitude, and phase of the sine wave were set to be the same as those used in the impedance recording. The resulting signal was processed in the same way as the impedance measurements, and the demodulated signal was analysed for significant changes. The purpose of this simulation was to test the algorithm and to quantify potential artefacts in the estimated impedance signal due to the presence of residual EPs, which may partially cohere with the carrier especially at lower frequencies.

3.3. Results

3.3.1. Results of alternative modelling

Modelling of cortical impedance using Cole's formula shows negligible change in tissue resistivity and reactance between DC and 2000 Hz. Consequently, the model predicted a constant decrease of 0.1% in tissue resistivity over the same frequency range due to neuronal depolarisation (Fig. 3.8). The modelled phase angle at 2000 Hz was less than 1°, and therefore the resistive component was >99% of the impedance modulus.

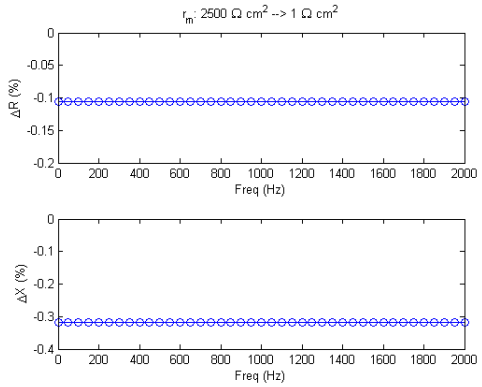

Figure 3.8.: The modelling shows no changes in tissue resistance and reactance for a simulated neuronal activity with a membrane resistivity change from 2500 Ωcm^2 down to 1 Ωcm^2 over frequency.

3.3.2. Results of frequency sweep recordings

3.3.2.1. EP amplitudes in the frequency sweep recordings

The EP amplitude in frequency sweep and the imaging recording was 0.99±0.1 mV (mean±SE, for n = 82 recordings in eight rats). The effect of the injected carrier frequency on the EP is discussed in 3.3.3.2 and graphically depicted in figure 3.16.

3.3.2.2. Impedance changes in the frequency sweep recordings

Significant impedance changes (dZ; 2-sided t-test, p<0.001) in more than one channel were detected in all ten recordings obtained from six rats. The negative peak impedance change at 225 Hz was -0.04 %±0.01, which decreased at 575 Hz down to -0.01±0.002 % to increase to -0.06±0.01% at 1575 Hz and even further to -0.08±0.02 at 1825 Hz (see image 3.9 for overview of entire frequency range, n=10 recordings (120 repeats per frequency) for 6 rats). The positive peak impedance change was 0 at 225 Hz, peaked to 0.07±0.02% at 675 Hz and decreased down to ≤0.01% at frequencies above 1500 Hz (see fig.3.9, (B)).

Figure 3.10 illustrates a typical set of dZ signals and evoked potentials (EPs) measured during an impedance recording (carrier frequency: 1025 Hz). The EPs were similar to those observed in an EP-only recording immediately prior to the impedance recording, and had maximum peak amplitude of 900 μV in channel 21. Significant impedance changes were detected in several channels (p<0.001, 2-sided T-test, obtained for each channel, n = 60 repeats), with a maximum amplitude of 0.06% in channel 17. Most of the channels with significant impedance changes exhibited a sharp positive peak followed by a negative peak in the dZ signal waveform. The timing of the positive impedance changes coincided with the initial rising edge of the EPs.

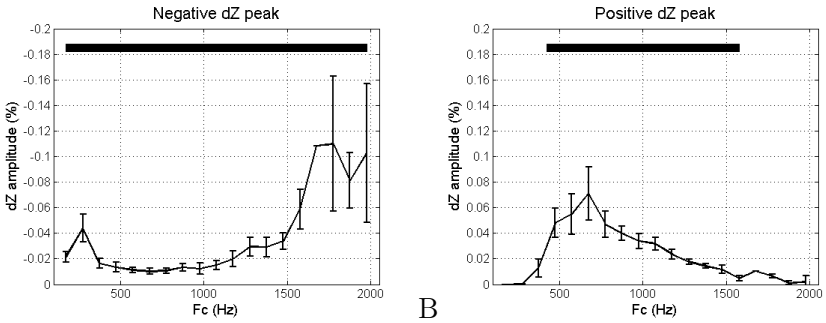

Figure 3.9.: Absolute values of dZ (A) negative absolute peak changes in impedance sweep and (B) positive peak changes in impedance over frequency (n = 10 recordings of 6 rats)

3.3.2.3. dZ signal waveforms over frequency

The dZ signal waveform varied with the frequency of the injected current. At both low (F_c <325 Hz) and high (F_c >1575 Hz) carrier frequencies, the dZ signal was unimodal and negative. In contrast, when measured with a carrier between 325 Hz and 1575 Hz, the dZ signal was bimodal, with a significant positive peak followed by a negative peak. Waveform patterns were similar across channels exhibiting significant impedance changes. Figure 3.11 shows the dZ signals measured from channel 17 (i.e., the channel with the largest impedance change in Fig. 3.10; signal was averaged over 60 trials in one recording and significance was computed using the variance within the recording) at different carrier frequencies (up to 1575 Hz in this set of recordings). The positive peak in the dZ signal becomes significant at 425 Hz, reaches its maximum value between 575-675 Hz, and gradually decreases thereafter.

The pattern of dZ signal waveforms was consistent across all six rats used in this study. However, there was a large variability in the maximum signal amplitude across rats: it ranged from 0.033% to 0.258%, with an average of 0.126 ± 0.085% (all reached statistical significance at $p<0.001$). Therefore, to obtain the population average (i.e., the average over the average dZ signals from each recording; significance was computed based on the variance between recordings), the dZ signals were normalised as described in 3.2.6.2. The normalised population dZ signals are shown in Fig. 3.12 below, and exhibit the same pattern of waveforms as described above. The amplitude of the positive peak in the dZ signal first became significant at F_c = 425 Hz, was maximal at 675 Hz, and then decreased linearly until it was no longer statistically significant at 1625 Hz (Fig. 3.9, A). In contrast, the amplitude of the negative peak was significant at all frequencies, but decreased from F_c = 325 Hz to 925 Hz, and then increased again at higher frequencies (Fig. 3.9, B).

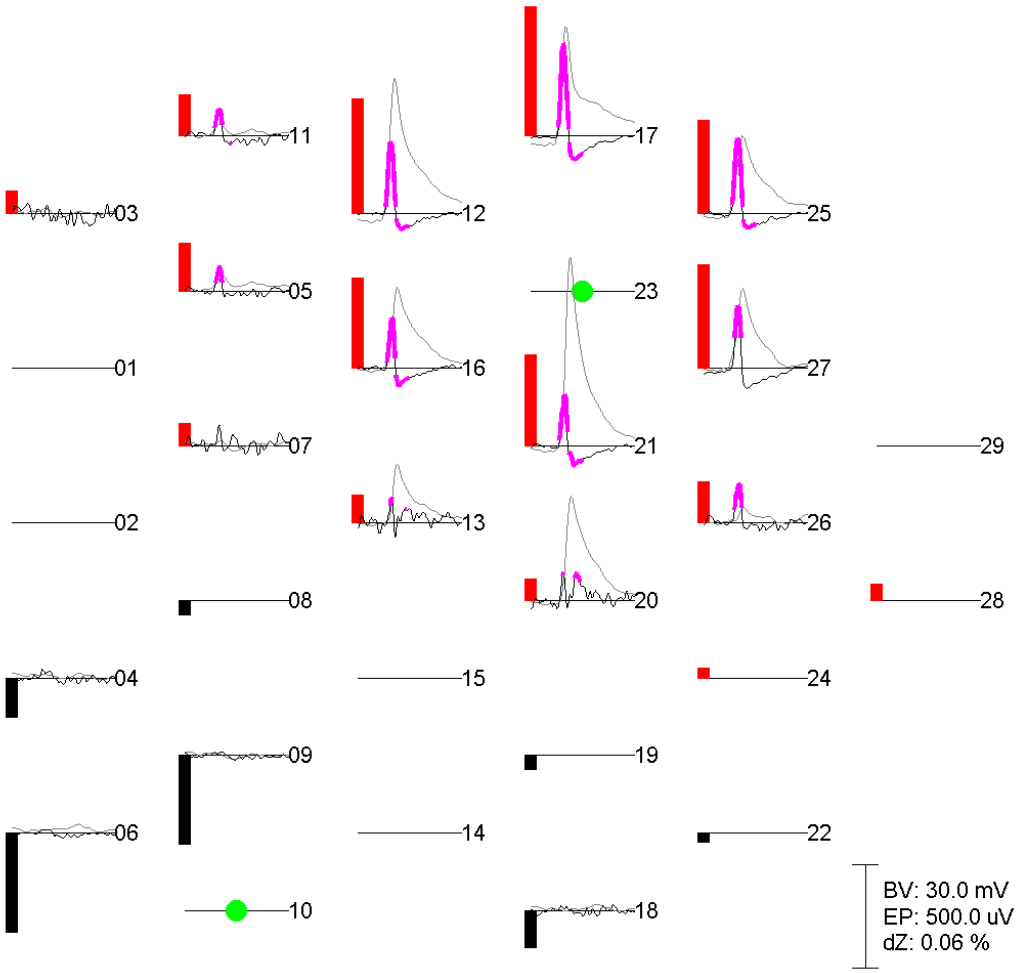

Figure 3.10.: Example of EP (grey lines) and impedance change (dZ) signals (black) measured over the electrode array. Electrode channels (numbered 1-29) are shown in their respective positions on the array. Green circles indicate the current-injecting channels, and the red (black) bars indicate the amplitude of the in-phase (out-of-phase) boundary voltage measured at the other channels (excluding broken ones). For channels with absolute boundary voltages (BV's) above 6 mV, the recorded EPs are plotted in grey and the estimated dZ signals are plotted in black over an interval of 50 ms following the forepaw stimulation. dZ values significantly different from zero ($p<0.001$, two-tailed t-test) are highlighted in magenta. The scale bar for BV, EP and dZ can be seen in the bottom right corner.

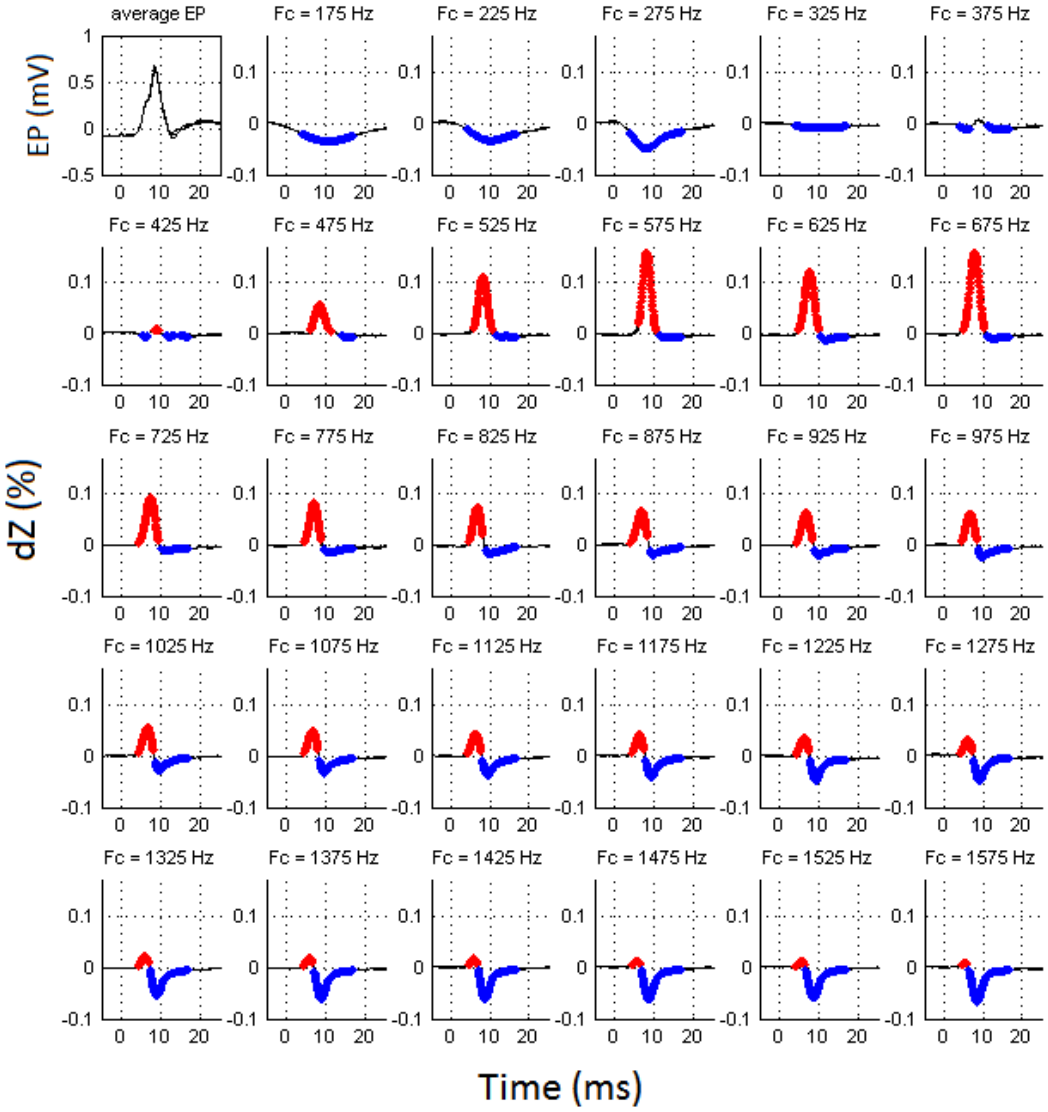

Figure 3.11.: Example of dZ signals from one set of recordings across carrier frequencies; Full frequency sweep recording as described in from a single rat. (Top left subpanel) Average EP recorded at channel with largest impedance changes. (All other subpanels) dZ signal measured from the same channel at different carrier frequencies (Fc). Solid lines indicate the average dZ signal (averaged over trials), dashed lines are ± s.e.m. (not visible in most plots; n≈60 trials in one recording). Significant positive dZ values are highlighted in red and significant negative values are in blue ($p<0.001$, two-sided T-test; variance taken over trials). The signal at Fc = 175 Hz appears smaller as the bandwidth is narrower (compare description in 3.2.6.2).

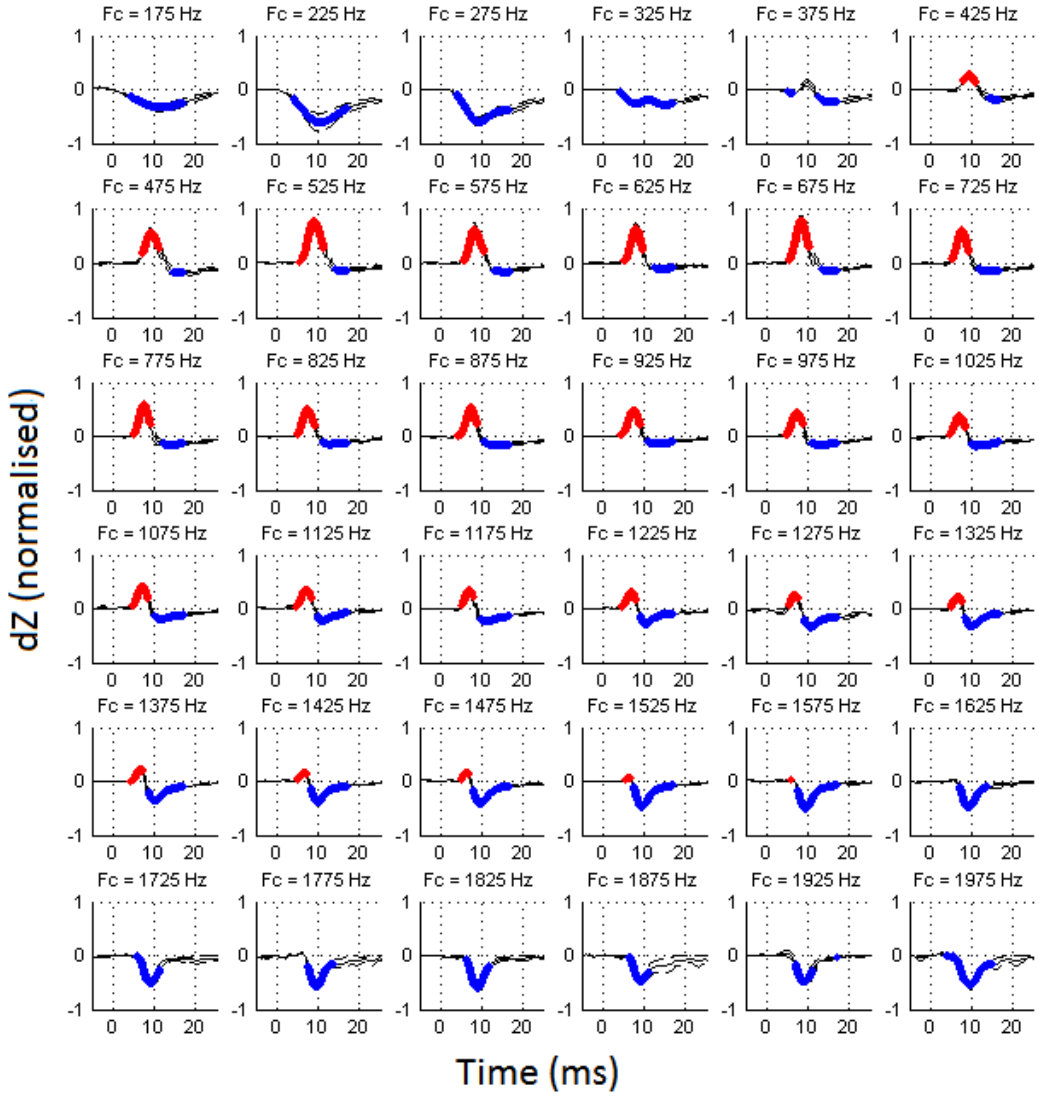

Figure 3.12.: Normalised population dZ signals across carrier frequencies. For each rat, the channel with the largest average impedance changes was identified and normalised by its maximum amplitude over all frequencies. Solid lines indicate the average normalised dZ signal (averaged over recordings), dashed lines are ± s.e.m. (not visible in most plots). Significant positive dZ values are highlighted in red and significant negative values are in blue ($p<0.01$, two-sided T-test; $n = 10$ in 6 rats; variance taken between recordings). The signal at Fc = 175 Hz appears lower than at 225 Hz due to the narrower bandwidth used (compare description in 3.2.6.2).

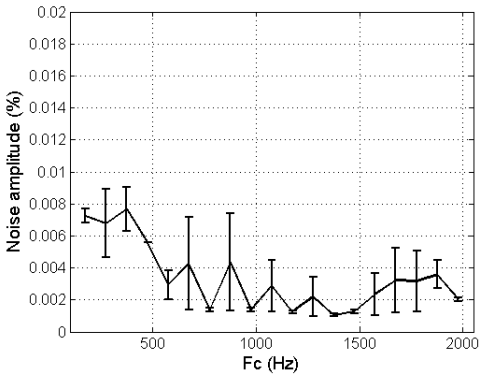

Figure 3.13.: Measured noise over frequencies as percentage of the baseline. Results from n = 10 recordings of 6 rats, errorbars represent 1 SEM

3.3.2.4. SNR of dZ peaks

The signal-to-noise ratio (SNR) was largest for the negative impedance changes measured using high-frequency (>1500 Hz) carriers. The size of the signal has been discussed in section 3.3.2.2, the noise decreased with increasing carrier frequencies, as above n=10 recordings (120 repeats per frequency) for 6 rats. At 275 Hz the mean noise amplitude was 0.06±0.002% while at 1975 Hz the noise amplitude dropped to 0.02±0.0001% (see figure 3.13 for full range of noise amplitudes). From these values the SNR was calculated over frequency. The SNR of the positive dZ signal was largest at 975 Hz, where it reached an average of 18.7 (Fig. 3.14, left). This was the case despite the positive dZ signal being larger at 675 Hz than at 975 Hz (Fig. 3.14, left) – this discrepancy between signal size and SNR can be explained by the higher noise level at lower frequencies due to the EPs. Similarly, the SNR of the negative impedance changes was higher at 1525 Hz (SNR = 27.3) than at 225 Hz (SNR = 12.2; Fig. 3.14, right), despite the signal amplitude being comparable between these two frequencies (compare fig. 3.9).

3.3.3. Validation of impedance recordings

In this section I report the results of the controls and analysis performed to validate the dZ signals measured in our experiments.

3.3.3.1. No-stimulation and ipsilateral-stimulation controls

No significant impedance changes were detected in any recording performed without stimulation of the rat's forepaw, or during stimulation of the ipsilateral forepaw ($p>0.05$, two-sided t-test). These control experiments were performed in two different rats, with the same results.

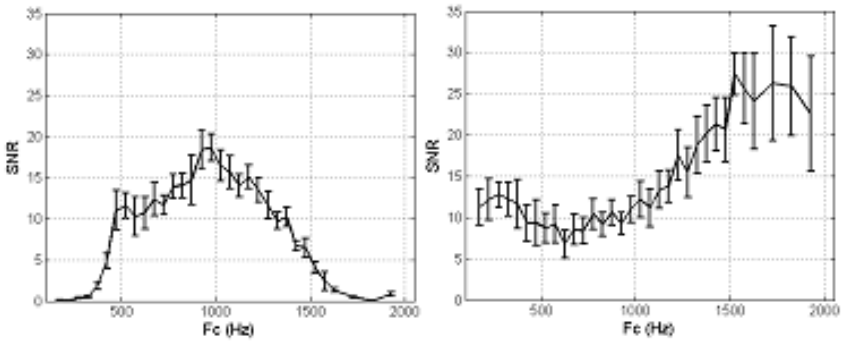

Figure 3.14.: Signal-to-noise ratio (SNR) of the positive (left) and negative (right) peaks in the dZ signal; solid line is average of 10 recordings from 6 rats, error bars are s.e.m.

3.3.3.2. Current level controls

The amplitude of the measured voltage changes was proportional to the injected current level. The current level was varied between 12 and 60 μA (steps of 6 μA; frequency was set at 1025 Hz), and the absolute amplitude (in μV) of the measured voltage was found to be proportional to the current level in all channels with significant changes (Fig. 7). When expressed as a proportional change (in % of the baseline signal amplitude), the impedance changes were uncorrelated to the current level ($p>0.05$, n=32 recordings from 2 rats).

The EPs were also analysed for possible effect of current injection on neuronal activity. Both peak amplitude and time of the EPs were tested for correlation to both current level and frequency, but no significant correlations were detected ($p>0.05$, n=36 recordings from 2 rats for current level, and n=72 recordings from 3 rats for frequency; see figure 3.16). Thus, there were no detectable changes in the EPs due to either amplitude or frequency of the injected current.

3.3.3.3. Current output control

There were no significant changes in current amplitude at the time of impedance changes, as measured across the series resistor in two separate recordings ($p>0.05$, n=60 samples for each recording, two-sided T-test). Thus, the current source delivered a constant current throughout the experiments. A linear drift of <0.01% / minute was present in the recordings due to battery depletion. This linear drift was corrected in the analysis. The impedance changes measured in the current output recordings were also decomposed into resistive and reactive changes, the relative phase was ~6^o between the injected current (frequency: 1925 Hz) and the potential of the measurement electrodes. The resistive changes accounted for >99% of the

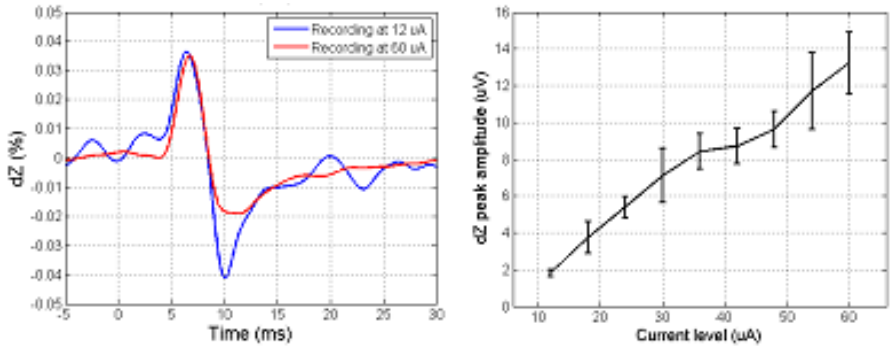

Figure 3.15.: Relation of impedance changes to current level. dZ (%) was independent of current level for applied currents of 12 μA to 60 μA (1025 Hz carrier frequency for n = 4 recordings in 2 rats). (Left) dZ (%) for injection amplitudes of 12 μA and 60 μA. (Right) Peak amplitude of the dZ signal (in μV) measured at different current levels; mean = solid line; error bars = 1 SEM (n = 4 recordings in 2 rats).

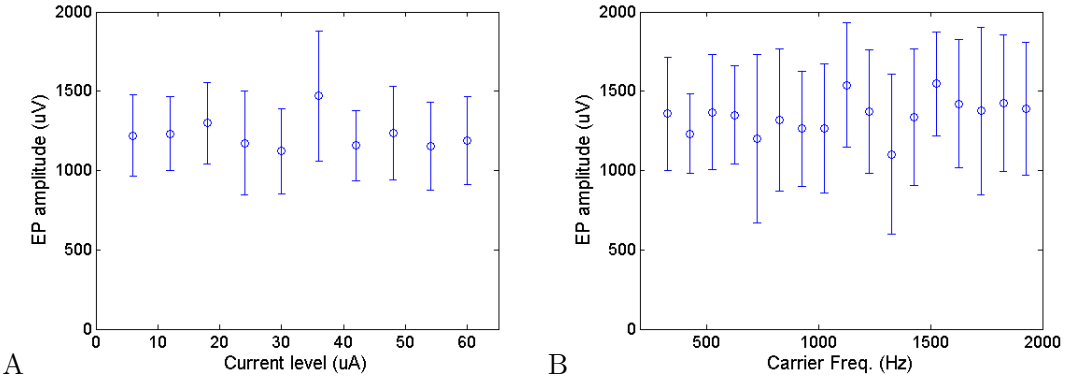

A B

Figure 3.16.: Effect of current on EPs. (A) No significant effect (p = 0.7; Pearson correlation) of the current amplitude from 5-60 μA on the EP amplitude with a 1025 Hz carrier frequency (n=36 recordings from 2 rats). (B) No significant effect (p = 0.2; Pearson correlation) of the carrier frequency on the EP amplitude with a current amplitude of 60 μA (n=72 recordings from 3 rats).

changes in the modulus of the measured frequencies.

3.3.3.4. Simulation analysis of dZ signal estimation

A simulation study was done to verify whether the EPs could have caused artefactual impedance changes due to partial coherence with the carrier signal (see Methods). This analysis was performed to verify the impedance recordings from all six rats, by adding a series of EP-only recordings of each rat to simulated carrier signals of the equivalent length (phase and amplitude of the carrier were the same as those measured in the impedance recordings). No significant impedance change was consistently detected across rats at any carrier frequency (2-sided t-test, significance level set at $p<0.01$, $n=60$ simulated samples for each of six rats). The EP causes fluctuations in the dZ signal at frequencies <600 Hz – but these fluctuations were within the margin of error and not statistically significant (compare fig. 3.17). No EP dependent statistically significant changes with respect to the baseline were obtained in any of the six rats, however the large standard error increases the noise at lower frequencies. The standard error of the EP artefact was 0.026% of the baseline at 225 Hz, 0.036% at 525 Hz and decreased thereafter to 0.02% at 725 Hz and 0.007% at 925 Hz and 0.003% at 1925 Hz (see fig. 3.18 for full range).

3.3.3.5. Relationship between EP and dZ

Finally, several examples were found from the impedance recordings demonstrating that impedance changes can be effectively dissociated from EPs. Figure 3.19 shows examples obtained from 3 different rats of channels that had large EPs but no significant impedance changes (left column) and, conversely, channels with significant impedance changes but very low EPs (right column). Thus, the presence of EPs was neither a sufficient nor necessary condition for the presence of impedance changes in any single channel.

3.3.4. Reconstructed conductivity changes across carrier frequencies

Conductivity changes ($d\sigma$) (the inverse of the resistiviy) were reconstructed, which occurred in the rat cortex during the evoked responses. To facilitate visualisation of $d\sigma$ over time, rasterised images were produced from every reconstructed set. The salient features of the $d\sigma$ images were consistent across rats, and are shown for one representative rat for 625 to 1925 Hz frequency range. The image for the 225 Hz recording is from a different rat as no rat had image recordings for all frequencies.

The distance of active areas in the reconstructed images using the different frequencies was calculated for each rat and then compared across rats. This allowed us to compare images that have been recorded with respect to the electrode array but not with respect to a standard brain. The centre of the active regions in the reconstructions of nine rats (defined as the regions above half-maximum conductivity change) were spatially close to one another across frequencies, with the exception of

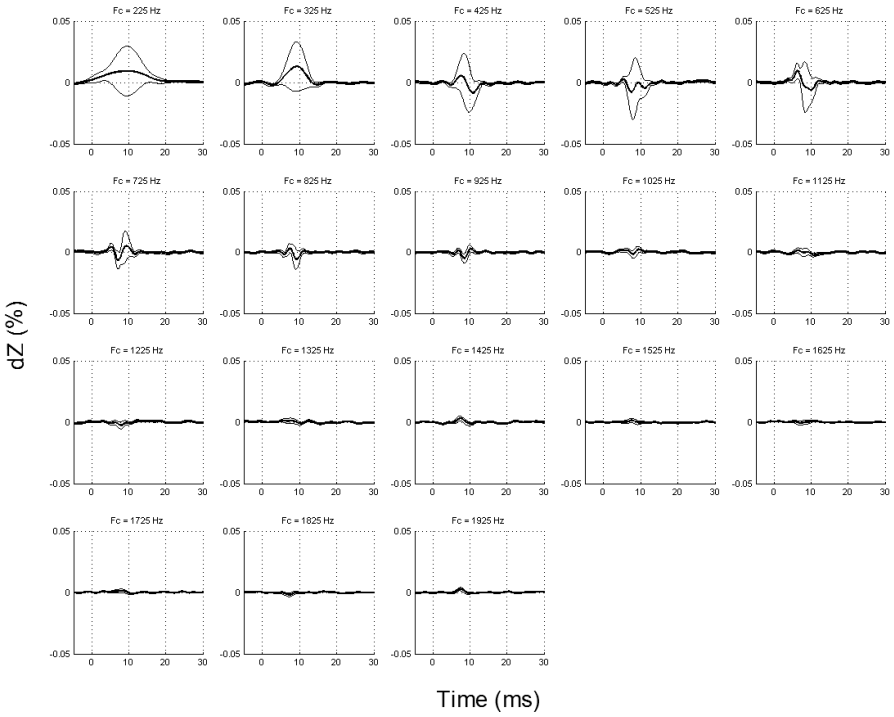

Figure 3.17.: EPs measured during EP-only recordings were added to simulated carrier signals and the resulting signal was processed for detection of artefactual impedance changes. dZ signal estimated from the resulting signal after addition of simulated carrier at different frequencies. Solid lines indicate the average dZ signal, dashed lines are ± s.e.m. (not visible in most plots). No significant dZ values were detected ($p>0.01$, $n=60$ samples each for 6 rats, two-sided t-test).

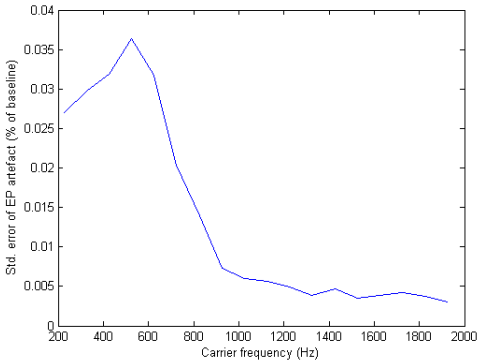

Figure 3.18.: Standard error of the EP artefact over frequencies expressed as % of the standing voltage. The error at frequencies <425 Hz is lower due to the decreased bandwidth (n=60 samples each for 6 rats).

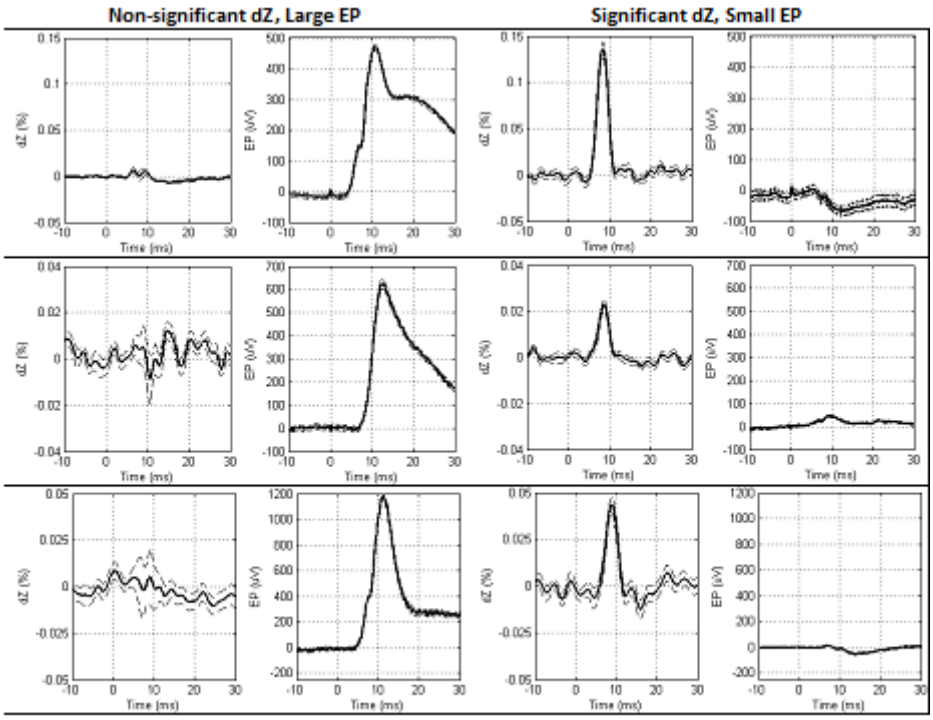

Figure 3.19.: Examples from three rats (rows) of channels with large EPs but non-significant dZ signals (left column), and channels with significant dZ signals (p<0.001, two-sided T-test) but small EPs (right column).

the active regions at 225 Hz. The relative distance between the centres of activity was computed using the active region at 625 Hz as reference; these distances were computed between recordings within the same rat and were averaged across rats. The average distance between active regions ranged from 265 μm to 570 μm (Fig. 3.26), with the active areas at 225 Hz being significantly farther away from the reference than the rest ($p<0.05$, Wilcoxon ranksum test, n = 25 recordings in 90 rats). The active regions at 225 Hz were also significantly more superficial (average depth: 611 μm) compared to the active regions at other frequencies (average depth: 1.1 mm; $p<0.01$, Wilcoxon ranksum test; n = 25 recordings in 9 rats, fig. 3.25).

To verify whether the observed anomaly in the location of the reconstructed activity at 225 Hz could be attributed to the impedance measurements, a correlation analysis between the raw dZ amplitudes in all combinations was performed to measure their similarity across frequencies. The peak impedance changes at 225 Hz were found to be significantly less similar to the chosen reference (the peak changes at 625 Hz) than the peak changes at other frequencies, as measured by their correlation coefficient ($p<0.01$, Wilcoxon ranksum test; fig 3.27, n = 24 recordings in 8 rats). Whereas the positive and negative peak dZ signals at 1025, 1525 and 1925 Hz were highly correlated with the positive peak changes at 625 Hz (averaged absolute correlation coefficients ranging from 0.7 to 0.9), the negative dZ peak at 225 Hz was less correlated (average absolute coefficient = 0.37). Therefore, the measured impedance changes at 225 Hz were relatively dissimilar to the impedance changes measured at higher frequencies.

3.3.5. Effect of demodulation bandwidth on the impedance signal and reconstructed conductivity changes

To illustrate the effect of the choice of bandwidth in the demodulation of impedance signals, a recording at 1925 Hz was processed using different bandwidths: 120 Hz, 300 Hz (the default), 500 Hz, 700 Hz, and 1000 Hz. The overall waveform of the dZ signals did not change with bandwidth but appeared noisier at higher bandwidths (Fig. 3.28, top). The reconstructed conductivity changes showed no apparent effect of bandwidth on the location of the active regions (Fig. 3.28, bottom) – the centre of the active regions occurred at a depth of 1.1 mm in all images. As expected, the relationship between bandwidth and temporal resolution was apparent in the images, as the time course of the impedance / conductivity changes appeared longer at 120 Hz bandwidth than at higher (>300 Hz) bandwidths.

3.4. Discussion

The purpose of this study was to find a suitable carrier frequency for fast-neural EIT imaging. Impedance changes in the rat somatosensory cortex were measured during evoked responses while varying the carrier frequency between 175 and 1975 Hz. The impedance recordings appeared to be technically sound, as evidenced by the: (1)

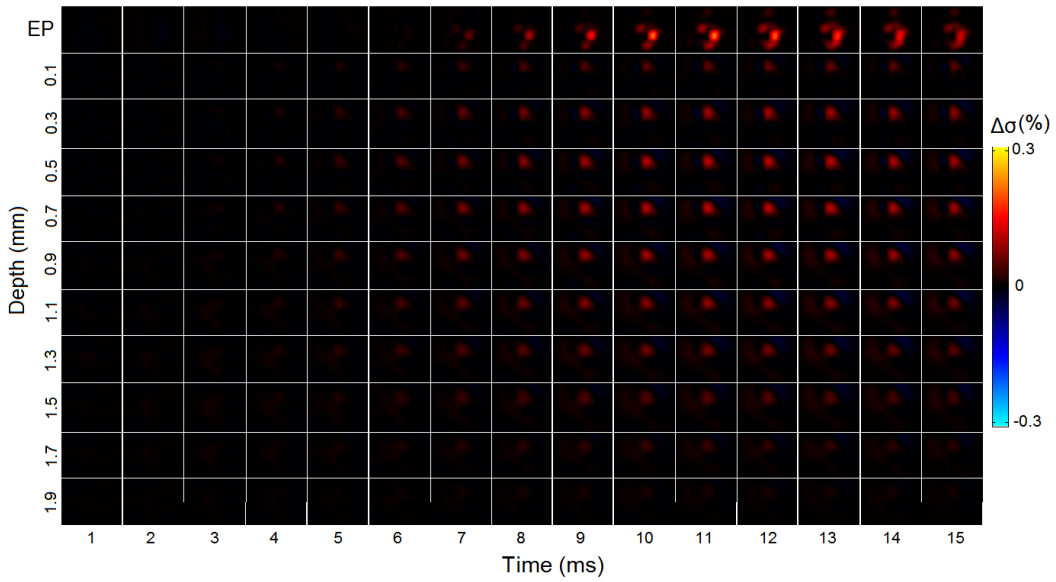

Figure 3.20.: Example of reconstructed conductivity changes in rat cortex during evoked responses, as measured with a 225 Hz carrier. (Top row) Rasterised images of EPs measured over electrode array. Colour coding is the same as in right colour bar, except that the scale ranges from 0 (black) to 1 mV (dark red). (Other rows) Rasterised images of conductivity changes. Each image corresponds to a slice parallel to the brain surface, beneath the electrode array; depth of slices as indicated on y-axis. Conductivity changes are colour-coded as indicated by the colour bar.

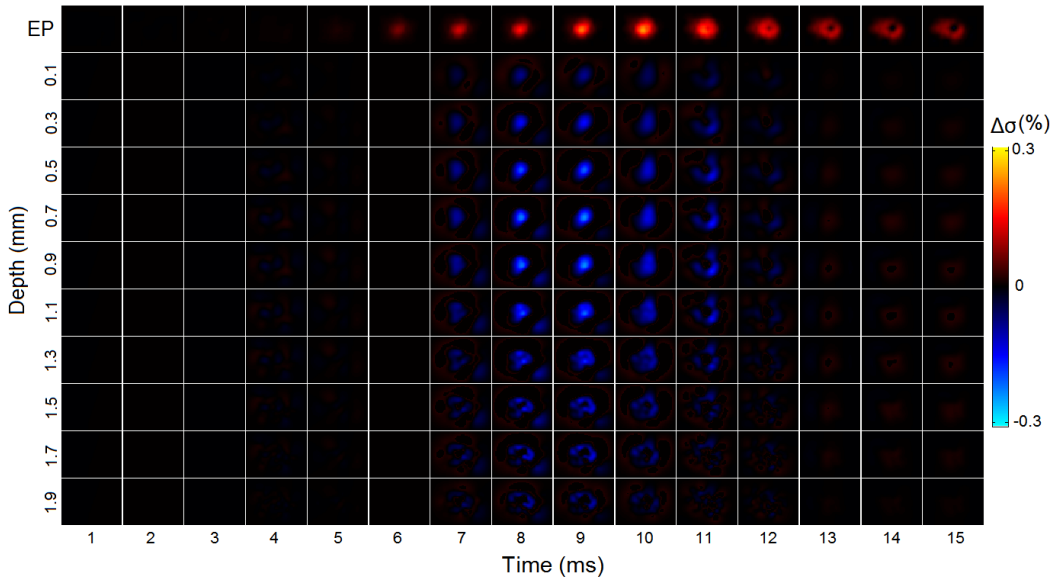

Figure 3.21.: Example of reconstructed conductivity changes in rat cortex during evoked responses, as measured with a 625 Hz carrier. Same format as in figure 3.20.

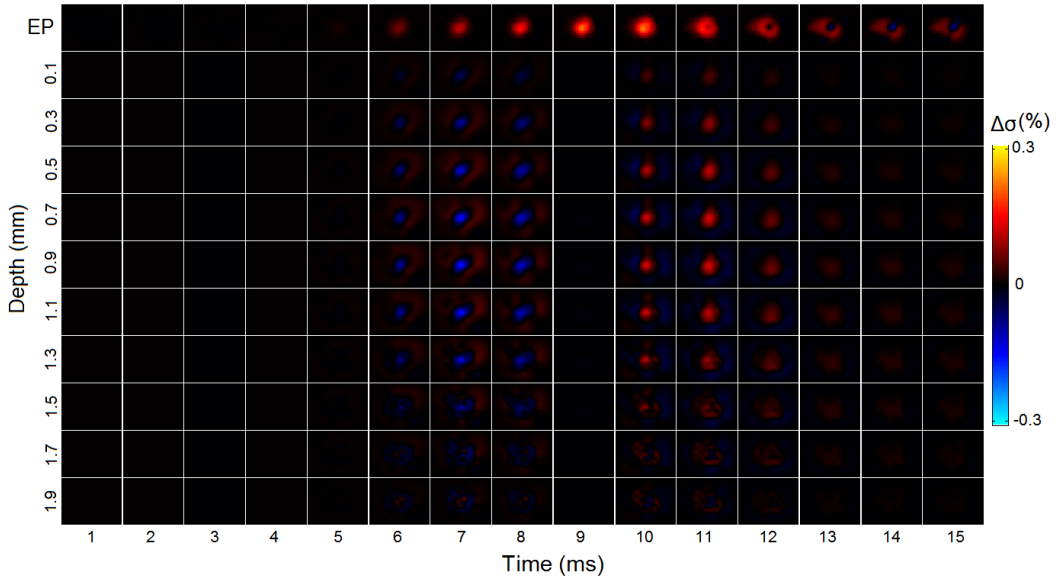

Figure 3.22.: Example of reconstructed conductivity changes in rat cortex during evoked responses, as measured with a 1025 Hz carrier. Same format as in figure 3.20.

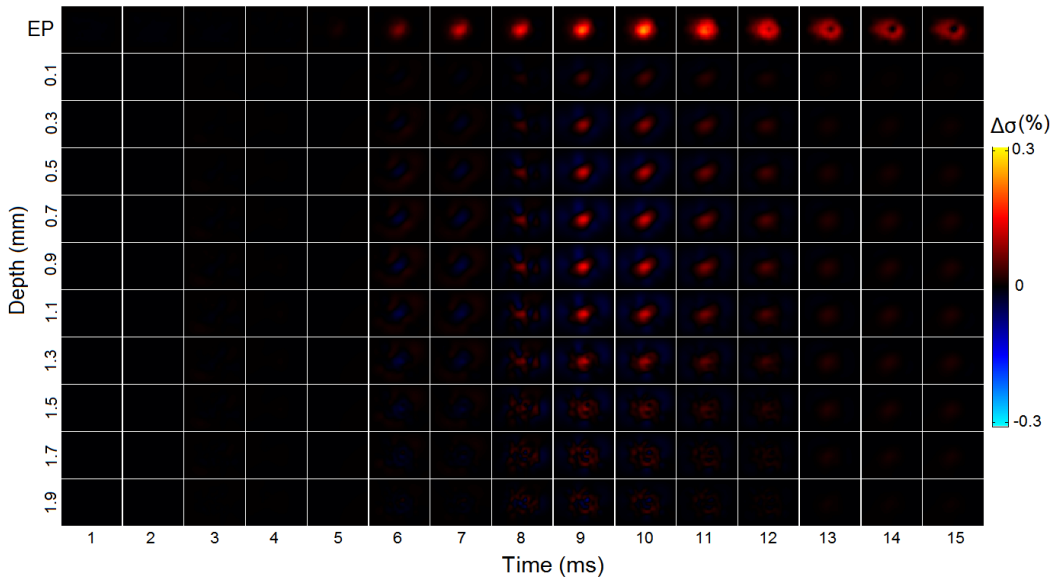

Figure 3.23.: Example of reconstructed conductivity changes in rat cortex during evoked responses, as measured with a 1525 Hz carrier. Same format as in Figure 3.20.

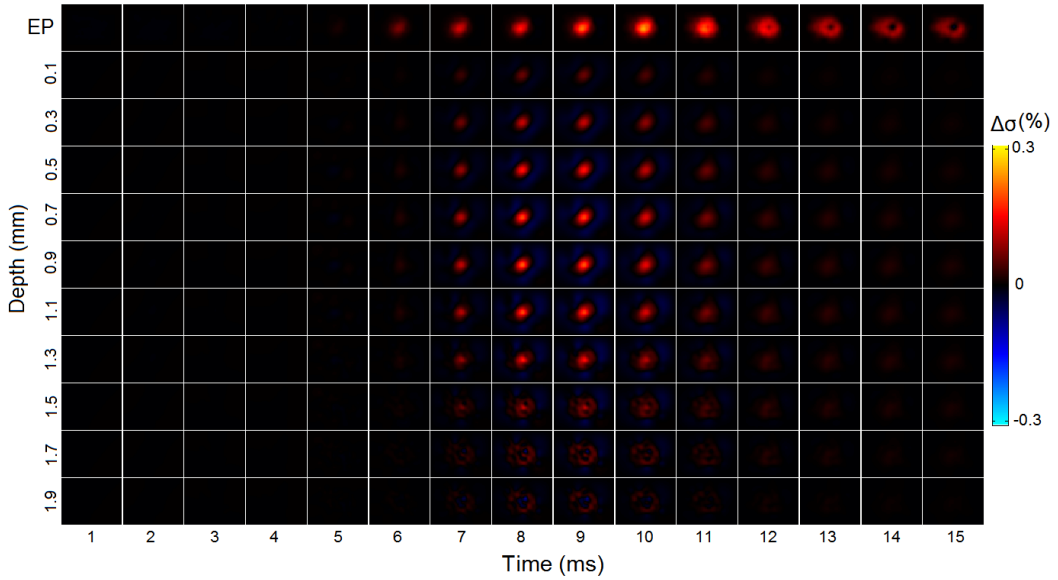

Figure 3.24.: Example of reconstructed conductivity changes in rat cortex during evoked responses, as measured with a 1925 Hz carrier. Same format as in Figure 3.20.

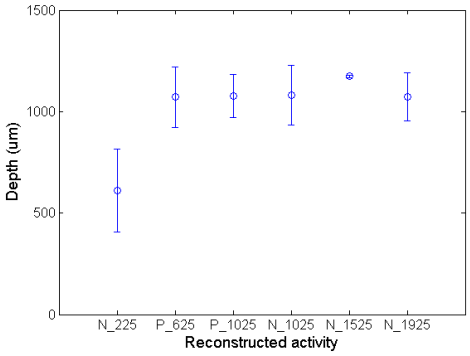

Figure 3.25.: Depth of reconstructed negative (N) and positive (P) impedance changes, measured with different carrier frequencies. N_225, N_1025, N_1525, N_1925 = Negative impedance peak, positive conductivity change at 225 Hz, 1025 Hz, 1525 Hz and 1925 Hz carrier frequency, respectively; P_625, P_1025 = Positive impedance peak, negative conductivity change at 625 Hz and 1025 Hz carrier frequency respectively; The mean values over all rats with full recordings at the respective frequencies are shown; error bars represent one standard deviation. The mean depth of the reconstructed activity for 225 Hz is significantly different from the reconstruction at all other frequencies ($p<0.01$, Wilcoxon ranksum test; n = 24 recordings in total, for five frequencies and eight rats).

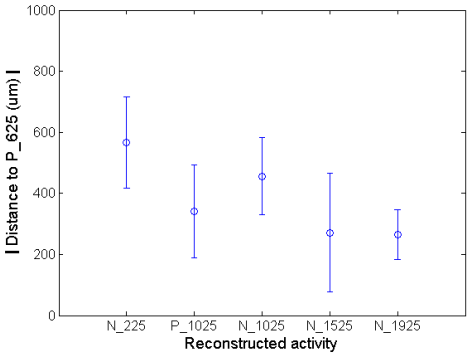

Figure 3.26.: Distance (in μm) of the reconstructed centre of activity at 625 Hz to the reconstructed centre of activity at other carrier frequencies. The reconstructed centre of activity at 225 Hz is significantly more distant than the distances at the other frequencies ($p<0.05$, Wilcoxon ranksum test; n = 24 recordings in total, for five frequencies and eight rats).

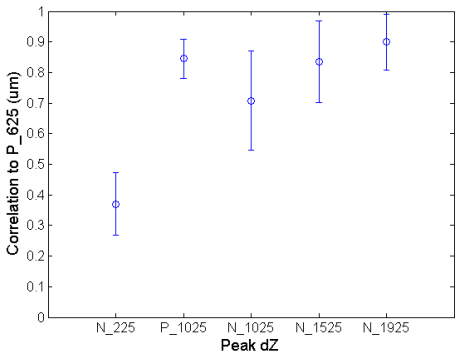

Figure 3.27.: Absolute value of the correlation coefficients between the peak dZ signals measured at 625 Hz (the 'reference') with the peak dZ signals measured at the other frequencies. The peak dZ signals at 225 Hz are significantly less correlated with the reference than those at the other frequencies ($p<0.01$, Wilcoxon ranksum test; n = 24 recordings in total, for five frequencies and eight rats).

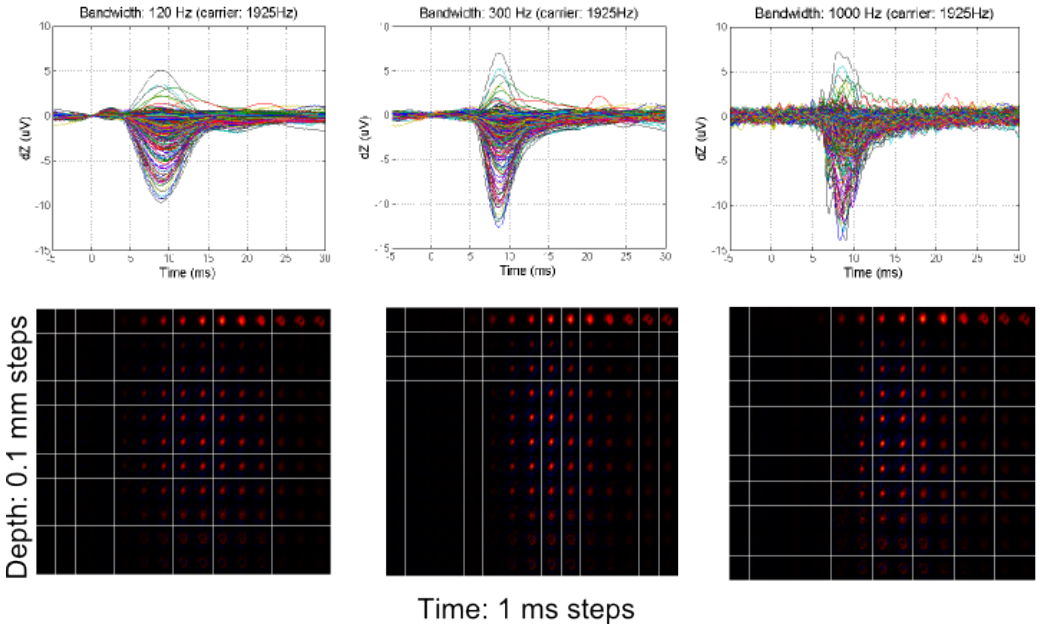

Figure 3.28.: Estimated dZ signals and reconstructed conductivity changes using variable bandwidths on a recording at 1925 Hz. Upper panel: dZ signals estimated using a bandwidth of 120 Hz (left), 300 Hz (middle) and 1 kHz (right). Lower panel: corresponding reconstructions of the conductivity changes (same format as in figure 3.24).

dipole pattern of the potential map over measurement electrodes (see Figure 3.10); (2) successful recovery of the EPs after cancellation of the carrier signal; and (3) physiologically plausible amplitude and timing of impedance signals. The results for the frequency at 225 Hz were consistent with those previously reported (Oh et al. [2011a]); both the amplitude and time of the negative dZ peak were consistent with those reported by Oh et al. A significant positive peak in the dZ signal (Fig. 3.12) was measured as the frequency was increased to around 625 Hz, which is consistent with unpublished results of the previous group (see 3.1.2.1). Thus, unlike the unimodal, negative dZ signal measured at 225 Hz, the dZ signal waveform measured at higher frequencies was bimodal, with a significant positive peak followed by a negative peak. Further increases in frequency, from 625 Hz to 1575 Hz, were followed by a decrease in the amplitude of the positive peak and increase in the amplitude of the negative peak (Fig. 3.12). In addition, the amplitude of the negative peak in impedance due to neuronal activity did not drop over frequency but was maintained at -0.08±0.02 at 1825 Hz carrier frequency compared to -0.04 %±0.01 at 225 Hz carrier frequency. The different bandwidth used at frequencies <425 Hz should be taken into account when comparing the amplitude of the impedance change. This lead to a smaller dZ amplitude at 175 Hz compared to 225 Hz.

This discussion is structured as follows. First, I examine the results of the various controls and demonstrate that, despite its unexpected waveform at higher frequencies, the dZ signal measured in our experiments is unlikely to be an artefact of the instrumentation or of the EPs. Then I discuss the observed trends in the characteristics of the dZ signal and, based on these results, determine the optimal carrier frequency for future EIT recordings. I will then discuss possible effects of the injected current on neuronal activity. Finally, I discuss some possible physiological explanations for the observed positive impedance changes.

3.4.1. Validity of impedance measurements

The results of the control experiments and analyses are consistent with the hypothesis that the measured dZ signals were genuine, activity-related impedance changes. So far, our results appear to rule out alternative explanations that the dZ signals were artefactual and caused by the instrumentation or the recorded EPs. Here I discuss the evidence against these alternative hypotheses.

The main evidence against the dZ signal being an instrumentation-related artefact comes from the controls performed in the animal model, which included a no-stimulation paradigm and an ipsilateral stimulation paradigm. These paradigms were not expected to elicit a significant neuronal activation and, consequently, any impedance changes. Since there were no impedance changes during these control recordings, it follows that the dZ signal during the normal recordings cannot be an artefact of the electrical stimulation or the hardware alone. To further rule out any instrumentation-related issues, each component of our system was tested or replaced. First, it was verified that our current source indeed delivered a constant current during our experiments. A small (1 kΩ) resistor was placed in series with

the current-injecting channel and recorded the voltage across the resistor during two rat recordings which had significant impedance changes. There were no significant changes in current amplitude as measured across the series resistor.

Secondly, our results were compared to unpublished validation data of Oh et al. (see 3.1.2.1), where they used a Neurolog system with a carrier frequency of 625 Hz. They came to same results as ours, even though they used a different system to ours for current injection and measurement. They recorded impedance changes in response to forepaw EPs and also recorded activity-related positive impedance changes at 625 Hz but not at lower frequencies.

Another potential concern was that the EPs could distort the measured dZ signals or EP shape might be altered by the injected current. EPs naturally vary from trial to trial, and so cannot be completely removed by subtracting samples between consecutive trials (as part of the signal processing; see Methods). A residual EP signal may be partially coherent with the carrier signal, manifesting as an artefactual modulation. However, several results indicate that this does not occur. First, there were no consistent impedance changes when recorded EPs were added to simulated sine waves at different frequencies – the EPs caused only small, statistically insignificant fluctuations in the resulting dZ signal (Fig. 3.17). Second, the size of the dZ signal in μV was directly proportional to the injected current amplitude (Fig. 3.15), consistent with an impedance change. The amplitude of any EP-related artefacts in the demodulated signal is unlikely to scale with current, since EP size was unaffected by higher current levels. An alteration of the shape of the EP due to the injected current is hence unlikely. Finally, several channels were found with significant impedance changes but low EPs, or with large EPs but no impedance changes (Fig. 3.19). Altogether, these results demonstrate that EP-related artefacts in the dZ signal were negligible and the recorded changes in the impedance physiological in origin.

3.4.2. Determining the optimal carrier frequency

Previous biophysical modelling of the cortical cells by Oh et al., based on the predictions of Liston et al. for the crab nerve, had predicted that the SNR would peak at around 250 Hz and monotonically decrease at higher frequencies (Figure 3.1, Oh et al. [2011a], Liston et al. [2012]). Had this been confirmed, the optimal carrier frequency for EIT neural recordings would have been 250 Hz, which would limit its temporal resolution to 8 ms (see Methods). However, the SNR did not follow the predicted trend and that the SNR at 1925 Hz was larger than at 225 Hz. This result is in accordance with our modelling using Cole's equation, as well as the measurements by Logothetis et al. (Logothetis et al. [2007]). A theoretical basis for the difference between the two models and the different results in the literature has been proposed by Bédard an Destexhe (Bédard and Destexhe [2009]). They modelled the effect of the accumulation of ions at the interface on the injecting electrode on the voltage measurement. They came to the conclusion that the $\alpha-$dispersion (frequency dependence) of the cortical impedance seen by authors

such as Klivington and Galambos and Gabriel et al. (Klivington and Galambos [1968], Gabriel et al. [1996]) is due to the accumulation of ions at the electrode interface when a two-electrode method is used. If additional non-injecting electrodes are used for voltage measurements as in our method, $\alpha-$dispersion of cortical tissue does no occur (Bédard and Destexhe [2009]). Using multiple non-injecting recording electrodes therefore allows us to apply higher carrier frequencies and increase the temporal resolution of the sine-wave EIT method and improve the SNR. The SNR of positive and negative impedance changes followed different trends with respect to carrier frequency (Figure 3.14). The maximal SNR for the positive dZ signal was achieved at around 625 Hz and decreased monotonically thereafter. In contrast, the SNR of the negative dZ signal increased at higher frequencies and reached a maximum between 1525 and 1975 Hz.

The centres of reconstructed activity within the same rat were remarkably similar, as seen in 3.3.4, with the exception of the reconstructed centre of activity at 225 Hz. The centre of activity in recordings at 225 Hz was located more superficially in the cortex than at other frequencies. Therefore, recordings at 225 Hz not only had a lower SNR than those at higher frequencies, but their reconstructed centre of activity was also not concordant with those at higher frequencies. This may be attributed to these recordings being noisier due to the residual EPs (see Fig. 3.17), and not simply to the lower bandwidth used for these recordings, since setting a lower bandwidth for a recording at 1925 Hz did not alter the reconstructed area of activity as shown in Fig. 3.28.

In conclusion, a carrier frequency of 1975 Hz appears to allow for maximal temporal resolution as well as the highest SNR, and the centre of the reconstructed activity is concordant with those at frequencies $\geqq$ 625 Hz. Hence, 1975 Hz appears to be the optimal carrier frequency for EIT imaging of fast neural activity from those frequencies tested. There is the potential that an even higher carrier frequency would improve the temporal resolution further whilst keeping the SNR stable, this could not be verified, due to hardware limitations.

3.4.3. Effect of sinusoidal current on neocortical activity

Recent reports have shown that weak sinusoidal electric fields can significantly alter cortical activity by entraining action potentials (Frohlich and McCormick [2010], Anastassiou et al. [2010]). Although these ephaptic effects are stronger at lower frequencies (<8 Hz; Anastassiou et al. [2010]), they raise the question of whether the current injected for impedance measurements was safe over the range of frequencies and amplitudes employed in this study. The previous study by Oh et al. (2011) addressed this concern for currents at 225 Hz by analysing the effect of current amplitude on the size of the recorded EPs and dZ signals. They found that both EP and dZ signals were not affected in size for current levels up to 50 μA, but EPs measured during 100 μA current injection were significantly smaller (Oh et al. [2011a]). A similar analysis in the present study for currents at 1025 Hz did not detect any significant effect of a 5-fold increase in current level (from 12 to 60 μA) on

either the amplitude or timing of EPs, or on the size of impedance changes. Neither EP amplitude nor timing were affected by the frequency of the injected current (amplitude of current was set at the maximum 60 μA). Although these results do not rule out an effect of the current at the cellular level, they suggest that cortical activity was not significantly altered at a macroscopic level (as measured by our instrumentation) by the current injected for the impedance measurements or that, if it was, the effect was linear.

3.4.4. Positive impedance changes during neural activity

By far the most important result in this work were the positive impedance changes during evoked responses at intermediate frequencies ($425 \leq$ Fc ≤ 1575 Hz). The result is in accordance with unpublished results of the previous group (see 3.1.2.1). This result directly contradicted the long held assumption that impedance of cortical tissue should only decrease during neural activity due to the opening of ion channels (Liston et al. [2012], Holder [2005]). Although positive impedance changes had been previously reported in the literature (Klivington, K Galambos [1967]), they were reported to occur after an initial impedance drop, and could thus be plausibly explained as the result of ion channels closing during membrane hyperpolarisation. However, the same explanation cannot be applied to the positive impedance changes observed in our recordings, since these occurred prior to both the impedance drop and the peak time of EPs. An alternative biophysical explanation is therefore needed for this newly discovered phenomenon.

First, it should be noted that the measured impedance changes were almost entirely resistive changes. The rat cortex was almost purely resistive, as evidenced by the relative phase of $\tilde{}6^o$ between the injected current (frequency: 1925 Hz) and the potential of the measurement electrodes. This result is consistent with measurements in the macaque cortex, which was reported to be resistive, homogeneous, and isotropic in the grey matter (Logothetis et al. [2007]) and with measurements from the pig cortex (Seoane et al. [2005]). Furthermore, impedance changes measured in two rats were decomposed into resistive and reactive changes, and the resistive changes accounted for >99% of the changes in the modulus. Thus, the observed increase in impedance was due to an increase in the resistivity of cortical tissue.

One possible explanation is membrane resonance of cortical neurons at 600 Hz. Resonance of central neurons at such a high frequency has not previously been described but I will outline here why I think this is feasible. Central neurons have a frequency dependent response due to the passive and active properties of their membranes. The passive components (the parallel leak conductance and capacitance of the outer membrane) of the cell membranes act as a high-pass filter and attenuate transmembrane current to voltage oscillations at low frequencies. The active components are specific classes of voltage gated currents, for example slowly activating, rectifying potassium currents, which act as a low-pass filter. The passive and active components of the neuron membrane taken together can produce membrane resonance, which can be modelled as inductance in parallel to the resistance

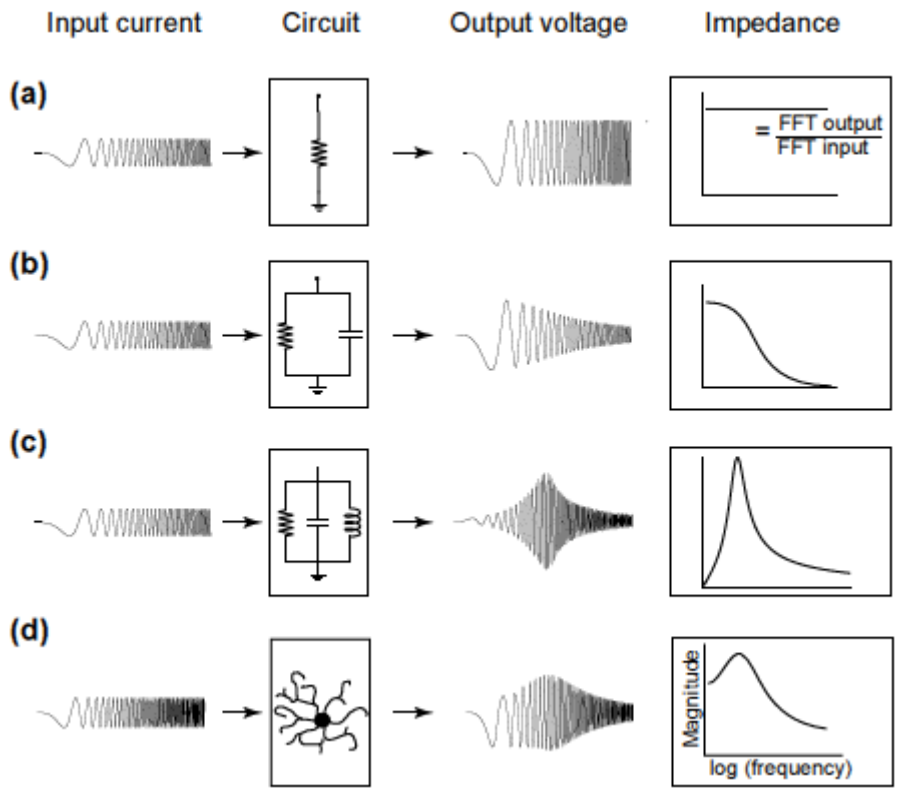

Figure 3.29.: Impedance spectrum of electronic circuits and neurons (Hutcheon and Yarom [2000], reproduced with permission). Subplot (a)-(c) show the output voltage of a current with steadily increasing frequency, passed through three different kinds of electronic circuits. (d) Depicts the measured output voltage of this current through a neuronal membrane.

and capacitance in an electronic circuit model (Hutcheon and Yarom [2000], see figure 3.29).

Resonance frequencies of various central neurons have been described in the past which is a possible mechanism of specific neurons to discriminate between their inputs, based on their frequency content, so that oscillatory inputs near the resonant frequency produces the largest response (Hutcheon and Yarom [2000]). The highest resonance frequency described for a nerve cell that was found in the literature was 300 Hz for the giant squid axon (Cole and Baker [1941]). Resonance and oscillations are closely linked as they represent two aspects of the same basic phenomenon of frequency preference (Hutcheon and Yarom [2000]). High frequency oscillations (HFO) as a component of the EEG or magnetic oscillations of 500-900 Hz in layer 4 of the somatosensory cortex have been described by several authors as part of the somatosensory EP. They are taken to be due to activation of fast spiking inhibitory

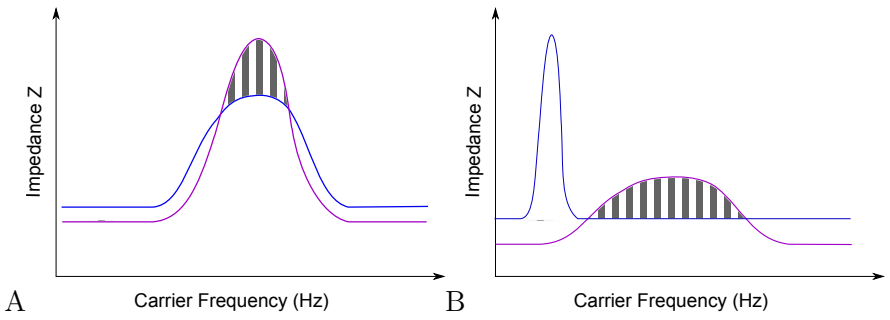

Figure 3.30.: Possible resonance response of the neurons; blue = baseline, purple = neuronal activation. (A) With the opening of voltage gated channels the resonance could be amplified as shown in purple, causing a positive change in impedance at intermediate frequencies (striped area between the curves). (B) Alternatively, with the depolarization of the membrane the resonance frequency could shift, causing a positive change in impedance (striped area between the curves).

neurons (FS interneurons) by monosynaptic thalamic input (Hashimoto et al. [1996], Buzsáki and Silva [2012], Ritter et al. [2008]). This finding could imply that the FS interneurons in layer 4 of the somatosensory cortex are resonant to frequencies around 600 Hz. Should this be the case, two mechanisms are possible that could cause a positive impedance change at frequencies around 600 Hz. The resonance could either be increased by amplifying currents which has been described to be due to persistent Na^+current which flows through NMDA-receptor channels or dyhydropyridine sensitive high-threshold Ca^{2+}currents. Amplifying currents interact with resonant currents without greatly altering the resonant frequency (Hutcheon and Yarom [2000], see figure 3.30, A). Alternatively, the resonant frequency could shift due to the change with the membrane potential and lead to a change in impedance as seen in figure 3.30 (B). Such a shift in the resonance frequency with the membrane voltage has been described in mesencephal neurons of rats (Wu et al. [2001]) and in thalamocortical neurons of guinea pigs (Puil et al. [1994]). The time difference between the positive and the negative peak in impedance at 1025 Hz carrier frequencies is roughly 3-4 ms apart, this could be due to the time difference between the thalamocortical input to inhibitory interneurons and excitatory neurons. Cruikshank et al. found the time difference between the firing of fast spiking inhibitory interneurons and regular spiking excitatory neurons to be 1.65 ms in response to thalamic stimulation, measured in patch-clamp recordings in thalamocortical slices of mice (Cruikshank et al. [2007]).

No inductance was included in the modelling using Cole's equation or in Liston et al.'s model of the impedance change over frequencies so it is not surprising that neither model predicted any positive changes in impedance. I am suggesting two separate steps to test whether the observed positive impedance changes could be

due to resonant behaviour of FS interneurons as suggested here. The testing of the resonance hypothesis suggested here will be discussed in the next chapter.

4. The source of the fast neural signal in EIT

4.1. Introduction

4.1.1. Orienting paragraph

In chapter 3 an unexpected activity evoked increase in impedance was recorded when a 600 Hz carrier frequency was used. I hypothesize that could be a resonance effect of ion channels of fast spiking interneurons at 600 Hz. In this chapter this possibility will be addressed. If the positive evoked impedance response is really due to a resonance effect on ion channels of one specific interneuron type then this poses the additional question of what percentage of the impedance signal is due to activity on interneurons. Fast-spiking interneurons are a subgroup of GABAergic interneurons, which in total only make up only 15-25% (Hendry and Schwark [1987]) of the total neurons in the brain. If the impedance increase is really due to resonance in this subgroup of neurons, then their effect appears to override the impedance drop in other cell types which are much larger in number. One possible reason for a resonance effect causing such a large signal could be that the subgroup of neurons involved open up a low resistivity path networked by gap junctions with very little electrical resistivity.

4.1.2. Background

4.1.2.1. 600 Hz high frequency oscillations

High frequency oscillations (HFO) are oscillations in the EEG in the 80 - 600 Hz frequency range (Engel and da Silva [2012]). Depending on their location, frequency and situation in which they occur they can either be part of normal function or are associated with pathology in epilepsy (Engel and da Silva [2012]). They have been shown to play a role in visual perception (Singer and Gray [1995]), in the sensorimotor cortex related to motor activity (Murthy and Fetz [1996]), whisker evoked potentials in rats (Jones and Barth [1999]), in verbal memory (Sederberg et al. [2007]) and spatial learning (Ego-Stengel and Wilson [2010]). HFOs in the 600 Hz range have been reported to appear in median nerve somatosensory evoked potentials of humans in EEG and snout stimulation elicited activation in pigs with MEG (Gobbelé et al. [2004], Restuccia et al. [2011], Ikeda et al. [2002]). The HFOs in somatosensory EPs are generally understood to be generated by GABAergic inhibitory interneurons in layer 4 of the cortex (Hashimoto et al. [1996], Swadlow [1989]).

4.1.2.2. Interneurons

Most neocortical neurons in mammals are excitatory pyramidal neurons (Hendry and Schwark [1987]), which have relatively stereotypical anatomical and physiological properties. The remainder of neurons are inter-neurons, which are mostly inhibitory and have more diverse characteristics (Markram et al. [2004]). Features which distinguish interneurons from pyramidal neurons are the presence of aspiny

dendrites, the occurrence of both excitatory and inhibitory synapses onto their somata and the branching characteristics of interneurons. Interneurons usually arborize within a cortical column and can project laterally across columns but do not project down into the white matter, which leads to them sometimes being called 'local circuit neurons' (Markram et al. [2004], Thomson and Deuchars [1994]). Interneurons can be put into three groups that express one of three marker: (1) the Ca^{2+}-binding protein parvalbumin (PV), (2) the neuropeptide somatostatin (SST) and (3) the inotropic serotonin receptor 5HT3aR (Rudy et al. [2011]). The PV group accounts for approximately 40% of all inter-neurons and is associated with a fast-spiking firing pattern (Rudy et al. [2011]). Fast spiking (FS) interneurons are of particular interest as they have particular fast acting ion channels to allow high firing rates and are therefore the most likely candidate to produce resonance at frequencies of around 600 Hz. They will therefore be discussed in more detail below.

4.1.2.3. Fast spiking interneurons

FS interneurons make up approximately 5-10% of the total neuron population in the neocortex; they occur in layer 2-6 and are particularly common in layer 4 (Rudy and McBain [2001]). They have 2 distinct special features: (1) they contain a specific arrangement of ion channels which allows them to produce exceptionally fast sustained trains of action potentials with little spike-frequency adaptation Chow et al. [1999], Erisir et al. [1999] and (2) they are interconnected with each other by gap junctions (Galarreta and Hestrin [1999], Gibson et al. [1999]).

To be able to produce such high frequency activity FS interneurons have specific ion channels whose time constant allows them to fire at high frequencies. They express a specific subfamily of potassium channels which contains Kv3.1-Kv3.2 proteins (Chow et al. [1999], Erisir et al. [1999], Rudy and McBain [2001]). Kv3.1 and Kv3.2 are expressed in the neocortex as well as in the hippocampus, two brain structures that contain fast spiking GABAergic interneurons (Weiser et al. [1995], Sekirnjak et al. [1997], Chow et al. [1999], Martina et al. [1998]). Kv3.1-3.2 enable sustained high frequency firing by facilitating the recovery of Na^+-inactivation and by minimizing the duration of the afterhyperpolarization in neocortical interneurons (Erisir et al. [1999]). It will be tested, whether the combination of this channel type together with the Na^+-channel in this neuron could cause resonance at frequencies of ~600 Hz by modelling as well as by selectively blocking the Kv3.1-2 channels with very low doses of 4-AP (Martina et al. [1998]). Low doses of 4-AP have been shown to inhibit fast delayed rectifier K^+-channels in brain slices (Martina et al. [1998]).

The other distinguishing feature of FS interneurons is the presence of gap junctions which couple them electrically. Simultaneous recording from FS interneurons revealed coupling ratios of 62-66% (Galarreta and Hestrin [1999], Gibson et al. [1999]). They are exclusively coupled to each other and not with any other cell type (Galarreta and Hestrin [1999]). Most commonly, gap junctions occur between dendrites but examples between a dendrite and a soma or two somata have been

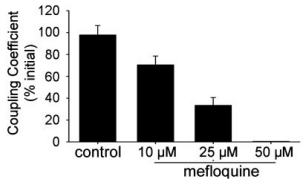

Figure 4.1.: Bar graph summarizing effect of different concentrations of mefloquine vs control on the coupling coefficient between cells. Figure from Cruikshank et al. (2004).

described in the past (Galarreta and Hestrin [2001]). Gap junction channels are composed of proteins called connexins. They allow ionic current and small organic molecules to pass directly between cells with symmetrical ease (Cruikshank et al. [2005]). In the cortex, interneurons and glia cells but not pyramidal cells form gap junctions (Cruikshank et al. [2005]). The gap junctions in different cells can be distinguished by the subtype of connexins they use. Connexins are membrane spanning proteins, six of which combine to form a hemichannel called connexon. Interneurons in the cortex all express connexin 36 channels (Cx36), named after their molecular weight of 36 kDa (Cruikshank et al. [2005]), whereas Cx32 and Cx43 are present in glial gap junctions (Dermietzel and Hertberg [1991], Rash et al. [2000]). Cx36 can be specifically blocked by low doses the antimalarial drug mefloquine in neocortical slice preparations of rats with minimal nonspecific actions (Cruikshank et al. [2004]). Mefloquine caused no significant change in evoked excitatory or inhibitory postsynaptical potentials, and intrinsic cellular properties in Cruikshank et al.s experiments (Cruikshank et al. [2004]).

4.1.3. Rationale

The purpose of the study presented here is two-fold: (1) To test whether the potassium channel of FS interneurons could be responsible for the resonance effect seen at 600 Hz injected current during activity and (2) to test whether part of the fast neural response is due to current flowing through the gap junction in interneurons.

4.1.4. Experimental design

The role of FS interneurons in the generation of high frequency resonance was tested by using a Hodgkin-Huxley type model using the equations and parameters of Pospischil et al. (Pospischil et al. [2008]), but using the conductivity values of FS interneurons as measured by Erisir et al. (Erisir et al. [1999]).

The role interneurons play in the generation of the fast neural dZ signal was tested by (1) blocking their gap-junctions using mefloquine and (2) by blocking the Kv3.1-2 channels using low-dose 4-AP. Mefloquine and 4-AP were injected into the cortex of a rat and forepaw EPs were measured during propofol anaesthesia before

and after injection.

4.2. Methods

4.2.1. Modelling

The membrane dynamics of fast-spiking interneurons were modelled using Hodgkin-Huxley equations (Hodgkin and Huxley [1952]) adapted for this specific neuron type (Pospischil et al. [2008]). The model parameters were obtained from Figure 3 of Pospischil et al. (2008), except that the maximal conductance of the delayed-rectifier K+ channel (gKd) was set to 220 mS/cm2 to model the fast dynamics of channels containing Kv3.1-Kv3.2 proteins (Erisir et al. [1999]). The impedance response of the simulated membrane was measured by injecting a small sinusoidal current at different frequencies. The impedance spectrum was measured both at the neuron's resting state (membrane potential = -70 mV) and at a sub-threshold, depolarized state (membrane potential = -55 mV).

4.2.2. In-vivo experiments

4.2.2.1. Animals, anaesthetic and surgical procedure

The animals, the anaesthetic and surgical procedure used in this study is the same as described in chapter 3 in 3.2.2.

4.2.2.2. EEG and impedance recordings

Electrodes The surface electrode arrays were produced in house using stainless steel foil in silicone rubber in a sandwich technique. The arrays were designed and produced by Mohamed Koronfel, they measured 6x8 mm and had 30 stainless steel contacts measuring 0.6 mm in diameter, which were platinised before implantation. As in chapter 3 the electrode was placed above the first sensory cortex on the forepaw localization.

EEG amplifier and current source The same EEG amplifier as in chapter 3 was used. The current source used in this study was the Keithley 6221 current source (Tektronix U.K. Ltd Keithley Instruments, UK). It produces AC currents from 2 pA to 100 mA up to a frequency of 100 kHz and has an output impedance of $10^{14}\Omega$. It was combined with a custom designed switching system based on the ADG714 CMOS (Analog Devices Ltd., UK) and was controlled via an Arduino (SmartProjects, Italy) through a custom made MATLAB interface (Mathworks, USA).

4.2.2.3. Mefloquine

Evoked potentials were elicited as described in chapter 3 were elicited in four rats while the impedance was recorded. Then 25μM mefloquine was injected through the array into the cortex in portions of 5μl as closely to the electrode with the largest activity in EEG as possible and the evoked changes in impedance were measured again. The carrier frequency for the impedance measurements was 1700 Hz in all recordings. As a control, 5 μl of saline was injected before the injection of mefloquine in one rat to ensure that the injection of fluid would not alter the EP or dZ. In one rat the needle was inserted and further EPs conducted without starting the mefloquine injection to test for an effect of the needle alone.

4.2.2.4. 4-AP

Evoked potentials were elicited as described in chapter 3 were elicited in four rats while the impedance was recorded. Then 10μM 4-AP was injected through the array into the cortex in portions of 3μl as closely to the electrode with the largest activity in EEG as possible and the evoked changes in impedance were measured again. The carrier frequency for the impedance measurements was 1700 Hz in all recordings.

4.2.2.5. Analysis of in-vivo recordings

The raw voltages were recorded as described in chapter 3 and the EEG and dZ were extracted. The EEG was extracted by low pass filtering it at 300 Hz. The impedance data was recovered by first band-pass filtering the recorded voltages with a filter of $\pm$ 300 Hz. The voltages were then demodulated as described in chapter 3. Outlier rejection was performed as explained in 3.2.6.3. The data was compared two-fold. Both the maximum EPs and dZs were compared and then the EPs and dZs for the channels with the largest initial dZ compared. The dZ and EP measurements were normalized by their first value to allow an easy comparison.

4.3. Results

4.3.1. Modelling

The membrane dynamics of a fast-spiking interneuron was simulated using modified Hodgkin-Huxley equations (Pospischil et al. [2008]). When stimulated with supra-threshold depolarizing current, the simulated neuron generated a fast sequence of action potentials (at ~500 Hz; Fig. 4.3.1). The simulation also revealed a change in the impedance spectrum of the neuron's membrane between its normal resting state (-70 mV) and a sub-threshold depolarized state (-55 mV). At rest, the membrane impedance had a resonant frequency at 80 Hz, but when depolarized the membrane exhibited a much higher resonant frequency at 540 Hz (Fig. 4.3.1). Due to this shift in resonance, the impedance change between resting and depolarized states

was initially negative at low frequencies but turned positive at higher frequencies, with peak amplitude at 540 Hz (Fig. 4.3.1).

4.3.2. In-vivo experiments

4.3.2.1. Mefloquine

49 evoked impedance recordings were conducted before and after injection of mefloquine in all four rats. The evoked potentials in EEG and accordingly the evoked dZ showed a large interindividual difference. The injection of mefloquine caused a decrease in both EP size and dZ size as seen in figure 4.3.2.1. This reached statistical significance in three of the four rats ($p<0.05$, Wilcoxon ranksum test). In the rat that did not show a statistical significant decrease of EP and dZ, there were very few data points in the first recording. The maximum EPs were normalized by their first value as well and remained much stable throughout the recording with a mean normalized value 1.02 ± 0.33 ($n = 32$).

4.3.2.2. 4-AP

Injection of 10 μM 4-AP caused epileptiform spiking in the EEG of two rats and the recordings were aborted.

4.4. Discussion

In this study the impedance spectrum of a membrane was modelled and values from the literature for Kv3.1-2 channels from fast spiking interneurons included. In modelling, the impedance spectrum of the membrane had a resonant frequency of 80 Hz at rest (-70 mV), which increased to 540 Hz when the membrane was depolarized to -55 mV (see figure 4.3.1). The modelling suggest that the positive impedance measured in chapter 3 at 600 Hz frequencies could be due to a resonance effect of the injected current on the cell membrane of fast spiking interneurons. The resonance frequency of the membrane shifts between the resting and the activating state according to our modelling. A shift in resonance frequency with depolarization has been described in mesencephalic neurons of rats (Wu et al. [2001]) and in thalamocortical neurons of guinea pigs (Puil et al. [1994]). As the resonance shifts with during activation an increase in voltage could be measured, when a resonant carrier frequency is used. As voltage recordings are used in our method, this increase in voltage would cause an apparent increase in impedance after analysis.

If the hypothesis, that the increase in impedance seen in our recordings is due to resonance in the cell membrane of one subtype of interneurons which makes up 5-10% of the total neurons, is accepted, the question on why our recordings are so sensitive to this effect should be asked. Why would resonance on such a small number of neurons give us a larger impedance signal than the drop of impedance in all other neurons?

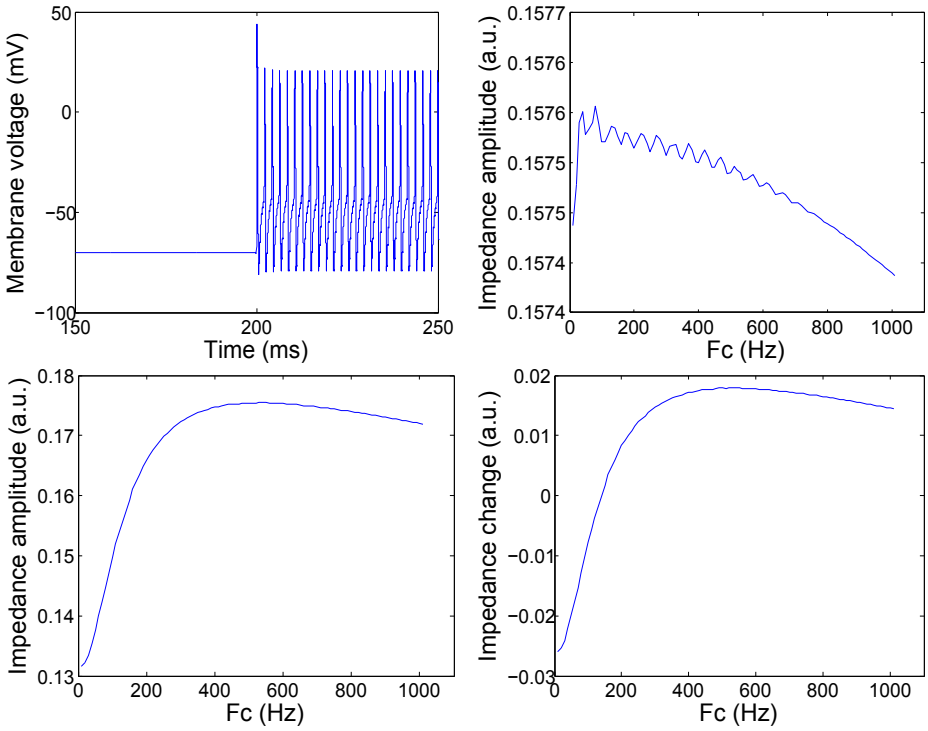

Figure 4.2.: (Top left) The simulated neuron generated a burst of action potentials when a supra-threshold depolarizing current was applied at t=200 ms. (Top right) Impedance spectrum of the membrane at resting state (-70 mV) with resonance at 80 Hz. (Bottom left) Impedance spectrum of the membrane at a depolarized state (-55 mV), showing a higher resonant frequency at 540 Hz. (Bottom right) Difference in membrane impedance between resting and depolarized states. The impedance change is positive at frequencies above 150 Hz, with peak amplitude at 540 Hz. Impedance is given in arbitrary units (a.u.) for all three graphs.

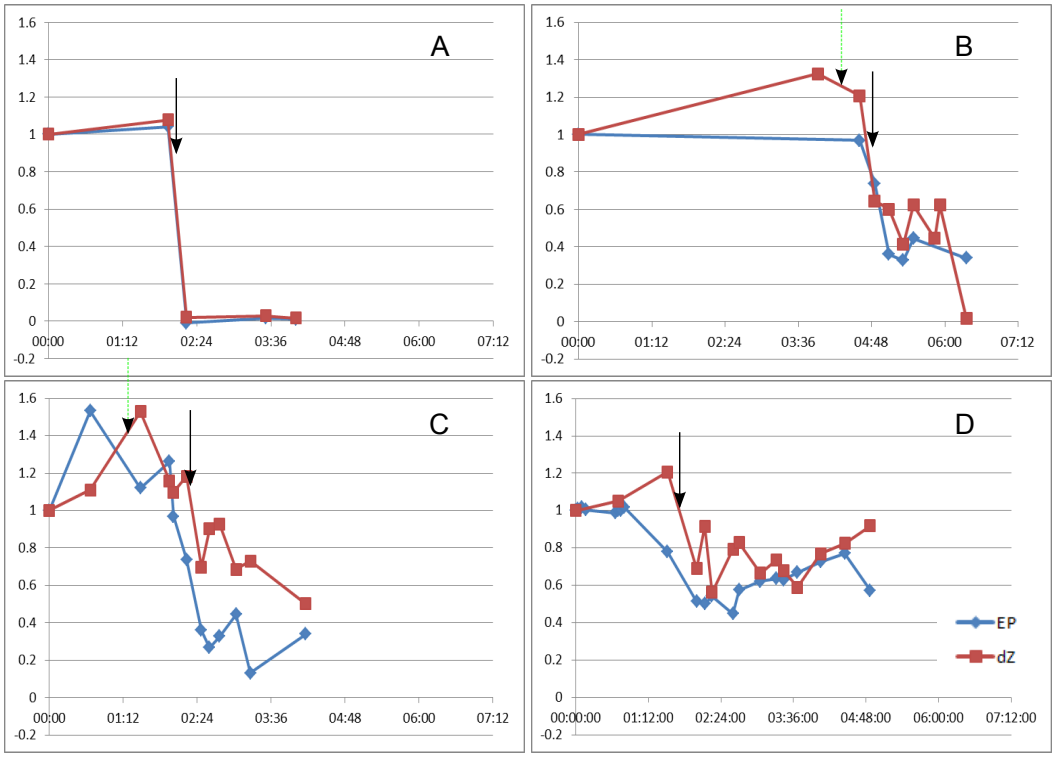

Figure 4.3.: Normalized dZ (red) and EP values for four individual rats are shown against time in hours (A)-(D). Each EP and dZ was normalized by its first value to allow better comparison between rats. The black arrows (solid line) indicate the time mefloquine was injected in (A)-(D), the dashed green arrow in (B) indicates the injection of 5 μl of saline and in (C) the insertion of a needle without injection of mefloquine.

When the ion channels open in neurons during depolarization an additional path is open for the current to pass which decreases the impedance overall. One possibility for the importance of FS interneurons could be that this additional current path is particularly low in resistivity because there is a direct connection from one of these cells to the next because they have gap junctions. Gap junctions would allow the current to pass from cell to the next without encountering much resistance. The junctional conductance of gap junctions has been measured as being 658-1600 pS in FS interneurons and an even higher junctional conductance of 2100 pS has been described for low threshold spiking (LTS) interneurons (Galarreta and Hestrin [1999], Gibson et al. [1999]). If gap junctions offer a favourable current path then LTS interneurons are likely to be involved as well, however their ion channel time constants are unlikely to play a role for the resonance effect seen in our recordings. Unfortunately, modelling of the effect of the gap junctions would be rather complex as it would involve several cell types. This is beyond the scope of this thesis, however a better knowledge of which cell types cause what percentage of the impedance change would allow a better interpretation of the images conducted. This knowledge might also be helpful for the choice of future paradigms as some subcortical structures such as the thalamus in rats lacks interneurons (Barbaresi et al. [1986], Williams and Faull [1987]).

This question was addressed by attempting to selectively block gap junctions as well as potassium channels. Unfortunately, both of these experiments remained inconclusive as in one case the evoked potential was affected and in the other epileptic potentials were caused. Cruikshank et al. reported a blockage of gap junctions with little other non-specific effects in experiments in brain slices of rats. In particular, they reported no significant changes in evoked excitatory or inhibitory postsynaptical potentials, and intrinsic cellular properties in his experiments. They pointed out that it took mefloquine 90 min to reach its maximal effect (Cruikshank et al. [2004]). In contrast, the evoked potential in our study was reduced after injection of mefloquine within 30 min (see fig. 4.3.2.1). This also caused a decrease in the activity evoked dZ which would be expected, as the evoked activity was reduced. Control injection with saline or just the placement of a needle did not lead to a decrease in EPs or dZs. It is thus unlikely that the drop of evoked activity in LFP or dZ is solely due the local damage caused. It appears that the action of mefloquine of a whole brain preparation of cortex yields different results than in brain slices in rats. Recordings after injection of 4-AP in an attempt to selectively block Kv3.1-2 were aborted as seizures developed even when a 10 μM solution was used. It was originally planned to try even smaller doses of 4-AP but this plan was aborted after it was noticed that seizures developed in other experiments even when electrode grids were re-used that had been in contact with 4-AP at any point in time, despite washing.

4.5. Conclusion and future work

In summary, it appears that there might be a resonance effect on fast spiking interneurons which may cause an apparent impedance change when measured with our method. The contribution of interneurons to the total activity-related impedance signal in the cortex remains inconclusive.

To further the issue on which neuron type contributes how much to the total activity related impedance change in the cortex, recordings in slice preparations could be used. A way of selectively activating FS interneurons vs activating the cortex in general should be found. This could for example take place by activating FS interneurons selectively by stimulating them with light in an optogenically modified rat vs stimulating the thalamus electrically causing activity in in general could be measured. An adequate chamber in which the impedance of a brain slice can be measured during activation would have to be designed. Optogenetically modified mice, in which FS interneurons can be selectively targeted by light have been produced in the past (Cardin et al. [2009], Sohal et al. [2009]). The optogenetical modification could potentially be extended to rats. Alternatively, recordings from mice could be conducted using the frequency sweep paradigm from chapter 3, if the results were similar to those in the rats the existing optogenetical mouse models could be used to evaluate the role of interneurons for the impedance signal further.

5. Feasibility of imaging the fast neural response in 3D using EIT

5.1. Introduction

5.1.1. Orienting paragraph

Imaging activity throughout the brain with a temporal resolution of milliseconds would permit assessment of activity between centres in the brain. This type of assessment would have an enormous impact on neuroscience. . EIT has the potential to image neuronal activity throughout the brain, which is tested in this study. The previous studies have shown that the activity within the cortex can be reliably imaged, therefore it will now be tested whether activity in subcortical structures can be imaged.

5.1.2. Background

5.1.2.1. Previous attempts of 3D EIT imaging

The alteration in carrier frequency discussed in chapter 3 allowed us to improve the SNR from 12.2 to 27. This encouraged testing of whether or not EIT could image neuronal activity throughout the brain. Previous attempts to image EIT throughout the brain have been made by Tidswell et al. and Gilad et al. (Tidswell et al. [2001b], Gilad et al. [2009]). Tidswell et al. however measured changes in the regional blood flow and volume rather than the fast neural impedance response. They measured impedance responses of about 0.5%, 6 seconds after visual, somatosensory, or motor activity using a 50 kHz carrier frequency. Gilad et al. attempted to measure EIT of the fast neural impedance response to visual evoked potentials throughout the brain in healthy human subjects (Gilad et al. [2009]). They injected a square wave (DC) and recorded the voltages from scalp EEG electrodes. They were able to show reproducible significant resistance decreases of $0.001 \pm 0.0005\%$ in these recordings reaching an SNR of 2:1, which was not sufficient for imaging. Imaging directly from the brain and with a higher carrier frequency compared to Gilad et al. (hence higher SNR) might allow us to conduct whole brain images of neuronal activity.

5.1.2.2. Impedance measurements from subcortical structures

As discussed in chapter 3 Klivington and Galambos recorded resistance changes in the cat cortex in response to auditory stimuli using two electrodes with 10 kHz current injection, recording via a Wheatstone bridge (Klivington and Galambos [1968], Klivington, K Galambos [1967]). Within the same group and using the same method, Velluti et al. measured evoked resistance changes in various subcortical nuclei following sensory stimuli (Velluti et al. [1968]). They measured the changes in response to visual stimuli in the lateral geniculate nucleus and the optic chiasm and the retina. In response to auditory stimuli, evoked resistance changes were measured in the medial geniculate nucleus, the inferior colliculus, the midbrain reticular formation, and the auditory cortex. Electrical stimulation of the sciatic nerve caused resistance shifts in the ventral posterolateral nucleus (Velluti et al.

[1968]). The changes in resistivity measured by Velluti et al. were very small (0.1 Ω with a baseline of 2000 to 5000 Ω) but were of similar magnitude in the cortex and the subcortical structures. It should also be taken into account that these measurements were taken with a two electrode set-up. The same electrodes were used for current injection as well as voltage measurement and hence include ionic diffusion due to accumulation of ions at the interface as well as surface polarization of cells (Bédard and Destexhe [2009]). This is probably why the authors present their dZ change in absolute rather than in relative terms. In our experiments, the electrodes recording the voltages were not the same as the electrodes injecting the current. Hence, the relative dZ change recorded by Velluti et al. and Klivington et al. can not be determined with certainty and the results from this study cannot be directly compared to theirs. However, it is very encouraging that the magnitude in resistivity change was similar between cortex and subcortical structures when the same method was used by Velluti et al. (Velluti et al. [1968]).

5.1.2.3. Somatosensory system

In this study stimulation of the forepaw and the whiskers were chosen to elicit activation of the brain. The pathways of the somatosensory system and the structures involved will briefly be discussed here.

Forepaw stimulation In our forepaw stimulation paradigm, the nerves of the forepaw (the median, the ulnar, and the radial nerve) are being stimulated. This is achieved by needle electrodes in the forepaw which stimulate enough to see the forepaw twitch. It is likely that pain receptors are also activated as the stimulating current is fairly high in the anaesthetised animal. The sensory part of the median, ulnar, and radial nerve transmits the information of sensory receptors in the skin. These can be divided into slowly, intermediate, and rapid adapting mechanoreceptors. The slowly adapting mechanoreceptors include Merkel and Ruffini endings and some free nerve endings. Merkel endings are particularly dense in follicles of sinus hairs of the face and Ruffini endings respond to tissue stress (Rice and Fundin [1997], Grigg [1996]). Free nerve endings respond to painful stimuli and can be slow, intermediate and rapidly adapting. They are found in the skin as well as in muscles and tendons, which is why they are likely stimulated by the current passed from the needle electrodes in our paradigm (Mense [1996]). The other rapidly adapting mechanoreceptors include small lamellated corpuscles, lanceloate endings, and Pacianian corpuscles. Pacianian corpuscles are particularly sensitive to vibration, and lanceloate endings are located in hair follicles (Paxinos [2004]). The cell bodies of all of these receptors lie in the dorsal root ganglia along the vertebral column by the spine. The somatosensory information reaches the somatosensory thalamus via two different pathways. Discriminative touch and proprioception are mostly transmitted via ascending fibres in the dorsal column which reach the medullary relay nuclei. These are the gracile, cuneate, and external cuneate nucleus as well as the nucleus Z. From there the somatosensory information mostly reaches the ventral posteoraleral

nucleus of the thalamus (VPL) via the internal arcuate fibres across the mid-line which enter the medial lemniscus. Pain, temperature, and innocuous stimuli are being transmitted via the spinothalamic tract directly to the contralateral VPL, the posterior thalamic group (Po), and the intralaminar nuclei (Paxinos [2004]). The main part of the somatosenosory thalamus is also called the ventrobasal complex (VB) which consists of VPL and ventroposteromedial nucleus (VPM). VPM mainly receives input from the whisker pad and is discussed in the next paragraph. The other parts of the thalamus that receive somotosensory inputs are the posterior group (Po, mainly nociceptive stimuli), the centrolateral and parafascicular nucleus, the gelatinosus nucleus, and the lateral ventromedial thalamus (Paxinos [2004]). The rat VPL does not contain any significant number of local interneurons (Barbaresi et al. [1986], Harris and Hendrickson [1987]) and all VPL neurons send their axons to the somatosensory cortex (Saporta and Kruger [1977]). There are GABAergic interneurons in the reticular nucleus, which is a thin layer lamina of neurons that surround the dorsal thalamus (Paxinos [2004]). However they seem to only play a role in selective attention (McAlonan [2000]). All neurons in the VB send their axons to the somatosensory cortex (Saporta and Kruger [1977]).VB and Po neurons project to the first and the second somatosensory area (S1 and S2, respectively) but relatively few of these neurons send axons to both cortical areas (Spreafico et al. [1987]). Neurons in the intralaminar nuclei project to wide areas of frontal cortex (Berendse and Groenewegen [1991]). Both the gelatinosus nucleus and the ventromedial thalamic nucleus are implicated in noxious stimuli (Backonja and Miletic [1991], Desbois and Villanueva [2001]). They project to the ventrolateral orbital cortex and a strip of dorsolateral frontal cortex, respectively (Yoshida et al. [1992], Desbois and Villanueva [2001]). Axons from the VB to S1 mostly terminate in layer 4 (Herkenham [1980], Kharazia and Weinberg [1994]), while the axons from Po mainly terminates in layers 1 and 5a (Herkenham [1980]). There is a single representation of the body surface in S1 which has partial overlap with the motor cortex. This area occupies a strip about 1 mm wide and contains the representation of the forepaw and hindpaw (Sapienza et al. [1981], Sanderson et al. [1984]). S2 is located laterally to S1 and contains a second complete representation of the body surface (Paxinos [2004]).

Whisker stimulation Whisker stimulation leads to activation of the maxillary division of the trigeminal nerve. Each follicle of the facial vibrissae of common laboratory rats is innervated by approximately 250 nerve fibres (Paxinos [2004]). The peripheral receptors in the follicles are Merkel cells, lanceolate endings, free nerve endings, reticular and Ruffini endings (Renehan and Munger [1986], Fundin et al. [1995], Rice and Fundin [1997]). The cell bodies of the afferents of the maxillary division of the trigeminal nerve supply, which supplies the whisker pad, lie in the trigeminal (or Gasserian) ganglion in the middle cranial fossa in the base of the skull, where they are arranged somatotopically (Paxinos [2004]). From there the information is transmitted to ipsilateral trigeminal brain stem nuclei. Of these, the

main or principal trigeminal nucleus (Pr5) and the spinal trigeminal nuclei (Sp5O (oral), Sp5I (interpolar) and Sp5C (caudal)) are of particular importance for the information transmission from the whisker pad to the cortex. Pr5 lies in the lateral pons and has two classes of whisker responsive cells which project to VPM and Po. VPM and Po also receive input from the spinal trigeminal nuclei Sp5I and Sp5C; Po receives additional input from Sp5O (Veinante et al. [2000], Paxinos [2004]). VPM is a thalamic subcortical nucleus, which is crescent shaped in coronal sections and lies dorso-medial to VPL (Paxinos [2004]). It contains thalamocortical relay cells and, unlike to carnivores and primates, there are no interneurons or GABAergic cells present in rat VPM (Barbaresi et al. [1986], Williams and Faull [1987]). Inputs to VPM are somatotopically organized and inputs from the vibrissae supply a disproportionately large topographic region (Waite [1973], Van Der Loos [1976], Sugitani et al. [1990]). Po surrounds VPM on the dorsomedial and caudal aspects. The rostral, dorsomedial sector of Po (PoM) receives the somatosensory input of the vibrissae. PoM and VPM lack GABAergic interneurons and receives inhibition from the reticular thalamic nucleus (Pinault et al. [1995]). Activity in PoM is largely suppressed during anaesthesia via inhibition from the zona inserta (Petersen [2007]). Both VPM and PoM receive dense projection from the somatosensory cortex, which modulates its activity (Diamond et al. [1992], Paxinos [2004]). VPM and PoM both project to the first sensory cortex (S1) to complementary regions (Lu and Lin [1993]). VPM mainly projects to layer 4 of S1 but also supplies supra- and infragranular layers in the cortex (Herkenham [1980], Jensen and Killackey [1987]). Po avoids the barrel centres and projects to the septa between barrels in layer 1, 4 and 5a, facilitating the lateral spread of activity, and to the surrounding dysgranular cortex as well as to S2 (Carvell and Simons [1987]). The dysgranular zone is located between the forelimb and hindlimb in S1 and is understood to correspond to gyri in mammals (Paxinos [2004]). Within S1 the body representation is somatotopic with the face areas occupying approximately 66% of the area (Welker [1971]). The input area is called the barrel field, which dominates the facial area. Each whisker has its own distinct representation in the barrel field (Paxinos and Watson [2007]).

5.1.2.4. Expectation regarding imaging in 3D

The two structures involved in evoked potential processing that could be imaged with EIT are the activity in the thalamus and the cortex. As discussed above, the VPM and VPL are expected to activate before the somatosensory cortex activates when whiskers or the forepaw are stimulated. The thalamic structures are expected to be active 2-6 ms prior to activation of the somatosensory cortex (Cruikshank et al. [2007]), which in our experience reaches its peak activity at 10-20 ms (see chapter 3). The size of the representation of whisker in VPM and forepaw in VPL should be taken into account. The whiskers have their representation in nearly the entire VPM, while the forepaw is only one of the areas with a representation in the VPL; The two structures have a similar total volume (Paxinos and Watson [2007], Paxinos [2004]). Therefore, most of the VPM is expected to be activated if all

whiskers are being moved on one side but only part of the VPL when the forepaw is stimulated. Other structures involved such as the medullary relay nuclei or the trigeminal nuclei are both too small and outside the area of the brain that these recordings are sensitive to.

5.1.2.5. Previous modelling

In a study by Aristovich et al. the feasibility of imaging deep brain neural activity with EIT was tested in modelling (Aristovich et al. [2014]). They tested whether a 0.5 mm spherical perturbation with a 10% conductivity change, located in the CA1 area of the hippocampus, could be detected in the image reconstruction. They used a 15 M element mesh for the forward solution, a 100 k inverse tetrahedral mesh and 256 electrodes placed around the brain. They came to the conclusion that deep brain activity in the hippocampus could be imaged with an accuracy of 0.5 mm with this set-up (Aristovich et al. [2014]). Neither a conductivity change of 10% in the thalamus can be expected nor is it possible to use 256 electrodes. However, both VPM and VPL have a substantially larger total area than the perturbation used in this paradigm. They are somewhat semicircular and oval in length but at the maximum width VPM measures approximately 0.9 x 2.8 mm and its total length is approximately 2.2 mm (Paxinos and Watson [2007]). The maximum width of VPL is approximately 0.75 x 2.5 mm with an approximate length of 2.3 mm (Paxinos and Watson [2007]). However, it should be appreciated that, especially in the forepaw paradigm, not the entire VPL is expected to be active, because the forepaw is just one of the structures represented in the thalamus. The minimum change in impedance in the thalamus required to image with EIT using brain surface electrodes determined by modelling in this study.

5.1.3. Rationale

The overall purpose of this study was to test whether impedance changes due to neuronal activity can be imaged throughout the brain using measurements from the brain surface. First, the magnitude of impedance change in the thalamus necessary to detect impedance changes on the surface of the brain was determined by modelling the changes. It was then tested whether any reproducible measurable impedance changes were recordable in subcortical structures from recordings of evoked potentials at the surface of the brain. The actual evoked impedance changes were also measured in the thalamus locally.

5.1.4. Experimental design

The minimum change in impedance in the thalamus needed to reconstruct activity was modelled and two further types of experiments were conducted in this study. 3D EIT recordings were attempted by covering most of the surface of the brain. For this purpose a custom made 60 channel electrode was designed and produced. This

electrode array covered approximately 90% of the hemisphere and one electrode was implanted subdurally on each hemisphere, so that a total of 120 channels could be used. The forepaw and the whisker were stimulated with this set-up under propofol or $\alpha-$chloralose anaesthesia in an attempt to image impedance changes throughout the brain. The other type of experiment involved impedance measurements directly from the cortex. For this purpose a 16 channel depth electrode was stereotactically implanted directly into the VB covering both the VPM and VPL. Large surface electrodes were used to inject current from either side or dorsal to ventral from the brain surface. This experiment was done to characterize the impedance response of the somatosensory thalamus.

5.2. Methods

5.2.1. Modelling

The VPM was modelled as a 1.5 mm diameter sphere located at AP -3, ML 3 and 6mm depth from the surface of the brain using a high-resolution 200,000 element mesh. The thalamic activity was modelled as a change with the following amplitudes: 0.1%, 0.5%, 1%, and 2% in this sphere. Forward modelling was used to model the changes in the boundary voltage due to the perturbation using the same current injection protocol as in one of the 3D experiments. $0.1\mu V$ random Gaussian noise was added to the simulated boundary voltages. The same method as in 5.2.5 was used for the reconstruction. The centre of mass was computed for the reconstructed perturbation (threshold at half-maximum impedance change) and the distance to the actual perturbation was used as a measure of the reconstruction error.

5.2.2. Animals and anaesthetic procedure

Fourteen female Sprague-Dawley rats aged 5-8 months, weighing between 300 and 450 g, were used in this study. They were obtained from Biological Services, University College London, which bred them on site. They were kept in a room with 12 hour dark/artificial light cycle with 18-20 air exchanges/hour, and had access to food and water ad libitum. All work was conducted under UK Home Office regulations. All rats were induced with isoflurane 4% in an induction box and the anaesthesia was maintained with an injectable anaesthetic. They were intubated as described in chapter 4 and in Vongerichten et al. (Vongerichten et al. [2014]) and either their femoral or their tail artery and vein were cannulated. Monitoring and ventilation was the same as in chapter 3. In one of the rats anaesthesia was maintained using propofol 10-50 mg/kg/h. However to maximise EPs, anaesthesia was maintained with $\alpha-$chloralose and fentanyl in the reamining rats. The dose rate for $\alpha-$chloralose was 25-35 mg/kg/h and 25-50 mcg/kg/h for fentanyl.

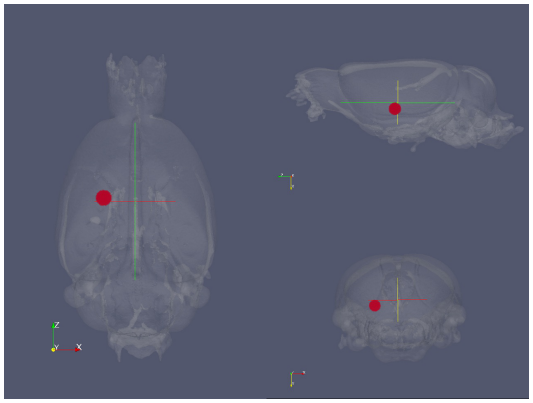

Figure 5.1.: Simulated perturbation in the 200.000 element brain mesh. The pertubation is 1.5 mm in diameter and located at AP -3, ML 3 and 6 mm depth from the surface of the brain

5.2.3. Surgical procedure

The skin on the top of the skull was incised in the mid-line and the skull freed of periost. The insertion of the temporal muscle on both sides was cauterized with bipolar forceps and then incised using a scalpel. The muscle was subsequently dissected off bluntly. Two craniotomies were performed, which were reaching from 4 mm rostral of bregma to 1mm rostral to lambda and laterally as wide as possible down to the insertion of the zygomatic arch. A small strip of bone remained in the mid-line to protect the superior saggital sinus.

5.2.4. EIT and EEG recordings

5.2.4.1. Electrodes

A 16 channel depth electrode of 10 mm total length was used for the thalamic impedance recordings (A1x16-10mm-100-703-A16, Neuronexus, MI, USA). Each contact was 703 μm^2 in size and they were 100 μm apart, so that the electrode area covered 1.5 mm of the tip of the electrodes.

The surface arrays was produced in house using stainless steel foil in silicone rubber in a sandwich technique. The arrays measured 15 x 9 mm at their longest points and had 60 contacts measuring 0.6 mm in diameter, which were platinised before implantation. The arrays covered ˜90% of the neocortex and one electrode was implanted on each hemisphere. The design had to be amended twice over the course of the study. The initial design was too large in surface area and the second design had a corner on the back which easily could slip caudally under the bone, damaging the feeding veins on the caudal area of the superior saggital sinus and the transverse sinus. The first design was used in one rat and the second design was

used in two rats.

5.2.4.2. Current source

The current source used in this study was the Keithley 6221 current source (Tektronix U.K. Ltd Keithley Instruments, UK). It produces AC currents from 2 pA to 100 mA up to a frequency of 100 kHz and has an output impedance of $10^{14}\Omega$. It was combined with a custom designed switching system based on the ADG714 CMOS and was controlled via an Arduino (SmartProjects, Italy) through a custom made MATLAB interface (Mathworks, USA).

5.2.4.3. EEG amplifier

The same Biosemi EEG amplifier as in chapter 4 and 3 was used.

5.2.5. 3D EIT recordings of evoked potentials

3D recordings were attempted in 11 rats, but data of only three of them was technically sound due to ongoing development of the surgical technique, the electrode design and other parts of the recording system such as the electrode holders. A whisker stimulation and a forepaw stimulation paradigm was used to elicit evoked activation in the brain. The forepaw paradigm is the same as described in chapter 3. The forepaw paradigm was performed with an increased stimulation pulse width in one rat. The whisker stimulation paradigm has been initially developed for a previous project and is discussed in more detail in Brett Packhams thesis (Packham [2013]). Briefly, for the whisker stimulation a piezoelectric actuator (PL140.10, PI Ceramic, Germany) was used, which had a deflection frequency of 1 Hz, amplitude of 4 mm and velocity of 800 $\frac{mm}{s}$. In our study all whiskers were tied together and displaced in the rostro-caudal axis by the stimulator. In one rat the whisker pad was stimulated electrically above twitch threshold as no EPs could be elicited mechanically. For the EIT recordings, current injection was performed choosing one electrode contact on either side of the brain, the current frequency was 1700 Hz but in two rats additional current injection with 600 Hz was performed; the current amplitude was 50-100 μA rms. The current was injected between two electrodes on either side of the brain and the remaining 118 electrodes recorded the resulting voltages. The electrodes chosen were as far lateral as possible and in the middle row ± 1 to allow as much current as possible to pass through the thalamic area. The current injection was switched between pairs every 15-60 s.

5.2.6. Thalamic impedance recordings of evoked potentials

Thalamic impedance recordings were conducted in three rats using the same whisker and forepaw stimulation described in 5.2.5. Current was injected either via large circular platinum electrodes (4 mm diameter) in the centre of each hemisphere or via

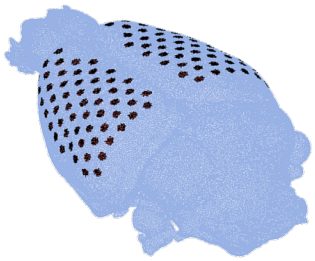

Figure 5.2.: 3D EIT electrode contacts displayed on the mesh used

one large current electrode (4 mm) on dorsal surface of the brain and a stainless steel screw (00-96, Plastics One, USA) in the hard palate of the rat. The field potentials generated from the neurons and the voltages generated by the current injection was measured with a depth electrode described in 5.2.4.1. The thalamic depth electrode was placed in AP -4 mm, ML 3.5 mm and 6.5 mm depth from the surface of the brain (coordinates according to the stereotactic atlas of Paxinos and Watson (Paxinos and Watson [2007])). In addition to this location, the depth electrode was also placed in 3-6 other locations (sampled ± 1mm around the above coordinate) for broader sampling. The placement of the electrode in the thalamus was confirmed by placement during EPs (which were visible in the local field potentials) and the post-mortem removal of the brain showing the tract of the electrode in slices.

5.2.7. Analysis of 3D data

The EEG data was recovered by low pass filtering the recorded voltages at 300 Hz when 1700 Hz current injection was used and 200 Hz when a 600 Hz carrier frequency was used. All results of the amplitude and latency of EEG EPs and dZ are given as mean±SD. The impedance data was recovered by first band-pass filtering the recorded voltages with a filter of ± 300 Hz for 1700 Hz and ± 200 Hz when a carrier frequency of 600 Hz was used. The voltages were then demodulated as described in chapter 3. Outlier rejection was performed as explained in 3.2.6.3. Significant impedance changes were detected by computing the t-statistic of the dZ signal at each time point, with the significance level set at $p<0.01$ (two-sided).

An anatomical realistic 60.000 element finite element model was used to model the rat brain. The electrodes were placed on either hemisphere and covered most of the hemisphere due to their surface area. A complete electrode model was used for the forward modelling, assuming 1 kΩ contact impedance for all electrodes and 0.3 S/m

baseline conductivity in the cortex. The baseline boundary voltages predicted by the finite element model closely matched those recorded during the experiments (from visual inspection). The forward model was used to estimate a sensitivity (Jacobian) matrix for the current injection protocol used in each experiment. Conductivity changes were estimated from the recorded dZ signals using the sensitivity matrix and applying zero-order Tikhonov regularization (Holder [2005]). The regularization parameter was optimised by the cross-validation method (Abascal et al. [2008]) as described in chapter 3.

5.2.8. Analysis of thalamic recordings

The local field data was recovered by low pass filtering the recorded voltages at 400 Hz. Similarly to the processing in 5.2.7, the voltage recordings were band-pass filtered at 500 Hz and then demodulated.

5.3. Results

5.3.1. Modelling of thalamic activity strength

The forward modelling predicted that an impedance change in the thalamus of 1% would produce a peak change in the boundary voltage of 0.025%; the remaining impedance changes are proportional to this so that a 2% change in impedance will cause a peak change in boundary voltage of 0.05%, 0.5 % change in impedance would be seen as a 0.0125% change in boundary voltage and an impedance change of 0.1% in the thalamus would cause a boundary voltage change of 0.0025%. The simulated change in impedance could be reconstructed when 0.1%, 0.5%, 1% and 2% impedance changes were used. However the image became increasingly blurred the smaller the impedance change was as seen in figure 5.3.1. The thresholded reconstructed volume (thresholded at half-maximum) increased with decreasing simulated dZ in the spherical perturbation, which had a volume of of 1.77 mm^3. The reconstructed volume was 108.35 mm^3 for a 2% simulated dZ change, 106.76 mm^3 for 1% simulated dZ change, 117.48 mm^3 for a simulated dZ of 0.5% and 254.34 mm^3 for a simulated dZ of 0.1%. The reconstruction error increased when the impedance change decreased. For an impedance change of 2% the reconstruction error was 0.27 mm (distance between original centre of perturbation to reconstructed centre of mass), for 1% it was 0.26 mm, for 0.5% it was 0.5 mm and for 0.1% it was 1.6 mm reconstruction error (see figure 5.3.1).

5.3.2. 3D EIT recordings of evoked potentials

Successful recordings were obtained in three rats, in which EIT recordings of forepaw and whisker stimulation were performed. A minimum of one of each paradigm was

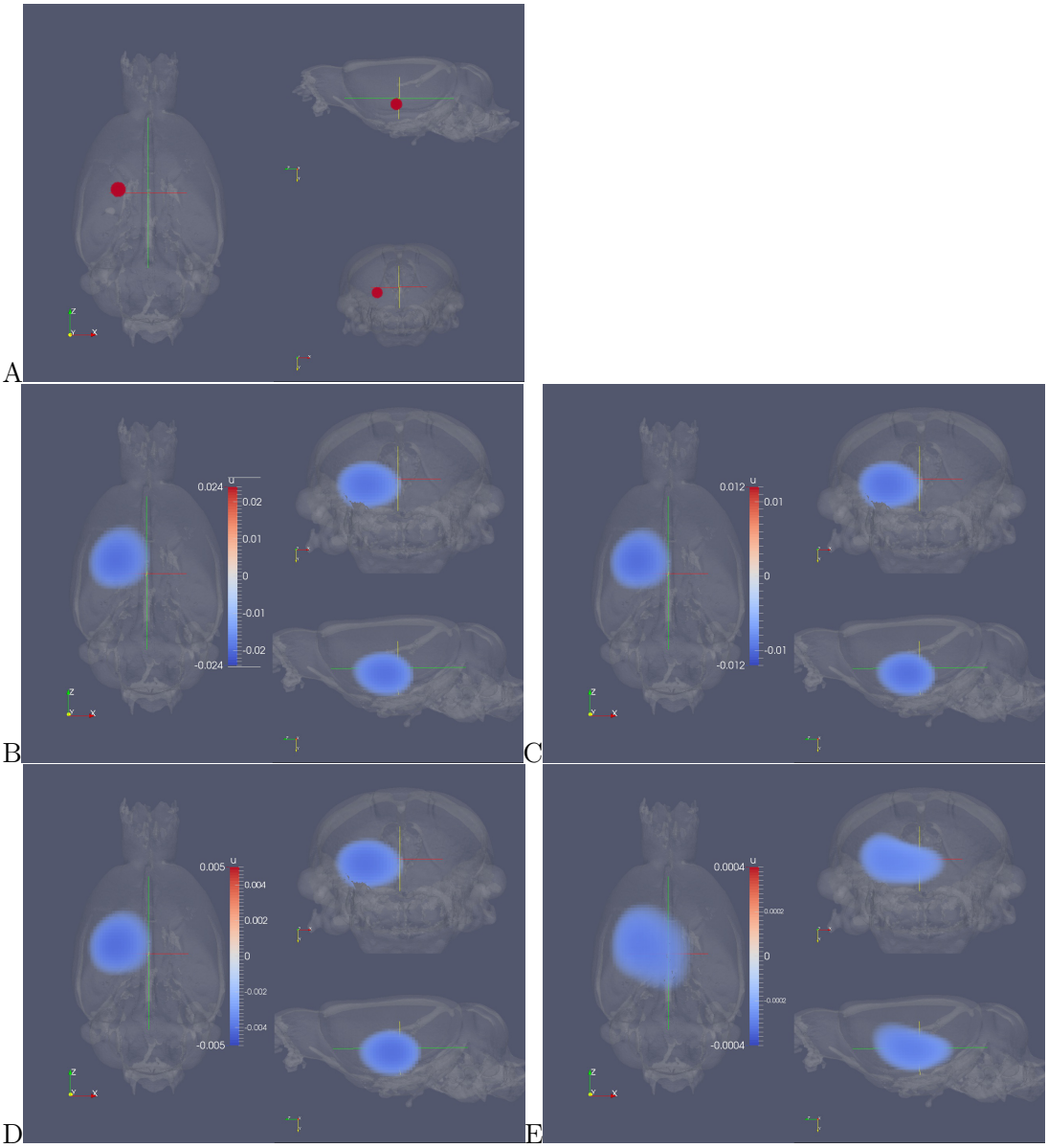

Figure 5.3.: Simulated perturbation (A) and reconstructions of the simulated perturbations in the thalamus shown on a 200.000 element rat mesh (B-E). The colourbar represents reconstructed impedance changes from 0.002% (red) to -0.002% (blue). (B) Reconstruction if an impedance change of -2% is simulated (C) for simulated change of -1% (D) for simulated change of -0.5%. (E) for simulated change of -0.1%. The amplitudes of the dZ seen in (B)-(E) are smaller than the originally simulated amplitudes as the images are increasingly blurred (resulting in a bigger volume for dZ creation).

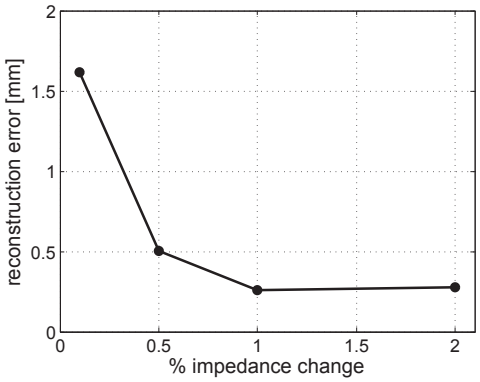

Figure 5.4.: Localization error in mm in relation to the originally modelled impedance change.

		Forepaw			
Frequency	n	EP (mV)	EP latency (ms)	dZ (%)	dZ latency (ms)
1700 Hz	10	1.16±0.4	14.76	-0.09±0.03	14.42
600 Hz	3	1.45±0.67	15.38	0.27±0.13	15.38
		Whisker			
1700 Hz	5	0.65±0.21	16.71	-0.14±0.07	16.75

Table 5.1.: Summary of the mean EPs and dZs recorded from the 120 channel electrode on the cortex in the 3D EIT recordings (n = number of recordings in 3 rats).

obtained in each rat and the total numbers were 13 EIT recordings of forepaw and 5 recordings of whisker stimulation.

The EPs and dZs are summarized in table 5.1. In the assessment of the raw dZ recordings a single brief drop in impedance of -0.095±0.04% was observed in response to the cortical forepaw evoked potential and a single -0.14±0.07% in response to whisker stimulation was seen on EEG when the recording was performed with 1700 Hz current injection.

A brief single increase in impedance of 0.269±0.13% was seen when a 600 Hz injection frequency was used in the forepaw paradigm. The latencies of the increase and decrease of the impedance matched the latencies of the EPs. However, no dZ change larger than the 0.01-0.03% noise which preceded the change in impedance due to the cortical EP and might have represented thalamic activity was seen. All 21 recordings were reconstructed showing cortical activity but no impedance changes in deep structures were seen. Active areas all reached t-values of >100 for each voxel and were thresholded at half-maximum. The mean centre of reconstructed activity

for whisker activity was AP -2.47, ML -4.6 and 2.87 depth in the Paxinos & Watson coordinate system (Paxinos and Watson [2007]), which corresponds to S1 barrelfield. Each individual reconstruction was in the S1 barrelfield as well except for one which reconstructed 0.3 mm medial to the S1 barrel field into the neighboring primary sensory dysgranular cortex (S1DZ). The mean centre of reconstructed activity for forepaw stimulation was AP -0.43, ML -3.77 and 2.7 mm depth which corresponds to S1 forelimb (Paxinos and Watson [2007]). All individual recordings reconstructed to the S1 forelimb area, except for one which reconstructed into the neighboring M1 approximately 0.4 mm medial to the S1 forelimb area. Recordings in which a 1700 Hz carrier frequency was used reconstructed to the same area as those which used a 600 Hz carrier frequency.

5.3.3. Thalamic impedance recordings of evoked potentials

Recordings were obtained in three rats; successful placement of the depth electrode in the VPM/VPL complex was confirmed post-mortem in all three rats. Evoked activity on the local field could be measured in the thalamus in 25 recordings but was unsuccessful in 7 recordings due to noise, these were excluded from further analysis. The EP amplitude was 50.31±35.74 μA with a latency of 7.67±2.95 ms for whisker stimulation and -174.61±130 μA with a latency of 13.5±1.925 ms for forepaw stimulation. No dZ >0.01% of noise was recorded for forepaw stimulation in any of the 15 recordings. The dZs recorded in the whisker EPs using a 1700 Hz carrier was -0.017±0.03% with a mean latency of 9.4 ms (n = 10) and 0.017±0.003 with a latency of 9.75 ms if a 600 Hz (n = 2) carrier frequency was used. Noise was 0.01% throughout the recordings.

5.4. Discussion

This study tested, whether impedance changes in the thalamus could be imaged using 3D EIT. Klivinton and Galambos as well as Velluti et al.s studies showed an impedance change in subcortical structures that was similar to the impedance changes recorded on the cortex (Velluti et al. [1968], Klivington, K Galambos [1967]). Our recordings in chapter 3 showed an average impedance change of 0.126 ± 0.085%. Our modelling predicted that such an impedance change could be reconstructed but would produce a localization error of 1.6 mm. However, no reproducible changes in dZ were detected in subcortical structures in response to evoked activity when the impedance was recorded with electrodes from the cortical surface. In contrast, the dZ changes in the cortex could be imaged reliably in every recording and the reconstruction showed activity in S1 of the whisker and forepaw area, respectively (see fig. 5.3.2).

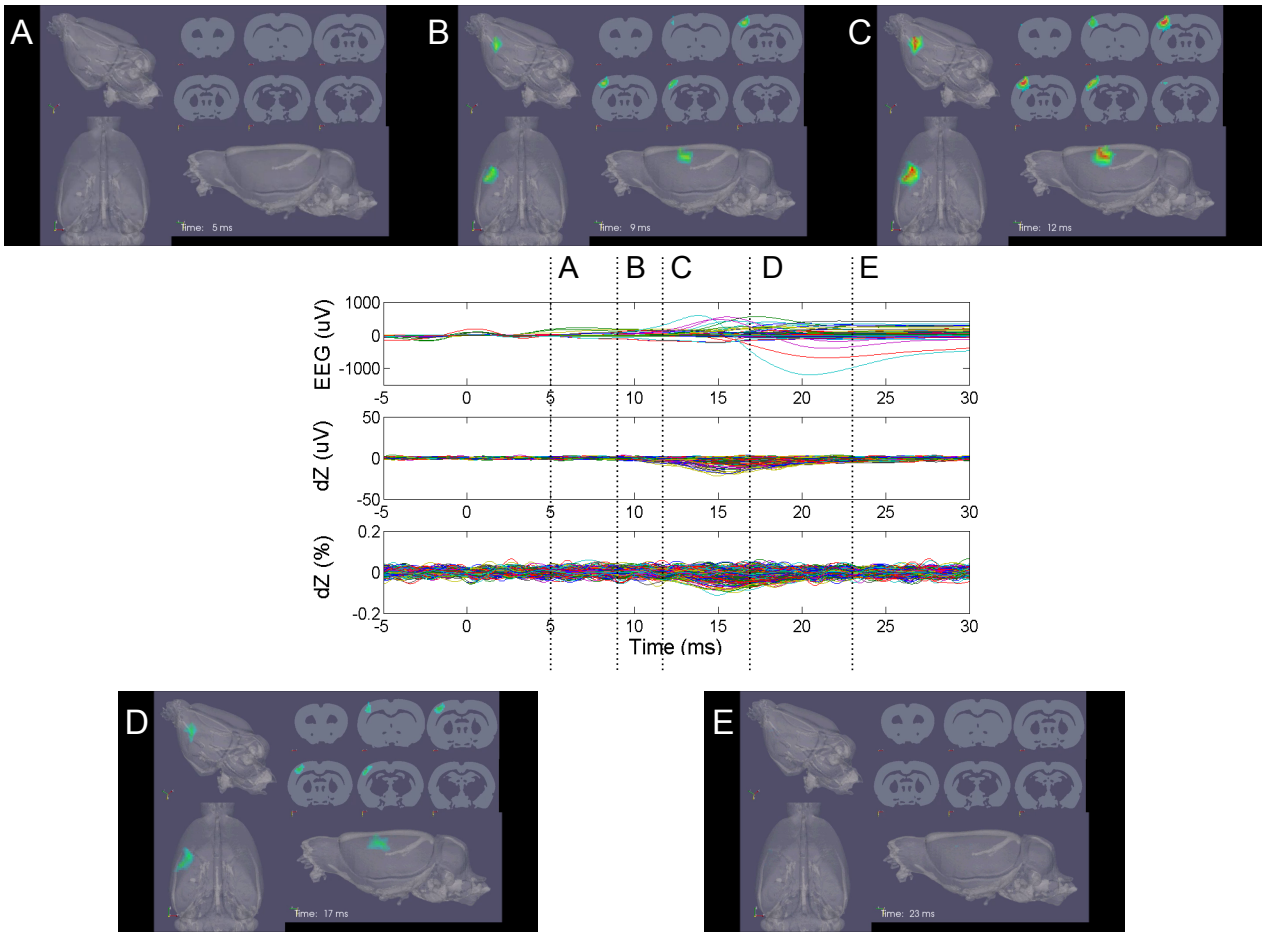

Figure 5.5.: Example of the reconstructed dZ in response to whisker EPs in one rat at 5 ms (A), 9 ms (B), 12 ms (C), 17 ms (D) and 23 ms (E). Each time point shows the mesh from 3 angles and 3 slices through the mesh to detail depth. Activity is seen in the cortex only. The central graph shows the EP as seen in EEG (top), the dZ in absolute terms (middle) and the relative dZ change (bottom).

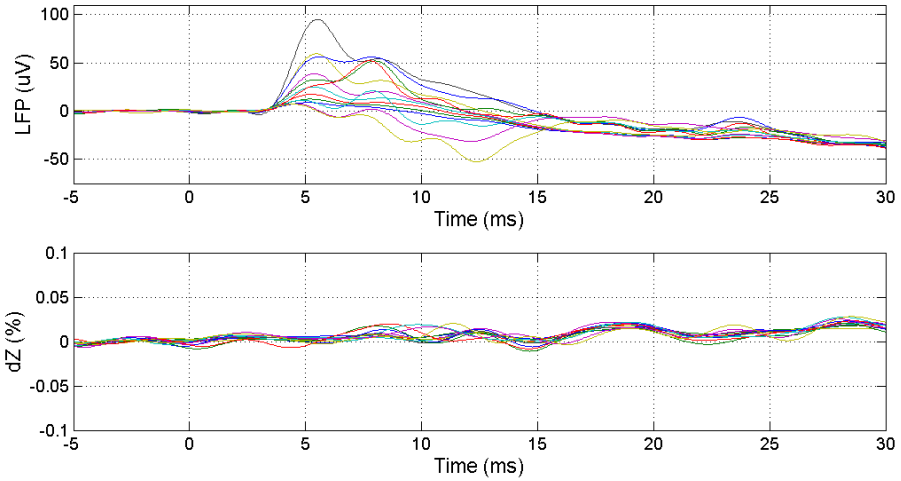

Figure 5.6.: Example of a dZ measurement directly from the thalamus. The current is injected with two large electrodes from either side and the recording obtained from a depth electrode located in the VPM.

To find the reason for this absence of a signal, recordings directly from the thalamus were conducted to assess whether the signal strength was too weak or other reasons such as noise might play a role. The average dZ recorded directly from the VPM/VPL was <0.01 % for the forepaw paradigm and 0.017% for the whisker paradigm which was measured against noise of 0.01%. This means that the dZ is substantially smaller than what modelling predicted would be necessary (0.1%) to image impedance changes in the thalamus from cortical electrodes and it so small that it could not be detected against the noise in the forepaw paradigm all together. The dZ signal in the thalamus could be subdued by sampling error which results in failure to record from the exact centre of activity with the depth electrodes or the anaesthesia might have suppressed the extend of the dZ signal. The evoked activity could be measured in the EEG on the surface of the brain as well as local field potentials from the depth electrode in the thalamus. This makes a failure to detect a signal due to sampling error or due to anaesthesia seem unlikely. The forepaw EPs on the brain surface were of similar amplitude and latency to those recorded with planar arrays in chapter 3 and the recorded dZ matched the recordings from the same chapter at the equivalent frequency. The method has been validated with control recordings in chapter 3 and the matching results to the same paradigm are taken as an indicator for the absence of any technical issues in this study. The evoked field potentials of the thalamic recordings matched the literature in amplitude and latency (Temereanca and Simons [2003], Sobolewski et al. [2010]).

The most likely explanation for the absence of an activity related impedance

change in the somatosensory thalamus is the volume of the activated tissue. The modelling predicted that a minimum of 0.1% impedance change would be necessary to be able to measure the impedance change on the surface. Recordings directly from the VPM/VPL confirmed the absence of a reproducible detectable impedance signal. It is likely that the total volume of synchronously active neuronal tissue in the somatosensory in too small to produce a detectable impedance signal. There was never any impedance change found if the forepaw was stimulated but there was a very small dZ recorded in some of the thalamic whisker recordings. This supports the hypothesis of the activated volume being too small in the thalamus further as the thalamic representation of the whisker pad in the VPM of the thalamus is much larger than the representation of the forepaw in the VPL.

Another factor that might have an impact on the impedance signal due to activation is the cell type involved. As discussed in chapter 4 interneurons might play an important part in generating the impedance response in cortical tissue. The VPM and VPL of the rat thalamus have no interneurons which might be an additional reason for the absence of an impedance signal in our recordings.

5.5. Conclusion and future work

The results of this study make successful recordings of fast neural impedance signals in response to physiological stimuli seem unlikely. As discussed in chapter 4 it would be of interest to clarify which cell type generates the fast neural signal in the cortex. This could for example be obtained by recordings of impedance in brain slices where only specific cell types are selectively activated. Furthermore more conclusive modelling might be required. Should the outcome of such studies be that the impedance signal depends crucially on the activity of interneurons then recordings of the fast neural impedance signal would be possible in 3D, provided the hypotheses to be tested involve the activity of interneurons in subcortical structures, as would be the case in primates (Somogyi et al. [1982]).

6. The impedance response of epileptic activity in neuronal tissue in vivo

6.1. Introduction

6.1.1. Orienting paragraph

This study tested whether EIT could be used to image the epileptic focus and the seizure spread in the cortex in in-vivo rat models of epilepsy with a sub-second time resolution. A set-up similar to the one used in chapter 3 would allow a high temporal resolution of 3.33 ms and the activity in the cortex could be imaged down to 2 mm from the surface. Localising the epileptic onset zone is of great importance, as it determines whether surgery can be offered to an epileptic patient, who did not respond to anti-epileptic drugs. This will be discussed in greater detail below. EIT could be potentially used in two ways in localising seizure onset zones: (1) by using the fast-neural component of the impedance signal for imaging and (2) by using the cell swelling that occurs shortly after the onset of seizures as it increases the local tissue impedance. In this chapter I discuss the characteristics and time course of the impedance signals and discuss their potential use in clinical pre-surgical diagnostics.

6.1.2. Background

6.1.2.1. Epilepsy

Epilepsy is the commonest neurological condition which affects people of all ages, races and social classes. The epilepsies are characterized by recurrent unpredictable seizures due to synchronized neuronal firing. It affects approximately 50 million people worldwide (Meinardi et al. [2001], Ngugi et al. [2010]). Of those with chronic epilepsy 20-30% will not respond to anti-epileptic drugs (AEDs) (Regesta and Tanganelli [1999], Cascino [2008]). In fact 20% of all patient treated with AEDs in the community had seizures at least monthly (Hart and Shorvon [1995]). There are over 30 recognized types of epilepsy; they can be categorized into focal seizures, generalized seizures or classified according to their electroclinical syndrome (Berg et al. [2010]). Generalized epileptic seizures are originating at some point within, and rapidly engaging bilaterally distributed networks. The individual seizure onsets can appear localised, but the localisation and lateralisation are not consistent from one seizure to another. Focal epileptic seizures are originating within networks limited to one hemisphere and the ictal onset is consistent from one seizure to another. Both focal and generalized epileptic seizures can involve cortical and subcortical structures (Berg et al. [2010]). Focal epilepsies make up the majority of epilepsies Kotsopoulos et al. [2002] and some can be treated with resective surgery if they are not responding to AEDs. In order to treat a focal epilepsy surgically, a clear seizure focus has to be found and deemed resectable; it has to be surgically accessible and in an area of the brain, where removal will not lead to an intolerable functional deficit (Duncan [2011]). Potential surgical candidates often undergo intracranial EEG recordings (ECoG), where EEG electrodes are implanted directly to the surface of the cortex suspected to contain the epileptogenic focus (Duncan [2011]). ECoG recordings generally suffer some drawbacks, as it is a summated po-

tential which is recorded on the surface. Depending on the brain architecture, such as deep-seated sources, source orientation tangential to the scalp, opposing source orientation in sulci or concentric neuronal architecture activity may have no EEG correlate (Schomer [2011]). Depth electrodes can be placed in the cortex but are limited in their spatial sampling and their number as they damage the tissue.

6.1.2.2. Imaging the epileptogenic focus

In recent years, additional measurements for seizure focus localization have been proposed. Methods measuring the secondary effects of the neuronal activity on the surrounding tissue instead of the electric signal itself have drawn particular attention. Changes in the bloodflow due to neuronal activity can be imaged using intrinsic optical measurements and spike-triggered fMRI (Bahar et al. [2006], Suh et al. [2005], Zhao et al. [2007], Haglund and Hochman [2004], Vulliemoz et al. [2010]). Functional MRI has the ability to show haemodynamic changes time-locked to epileptic activity in the whole brain non-invasively (Vulliemoz et al. [2010]) The BOLD signal is due to oxygenation changes in the microvascular tissue bed as well as downstream venous pooling, leading to potential responses in draining veins remote from the neural source Vulliemoz et al. [2010]. This could be the reason why sensory cortex mapping with fMRI and microelectrode arrays showed an overlap of only 55% in anaesthetized monkeys in a study by Disbrow et al. (Disbrow et al. [2000]).

Research with intrinsic optical methods has recently produced rather intriguing results, as it allows a mapping of the areas with changes in blood volume as well as specific mapping of areas of changed blood oxygenation, depending on the wavelength used (Zhao et al. [2007], Bahar et al. [2006], Suh et al. [2005]). In a study conducted by Haglund and Hochmann this appeared to give a much more accurate mapping of the epileptogenic focus than blood volume changes by itself (Haglund and Hochman [2004]). Bahar et al. could show a lowered oxygenation of the blood in the centre of the ictal focus with increased blood volume in the tissue surrounding it (Bahar et al. [2006]). Generally, the optical methods suffer the drawback of needing an open skull to measure epileptic activity. Only few patients will have enough seizures to image their seizure focus during surgery with this method.

Another effect of the neuronal activity that can be measured in epilepsy models is the change in the extracellular space (ECS). As neurons activate, potassium is released into the ECS and immediately removed from the ECS by astrocytes. Water then follows the ions into the astrocytes which reduces the ECS temporarily (Florence et al. [2012], Haj-Yasein et al. [2012], Ø stby et al. [2009]). Alterations in the potassium channels in astrocytes have been described in some epilepsy syndromes and abnormal cell swelling has been proposed as a seizure maintaining mechanism (David et al. [2009]). The change in the ECS can be visualized by diffusion of labelled molecules such as radiotracers, tetramethylammonium^{+}(TMA^{+}) and fluorocently labelled macromolecules in brain slices or with photobleaching in vivo (Binder et al. [2004]).

6.1.2.3. Previous work on EIT/impedance recordings in epilepsy models

Several authors have reported an increase in cortical impedance during seizures and inter-ictal spikes (IIS), the time-course of which however differs vastly in the literature. All of these authors explained the increase in impedance with cell swelling occurring during seizures and IIS. There are no reports in the literature of a fast neural signal measured in response to epileptic activity but this may be due to the temporal resolution of the impedance measurement systems employed in the past. Traynelis et al. measured the impedance response of seizures in hippocampal rat slices with a high potassium model and reported a 2% increase in impedance before the start of the seizure which then increased further to 8% (Traynelis and Dingledine [1989]). They could also show that the impedance response was abolished when mannitol was added to the bathing fluid and that seizures could be abolished with adequate doses of mannitol in 21/23 cases and concluded that the increase in impedance was due to cell swelling (Traynelis and Dingledine [1989]). Fox et al. in contrast did not report an increase in impedance in hippocampal slices until up to 1 s after the seizure started using a low calcium model of epilepsy and an impedance measurement system with a temporal resolution of 500 ms. (Fox et al. [2004]). In in an in-vivo model of epilepsy Elazar et al. reported an increase in impedance in a tungsten acid model of epilepsy reaching 3.5-5% above baseline but also reported that 2% of the seizures were preceded by impedance increases. The system they used gave them a temporal resolution of 500 ms (Elazar et al. [1966]). In more recent experiments Olsson et al. reported a continuously increasing impedance in picrotoxin, kainate acid and fluorocitrate seizure models and he could see an acceleration in the impedance increase just prior to the seizure onset (Olsson et al. [2006]). They used a similar set up to ours with a current source and an EEG amplifier reaching a temporal resolution of ~33ms but only 6 screw electrodes in the scull. Their temporal resolution was an order of magnitude higher than that of Elazar et al. (Olsson et al. [2006]). They reported a peak increase in impedance of 13.2Ω with picrotoxin, 1.1Ω for kainic acid and 0.3Ω for fluorocitrate during seizures and calculated that the measured change in impedance would correspond to a 7-10% increase in cell size (Olsson et al. [2006]). The increase in impedance prior to seizures in the fluorocitrate model were reproduced by Broberg et al., who could also show concomitant high frequency activity (150-300 Hz) in the EEG and an increase in extracellular potassium and a calcium decrease (Broberg et al. [2008]). These results are intriguing as they point towards a potential for impedance measurements to act as an early seizure detecting method. It should however be appreciated that these measurements were taken with very few electrodes and that the measured cell swelling prior to seizures appeared to be seizure model dependent.

Previous attempts in our group to image seizures with EIT have been undertaken by Anling Rao for her PhD project in the late 90s' (Rao [2000]). She used the Sheffield Mark 1 system to produce EIT images with a carrier frequency of 47 kHz and a temporal resolution of one min. She used cortical electrical stimulation in the anaethetized rabbit as a model of epilepsy and her 16 electrodes were arranged

in a circle on the cortex. She detected significant increases in impedance 80s after electrical stimulation of the cortex. Due to her set-up, she was unable to record EIT and EEG at the same time, but noted that the average increase in impedance outlasted the average epileptic discharges after stimulation. She came to the conclusion that the increase in impedance was due to cell swelling as a result of the epileptiform activity. She could reconstruct the impedance change to the same location as the stimulating electrode was placed. This study clearly showed that it is possible to image epileptic seizures using the effect of cell swelling with EIT, however with our new hardware it will potentially be possible to achieve a temporal resolution of several milliseconds and to record seizures with an electrode arrangement similar to that in epilepsy patients. Our set-up could could allow us to image epileptic activity using the fast neural signal. Furthermore, epilepsy models that elicit spontaneous seizures without texternal triggering were used. This is a further step towards the situation we would be faced with, in human epilepsy subjects.

6.1.3. Epilepsy models

Focal epilepsy models that would work under anaesthesia had to be found, seizures had to occur frequent and spontaneously and within a relatively short time course. EIT imaging of seizure foci was tested in more than one epilepsy model to ensure that the imaging could be conducted independently of the used model. Chemical models of epilepsy were used as direct electrical stimulation would interfere with our recordings. In the chosen models, the substance was injected directly into the cortex as this would most likely produce a localized seizure focus. 4-aminopyridine (4-AP) is a commonly used epilepsy model in anaethetized rats is and it is usually used in conjunction with urethane anaesthesia (Bahar et al. [2006], Ma et al. [2013], Macé et al. [2011]). As urethane is not available to us due to university policy, we used $\alpha-$chloralose anaesthesia instead. Droperidol in conjunction with fentanyl anaesthesia was used for all other models as it was shown to be the anaesthetic agent most permissive for seizure discharges for a number of epilepsy models in a study by Hunfeld et al. (Hunfeld et al. [2013]). The seizure models tested for the purpose of this study were: 4-AP, pilocarpine, cobalt chloride, kainic acid (KA), picrotoxin and penicillin. All of these substances are well described seizure models and were injected into the cortex of anaethetized animals. 4-AP is a potassium channel blocker, while pilocarpine is an agonist of muscarinic ACh receptors which it activates (Pitkaenen et al. [2005]). The mechanism of action of cobalt chloride remains mostly unclear and may be due to local irritation of the brain. KA is an agonist for a ionotropic glutamate receptor causing seizures by activation. Picrotoxin and penicillin both interfere with the inhibitory GABAergic system. Picrotoxin blocks the $GABA_A$-receptor chloride channel and penicillin is a selective $GABA_A$-antagonist which block $GABA_A$ mediated inhibitory postsynaptic potentials (Pitkaenen et al. [2005]).

6.1.4. Rationale

The overall purpose of this study was to determine if EIT could be used to produce reliable images of impedance changes during spontaneous epileptic seizures using a planar array of subdural electrodes. Planar grids of electrodes are also used in the pre-surgical assessment of patients when their seizure focus is being determined. If the seizure focus can be reliably identified with EIT in the rat model, then it could potentially be used in the pre-surgical assessment of epilepsy patients. Compared to previous works, this study contained several novelties: the temporal resolution necessary to detect the fast neural response to epilepsy was reached for the first time; (2) the onset and time course of cell swelling was characterized in unprecedented detail; and (3) using a high-density electrode grid and new reconstruction algorithms, the spatial resolution was improved to 0.4 mm in the cortex. The specific questions this study set out to answer were:

- Can fast neural impedance changes be imaged in epilepsy and what are their spatial and temporal characteristics?
- What are the spatial and temporal characteristics of cell swelling in our epilepsy models, as reflected in our impedance measurements?
- How do the observed changes relate to the known pathophysiology and the EEG?

6.1.5. Experimental design

In this study, seizures were imaged in three well described rat models of seizures using EIT. Further epilepsy models were tested but did not produce sufficient epileptiform activity. A similar set up to the one described in Chapter 3 was used. The same electrode type as in Chapter 3 was used with the amendment of having pre-cut holes between the electrode contacts to allow injection of substances to induce epilepsy. Epileptic activity was induced by injecting either 4-aminopyridine (4-AP), picrotoxin or penicillin into the cortex of anaethetized rats. The impedance response to inter-ictal spikes and to seizures was assessed. The use of both the fast neural signal as well as the cell swelling dependent impedance changes during IIS or seizures were assessed for imaging the epileptic focus and the resulting images were compared.

6.2. Methods

6.2.1. Animals

Thirteen female Sprague-Dawley rats aged 5-8 months, weighing between 300 and 450 g, were used in this study. They were obtained from Biological Services, University College London, which bred them on site. They were kept in a room with

12 hour dark/artificial light cycle with 18-20 air exchanges/hour, and had access to food and water ad libitum. All work was conducted under UK Home Office regulations.

6.2.2. Anaesthetic and surgical procedure

The rats were initially anaethetized using isoflurane 4% in 100% oxygen. They were intubated as described in appendix B and in Vongerichten et al. (Vongerichten et al. [2014]) and ventilated with 4% isoflurane in 30/70 oxygen/air with a small animal ventilator (Inspira, Harvard Apparatus, UK). Either the femoral or the tail vein and artery were cannulated and anaesthesia was continued with either $\alpha-$chloralose in 2-hydroxypropyl-β-cyclodextrin as described by Storer et al. (both Sigma Aldrich Ltd., 30-45 mg/kg/h; Storer et al. [1997]) or droperidol/fentanyl (Sigma Aldrich Ltd., UK and Martindale Pharma, UK, respectively, mixed as 0.5 mg/ml droperidol and 10 mg/ml fentanyl, 1.5-2.5 ml/h) intravenously. The animals were relaxated with 2 mg/kg of pancuronium bromide (Hospira, UK) just prior to the induction of epileptiform events if penicillin was used. The blood pressure was monitored invasively during the recording and a mean arterial pressure (MAP) between 90-110 mmHg was maintained using adrenalin iv (Adrenaline, diluted to 1:20 000, 0-0.6 ml/h, Martindale Pharmaceuticals, UK) or labetolol iv (Trandate, 0-0.5 ml/h, RPH Pharmaceuticals AB, Sweden) as necessary. The body temperature of the rat was controlled with a homoeothermic heating unit (Harvard Apparatus, Kent, UK).

The rat was fixed in a stereotactic frame in prone position using ear-bars. The rat's head was then shaved, the skin was infiltrated with subcutaneous lidocaine (Lignol, Dechra Ltd., UK) and subsequently incised using a scalpel. The bone was freed from periosteum and the suture lines identified. The insertion of the temporal muscle on the left side was incised with a scalpel and the muscle bluntly dissected off the bone until the zygomatic arch came into view. A craniotomy reaching paramedial from 2 to 3mm rostral to the bregma to just rostral of the lambda suture in a triangular fashion with the tip of the triangle reaching down laterally to 1 mm above the level of the junction of zygoma to temporal bone. A veterinary bone drill was used for the craniotomy (Ideal Micro-Drill ^{TM}). The bone flap was then lifted and the dura incised in a crescent shape and deflected over the mid-line to avoid damage to the superior saggital sinus. The brain was kept moist with warm (38°C) 0.9% NaCl solution.

6.2.3. Induction of epileptiform events

Seven different chemical were injected via a 30 G (BD Insyte, BD, UK) needle using a AL1000-220 syringe driver. The needle was introduced using a stereotactic micromanipulator (SM-15, Narishige, Japan) through a pre-cut hole in the subdural electrode array and advanced to a depth of 1.5 mm measured from the array. All dosages depended on the clinical response (epileptiform spikes in EEG). The needle was withdrawn once changes in the EEG became visible. 6-15 μl of 50-100 mM 4-

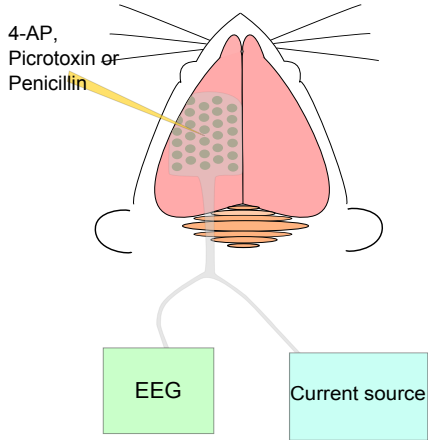

Figure 6.1.: Experimental set-up. As previously, an electrode grid is implanted subdurally and the EEG and current source run in parallel. Seizures and IIS are elicited by injecting one of three chemicals (4-AP, picrotoxin or penicillin) into the cortex.

AP in 0.9% saline was injected in 3 rats under $\alpha-$chloralose anaesthesia. 3-10 μl of 10 mM picrotoxin was injected in 3 rats under $\alpha-$chloralose or droperidol/fentanyl anaesthesia and 6.5 to 20 μl of 100-200 mM penicillin was injected in 3 rats under droperidol/fentanyl anaesthesia.

Further models that were tried but did not produce spikes or seizures were: Pilocarpin (n = 2, 35μl of 5 M solution), Cobalt chloride (n = 1, 26μl of 0.1 M solution) and kainic acid (n = 1, 14μl of 23.5 M solution).

6.2.4. Control experiments

As a control baseline impedance recordings without an epileptic focus were performed. The same recordings were repeated after injection of saline into the cortex to ensure that the found changes were not merely the reconstruction of an alteration in the cortical volume due to the epileptiform agent. Furthermore, EEG recordings of interictal spikes and seizures were performed without any current injection to test whether the current injection altered the seizure activity.

6.2.5. EEG and Impedance recordings

6.2.5.1. Electrodes

The electrode used in this study was the same as in chapter 3, with the amendment of pre-cut holes of 0.3 mm diameter between the contacts to allow the injection of the chemical substances. The reference electrode was a 1.5 x 1.5 cm silver/silver chloride plate which was placed under the skin of the right side of the skull, opposite the

recording electrode grid. In some recordings a 16 channel depth electrode (A1x16-3mm-100-703-A16, Neuronexus, MI, USA) was placed through the holes in the grid electrode array. The depth electrode was used in conjunction with a headstage pre-amplifier (33504-20, Plexon, TX, USA). The depth electrode was placed in the area that the epileptogenic substance was injected by maintaining the angle and rotation on the micomanipulator used for the injection of the chemicals (see description in 6.2.3).

6.2.5.2. Current source

The same current source as in chapter 3 was used.

6.2.5.3. EEG system

The system used to record both, the EEG and voltages from the epicortical array and the depth electrode, was the same as in chapter 3.

6.2.6. Analysis of the EEG and Impedance data

Recorded voltages were loaded into matlab and processed offline. To extract the EEG, the recorded voltage signals were low pass filtered $<$300 Hz. The same recorded voltage signals were bandpass filtered at 1700$\pm$300 Hz and subsequently demodulated to extract the impedance signal.

6.2.6.1. Analysis of the EEG data

Spikes were detected automatically by thresholding for amplitude ($>$ 2mV), events with $<$ 70 ms in width and inter-spike interval of $>$ 1 s. The EEGs were examined for seizures and those were labelled by hand marking out the start, duration and end. The start of the seizure was either determined by the beginning of spiking or - in the case of the 4-AP model - as the DC shift marking the beginning of a seizure. The seizures themselves were defined as a run of spikes that was had a frequency of $>$ 1 Hz and lasted a minimum of 2 seconds.

6.2.6.2. Analysis of impedance signal

The spike related impedance response was reconstructed for each spike and then averaged. A time frame of -200 ms to +2 s was considered as the event time. Seizures were also reconstructed from a single injection pair and then focus was subsequently averaged.

6.2.6.3. Reconstruction of impedance signals

The same method for reconstruction and the same cylindrical mesh as in chapter 3 was used.

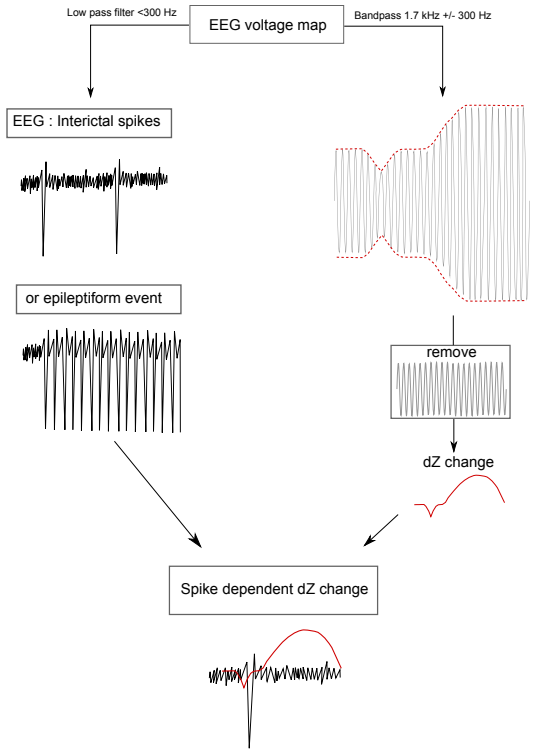

Figure 6.2.: Analysis of voltage signals. The voltage signals are low passed filtered to extract the EEG. The same raw signal is bandpass filtered and demodulated to extract the dZ signal.

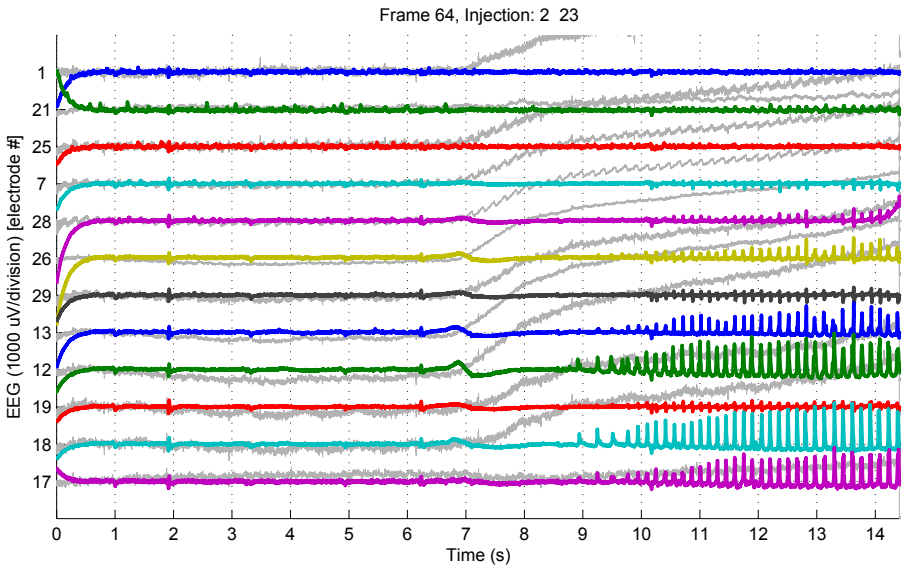

Figure 6.3.: Example frame showing the beginning of a seizure elicited by 4-AP; the coloured lines each represent a channel of the EEG (1mV/division) and the relative dZ in that channel is plotted in grey on top of them.

6.2.6.4. Comparison of the location of the reconstructed foci

The spatial differences between the foci reconstructed using (1) the fast neural component of IIS, (2) the slow component of IIS and (3) the seizures were measured and compared using a one-way anova (see 6.3.3.1 for the definition of the fast and slow component of the IIS impedance signal). The distances of the reconstructed foci using these three signals were also assessed for the distance to the site of injection of the chemical causing the seizures and the distances were compared using a one-way anova.

6.3. Results

6.3.1. EEG recordings of epileptiform events

6.3.1.1. 4-AP model

Injection of 4-AP into the cortex lead to both IIS as well as seizures. One rat only developed seizures and no IIS and the other two rats had IIS and seizures. The beginning of the seizures was characterized by a DC shift followed by an electrodecremental period of varying length with then lead to spiking with a 4-5 Hz frequency. The seizures occurred every 8-30 s lasting between 2 and 20 seconds.

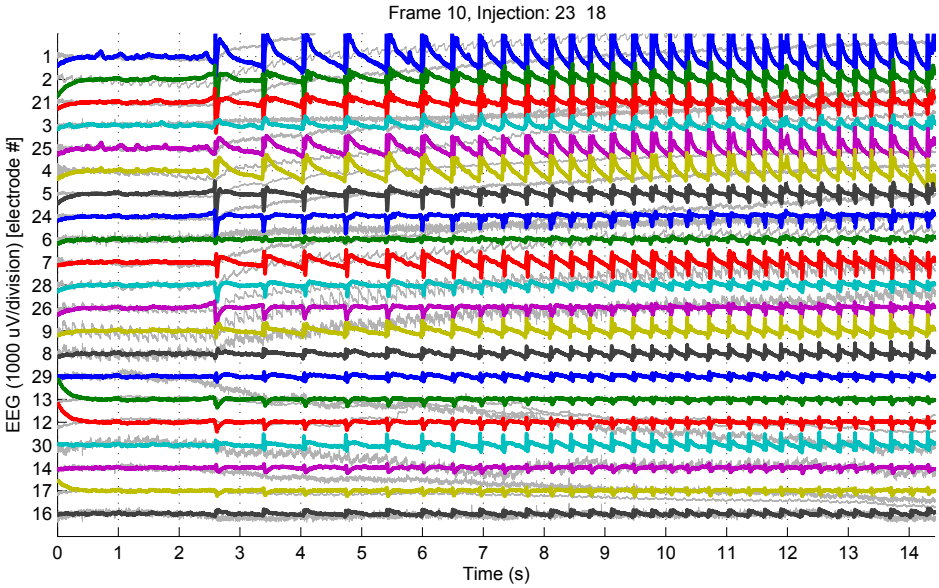

Figure 6.4.: Example frame showing the beginning of a seizure elicited by penicillin, the coloured lines each represent a channel of the EEG (1mV/division) and the relative dZ in this channel is plotted in grey on top of them.

There were 74, 94 and 205 seizures in each rat, respectively. There were no IIS in one rat, while 596 and 158 IIS were recorded in the other rats, respectively.

6.3.1.2. Picrotoxin model

The EEG of the picrotoxin model was characterized by IIS occurring with a frequency of 0.3 - 1Hz. Only 16 self-limiting seizures were elicited in total so that averaging of seizures was not possible. There were 630, 821, and 828 IIS recorded in each rat.

6.3.1.3. Penicillin model

After injection of penicillin sporadic IIS developed which slowly progressed self-limiting seizures. The spike frequency during the seizures was 6-8 Hz. There were 72, 7 and 145 seizures in each rat of this group, respectively. There were 279, 292, and 1128 IIS recorded in each rat.

6.3.1.4. Other epilepsy models

Injection of pilocarpin, cobalt chloride or KA did not produce spikes or seizures in the EEG of the anaethetized animals in our experiments.

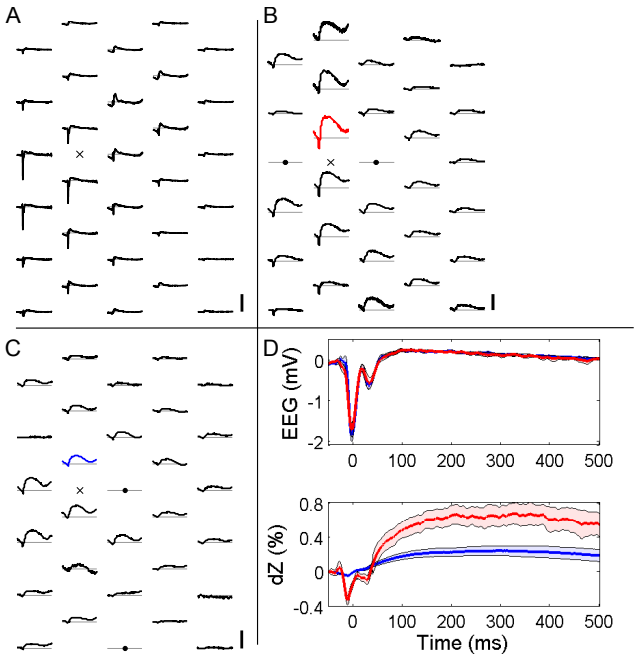

Figure 6.5.: The recorded dZ depends on the location of the current injection. (A) Shows IIS in the EEG in an example rat, the seizure focus (point of 4-AP injection) is marked with a 'x'. (B) shows the dZ (n = 54 IIS) recorded at the same electrode grid during one current injection (pairs marked with dots) and (C) shows the dZ recorded during a different recording pair (n = 39 IIS). (D) The upper panel shows the IIS in EEG recorded from the electrode marked with red in B and blue C during the two different injection pairs with no difference to the EEG. The lower panel shows the dZ recorded during these injection pairs (pale blue and red represents 99% CI respectively).

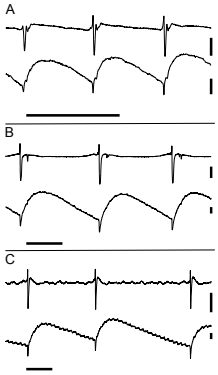

Figure 6.6.: EEG (upper) and dZ (lower) traces for 3 different seizure models. All horizontal scale bars represent 1 s and all perpendicular represent 2 mV for the EEG and 0.2% for dZ. (A) Seizures elicited with 4-AP, (B) picrotoxin and (C) penicillin.

6.3.2. Control experiments

No epileptic focus was recorded when baseline recordings were used for reconstruction or measurements after saline injections were reconstructed. The current injection did not alter the seizure frequency or morphology.

6.3.3. The Impedance recordings of epileptiform events

6.3.3.1. Impedance response to single spikes

IISs caused a brief decrease in impedance prior to the peak of the epileptic spike in the EEG, this will be called the fast component of the impedance signal. The initial decrease was followed by a significant increase in impedance following the peak of the epileptic spike and lasting for up to 2 sec; this will be called the slow component of the impedance signal. The impedance response to IIS is illustrated in figure 6.6. The fast component had a median of -0.04 to -0.17 % and occurred between -10.82 to +1.82 ms relative to the peak of the IIS. The slow component had a median of 0.15 to 0.43%, the time to reach significance was 16-117 ms. The slow component reached its maximum within 336 to 930 ms. The results are summarized in table 6.1 and all stats for an example rat are shown in figure 6.7.

The correlation between the amplitude of the fast and the amplitude of the slow dZ component fast calculated in each rat and averaged. The mean correlation was 0.83±0.11, see figure 6.8 for an example. The correlation between the size of the spikes in the EEG and the extent of the event related dZ was calculated for each rat and then averaged. The mean correlation was r = 0.73±0.2 for the fast and r = 0.64±0.31 for the slow component (see fig.6.9 for the correlation in an example rat and table 6.1 for the full set of results).

	Rat #	n IIS	Fast neural signal				Slow signal				
			Min. (%)	Median (%)	t (ms)	r	Max. (%)	Median (%)	t_{max} (ms)	t_{sig} (ms)	r
4-AP	2	596	-0.59	-0.04	-9.96	0.88	0.69	0.15	336	16	0.80
	3	148	-0.26	-0.07	-7.15	0.75	1.27	0.19	713	39	0.81
Picrotoxin	1	630	-0.64	-0.12	-10.82	0.9	1.62	0.28	734	58	0.9
	2	821	-0.42	-0.1	-6.36	0.35	0.61	0.14	406	32	0.13
	3	828	-0.26	-0.07	-12.1	0.51	0.93	0.21	766	117	0.17
Penicillin	1	279	-0.93	-0.13	-0.56	0.83	2.34	0.29	930	46	0.79
	2	292	-0.47	-0.17	-1.17	0.71	1.55	0.43	699	62	0.74
	3	1128	-0.47	-0.12	1.82	0.88	1.07	0.17	537	46	0.8

Table 6.1.: Summary of the results for the dZ changes due to IISs for the fast and slow component separately. All times are relative to the peak of the IIS. t_{max} = time to maximal impedance change; t_{sig} = time to significant impedance change, r = the correlation between the amplitude of the IIS and the amplitude of the dZ change.

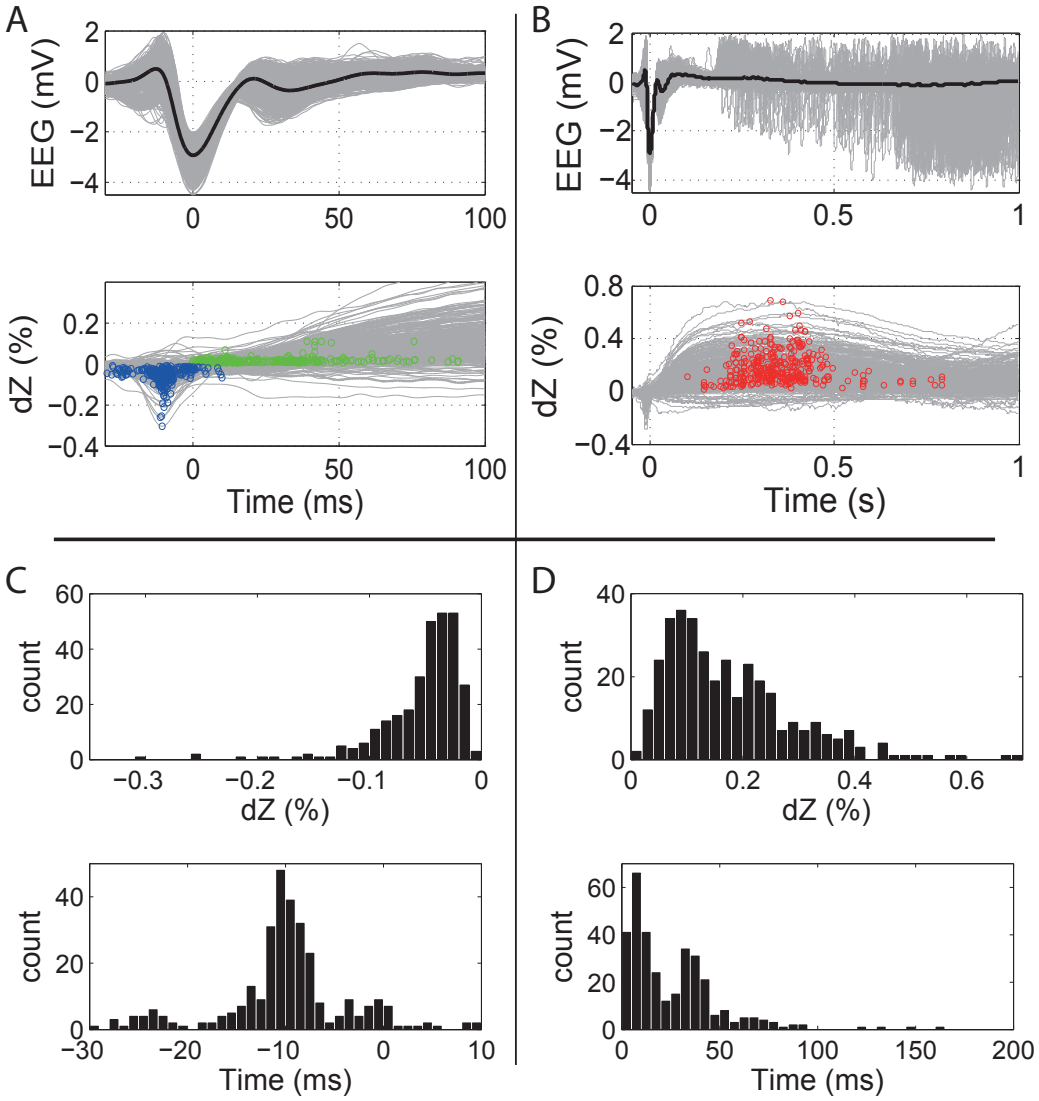

Figure 6.7.: Statistics for the IIS of an example rat using 4-AP as a seizure model. (A) Upper panel: IIS in EEG in mV in one channel over 130 ms (grey lines: individual traces, black: mean). Lower panel: dZ (in %) recorded in all injection-measurement combinations over the same time frame. The blue circles indicate the minimum dZ and the green circles the first significant positive dZ. (B) Shows the dZ (%) recorded on all injection-measuremen combinations on a longer time scale (1s). (C-F) Histograms of the distribution of peak negative dZ (C), peak positive dZ (D), time of the peak negative dZ (E), and time of the first significant positive dZ (F).

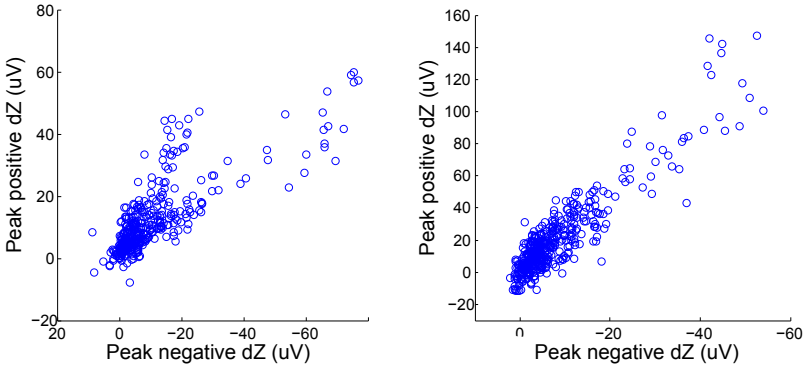

Figure 6.8.: Correlation between the amplitude of the fast and slow dZ. (A) and (B) show examples for one rat each.

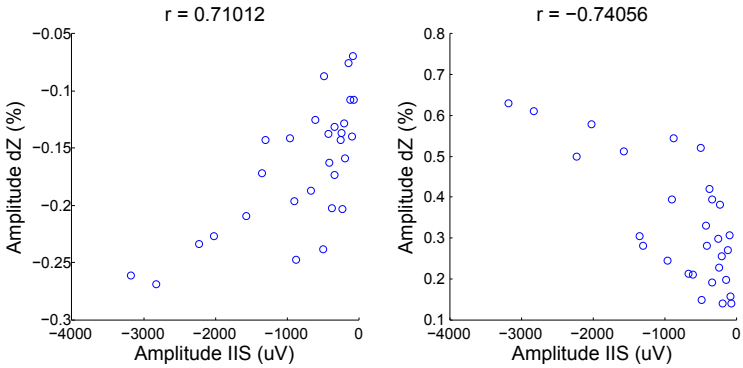

Figure 6.9.: Example of the correlation between the amplitude of the IIS and the event related dZ in the same channel in one rat.

6.3.3.2. Impedance response to seizure-like event

Seizures caused a significant increase in impedance which peaked at 2.21±1.16% (n = 201 seizures in total) in the 4-AP and penicillin model.

6.3.4. Reconstructed images of epileptiform events

6.3.4.1. Reconstruction of epileptogenic focus using single spikes

Images of the impedance changes during IIS were reconstructed using measurements of single injection pairs. Both the fast and the slow component of the impedance signal can be used for the reconstruction of the epileptogenic focus (fig. 6.10). Both signal components localize the focus to the same location and to the known site where the epileptogenic substances were injected (see fig. 6.12, left for a summary). The mean spatial difference between the centre of mass of the epileptogenic focus reconstructed using the fast component and the slow component was 0.45±0.35 mm, see table 6.2.

6.3.4.2. Reconstruction of epileptogenic focus using seizure-like events

Individual seizures were reconstructed from measurements of single injection pairs (compare figure 6.11 for an example). The spatial difference between the epileptogenic focus reconstructed using IIS and the focus reconstructed from seizures was 0.62±0.22 mm using the fast component of the IIS and 0.54±0.17 mm using the slow component of the IIS, respectively. There was no statistical significant difference between the distance of the reconstructed foci of the IIS using the fast and slow component compared to using the seizures ($p>0.05$, one-way ANOVA), see table 6.2 for the full set of results.

6.3.4.3. Comparison of the location of the reconstructed foci

The mean distance of the reconstructed focus from the site of injection of the chemicals (4-AP, picrotoxin and penicillin) was 0.63±0.29 mm for the fast component of the IIS, 0.75±0.3 mm for the slow component of the IIS and 0.61±0.33 mm for the seizures. There was no statistically significant difference between the groups ($p>0.05$, one-way anova), see table 6.2 for the full set of results.

6.4. Discussion

6.4.1. Summary of results

In this study the impedance response of cortical tissue to IIS and seizures was characterized for three different seizure models and two distinct signal components were found. These consisted of a brief drop in impedance in response to synchronous activity in conjunction with the peak of IIS and peaks in spiking during seizures.

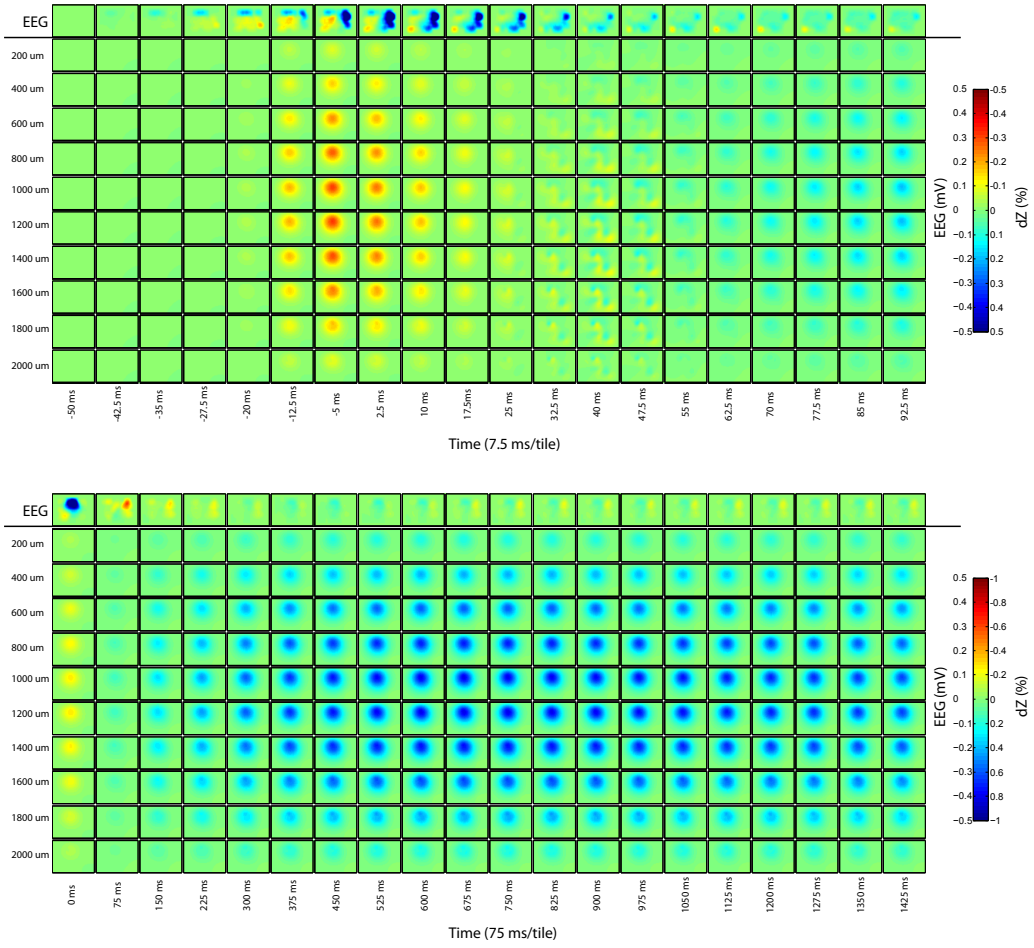

Figure 6.10.: Reconstruction of the epileptic focus in one of the 4-AP rats using IIS. Upper panel: fast component; lower panel: slow component.

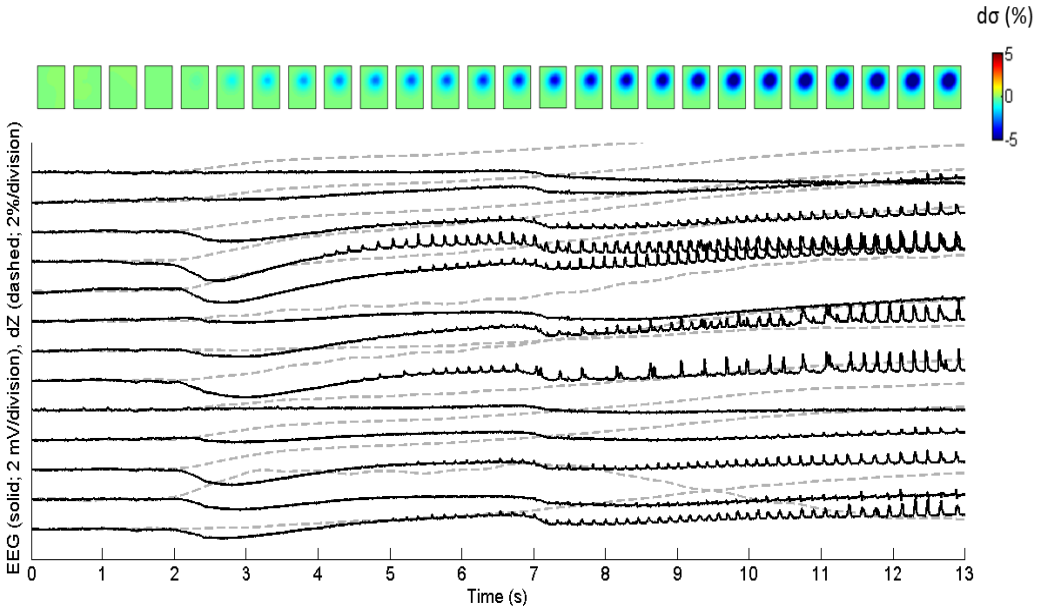

Figure 6.11.: Example of a single seizure elicited by 4-AP and its reconstruction. The reconstructed changes are shown at a depth of 1 mm. Each tile represents a 0.5 s time point. The change in conductivity is given in (%). The EEG shown as solid lines (2 mV/division) and the dZ changes are plottet as dottet lines for the same channel on top of the EEG.

	Rat #	fast vs slow	fast vs seizure	slow vs seizure	fast vs injection	slow vs injection	seizure vs injection
4-AP	1						0.64
	2	0.21	0.63	1.06	1.06	0.93	0.7
	3	0.7	0.93	0.95	0.95	0.58	0.9
Picrotoxin	1	0.13	0.43	0.27	0.27	0.36	0.31
	2	0.68		0.56	0.56	1.22	
	3	0.79	0.76	0.48	0.48	0.44	0.28
Penicillin	1	0.17	0.49	0.81	0.81	0.96	0.32
	2	0.04	0.79	0.54	0.54	0.58	1.23
	3	0.92	0.31	0.34	0.34	0.9	0.52
mean		0.46	0.62	0.54	0.63	0.75	0.61
SD		0.35	0.22	0.29	0.29	0.3	0.33

Table 6.2.: Summary of the distances in millimetre of the reconstruced foci using the fast or the slow component of the IIS or seizures and of the distances of the reconstructed foci using the fast and slow component of the IIS and seizures to the injection site of 4-AP, picrotoxin, and penicillin.

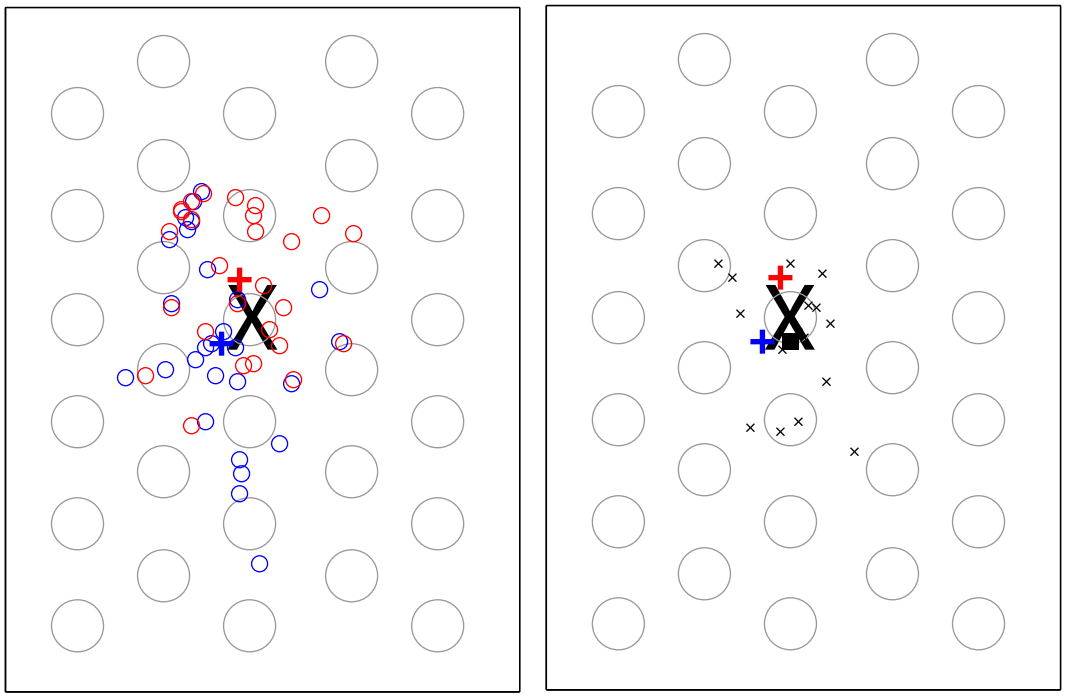

Figure 6.12.: Examples of the location of the reconstructed epileptic foci one example rat. The large black 'X' indicates the location of injection of the chemical causing the epileptic activity. Left: the red circles represent the reconstruced epileptic foci using the fast component of the IIS impedance signal; red cross: mean location of the foci using the fast component; blue circles: the reconstructed epileptic foci using the slow component of the IIS impedance signal; the blue cross indicates the mean location. Right: the small black 'x' represents the reconstructed foci using individual seizures; the black square represents the mean of the reconstructed foci using seizures. The red and blue cross indicate the mean reconstructed location using the IIS which occured in the same rat.

They were were followed by an increase in impedance which became significant within approximately 50 ms of the peak of the spike and I argue that this increase is due to cell swelling. The epileptic foci was imaged with event related EIT using either IIS or seizures in the EEG as the event. The focus of the IIS and seizures matched in location and matched the EEG signal. The reconstructed foci using either of these signals were less than one millimetre apart and there was no statistically significant difference between them. When the epileptic foci was set, the needle was not perfectly perpendicular to the brain. This caused inaccuracy, which might explain a discrepancy of up to 1 mm between the entering point of the needle to the reconstructed epileptic focus. The spread between the reconstructed foci using single current injection pairs however clearly shows variability with respect to the injection pair. This variability can be reduced in two different ways: either by switching between current injection pairs and using all pairs for the reconstruction or by injecting current in parallel by frequency multiplexing. It should be taken into account that only the area under electrode grid, down to 2 mm from the surface, was imaged with the method employed in this study. Hence, only the behaviour of the impedance signal in the cortex can be discussed. There are further limitations in imaging seizure foci with the EIT method used, as the switching current injection makes it difficult to average the recordings and single injection pairs were used instead.

6.4.2. Spatial and temporal characteristics of the impedance response to inter-ictal spikes and seizures

The brief drop in impedance in response to the IIS most likely represents a brief drop in tissue resistivity during the opening of ion channels occurring at the synchronized depolarization during local activation similar to the decreases in impedance due to physiological stimuli in chapter 3 and 5. Apart from ourselves, a brief decrease in electrical impedance due to synchronous opening of ion channels has been described by previous authors who measured the impedance response to activity in-vivo of the cortex of cats and rats (Klivington, K Galambos [1967], Oh et al. [2011a]). Klivington et al. measured the impedance response of the cortical tissue to auditory stimuli in the cat and Oh et al. measured the impedance response of the cortical tissue to electrical stimulation of the forepaw in the rat. In line with our results, both authors reported a brief drop in the impedance time-locked to the neuronal activation of 0.03Ω and 0.01%, respectively (Klivington, K Galambos [1967], Oh et al. [2011a]). The larger amplitude of our impedance drop compared to our previous results and Oh et al. could feasibly be due to the difference in stimulation as relatively physiological sensory stimulus were used in the past while the impedance response to a pathological synchronized activation producing EEG signals of >2 mV were measured, while the evoked potentials previously reached amplitudes of around 1 mV in amplitude.

The behaviour of the cortical impedance signal in response to seizures matched was similar to that of IIS in the sense that each further spike during the seizure

increased the local impedance further until a plateau was reached. A brief drop with each initial spike could be distinguished apart from the recordings using 4-AP as the seizure model, which started with a DC shift and not a sharp spike. In order to conduct images in a volume, injection pairs were switched, to allow to reconstruct from multiple injection pairs. This approach adds the difficulty of not having enough dZ changes with the same injection pair in each rat to directly compare the impedance changes in relation to the model directly. A possibility of avoiding this problem in future could be to use non-switching multiple current injection, which will be discussed in the future work section.

An increase in cortical impedance during seizures and IIS has been reported by several authors, the time-course of which however differs vastly in the literature. All of these authors explained the increase in impedance with cell swelling occurring during seizures and IIS. In contrast to our findings, none of these authors reported a brief drop in impedance before the increase, which might be due to the temporal resolution of the devices used and the measurement methods employed. Traynelis et al. reported an impedance in impedance before the seizure started, while Fox et al. reported impedance increases after seizures (Traynelis and Dingledine [1989], Fox et al. [2004]). In recent experiments, Olsson et al. reported a continuously increasing impedance in picrotoxin, kainate acid and fluorocitrate seizure models with an acceleration in the impedance increase just prior to the seizure onset (Olsson et al. [2006]). Olsson et al. used a similar set up to ours, with a current source and an EEG amplifier reaching a temporal resolution of ~33 ms, a magnitude higher than the temporal resolution in Elazar et al.s experiments. They calculated that the measured change in impedance would correspond to a 7-10% increase in cell size. The increase in impedance prior to seizures in the fluorocitrate model were reproduced by Broberg et al., who could also show concomitant high frequency (150-300 Hz) in the EEG and an increase in extracellular potassium and a decrease in extracellular calcium (Broberg et al. [2008]).

There are two possible reasons why there was an increase in impedance prior to EEG changes seen in Olsson et al.'s data but not in our data. One possible reason is that the cell swelling occurs prior to the onset of the seizure in the kainate acid and fluorocitrate model but not in the picrotoxin, the 4-AP and the penicillin model. Alternatively, the sensitivity of the impedance measurements in Olsson et al.s experiment could be higher than that of the EEG with the set up of screw electrodes they used. This would lead to a delay of changes seen in the EEG when the impedance change is already visible. When looking at the time course of the impedance increase, it should take into account which physiological processes take place after activation. From optical measurements it is known, that the electric activity causes a brief focal deoxygenation in the epileptic focus together with an increase in CBV both significant at 100 ms, which was the temporal resolution of their method (Suh et al. [2005]). It is easy to understand how a local deoxygenation could contribute to cell swelling, an increase in blood volume however should decrease the impedance of the tissue locally as blood is more conductive than brain tissue. It is possible

that the focal increase in impedance due to cell swelling causes a much larger signal in the impedance than the focal increase in blood volume. In response to activity the capillaries react with a focal dilatation of 6.7% which occurs 1.3 s before the arterioles dilate (Hall et al. [2014]). Capillaries take up approximately 2% of the total cortical volume (Weiss [1988]) while the total extracellular space is approximately 20% of the total cortical volume and it changed in response to electrical stimulation by approximately 4% in brain slices as measured with near-infrared dark-field microscopy (Holthoff and Witte [1996]). The decrease in impedance due to the change in the small volume fraction of the capillaries might not be measurable if the larger volume fraction, the extracellular space, is reducing causing an impedance increase at the same time. In contrast to blood volume, changes in blood flow increases or decreases impedance, dependent on whether the impedance is measured longitudinally or radially to the blood vessel (Visser et al. [1976]). If a non-uniform direction of the blood flow in the cortex underlying the electrode grid is assumed then changes in blood flow itself would not alter the impedance much. In summary, I argue that cell swelling in conjunction with seizures or epileptic spikes is a well described phenomenon and it is mainly the time course of the cell swelling which requires further clarification. A very quick onset of the cell swelling within 50 ms was seen, but no cell swelling prior to the onset of IIS or seizures with the seizure models used.

6.4.3. Comparison of the reconstructed impedance changes due to inter-ictal spikes and seizures

This study showed, that seizure focus and spread can be imaged using impedance measurements. Both the fast and slow component of the impedance signal can be used individually for the IIS. Seizures as well as IIS can be used to image the seizure focus using the slow impedance signal, the imaged focus was in the same area in the animal models used in this study. In order to image seizures they have to occur in a fairly stereotypical fashion and adequate numbers have to be available to average. This was partially given in our experimental set-up but may be difficult in human epilepsy patients. It is feasible that single seizures may be imaged in the future as the development of the EIT system progresses.

6.4.4. Comparison of the reconstructed impedance changes due to inter-ictal spikes and seizures with the surface EEG

The EEG signal and the reconstructed EIT images correlated highly with each other so that the assumption, that the same neuronal networks producing the spikes also produce the impedance signal, can be made. Other events such as the DC shift in the 4-AP model followed by the electrodecremental period also increased the impedance which represents associated cell swelling. The correspondence of the EEG signal to the EIT signal in the agyrate cortex of the rat was validated and I propose that EIT might yield additional information when performed in the gyrated

human brain where dipoles can cancel each other out in EEG but the EIT signal would remain unaffected.

6.4.5. Future work

The results obtained in this study are promising but limited due to only impedance changes in the cortex being be imaged. The clinical information obtained by these recordings could have also been obtained by EEG recordings alone. However, the characterization of the impedance signal due to epileptic activity will allow us to proceed to recordings of epilepsy in the three-dimensional space using large electrodes covering most of the neocortex of both hemispheres. A further limitation in this study was, that switching was used to reconstruct the epileptic focus and spread. Ideally, a single seizure at a time could be imaged reliably. Imaging using single injection was possible if the seizure focus was directly in the sensitive area of the injection pair. However using a single injection pair meant that less data is available for the reconstruction, which lowers the image quality as well as reliability. A possible way forward would be to use multiple current sources which continuously inject currents of various frequencies through multiple injection pairs in parallel.

In the next study, the use the full potential of EIT in tomographic imaging of seizure spread throughout the brain in a rat model of epilepsy is planned. A model will be chosen in which activity is expected to spread from a subcortical structure to the other hemisphere and/or to the cortex. Furthermore, an attempt to use parallel current injection to improve the imaging of single seizures with less prior knowledge of the epileptic focus will be made.

7. Feasibility of imaging epileptic activity in a rat model in 3D using EIT

7.1. Introduction

7.1.1. Orienting paragraph

As discussed in the previous chapter, a method that would allow us to image seizures spreading throughout the brain would allow a better understanding of epileptic networks and localisation of the focus, which may lead to a better post-operative outcome. Spike triggered fMRI is successfully being used to image epileptic foci (Vulliemoz et al. [2010]), however, it has the disadvantage of the time limit a patient may remain in the scanner as well as depending on changes in the blood flow to map neuronal activity. In the previous chapter, the impedance response of neocortical tissue to epileptic activity has been characterized using a planar array. These results were promising as they showed a stereotype impedance response to IIS and seizures and could be reconstructed to show the seizure focus. In particular, the slow component of the epilepsy dependent impedance signal seems large enough to be detected from subcortical structures. In this chapter the possibility of imaging epileptiform activity throughout the brain of a rat using EIT was examined. Furthermore, a novel EIT paradigm that uses frequency multiplexing for making parallel measurements was tested, which increases the amount of data obtained from every seizure without loss of temporal resolution.

7.1.2. Background

7.1.2.1. Previous attempts of EIT imaging of seizures

A previous attempt to image epilepsy in 3D has been undertaken by Fabrizi et al. in our group (Fabrizi et al. [2006]). They used the UCLH Mark 1b which utilized a single impedance four-terminal measuring circuit multiplexed to up to 31 electrodes to measure impedance (Yerworth et al. [2002]) on the scalp of patients undergoing pre-surgical EEG-telemetry. Fabrizi et al. injected current with a frequency of 38.4 kHz and an amplitude of 2.2 mA from diametrically opposed electrodes in an attempt to measure cell swelling and blood flow dependent changes to the impedance (Fabrizi et al. [2006]). Their method could record EIT and EEG simultaneously on different electrodes, but no reproducible impedance changes were found during seizures. This was presumably due to low SNR and movement artefacts as they attempted to measure through the skull. Using a single measuring circuit meant that switching was necessary, which introduced a switching artefact in the EEG requiring hardware and software filters for its removal, and the switching reduced the temporal resolution of the measured impedance signal.

7.1.2.2. Single and multiple current injection for EIT

Parallel current injection by frequency multiplexing was tested for EIT recordings in this study as it has the advantage of allowing continuous EIT recordings without switching. This has the advantage of avoiding switching artefacts in the EEG as

well as allowing comparison of spontaneous events such as seizures. If a single injection pair is switched to obtain a tomographic image the recordings using one injection pair is not directly comparable with other injection pairs during the same event and does not allow statistical analysis. This is not a problem if the event is triggered externally and can be repeated in large numbers as it is the case for EPs but makes recording difficult when a spontaneously occurring event is imaged. Using multiple current injections however does add some challenges to the EIT recordings. Care must be taken to separate the frequencies of the injected current far enough to avoid overlap between the modulated signals. This bandwidth depends on frequency spectrum of the impedance signal that we want to measure. The slow component of the seizure dependent impedance signal only has a few Hz but the fast component has a wider frequency range of approximately 200 Hz (see chapter 3). The distance between the injected frequencies was hence chosen to be 1.4 kHz, 1.8 kHz, 2.2 kHz and 2.6 kHz. This unfortunately means that we measured at frequencies which are higher than 1925 Hz, which was the maximum frequency tested during the frequency sweep in chapter 3. We worked on the assumption that the behaviour of the impedance signal at these frequencies is similar to the one used in chapter 6. Furthermore safety considerations are more difficult as the total injected current is a multiple of the current injected with a single frequency pair even though the more important current density remains unchanged.

7.1.2.3. Cortical and hippocampal seizure models

An overview of the epilepsies has been given in the previous chapter and the choice of epilepsy models has been discussed as well. The cortical 4-AP model was used again to image seizure spread throughout the brain. In a functional ultrasound study, Macé et al. showed seizure spread from the cortex to the thalamus in 3D (Macé et al. [2011]). However, it remains unclear in how many rats such a seizure spread could be imaged, as the video of a single rat was presented as supplementary material. Considering that 4-AP is one of the cortical seizure models which was characterized in the previous chapter, we attempted to image seizure spread throughout the brain with this model. Furthermore it was tested whether seizure spread can be imaged from a focus in the hippocampus. Hippocampal sclerosis is the single most common pathology which underlies refractory focal epilepsy that is amenable to surgical treatment (Hauser et al. [1996]). Hippocampal epilepsy usually either spreads initially to the contralateral hippocampus, to the ipsilateral neocortex, or simultaneously to the ipsilateral neocortex and contralateral hippocampus (Spencer et al. [1987]).

7.1.3. Rationale

This chapter assesses the use of EIT for imaging the spread of different types of epilepsies throughout the whole rat brain. An epileptic focus was set either in the cortex or in the hippocampus to test EIT's ability to image subcortically and track

different patterns of seizure spread. It was also tested whether seizure activity could be imaged using a novel EIT paradigm of parallel current injection by frequency multiplexing, as this method could obviate the need to pool measurements across multiple seizures for the image reconstruction, and therefore increase our ability to find an epileptic focus from single seizure events.

7.1.4. Experimental design

Two different types of epileptic foci were tested: one in the cortex and one in the hippocampus. In both cases 3D EIT images were obtained to assess the spread of the activity. For validation purposes, depth electrodes were used in the hippocampal model to measure LFPs which would indicate the start of epileptic activity. The measurements of LFPs in the hippocampus also allowed for local measurements of impedance changes.

7.2. Methods

7.2.1. Animals, anaesthesia and surgical preparation

Five female Sprague-Dawley rats aged 5-8 months, weighing between 300 and 450 g, were used in this study. They were obtained from Biological Services, University College London, which bred them on site. They were kept in a room with 12 hour dark/artificial light cycle with 18-20 air exchanges/hour, and had access to food and water ad libitum. They were anaesthetized with isoflurane followed by $\alpha-$chloralose and fentanyl as described in chapter 5. The skin on the top of the skull was incised in the mid-line and the skull freed of periost. Two craniotomies were performed, which were reaching from 4 mm rostral of bregma to 1mm rostral to lambda, the lateral boundary was the insertion line of the temporal muscle. A small strip of bone remained in the mid-line to protect the superior saggital sinus. The dura was incised and the 3D electrodes were slid under the dura on either side.

7.2.2. EEG and EIT recordings

7.2.2.1. Electrodes

Two of the 60 contact electrode mats described in chapter 5 and 2 of the depth electrodes described in the same chapter have been used in this study.

7.2.2.2. EEG amplifier

The same Biosemi EEG amplifier as in chapter 5, 6, 4 and 3 was used.

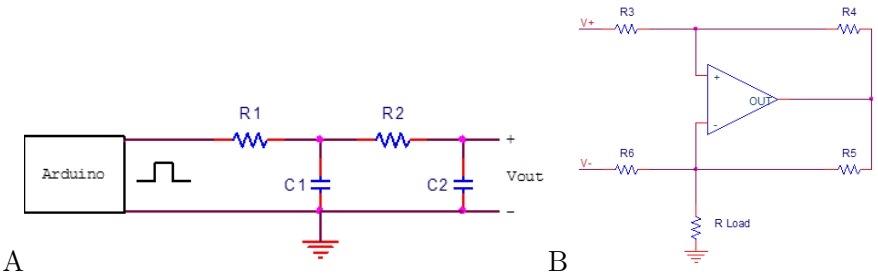

A B

Figure 7.1.: (A) Sine wave generator. An arduino nano (SmartProjects, Italy) was programmed to generate a square wave with variable duty cycle, passing this signal to a low pass filter produces a sine wave at the output node (Alter and Texas Instrumens [2008]). The frequency can be adjusted by modifying the Arduino source code, with values up to 10kHz achievable. A second order RC filter is used to produce a smooth output waveform. Nominal values for R1/R2 and C1/C2 used 10kΩ and 1nF, which produces an output signal with approximately 0.5 V amplitude. In practice, R1 is replaced with a variable resistor, to allow for the gain of the filter, and the amplitude of the output, to be adjusted. (B) Howland current pump circuit. It operates as a transconductance amplifier (Texas Instruments [2013]). The output voltage from (A) is applied to the V_+ and V_- terminals, which in turn produces an output current across the load resistance, R_{Load}.

7.2.2.3. Current sources

Two types of current sources have been used in this study. Two Keithley current sources which are described in chapter 5 were used in conjunction with a custom designed system containing two parallel current sources. Each custom made current source comprised two elements: a sine wave generator (an Arduino nano (SmartProjects, Italy)) and a voltage to current converter (Howland current pump), see figure 7.1. The minimum output impedance of the system is 10 MΩ, current with frequencies from 1 Hz to 10 kHz and amplitudes of 25-60 μA could be produced by each current source. Multiple current sources can be operated in parallel, providing each is running from a separate power source. In this instance, the power source used was a 6V, 15Ah, lead-acid battery, capable of powering the entire circuit for >100 hours.

7.2.2.4. Current injection pairs

The current injection pairs were determined by modelling a perturbation in the hippocampus and finding the injection pairs with the highest distinguishability for the region of interest.

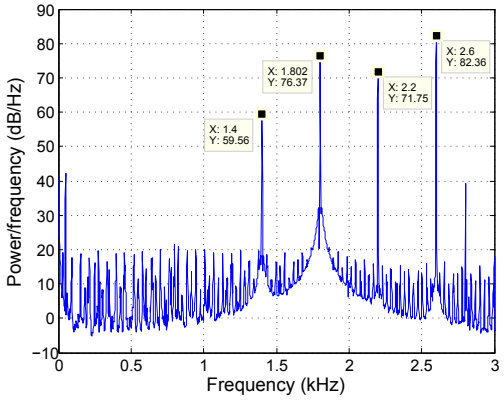

Figure 7.2.: Frequency spectrum of the recorded voltage spectrum in the hippocampal epilepsy experiment. The four peaks indicate the injected currents.

7.2.3. Cortical epilepsy model

100 mM 4-AP was injected into the cortex of two rats through the electrode array as in chapter 6 to elicit epilepsy with a cortical focus.

7.2.4. Hippocampal epilepsy model

Two different types of hippocampal epilepsy models were tried. 100 μg of γ-hydroxybutyric acid were injected in the hippocampus of one rat. This however did not produce any seizures and hence no results are reported on this rat. 15 μl of 100 mM 4-AP was injected into the hippocampus in two rats which elicited seizures that spread from the hippocampus to the cortex. The location of the 4-AP injection was AP -4 mm, ML 2.2 mm(left) and a depth of 3.5 mm from the surface of the brain in rat P1. In the second rat the coordinates were AP -3.8 mm, ML 1.8 mm (left) and depth of 3.5 mm from the surface of the brain (Paxinos&Watson coordinate system (Paxinos and Watson [2007])). All results will be reported in the same coordinate system. These recordings were obtained with two depth electrodes in place and recordings using two Keithley current sources injecting continuously through 2 fixed electrode pairs together with the custom made current source injecting to another 2 fixed electrode pairs.

7.2.5. Analysis of EEG and EIT data

The same criteria for seizures as in chapter 6 were used. The LFP and EEG signals were analysed for the propagation of seizures from the depth to the surface electrodes. The cross-correlation was computed between depth and surface recordings for a time window of 4 s around the beginning of each seizure. The peak delay in the average cross-correlation function was taken as the delay in the propagation of

activity from the depth to the surface electrodes.

7.2.5.1. Analysis of recordings with switching injection pairs

The voltage recordings were lowpass filtered at 300 Hz to extract the EEG. The recordings were also bandpass filtered at 1700±2 Hz to extract the dZ signal. The start of each seizure in the EEG was annotated by hand.

7.2.5.2. Analysis of recordings with parallel current injection

The voltage recordings were lowpass filtered at 300 Hz to extract EEG and also bandpass filtered at their injecting frequency of 1.4 kHz, 1.8kHz, 2.2 kHz and 2.6 kHz to extract the dZ signal. The start of each seizure was recorded and the cortical EEG and the LFP in the hippocampus was cross correlated to check for the time difference between seizure onset. A time window of 4 s around the start of each seizure was used for correlation.

7.3. Results

7.3.1. Results of cortical epilepsy model

As in chapter 6, the injected 4-AP produced recurrent seizures which spread in the cortex in one rat but failed to produce stereotypical seizures in another. 60 seizures were recorded in 1 rat, and the mean timecourse of the seizures was reconstructed (see figure 7.3). No seizure spread to subcortical structures or the contralateral cortex was observed in the reconstructed images. From visual inspection, the seizure spread in the impedance measurements matched the spread in EEG. The pattern of seizure and IIS spread changed over time, an example of which is shown in figure 7.4.

7.3.2. Results of hippocampal epilepsy model

In both rats injection of 4-AP into the hippocampus led to spiking and seizures first detectable on the depth electrode and the seizure activity also spread to the cortex. The average cross-correlation between the cortical EEG and the LFP in the hippocampus had the largest peak at -34 ms for 209 seizures in the second rat (figure 7.5), indicating a time lag of 34 ms between the activity on the depth electrodes to that of the cortical electrodes.

Unfortunately, the impedance data of the first rat was unusable because of a broken connector. In the second rat, the two Keithley current sources delivered constant currents at 2.2 and 2.6 kHz, respectively. Because of an error in calibration, the custom-made current sources delivered variable current and therefore the impedance changes from these current sources are not considered further. There was continuous spiking on the depth electrode in addition to 209 annotated seizures,

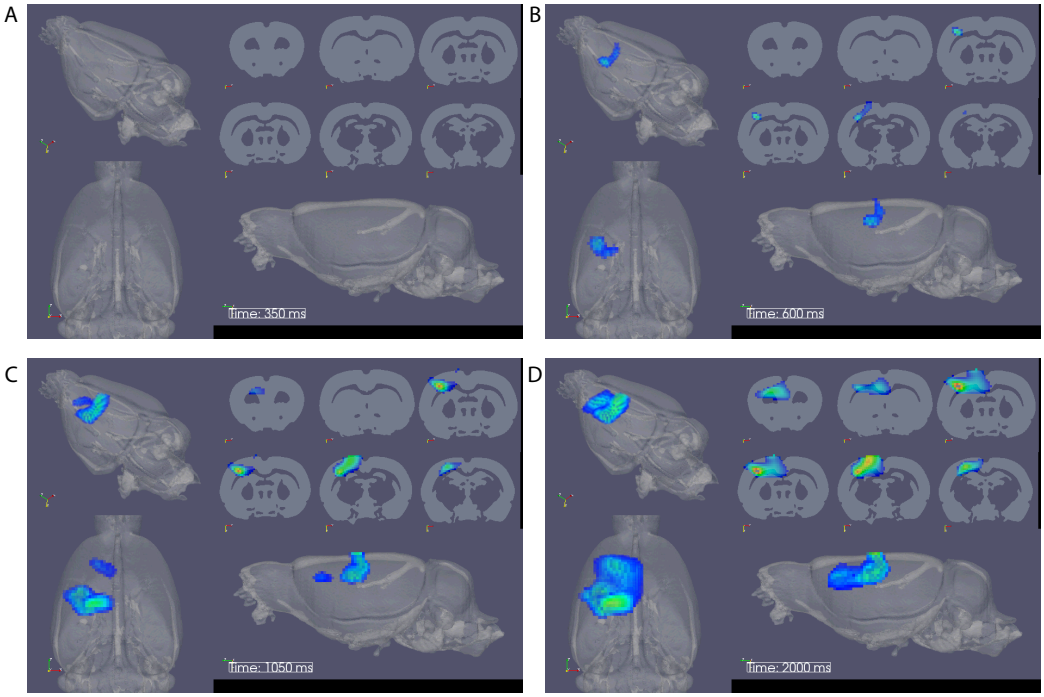

Figure 7.3.: Reconstructed mean seizure spread after injection of 4-AP in the cortex at four different time points (A) 350 ms; (B) 600 ms; (C) 1050 ms and (D) 2000 ms.

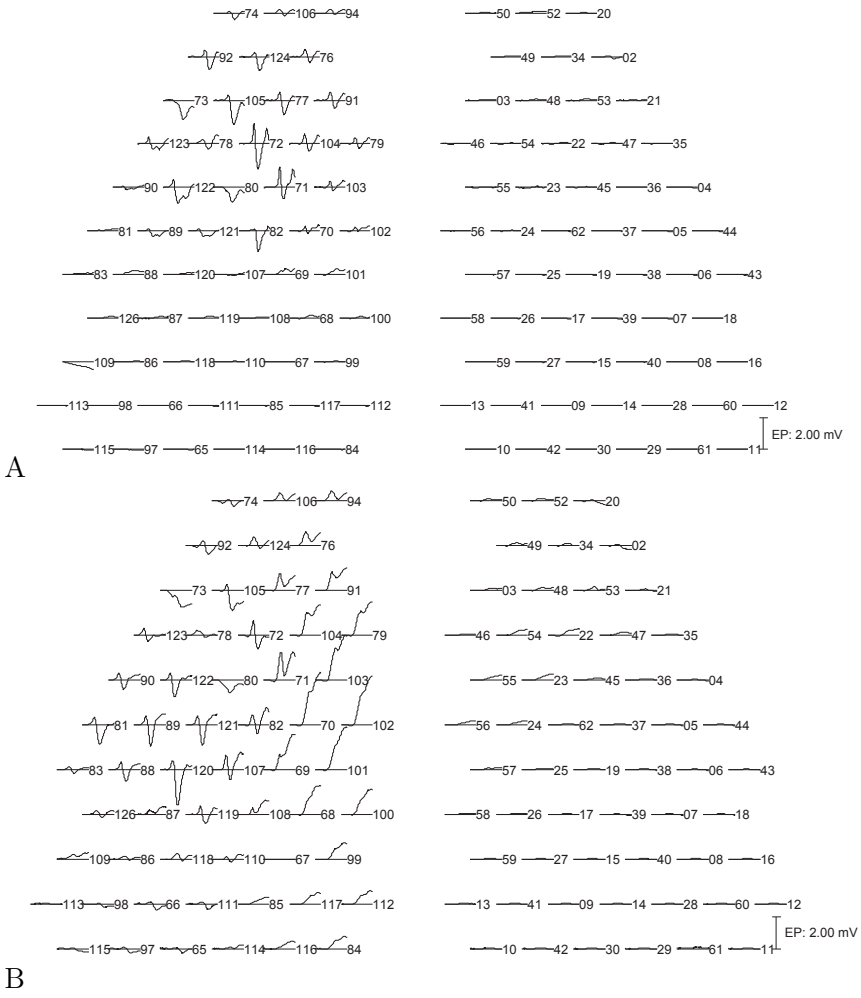

Figure 7.4.: Two example IIS recorded from a cortical epilepsy focus. Each horizontal bar represents one electrode. IIS in (A) and (B) are 20 min apart and a change in the spiking pattern is seen.

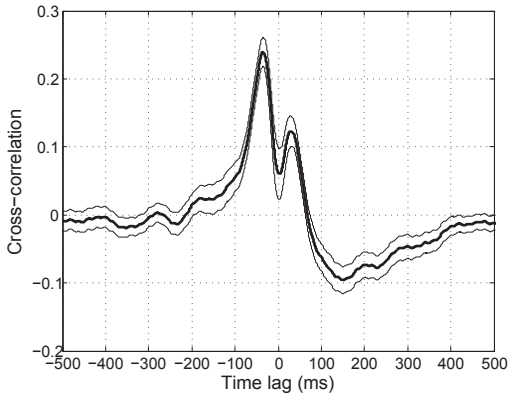

Figure 7.5.: Cross correlation between the cortical EEG and the LFP measured in the hippocampus in the time around the seizure start. The largest peak is at -34 ms indicating a time lag of 34 ms of the cortical activity behind the hippocampal activity.

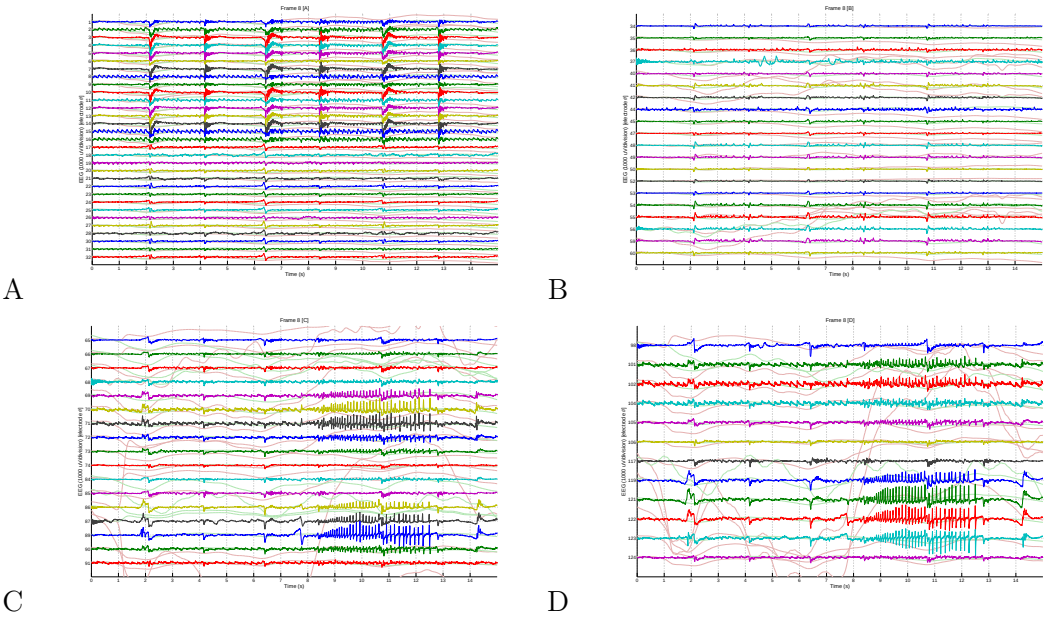

Figure 7.6.: Example of raw recorded data. Solid colours are the EEG frame in the hippocampal seizure model; the dZ values are plotted on top of each EEG channel. (A) Depth electrodes: Channel 1-16 left hippocampus and 17-32 right hippocampus. (B) Electrodes on the right hemisphere; (C) and (D) electrodes on the left hemisphere. Noisy channels were excluded.

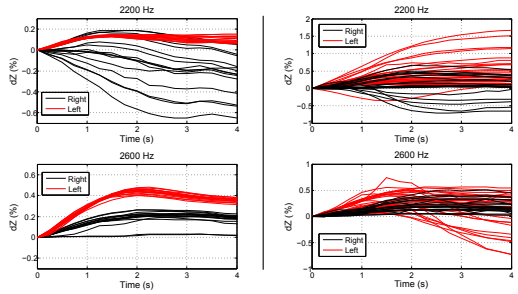

Figure 7.7.: dZ changes in the hippocampal epilepsy model measured on the depth electrode (left) and on the cortical electrodes (right) at 2.2 kHz and at 2.6 kHz. Right and left refers to the site of the electrode placement.

which spread to the cortex (see figure 7.6 for an example). For the cortical electrode the dZ measurements were 0.02-6.28% for 2.2 kHz and 0.07-3.91% for 2.6 kHz (compare figure 7.7), comparable to in chapter 6. No fast neural component could be measured due to the lack of a precise trigger in the 4-AP seizures.The measured impedance changes on the depth electrodes during seizures were 0.03 - 0.99% for the 2.2 kHz current injection and for the 2.6 kHz injection the impedance changes were 0.06 - 1.37%, measured on all channels on the side of 4-AP injection. The impedance changes were reconstructed for each seizure. The mean of the reconstructed images (n=209 seizures) at the 0.5 s time point in one rat was AP -2.95 mm, ML 3.75 and depth 3.75 mm (see figure 7.8), which corresponds the lateral edge of the hippocampus. The reconstructed starting points of each seizure cluster around their average location (figure 7.9).

7.4. Discussion

In this chapter, a novel set-up for EIT imaging of epileptic seizures throughout the brain has been tested. Two different kinds of epileptic models were used for this purpose: a cortical and a hippocampal model of epilepsy. In the cortical model activity started from, and spread through the cortex of two rats. Due to missing cross-validation, it is unclear whether activity spread to subcortical structures at all, or whether it was not possible to image an occurring spread of activity to subcortical structures. To circumvent this problem, an epileptic focus in the hippocampus has been set and depth electrodes were inserted in the site of 4-AP injection into the hippocampus as well as in the contralateral hippocampus. This novel set-up allowed for both validation of the reconstructed activity and measurements of dZ locally. With the LFPs, it could be confirmed that spiking occurred in the hippocampus, which lead to seizures on the cortex on the left side with a time difference of 34 ms. The impedance measurements on the hippocampal epilepsy model were plagued by technical difficulties but the usable data from these experiments showed

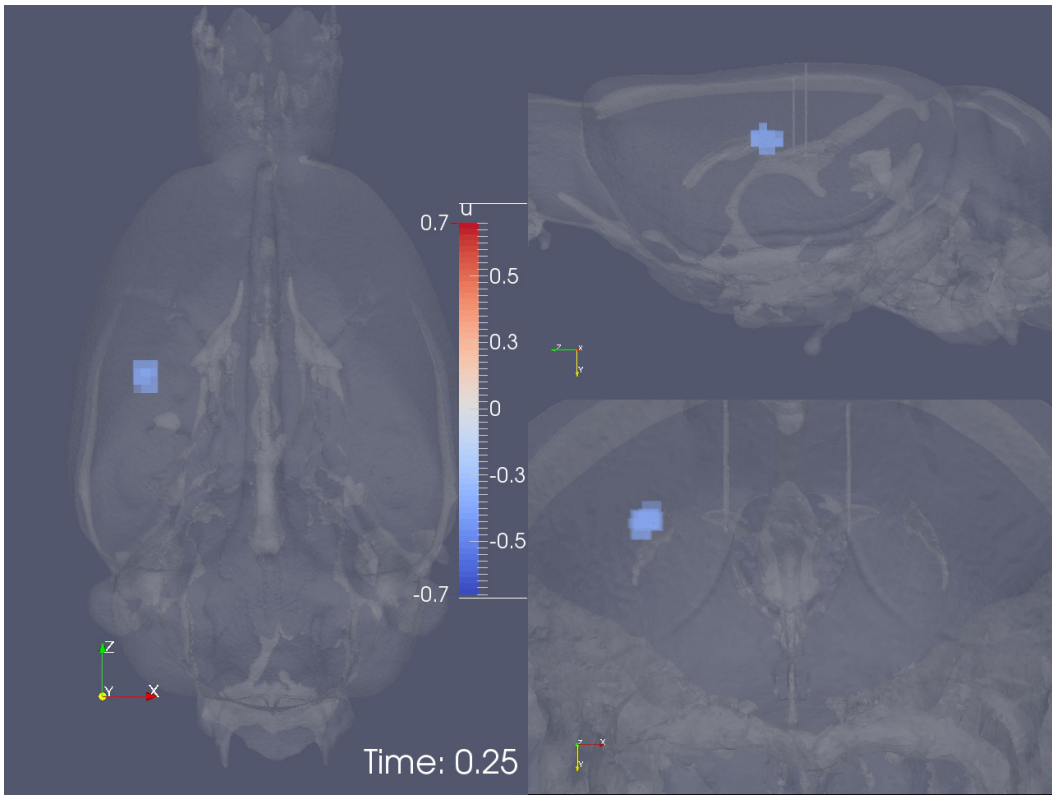

Figure 7.8.: The average of the reconstructed seizure foci in the hippocampal seizure model. The colour bar shows the dZ in (%).

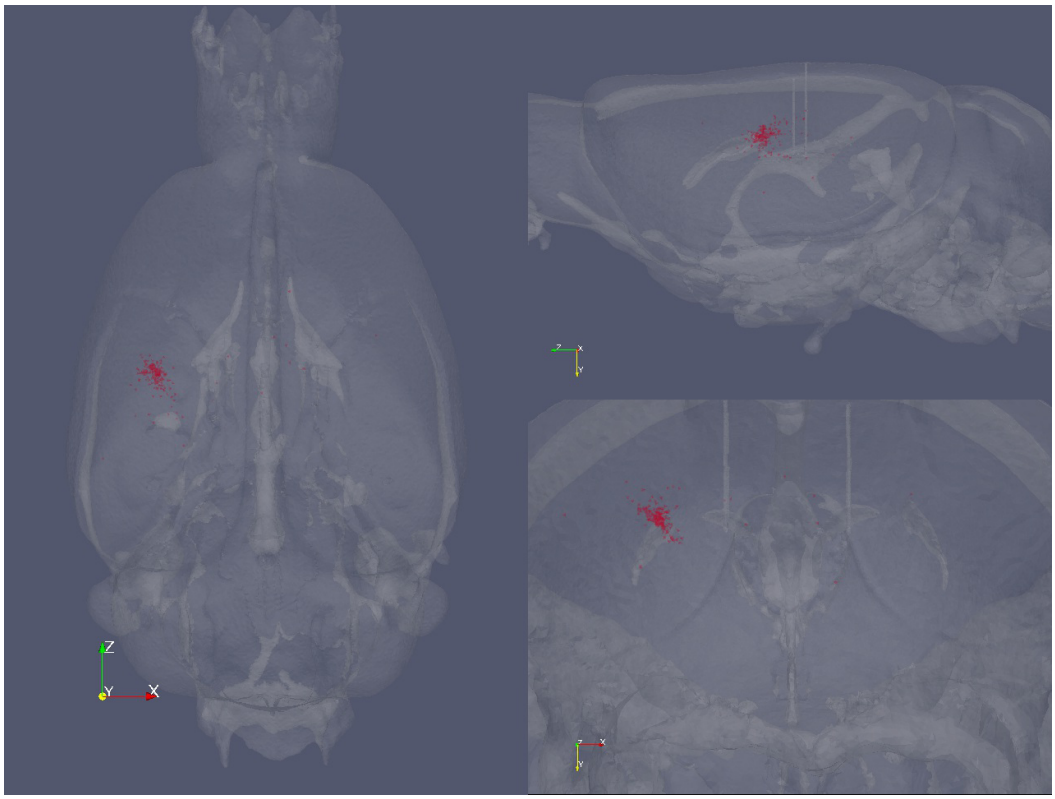

Figure 7.9.: Reconstructed centre of mass of each individual reconstructed seizure in the hippocampal model.

some promise. Firstly, the locally measured impedance changes during seizures in the hippocampus reached more than 1%, which should allow imaging, according to our modelling from chapter 5. Secondly, the impedance recordings could be reconstructed showing foci in the subcortical area but errors in the localization occurred. The reconstructed focus was 0.8 mm further rostral and 1.95 mm further lateral than the set focus. This localization error might have occurred due to the inaccuracy of the electrode localization on the mesh compared to the brain. Due to the size of the electrode arrays it was assumed that most of the cortex was covered and the electrodes were placed on the mesh for the forward solution accordingly. As no method to localize the electrodes in 3D (such as micro-CT) was employed, these locations might have been inaccurate. Further errors might have been introduced due to errors in the mesh and the use of a standardized rat mesh, which does not take individual anatomy into account. To produce individual meshes a high resolution CT or MRI scan would have been necessary from each rat. Manipulation on the electrodes, to allow injection of 4-AP through the mesh into the hippocampus, might have contributed to the localization error. Unfortunately, the purpose made current source failed to produce constant current so that only two of the four current injection pairs were usable in parallel for the hippocampal epilepsy recordings. This might have reduced the accuracy of the image reconstruction further as each current injection pair will bias the reconstructed focus according to its current path.

7.5. Conclusion and future work

The focus of seizures in a hippocampal epilepsy model has been imaged successfully in whole brain measurements in a rat. Due to lack of time these recordings were not reproduced in further rats. In future studies it would be of paramount importance to localize the electrodes reliably and to test whether individual meshes should be produced for each rat tested. The localization error in localizing epileptic foci could then be reassessed. Furthermore, more than two parallel current injections should be used, to allow to image individual seizures reliably.

8. Summary and future work

8.1. Imaging fast neural activity with EIT

It was possible to use the fast neural signal to image neuronal activity in the cortex. In contrast, the size of the fast neural signal in the thalamus was too small to allow imaging of activity in the deep structures. The SNR of EIT imaging was improved significantly by increasing the carrier frequency of the EIT measurements. Previous modelling had led to the assumption that higher carrier frequencies would lead to a decrease in SNR in EIT, which has been disproven in this work. The results of this work highlight the need for a full biophysical model which includes several cell types with active channels and which explains the path of the current in the tissue. This could be used to evaluate the contribution of the different cell types in the generation of the impedance signal. This modelling can be validated experimentally in slices preparations using genetically modified rats, in which different cell types are selectively activated. If interneurons are confirmed to play a disproportionately large role in the generation of the dZ signal, then the lack of dZ signal in our recordings would have been due to the use of the rodent model (rats lack interneurons in their thalamus), and consequently 3D imaging of fast neural activity may be possible in primates. Should, however, results from slice preparations and biophysical modelling show that the interneurons only play a minimal role in the generation of the fast neural signal then it has to be asumed that a substantial cell densitiy of neurons firing synchronously is needed. This would make 3D imaging of the fast neural signal more difficult as it would miss out on activity of the subcortical relay stations such as the thalamus and other subcortical nuclei. Even if the neuronal activity that can be imaged with fast neural EIT is limited to the cortex then there is still the added advantage of EIT being independent on the dipole orientation in the cortex. This makes little difference to EEG recordings in rodents as their cortex is not gyrated. However, EIT could yield additional information about the course of activity in gyrated cortices such as in primates, including humans. It could, for example, be used to map the path of epileptic activity on the ECoG more clearly. If EIT is proved safe to use, and any possible damage to human cortices resulting from EIT may be ruled out, then human experiements may be conducted. Damage to the cortex due to the current injection is less likely with higher carrier frequencies than with the very low frequencies of around 250 Hz that have been used in the past. The improvement in SNR with the use of higher frequencies has been shown in chapter 3 and has the positive side-effect of being safer.

Possible damage to the cortex could stem from one of three possible sources:

1. Brief DC discharges during the switching of the current injection electrodes as DC current can alter neuronal activity at much smaller current amplitudes compared to AC current.

2. Charge transfer across electrode-tissue interface causing electrochemically produced toxic changes such as pH alterations, chloride oxidation, oxidation of organics etc. or electrode dissolution products (soluble salts of metals).

3. Passage of current through tissue causing neuronal hyperactivity or changes in membrane potentials, power dissipation (tissue heating) or electropoation and cell destruction due to dielectric forces excerted.

Most of these possible sources of damage can be circumvented if the recording parameters are chosen according to safety concerns and the effect of the remaining concerns should be tested in animal models before human studies are conducted. The DC discharge during the switching of the current injection pairs could be avoided by using parallel current sources instead of switching current sources. Electrode dissolution products could be avoided by using platinum instead of stainless steel electrodes in human subjects. The effect of possible electrochemically produced products would have to be tested by continuous current application to the cortex of an animal and subsequent histology to assess any possible damage due to the current. Changes in the activity in the cortex due to current injection has not been seen in any of our experiemnts and should not play a major role provided the currents are kept at a amplitude and a frequency away from the EEG band. Tissue heating should not play any role as long as carrier frequencies are kept below radiofrequency. Electropoation and cell distruction is also only a problem if AC current of very high frequencies of 5 kHz and above with rather large amplitudes (several volts) are used.

In summary, if the recording parameters are set correctly, with carrier frequencies of above 1.5 kHz but below 3 kHz with a small cuurent amplitude below 100 μA, then EIT should be very safe. Changes to the neuronal activity has not been seen in any of the recordings conducted in this thesis. Safety experiments in animals should be conducted to test whether toxins that might potentially be produced electrochemically play a significant role. If the safety of EIT is fully proven then human fast neural experiments may be conducted on epilepsy patients during presurgical evaluation using ECoG electrodes.

8.2. Further work on the resonance effect

In our work we showed that using a carrier frequency of ~600 Hz during evoked forepaw activity leads to a resonace effect presumably on the interneurons involved. The source of this effect would need some further evaluation for example with slice preparations and biophysical modelling as discussed above. If the resonance effect is due to interneuronal activity, however, then it could be used to image certain cells such as the interneurons selectively during activity. Interneuronal activity is difficult to grasp on EEG due to their dipole orientation, which makes the role they play, in epilepsy for example, difficult to assess. A frequency sweep during interictal spikes or seizures could potentially show some resonance effect reflecting the interneuronal acitivity during epileptic activity. If resonance effects are shown in the frequency sweep then these frequencies could be chosen for selective imaging and foci of interneuronal activity could be found. There is a chance that the application of a resonant frequency alters the activity in the epileptic focus which may alter

the results. However, it would still be a major advance to learn more about the relationship of the pyramidal and interneuronal fireing in an epileptic focus if the epileptic activity remains unchanged.

8.3. Imaging epilepsy using EIT

The impedance response of neuronal tissue to epileptiform activity has been characterized in this work. A stereotypical response was found in response to IIS and seizures, which was consistent across three different rat seizure models. The impedance response consisted of a fast neural component during IIS followed by a slow impedance rise. It was concluded that the fast neural component in response to the IIS has the same physiological basis as the fast neural component in measurements of evoked activity. The slow rise in impedance, however, is specific to epilepsy and is due to cell swelling. This cell swelling does occur faster than described previously, and reaches significant values at ~50 ms. The increase in impedance following IIS and seizures is large enough to be imaged from subcortical structures. A local rise of impedance in an hippocampal epileptic focus has been confirmed experimentally. It was possible to image the epileptic focus in the hippocampus despite only being able to use two of the four desired current sources. Errors in localization of the focus did occur and suggestions to improve the spatial accuracy in future experiments have been made. Due to lack of time, only one successful experiment imaging a hippocampal epileptic focus was conducted. However, the results of this experiment were very promising, and a full study should be conducted. This study should include a full set of paralell current sources to compensate the lack a priori knowledge on where the epileptic activity will occur primarily in future human work. This would allow unprecedented detail and real time imaging and also prove the usefulness for human imaging. To localize the electrodes micro-CT scans could be conducted at the end of the experiments. This would minimize localization error due to uncertainty of the electrode localization and hence of the recorded foci. This is of paricular importance as the epileptic focus in these experiments was set using stereotactic coordinates while the electrodes were matched on the mesh mainly my matching the expected and measured voltages in software. This could have lead to a substantial localization error. Tests on whether the impedance signal behaves the same way in humans should be conducted if a full 3D EIT study of imaging epileptic foci proves successful.

A. Material considerations for EIT electrodes

A.1. Introduction

A.1.1. General requirements for subdural EIT-electrodes

There are a number of aspects that we should take into account when designing an electrode for EIT-measurements on the rat cortex. The electrode should avoid damage of the neural tissue but provide good contact. The electrode should therefore be very flexible to allow good contact between electrode array and the brain without causing neuronal damage. We are intending to design sliding electrodes eventually that will cover most of the brain. For the planned 3D project we should find a backing material that can be slid easily without kinking. In order to improve our signal-to-noise ratio the conductive material needs to produce as little noise as possible and have low contact impedance. When deciding about the size of the contact are we should take two considerations into account. We should consider that the larger the surface is the more current can be injected as the relative current density decreases with size. On the other hand the resolution decreases due to shunting effects with larger electrode areas (Oh et al. [2011a]). When measuring with an electrode array we should also consider that the distance between the contact points determines the depth to which measurements can be undertaken. The measurable depth equals twice the distance between the contact points of the array (Barber et al. [1984]). This poses another restriction on how large the contacts can be and it also means that we should keep the distance between all neighbouring contact points the same to allow measurements over the same depth throughout the array. When it comes to the tract width we have to consider that the resistance of the tracts depends on the resistivity of the material p as well as the length l and the diameter of the tracts:

$$R = p * \frac{l}{s} \tag{A.1}$$

We therefore have to find a tract width that allows a small enough electrode array and does not interfere with the flexibility of the array whilst not posing too much resistance.

A.1.2. Intended recording application

We are planning to undertake two different types of recordings.

A.1.2.1. Planar array measurements

In the first instance we will measure with a planar array where current is injected between two neighbouring electrodes and the remaining electrodes of the array are used to measure the voltage. This provides us with measurements of fast neural activity directly under the array down to a depth of 2.4 mm. We performed these measurements with 29 channels and 225 Hz to then progress higher frequencies. We performed these measurements with the electrode seen in figure A.1, but started work on the development of in-house produced arrays as well.

A.1.2.2. Whole brain measurements

In the second setting we will inject current between two opposing electrodes and use the remaining electrodes to measure the voltage. This setting will provide us with measurements of fast neural activity in the entire area of the brain covered and include deep structures. We are intending to use 128 channels for this set-up.

A.1.3. Previous EIT array electrodes

There have been various designs for electrodes for EIT measurements from this group. One of the past methods used was an electrodes made from silver wire in an araldite block. This electrode however proved to be too stiff and caused bleeding and neuronal damage. The next method tried where wires in which the tip was burned into a ball and that where arranged in glass capillaries to be able to slide cite Anthony's thesis. Unfortunately this electrode was too heavy and again caused bleeding and neuronal damage. The next approach used was done in collaboration with a group in Freiburg, Germany. This electrode consisted of an electrode array with electrode contacts, a flat ribbon cable connected to the electrodes and a contact area (Schuettler et al. [2008]). The electrode was fabricated in platinum-in-silicone technology which means that a patterned layer of platinum (12.5 µm thickness) was sandwiched between two layers of silicone rubber. The design of the electrode array is shown in Fig. 1. The electrode sites had a diameter of 0.6 mm and were hexagonally arranged at a 1.2 mm centre-to-centre distance. The 29 tracks in the ribbon cable were 25 µm wide. A 75 µm gap separated adjacent tracks. The tracks end was soldered to a ZIF-connector (Schuettler et al. [2008]). Our experience with this electrode was quite positive. The only drawback was that the tracts commonly broke on the transition between connector pad and ribbon cable.

A.2. Materials

A.2.1. Conductive Materials

A.2.1.1. General considerations

The conductive material within the electrode will provide the direct interface between the EIT-device and the brain. It will be in contact with electrolytes in solution so that an electrode-electrolyte interface will occur (Webster and Clark [1995]). When the electrode is brought into the electrolyte solution oxidization (and reduction) reactions will ensue and a half-cell potential will occur. This means that the there is a different potential in the solution surrounding the metal compared to the rest of the solution. The value of this potential is dependent on the metal as well as the concentration of electrolytes. It is desirable to have a low and stable half-cell potential in a biological measurement electrode (Webster and Clark [1995]). Furthermore the electrode should be non-polarizable. Perfectly polarizable electrodes are those in which no actual charge crosses the electrode-electrolyte interface when

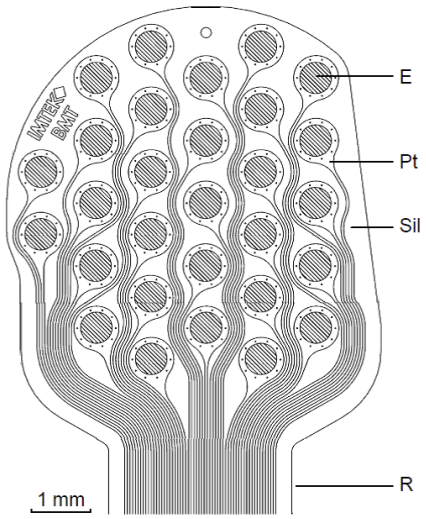

Figure A.1.: Design of electrode array (Schuettler et al. [2008]), E:electrode site, Sil: Silicon rubber, R: ribbon cable

current is applied, they behave as a capacitor and only displacement current occurs. Perfectly non-polarizable electrodes are those in which current passes freely requiring no energy to make the transition (Webster and Clark [1995]).

A.2.1.2. Material Choice

The two noble materials that have particular desirably properties for our purpose are silver and platinum. Both can be treated to decrease their impedance, their polarizability and to provide low and stable half-cell potentials. Silver can be coated with silver chloride which brings the electrode very close to a perfectly non-polarizable state. Silver/silver-chloride electrodes have a very low impedance and low stable half-cell potentials (Webster and Clark [1995]). These features make silver/silver-chloride electrodes the ideal electrode for scalp recordings. Silver is however neurotoxic which limits its use for subdural recordings (Stensaas and Stensaas [1978]). Whether or whether not this excludes silver electrodes from use for our purposes is arguable since our experiments are terminal. The other noble material with very desirable features is platinum. Platinum electrodes can be platinized (coated with platinum black) which increase its surface area and hence lowers its contact impedance greatly. Platinum is biocompatible and unlike silver it is not neurotoxic (Stensaas and Stensaas [1978]). Platinum is therefore a commonly used metal for long-term nervous interface implants.

A.2.2. Base Materials

The following is a review of the literature that describes the production and the base materials of the flexible microelectrodes used for neural recordings. There are three different types of base materials that have been successfully used to produce microelectrodes. All three of them are polymers and can be spun to be formed. They do however differ in their density, their Young's modulus and their tensile strength. The substance that is used for the longest time is silicone which has been used for a wide range of implants since the 1960's (Schuettler et al. [2007]). The other two polymers that have been used for neural electrodes are polyimide and parylene (Rodger et al. [2008], Stieglitz et al. [2011]). There also have been groups that reported good results with a combination of silicone with polyimide (Kim et al. [2009]) and polyimide with parylene (Feili et al. [2006]).

	Polyimide[a]	Parylene C	Silicone[b]
Possible thickness (µm)	1-15	1-100	10-100 for spin coating
Young's modulus (MPa)	845	2756	0.8
Tensile strength (MPa)	392	69	6.2x10-6
Elongation (percent)	30	200	600

Table A.1.: Properties of Polymers, (a = UBE U-Varnish-S, b = NuSil Med-100), sources: (Hassler et al. [2011], Schuettler et al. [2009])

A.2.2.1. Silicone

Silicone has been in use for implantable devices for a long time. Silicone rubber is a rubber-like material composed of silicon - itself a polymer - together with carbon, hydrogen, and oxygen. It has excellent biocompatibility (Roggendorf [1976], Stensaas and Stensaas [1978]). It is easily available, relatively low cost and can be easily moulded or spun. The main advantage of silicone is its superior flexibility; it has a Young's modulus of 0.8 MPa and forms no sharp edges. It does however have very low tensile strength (6.2x10-6MPa) and therefore breakage of imbedded metal tracts can pose a significant problem (Schuettler et al. [2009]). Some groups therefore reinforce their silicone electrodes with polyester fibre meshes to improve the tensile strength of the electrode (Bhadra et al. [2001]), sputter metal onto stretched silicone or implement woven tracts (Schuettler et al. [2009]). A further difficulty with silicone based electrodes is that connection to the cables of the EIT machine can pose a problem. Due to the softness of the material there will be a transition of a metal tract embedded in a flexible material to a rigid connector-board. The connection between these two often poses a problem and breakage of the tracts on the transition from soft to hard material occurs often. Conductive metals can be bonded onto spun silicone by pressing a piece of metal foil onto the freshly cured material. Alternatively metal can be sputtered onto silicone. The metal on sili-

cone can then be laser ablated or dry etched with finer pattern size of dry etching (Schuettler et al. [2007]).

A.2.2.2. Polyimide

Polyimide is a polymer of imide monomers. Thermosetting polyimides are known for their good thermal stability, chemical resistance and mechanical properties. It has a characteristic yellow/orange colour. For example UBE U-Varnish Polyimde has a Young's modulus of 845 MPa and a tensile strength of 392 MPa (Table 1). Polyimide got a bad reputation in the early years due to a short life-time in vivo and fast degradation and failure. Nowadays, polyimides have different chemical structures and promise high stability, low water uptake and a long life-time. Polyimide has a good biocompatibility with even less formation of fibrous tissue when implanted for 6 months than silicone (Stieglitz et al. [2011]). Metal can be sputtered onto it. Unfortunately the desirable tensile strength of Polyimide (see Table 1) is countered by a very high Young's modulus. Polyimide can therefore only be used for micro-electrodes if it is extremely thin. We found a sample electrode with a total thickness of 12 µm to be potentially useful but perceived a sample foil of 30µm as not flexible enough for implantation. Most polyimide-based electrodes described in the literature are around 10µm thick in total (Cheung et al. [2007], Stieglitz et al. [2000]). As we are looking at designing sliding electrodes on the longer term we see the problem of polyimide not having the strength to be slid when it is thin enough to be flexible. However Polyimide can be bonded to silicone if it is treated appropriately e.g. oxygen plasma treatment (Kim et al. [2009]). Polyimide can be spun or purchased as sheets. One of the advantages of using polyimide as well as Parylene as a base material in electrodes is the ease forming tracts on them by the means of chemical etching processes and photolithography. This makes micromachining for their production fairly easy and allows a very small feature size (10µm) (Stieglitz et al. [2011]). This process proved unsatisfactory in silicone (Schuettler et al. [2007]).

A.2.2.3. Parylene

Parylene is the trade name of poly(p-xylyene) polymer. It is self-initiated and un-terminated with no solvent or catalyst required and it can be vapor deposited (Rodger et al. [2008]). It has often been used to increase biocompatibility of polyimide (Feili et al. [2006]) but has also been used as the sole base material (Rodger et al. [2008]). Metal can then be sputtered onto it. It has a good tensile strength of 69 MPa (Parylene Properties, 2010) (see table 1). It is moderately flexible (2756 MPa), keeping its shape very well in its final form (high conformality), having a low water permeability and being highly biocompatible (Rodger et al. [2008]). In fact its insulation properties are so superior that it has been used to coat devices for insulation of implanted devices (Pang et al. [2005], **?**). Unlike Silicone it does not hydrate over time and it can also be vaporized onto silicone directly (Pang et al.

[2005]). It can be processed at room temperature and can be heat moulded after that (Rodger et al. [2008]). However a high temperature stable version of Parylene is available (Parylene HT instead of Parylene C). If layers of parylene need bonding then it needs annealing in vacuum (Rodger et al. [2008]).

A.2.3. Conclusion and Summary

Each of the discussed materials has its advantages and its disadvantages but all of them have been used by other groups successfully. I believe that a combination of materials i.e very thin polyimide combined with a layer of silicone would be desirable for the design of sliding electrode. For the short term our collaborators in Freiburg, Germany will produce more of the previously used planar arrays for us but coat them with parylene on the back to avoid tract breakage (Schuettler et al. [2008]). To provide planar arrays for the longer term an array similar to the Schuettler array would be favorable, we hope to get an array made with a similar design but with stainless steel instead of plantinum to avoid tract breackage, the contacts could be metalized with platinum. The stainless steel in silicone electrode arrays will be produced by Elliot Magee in the implanted devices group of UCL. Within our group Mohammed Koronfel will take on the part of desinging microelectrodes on polyimide basis.

B. Design of a laryngoscopic blade for intubation of rats

B.1. Introduction

B.1.1. Orienting paragraph

In our protocols we initially were performing tracheostomies on the rats to ensure safe ventilation during experiments which might last >10 h. This practice is invasive and can cause unnecessary blood loss. Intubation of the rats would be preferable but no laryngoscope is commercially available for rats. To address this issue a laryngoscope blade has been designed and produced by 3D printing.

B.1.2. Background

B.1.2.1. Intubation

Endotracheal intubation in rats is commonly needed to secure the airway in biomedical experiments that require deep anaesthesia with or without neuromuscular blocking agents. Alternatively, a tracheotomy can be performed, if the experiment is terminal, but should not be used in recovery experiments as wound infections, pneumonia and tracheal stenosis can occur. Endotracheal intubation in rodents poses a challenge to the experimenter due to the anatomy of their pharynx, with its large tongue, small larynx and trachea and a relatively long distance from the incisor teeth to the trachea. Previously published methods for intubating rodents include blind intubation (Stark et al. [1981]), paediatric laryngoscopes (Schaefer et al. [1984]), spatulas (Remie et al. [1990]), modified nasal specula (Proctor and Fernando [1973]), otoscopes (Weksler et al. [1994]) and transillumination (Cambron et al. [1995], Yasaki and Dyck [1991]). Designs of laryngoscopes specifically for rats have been presented (Linden et al. [2000], Molthen [2006]); however, most of these are not commercially available and require the experimenter to manufacture the item themselves. The advantage of using a tilt table for intubation of rodents has been presented in the past (Kastl [2004], Molthen [2006]); but again these are not commercially available.

B.1.2.2. 3D-printing

3D printing is a process of making a three-dimensional solid object from a digital model. This is achieved by an additive process; where successive layers of material are laid down to form the desired shape. In the process used here the 3D printer deposited melted plastic in layers to form the laryngoscope. We used uncoloured polyactide (PLA) filament for our design to avoid possible toxicity from added colouring. PLA is a biocompatible transparent plastic produced from corn or dextrose which generally recognized as safe for food contact (Conn et al. [1995]) and is used in the medical field for suture material (Athanasiou et al. [1996]), drug delivery (Dorj et al. [2013]) and as an implantable scaffolding in regenerative medicine (Charles-Harris et al. [2008], Athanasiou et al. [1996]).

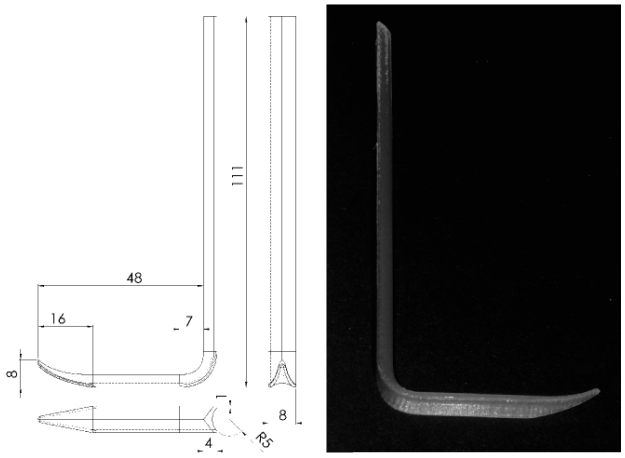

Figure B.1.: Laryngoscope blade, left: drawing, all measurements are in millimetres; R5 = radius 5 mm; right: photograph of finished product.

B.2. Methods

B.2.1. Laryngoscope

B.2.1.1. Design

The laryngoscope blade is 8 mm wide and has an angled shaft of 16 mm length. The total length of the blade is 48 mm and the handle is 111 mm long (see figure B.1). The laryngoscope was printed using a Makerbot Replicator 2 3D-printer with uncoloured polylactide (PLA) filament (both Makerbot Industries LLC, NY, USA). Printing was accomplished in 10 minutes; the material cost for each laryngoscope was approximately 7 pence. The laryngoscope was inspected for any sharp edges and these were rounded with sanding paper where required.

B.2.1.2. Testing of chemical resistance of the laryngoscope blade

We tested the chemical resistance of PLA in ethanol (AnalR Normapur, VWR International, France) for 12 hours and in sodium hypochlorite (Sigma Aldrich Company Ltd, UK) 2.3% (equals 1/2.5 of 5.25% bleach) for 20 min for n = 5 samples.

B.2.2. Design tilt-table

The tilt table was constructed of 1 cm thick cut-to-size sheets of acrylic. It was designed to support adult rats (300-400 g) and to tilt them by 45°. A wire attached to a velcro pad was attached to the front end to hook under their front teeth. The measurements for the tilt table can be seen in figure B.2.

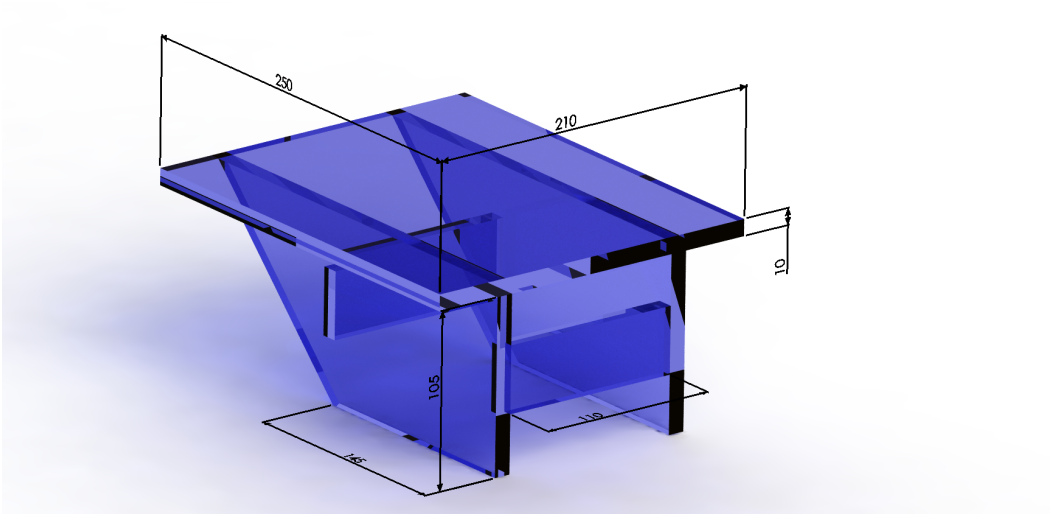

Figure B.2.: Tilt table, all measurements in millimetres; the table presented here was constructed from cut-size sheets of acrylic of 1 cm thickness. A wire loop was attached to the top end of the table to allow the rat to be kept in position by hooking the loop under its incisor teeth. The loop was fixed to the table with Velcro.

B.2.3. Animals

All the animals in which the laryngoscope and tilt-table was tested were used for other studies. The rats used for the assessment of this system are described in chapter 6.

B.2.4. Intubation procedure

The rats were induced in an induction box using 5% isoflurane in 100% oxygen. Once unconscious they were moved onto a nose cone and, once their breathing had slowed to ~30 breaths per minute, were moved into supine position on a tilt table (figure 2). A wire loop was hooked under the superior incisors of the rat which was then attached to the top end of the tilt table using Velcro pads. The table was then tilted and the tongue was grasped with a non-toothed forceps and pulled to one side of the incisor teeth. The laryngoscope was introduced with the acute angle rostral, and the vocal cords were visualised by pointing the angled tip slightly upwards; lighting was provided with a LED headlight. It was only necessary to introduce the first 2 cm or so of the laryngoscope presented here; the remaining shaft was used for grasping and manipulation. The pharynx was then sprayed with lidocaine hydrochloride (Intubeaze, Dechra Pharmaceuticals, UK) to desensitize the vocal cords and prevent laryngospasm. A soft stainless steel wire, which had been removed from a 14 G human central venous catheter set (Leader-Cath, Laboratoires

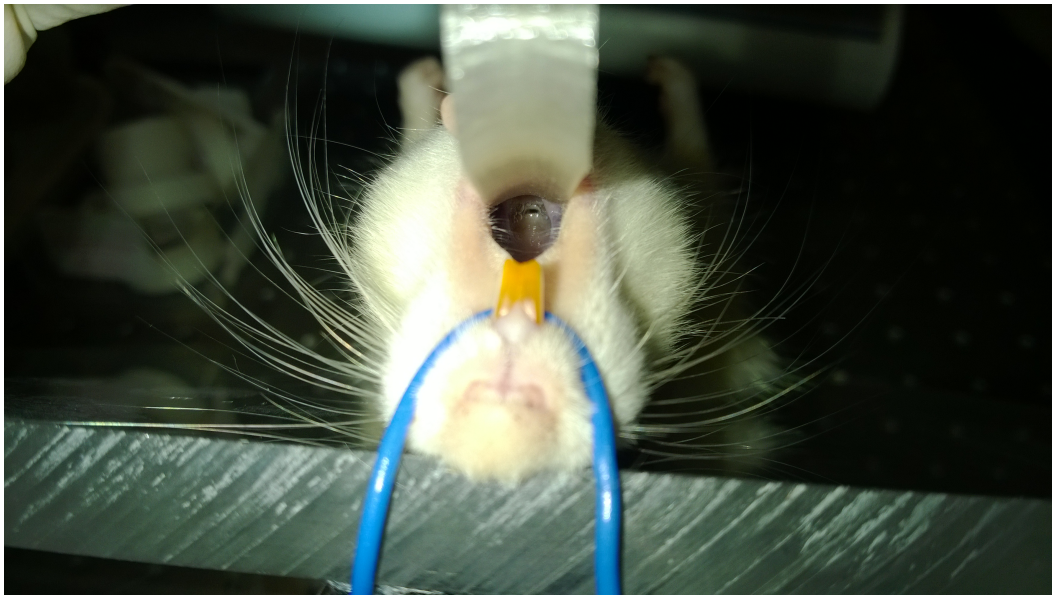

Figure B.3.: Photograph of a rat positioned on the tilt table with the laryngoscopic blade inserted.

pharmaceutiques Vygon, France), was passed through a 14 G straight intravenous cannula measuring 51 mm in length (Abbocath-T, Hospira, Ireland). The wire was introduced through the vocal cords into the trachea under vision and the cannula was pushed over the guide wire. The wire was subsequently removed. Endotracheal placement was confirmed by condensation on a dental mirror held in close proximity of the tracheal tube. Ventilation was started using a Harvard Apparatus Inspira Ventilator (Harvard Apparatus Ltd., UK).

B.3. Results

It was possible to perform the intubation in approximately 3 min in all rats. No oesophageal intubations occurred in any of the 35 intubations, no other ventilatory difficulties occurred in the recordings lasting between 6-10 hours. A single printed laryngoscope could be used in all the intubations. No ventilatory difficulties occurred during the experiments lasting up to 10 hours following the intubation. The intubation allowed stable anaesthesia for craniotomy and electrode placement, as well as subsequent imaging of epileptic seizures. . No obvious damage to the plastic occurred after 12 hours of soaking the item in ethanol or 20 minutes in 2.3% sodium hypochlorite.

B.4. Discussion

The laryngoscope presented here is stable enough to be used multiple times and withstood disinfection with ethanol and sodium hypochlorite. Alternatively, sterilization of PLA based implants using ethylene dioxide has been described previously and could be used in experiments requiring a higher standard of disinfection (Athanasiou et al. [1996]). 3D printing allowed us to design and produce small items according to our individual need at a low cost and with a quick turn-over, the advantage is multiplied if the design is subsequently made available to the bio-scientific community. This has been done by publishing both the design and the description of the laryngoscope and tilt table. The laryngoscope has been used for intubation of all animals in chapters including animal work apart from chapter 2 and 3.

Bibliography

Juan-Felipe P J Abascal, Simon R Arridge, Richard H Bayford, and David S Holder. Comparison of methods for optimal choice of the regularization parameter for linear electrical impedance tomography of brain function. *Physiological measurement*, 29(11):1319–34, November 2008. ISSN 0967-3334. doi: 10.1088/0967-3334/29/11/007. URL http://www.ncbi.nlm.nih.gov/pubmed/18854604.

David J. Aidley. *The physiology of excitable cells*. Cambridge University Press, 1998. ISBN 0521574218. URL http://books.google.com/books?id=3JgC_rE8ZVwC&pgis=1.

T Allison, G McCarthy, C C Wood, P D Williamson, D D Spencer, and T M Darcey. Human cortical potentials evoked by stimulation of the median nerve. I. Cytoarchitectonic areas generating short-latency activity. *Journal of neurophysiology*, 62(3):694–710, September 1989. ISSN 0022-3077. URL http://www.ncbi.nlm.nih.gov/pubmed/2769354 http://www.ncbi.nlm.nih.gov/pubmed/2769355.

David Alter and Texas Instrumens. Using PWM Output as a Digital-to-Analog Converter on a TMS320F280x Digital Signal Controller. Technical report, 2008.

Tamas D Ambrisko, Craig B Johnson, and Paul Chambers. Effect of alfaxalone infusion on the electroencephalogram of dogs anaesthetized with halothane. *Veterinary anaesthesia and analgesia*, 38(6):529–35, November 2011. ISSN 1467-2995. doi: 10.1111/j.1467-2995.2011.00650.x. URL http://www.ncbi.nlm.nih.gov/pubmed/21988807.

Costas Anastassiou, Sean M Montgomery, Mauricio Barahona, György Buzsáki, and Christof Koch. The effect of spatially inhomogeneous extracellular electric fields on neurons. *The Journal of neuroscience : the official journal of the Society for Neuroscience*, 30(5):1925–36, February 2010. ISSN 1529-2401. doi: 10.1523/JNEUROSCI.3635-09.2010. URL http://www.ncbi.nlm.nih.gov/pubmed/20130201.

a Angel. Central neuronal pathways and the process of anaesthesia. *British journal of anaesthesia*, 71(1):148–63, July 1993. ISSN 0007-0912. URL http://www.ncbi.nlm.nih.gov/pubmed/8102065.

Kirill Y Aristovich, Gustavo Sato Dos Santos, Brett C Packham, and David S Holder. A method for reconstructing tomographic images of

evoked neural activity with electrical impedance tomography using intracranial planar arrays. *Physiological measurement*, 35(6):1095–1109, May 2014. ISSN 1361-6579. doi: 10.1088/0967-3334/35/6/1095. URL http://www.ncbi.nlm.nih.gov/pubmed/24845144.

Kyriacos A Athanasiou, Gabriele G Niederauer, and C Mauli Agrawal. Sterilization, toxicity, biocompatibility and clinical applications of polylactic acid/polyglycolic acid copolymers. *Biomaterials*, 17(2):93–102, 1996.

V C Austin, A M Blamire, K a Allers, T Sharp, P Styles, P M Matthews, and N R Sibson. Confounding effects of anesthesia on functional activation in rodent brain: a study of halothane and alpha-chloralose anesthesia. *NeuroImage*, 24(1): 92–100, January 2005. ISSN 1053-8119. doi: 10.1016/j.neuroimage.2004.08.011. URL http://www.ncbi.nlm.nih.gov/pubmed/15588600.

M Backonja and V Miletic. Responses of neurons in the rat ventrolateral orbital cortex to phasic and tonic nociceptive stimulation. *Brain research*, 557(1-2):353–355, 1991. ISSN 00068993. doi: 10.1016/0006-8993(91)90160-W.

Sonya Bahar, Minah Suh, Mingrui Zhao, and Theodore H Schwartz. Intrinsic optical signal imaging of neocortical seizures: the 'epileptic dip'. *Neuroreport*, 17(5):499–503, April 2006. ISSN 0959-4965. doi: 10.1097/01.wnr.0000209010.78599.f5. URL http://www.ncbi.nlm.nih.gov/pubmed/16543814.

G U Balis and R R Monroe. The pharmacology of chloralose. A review. *Psychopharmacologia*, 6(1):1–30, July 1964. ISSN 0033-3158. URL http://www.ncbi.nlm.nih.gov/pubmed/5318644.

P Barbaresi, R Spreafico, C Frassoni, and A Rustioni. GABAergic neurons are present in the dorsal column nuclei but not in the ventroposterior complex of rats. *Brain research*, 382:305–326, 1986. URL http://www.sciencedirect.com/science/article/pii/0006899386913405.

DC Barber, BH Brown, Home Search, Collections Journals, About Contact, My Iopscience, and I P Address. Applied potential tomography. *Journal of Physics E: Scientific Instruments*, 17:723–731, September 1984. ISSN 0163-2116. URL http://www.ncbi.nlm.nih.gov/pubmed/15282004.

Gregory L Barkley and Christoph Baumgartner. MEG and EEG in epilepsy. *Journal of clinical neurophysiology : official publication of the American Electroencephalographic Society*, 20(3):163–78, 2003. ISSN 0736-0258. URL http://www.ncbi.nlm.nih.gov/pubmed/12881663.

Claude Bédard and Alain Destexhe. Macroscopic models of local field potentials and the apparent 1/f noise in brain activity. *Biophysical journal*, 96(7):2589–603, April 2009. ISSN 1542-0086. doi: 10.1016/j.bpj.2008.12.3951.

H. W. Berendse and H. J. Groenewegen. Restricted cortical termination fields of the midline and intralaminar thalamic nuclei in the rat. *Neuroscience*, 42(1):73–102, 1991.

Anne T Berg, Samuel F Berkovic, Martin J Brodie, Jeffrey Buchhalter, J Helen Cross, Walter van Emde Boas, Jerome Engel, Jacqueline French, Tracy a Glauser, Gary W Mathern, Solomon L Moshé, Douglas Nordli, Perrine Plouin, and Ingrid E Scheffer. Revised terminology and concepts for organization of seizures and epilepsies: report of the ILAE Commission on Classification and Terminology, 2005-2009. *Epilepsia*, 51(4):676–85, April 2010. ISSN 1528-1167. doi: 10.1111/j.1528-1167.2010.02522.x. URL `http://www.ncbi.nlm.nih.gov/pubmed/20196795`.

N Bhadra, K L Kilgore, and P H Peckham. Implanted stimulators for restoration of function in spinal cord injury. *Medical engineering & physics*, 23(1):19–28, January 2001. ISSN 1350-4533. URL `http://www.ncbi.nlm.nih.gov/pubmed/11344004`.

Devin K Binder, Marios C Papadopoulos, Peter M Haggie, and a S Verkman. In vivo measurement of brain extracellular space diffusion by cortical surface photobleaching. *The Journal of neuroscience : the official journal of the Society for Neuroscience*, 24(37):8049–56, September 2004. ISSN 1529-2401. doi: 10.1523/JNEUROSCI.2294-04.2004. URL `http://www.ncbi.nlm.nih.gov/pubmed/15371505`.

N. Boisseau and M Madany. Comparison of the effects of sevoflurane and propofol on cortical somatosensory evoked potentials. *British journal of anaesthesia*, 88(6):785–789, June 2002. ISSN 14716771. doi: 10.1093/bja/88.6.785. URL `http://www.bja.oupjournals.org/cgi/doi/10.1093/bja/88.6.785` `http://bja.oxfordjournals.org/content/88/6/785.short`.

Marita Broberg, Kenneth J Pope, Trent Lewis, Torsten Olsson, Michael Nilsson, and John O Willoughby. Cell swelling precedes seizures induced by inhibition of astrocytic metabolism. *Epilepsy research*, 80(2-3):132–41, August 2008. ISSN 0920-1211. doi: 10.1016/j.eplepsyres.2008.03.012. URL `http://www.ncbi.nlm.nih.gov/pubmed/18440781`.

György Buzsáki and Fernando Lopes Da Silva. High frequency oscillations in the intact brain. *Progress in neurobiology*, 98(3):241–9, September 2012. ISSN 1873-5118. doi: 10.1016/j.pneurobio.2012.02.004. URL `http://www.ncbi.nlm.nih.gov/pubmed/22449727`.

H Cambron, J F Latulippe, T Nguyen, and R Cartier. Orotracheal intubation of rats by transillumination. *Laboratory animal science*, 45(3):303–4, June 1995. ISSN 0023-6764. URL `http://www.ncbi.nlm.nih.gov/pubmed/7650904`.

JA Cardin, M Carlén, K Meletis, and U Knoblich. Driving fast-spiking cells induces gamma rhythm and controls sensory responses. *Nature*,

459(7247):663–667, 2009. doi: 10.1038/nature08002.Driving. URL http://www.nature.com/nature/journal/v459/n7247/abs/nature08002.html.

G E Carvell and D J Simons. Thalamic and corticocortical connections of the second somatic sensory area of the mouse. *The Journal of comparative neurology*, 265(3): 409–427, 1987. ISSN 0021-9967. doi: 10.1002/cne.902650309.

Gregory D Cascino. When drugs and surgery don't work. *Epilepsia*, 49 Suppl 9: 79–84, December 2008. ISSN 1528-1167. doi: 10.1111/j.1528-1167.2008.01930.x. URL http://www.ncbi.nlm.nih.gov/pubmed/19087121.

Montse Charles-Harris, Martin a Koch, Melba Navarro, Damien Lacroix, Elisabeth Engel, and Josep a Planell. A PLA/calcium phosphate degradable composite material for bone tissue engineering: an in vitro study. *Journal of materials science. Materials in medicine*, 19(4):1503–13, April 2008. ISSN 0957-4530. doi: 10.1007/s10856-008-3390-9. URL http://www.ncbi.nlm.nih.gov/pubmed/18266084.

Karen C Cheung, Philippe Renaud, Heikki Tanila, and Kaj Djupsund. Flexible polyimide microelectrode array for in vivo recordings and current source density analysis. *Biosensors & bioelectronics*, 22(8):1783–90, March 2007. ISSN 0956-5663. URL http://www.ncbi.nlm.nih.gov/pubmed/17027251.

a Chow, a Erisir, C Farb, M S Nadal, a Ozaita, D Lau, E Welker, and B Rudy. K(+) channel expression distinguishes subpopulations of parvalbumin- and somatostatin-containing neocortical interneurons. *The Journal of neuroscience : the official journal of the Society for Neuroscience*, 19(21):9332–45, November 1999. ISSN 1529-2401. URL http://www.ncbi.nlm.nih.gov/pubmed/10531438.

Anthony J Clapcich, Ronald G Emerson, David P Roye Jr, Hui Xie, Edward J Gallo, Kathy C Dowling, Brian Ramnath, and Eric Heyer. The Effects of Propofol, Small-Dose Isoflurane, and Nitrous Oxide on Cortical Somatosensory Evoked Potential and Bispectral Index Monitoring in Adolescents Undergoing Spinal Fusion. *Anaesthesia and Analgesia*, 99(5), 2004.

K Cole. ELECTRIC IMPEDANCE OF SUSPENSIONS OF SPHERES. BY. *The Journal of general physiology*, 109(1):29–36, January 1928. ISSN 0022-1295.

K S Cole and R F Baker. Longitudinal Impedance of the Squid Giant Axon. *The Journal of general physiology*, 24(6):771–88, July 1941. ISSN 0022-1295.

K S Cole and H J Curtis. Electric Impedance of Nitella During Activity. *The Journal of general physiology*, 22(1):37–64, September 1938. ISSN 0022-1295.

K S Cole and H J Curtis. Electric Impedance of the Squid Giant Axon During Activity. *The Journal of general physiology*, 22(5):649–70, May 1939. ISSN 0022-1295.

E J Colon and S L Visser. *Evoked potential manual: a practical guide to clinical applications*. Kluwer Academic Publishers, 1990. ISBN 0792307917. URL http://books.google.com/books?id=j9FrAAAAMAAJ&pgis=1.

RE Conn, JJ Kolstad, JF Borzelleca, DS Dixler, LJ Filer, BN LaDu, and MW Pariza. Safety Assessment of Polylactide (PLA) for Use as a Food-contact Polymer. *Fd Chem. Toxic*, 33(4):273–283, 1995.

Eduardo Lv Costa, Raul Gonzalez Lima, and Marcelo Bp Amato. Electrical impedance tomography. *Current Opinion in Critical Care*, 15(1):18–24, February 2009. ISSN 1070-5295. doi: 10.1097/MCC.0b013e3283220e8c.

James E. Cottrell and David Stuart Smith. *Anesthesia and neurosurgery*. Mosby, 2001. ISBN 0815103212. URL http://books.google.com/books?id=3z5sAAAAMAAJ&pgis=1.

Scott J Cruikshank, Matthew Hopperstad, Meg Younger, Barry W Connors, David C Spray, and Miduturu Srinivas. Potent block of Cx36 and Cx50 gap junction channels by mefloquine. *Proceedings of the National Academy of Sciences of the United States of America*, 101(33):12364–9, August 2004. ISSN 0027-8424. doi: 10.1073/pnas.0402044101.

Scott J Cruikshank, Carole E Landisman, Jaime G Mancilla, and Barry W Connors. Connexon connexions in the thalamocortical system. *Progress in brain research*, 149:41–57, January 2005. ISSN 1875-7855. doi: 10.1016/S0079-6123(05)49004-4.

Scott J Cruikshank, Timothy J Lewis, and Barry W Connors. Synaptic basis for intense thalamocortical activation of feedforward inhibitory cells in neocortex. *Nature neuroscience*, 10(4):462–8, April 2007. ISSN 1097-6256. doi: 10.1038/nn1861.

R D Daube. *Clinical neurophysiology*. Oxford University Press, 2002. ISBN 019514080X. URL http://books.google.com/books?id=K5QiZzacCjgC&pgis=1.

Yaron David, Luisa P Cacheaux, Sebastian Ivens, Ezequiel Lapilover, Uwe Heinemann, Daniela Kaufer, and Alon Friedman. Astrocytic dysfunction in epileptogenesis: consequence of altered potassium and glutamate homeostasis? *The Journal of neuroscience : the official journal of the Society for Neuroscience*, 29 (34):10588–99, August 2009. ISSN 1529-2401. doi: 10.1523/JNEUROSCI.2323-09.2009.

W Davies, H Mantzaridis, G N C Kenny, Fisher A C, and FW Davies. Middle latency auditory evoked potentials during repeated transitions from consciousness to unconsciousness. *Anaesthesia*, 51(February 1995):107–113, 1996. URL http://onlinelibrary.wiley.com/doi/10.1111/j.1365-2044.1996.tb07694.x/abstract.

R Dermietzel and EL Hertberg. Gap junctions between cultured astrocytes: immunocytochemical, molecular, and electrophysiological analysis. *The Journal of Neuroscience*, 11(May):1421–1432, 1991. URL `http://www.jneurosci.org/content/11/5/1421.short`.

C. Desbois and L. Villanueva. The organization of lateral ventromedial thalamic connections in the rat: A link for the distribution of nociceptive signals to widespread cortical regions. *Neuroscience*, 102(4):885–898, 2001.

Rights Desk, Lippincott Williams, Kluwer Health, K Sakatani, H Iizuka, and W Young. Somatosensory evoked potentials in rat cerebral cortex before and after middle cerebral artery occlusion K Sakatani, H Iizuka and W Young Stroke 1990;21;124-132. *Stroke*, 21:124–132, 1990.

M E Diamond, M Armstrong-James, M J Budway, and F F Ebner. Somatic sensory responses in the rostral sector of the posterior group (POm) and in the ventral posterior medial nucleus (VPM) of the rat thalamus: dependence on the barrel field cortex. *The Journal of comparative neurology*, 319 (1):66–84, May 1992. ISSN 0021-9967. doi: 10.1002/cne.903190108. URL `http://www.ncbi.nlm.nih.gov/pubmed/1592906`.

E a Disbrow, D a Slutsky, T P Roberts, and L a Krubitzer. Functional MRI at 1.5 tesla: a comparison of the blood oxygenation level-dependent signal and electrophysiology. *Proceedings of the National Academy of Sciences of the United States of America*, 97(17):9718–23, August 2000. ISSN 0027-8424. doi: 10.1073/pnas.170205497.

Biligzaya Dorj, Jong-Eun Won, Odnoo Purevdorj, Kapil D Patel, Joong-Hyun Kim, Eun-Jung Lee, and Hae-Won Kim. A novel therapeutic design of microporous-structured biopolymer scaffolds for drug loading and delivery. *Acta biomaterialia*, (November), November 2013. ISSN 1878-7568. doi: 10.1016/j.actbio.2013.11.002. URL `http://www.ncbi.nlm.nih.gov/pubmed/24239677`.

John S Duncan. Selecting patients for epilepsy surgery: synthesis of data. *Epilepsy & behavior : E&B*, 20(2):230–2, February 2011. ISSN 1525-5069. doi: 10.1016/j.yebeh.2010.06.040. URL `http://www.ncbi.nlm.nih.gov/pubmed/20709601`.

V Ego-Stengel and MA Wilson. Disruption of ripple-associated hippocampal activity during rest impairs spatial learning in the rat. *Hippocampus*, 20(1):1–10, 2010. doi: 10.1002/hipo.20707.Disruption. URL `http://onlinelibrary.wiley.com/doi/10.1002/hipo.20707/full`.

Z Elazar, R T Kado, and W R Adey. Impedance changes during epileptic seizures. *Epilepsia*, 7(4):291–307, December 1966. ISSN 0013-9580. URL `http://www.ncbi.nlm.nih.gov/pubmed/16636408`.

R H Elliott and L Strunin. Hepatotoxicity of volatile anaesthetics. *British Journal of Anaesthesia*, 70:339–348, 1993.

Jerome Engel and Fernando Lopes da Silva. High-frequency oscillations - where we are and where we need to go. *Progress in neurobiology*, 98(3):316–8, September 2012. ISSN 1873-5118. doi: 10.1016/j.pneurobio.2012.02.001.

a Erisir, D Lau, B Rudy, and C S Leonard. Function of specific K(+) channels in sustained high-frequency firing of fast-spiking neocortical interneurons. *Journal of neurophysiology*, 82(5):2476–89, November 1999. ISSN 0022-3077. URL `http://www.ncbi.nlm.nih.gov/pubmed/10561420`.

L Fabrizi, M Sparkes, L Horesh, J F Perez-Juste Abascal, a McEwan, R H Bayford, R Elwes, C D Binnie, and D S Holder. Factors limiting the application of electrical impedance tomography for identification of regional conductivity changes using scalp electrodes during epileptic seizures in humans. *Physiological measurement*, 27(5):S163–74, May 2006. ISSN 0967-3334. doi: 10.1088/0967-3334/27/5/S14. URL `http://www.ncbi.nlm.nih.gov/pubmed/16636408`.

D Feili, M Schuettler, T Doerge, S Kammer, K P Hoffmann, and T Stieglitz. Flexible organic field effect transistors for biomedical microimplants using polyimide and parylene C as substrate and insulator layers. *Journal of Micromechanics and Microengineering*, 16(8):1555–1561, August 2006. ISSN 0960-1317. URL `http://stacks.iop.org/0960-1317/16/i=8/a=016?key=crossref.8726c51276be5719200aa7596e`

Paul Flecknell. *Laboratory Animal AnaesthesiaÂ (Google eBook)*. Academic Press, 2009. ISBN 0123693764. URL `http://books.google.com/books?id=zMfSuAuyKwUC&pgis=1`.

Clare M Florence, Landon D Baillie, and Sean J Mulligan. Dynamic volume changes in astrocytes are an intrinsic phenomenon mediated by bicarbonate ion flux. *PloS one*, 7(11):e51124, January 2012. ISSN 1932-6203. doi: 10.1371/journal.pone.0051124.

L Forsgren, E Beghi, a Oun, and M Sillanpää. The epidemiology of epilepsy in Europe - a systematic review. *European journal of neurology : the official journal of the European Federation of Neurological Societies*, 12(4):245–53, April 2005. ISSN 1351-5101. doi: 10.1111/j.1468-1331.2004.00992.x. URL `http://www.ncbi.nlm.nih.gov/pubmed/15804240`.

John E Fox, Marom Bikson, and John G R Jefferys. Tissue resistance changes and the profile of synchronized neuronal activity during ictal events in the low-calcium model of epilepsy. *Journal of neurophysiology*, 92(1): 181–8, July 2004. ISSN 0022-3077. doi: 10.1152/jn.00123.2004. URL `http://www.ncbi.nlm.nih.gov/pubmed/14999050`.

Maria Angela Franceschini, Sergio Fantini, John H Thompson, Joseph P Culver, and David a Boas. Hemodynamic evoked response of the sensorimotor cortex measured noninvasively with near-infrared optical imaging. *Psychophysiology*, 40(4):548–60, July 2003. ISSN 0048-5772. URL http://www.ncbi.nlm.nih.gov/pubmed/14570163.

S Freeman and H Sohmer. A comparison of forepaw and vibrissae somatosensory cortical evoked potentials in the rat. *Electroencephalography and clinical neurophysiology*, 100(4):362–9, July 1996. ISSN 0013-4694. URL http://www.ncbi.nlm.nih.gov/pubmed/17441306.

Flavio Frohlich and David A. McCormick. Endogenous Electric Fields May Guide Neocortical Network Activity. *Neuron*, 67(1):129–143, 2010. doi: 10.1016/j.neuron.2010.06.005.Endogenous.

B. T. Fundin, J. Arvidsson, and F. L. Rice. Innervation of nonmystacial vibrissae in the adult rat. *Journal of Comparative Neurology*, 357(4):501–512, 1995.

S Gabriel, R W Lau, and C Gabriel. The dielectric properties of biological tissues: III. Parametric models for the dielectric spectrum of tissues. *Physics in medicine and biology*, 41(11):2271–93, November 1996. ISSN 0031-9155. URL http://www.ncbi.nlm.nih.gov/pubmed/8938026.

M Galarreta and S Hestrin. A network of fast-spiking cells in the neocortex connected by electrical synapses. *Nature*, 402(6757):72–5, November 1999. ISSN 0028-0836. doi: 10.1038/47029. URL http://www.ncbi.nlm.nih.gov/pubmed/10573418.

M Galarreta and S Hestrin. Electrical synapses between GABA-releasing interneurons. *Nature reviews. Neuroscience*, 2(6):425–33, June 2001. ISSN 1471-003X. doi: 10.1038/35077566. URL http://www.ncbi.nlm.nih.gov/pubmed/15927686.

A P Gibson, J C Hebden, and S R Arridge. Recent advances in diffuse optical imaging. *Physics in Medicine and Biology*, 50(4):R1–R43, February 2005. ISSN 0031-9155. doi: 10.1088/0031-9155/50/4/R01. URL http://stacks.iop.org/0031-9155/50/i=4/a=R01?key=crossref.e5794ad4b1ac401d7bf971db7c

J R Gibson, M Beierlein, and B W Connors. Two networks of electrically coupled inhibitory neurons in neocortex. *Nature*, 402(6757):75–9, November 1999. ISSN 0028-0836. doi: 10.1038/47035. URL http://www.ncbi.nlm.nih.gov/pubmed/10573419.

O Gilad and D S Holder. Impedance changes recorded with scalp electrodes during visual evoked responses : Implications for Electrical Impedance Tomography of fast neural activity. *NeuroImage*, 47(2):514–522, August 2009. ISSN 1053-8119. doi: 10.1016/j.neuroimage.2009.04.085.

Ori Gilad, Anthony Ghosh, Dongin Oh, and David S Holder. A method for recording resistance changes non-invasively during neuronal depolarization with a view to imaging brain activity with electrical impedance tomography. *Journal of neuroscience methods*, 180(1):87–96, May 2009. ISSN 1872-678X. doi: 10.1016/j.jneumeth.2009.03.012. URL http://www.pubmedcentral.nih.gov/articlerender.fcgi?artid=2813208&tool=pmcentrez&ren

R Gobbelé, T D Waberski, H Simon, E Peters, F Klostermann, G Curio, and H Buchner. Different origins of low- and high-frequency components (600 Hz) of human somatosensory evoked potentials. *Clinical neurophysiology : official journal of the International Federation of Clinical Neurophysiology*, 115(4): 927–37, April 2004. ISSN 1388-2457. doi: 10.1016/j.clinph.2003.11.009. URL http://www.ncbi.nlm.nih.gov/pubmed/15003775.

B Y David E Goldman. Potential, Impedance and Rectification in Membranes. *The Journal of general physiology*, 27:37–60, 1943.

M a Goss-Sampson and a Kriss. Effects of pentobarbital and ketamine-xylazine anaesthesia on somatosensory, brainstem auditory and peripheral sensory-motor responses in the rat. *Laboratory animals*, 25(4):360–6, October 1991. ISSN 0023-6772. URL http://www.ncbi.nlm.nih.gov/pubmed/1753698.

P Grigg. Stretch sensitivity of mechanoreceptor neurons in rat hairy skin. *Journal of neurophysiology*, 76(5):2886–95, November 1996. ISSN 0022-3077. URL http://www.ncbi.nlm.nih.gov/pubmed/8930241.

Frédéric Grouiller, Rachel C Thornton, Kristina Groening, Laurent Spinelli, John S Duncan, Karl Schaller, Michael Siniatchkin, Louis Lemieux, Margitta Seeck, Christoph M Michel, and Serge Vulliemoz. With or without spikes: localization of focal epileptic activity by simultaneous electroencephalography and functional magnetic resonance imaging. *Brain : a journal of neurology*, 134(Pt 10):2867–86, October 2011. ISSN 1460-2156. doi: 10.1093/brain/awr156.

Michael M Haglund and Daryl W Hochman. Optical imaging of epileptiform activity in human neocortex. *Epilepsia*, 45 Suppl 4(8):43–7, January 2004. ISSN 0013-9580. doi: 10.1111/j.0013-9580.2004.04010.x. URL http://www.ncbi.nlm.nih.gov/pubmed/15281958.

Nadia Nabil Haj-Yasein, Vidar Jensen, Ivar Ø stby, Stig W Omholt, Juha Voipio, Kai Kaila, Ole P Ottersen, Ø ivind Hvalby, and Erlend a Nagelhus. Aquaporin-4 regulates extracellular space volume dynamics during high-frequency synaptic stimulation: a gene deletion study in mouse hippocampus. *Glia*, 60(6):867–74, May 2012. ISSN 1098-1136. doi: 10.1002/glia.22319. URL http://www.ncbi.nlm.nih.gov/pubmed/22419561.

Catherine N Hall, Clare Reynell, Bodil Gesslein, Nicola B Hamilton, Anusha Mishra, Brad a Sutherland, Fergus M O'Farrell, Alastair M Buchan, Martin

Lauritzen, and David Attwell. Capillary pericytes regulate cerebral blood flow in health and disease. *Nature*, 508(7494):55–60, April 2014. ISSN 1476-4687. doi: 10.1038/nature13165. URL `http://www.ncbi.nlm.nih.gov/pubmed/24670647`.

Pol Hans and Vincent Bonhomme. Why we still use intravenous drugs as the basic regimen for neurosurgical anaesthesia. *Current opinion in anaesthesiology*, 19(5):498–503, October 2006. ISSN 0952-7907. doi: 10.1097/01.aco.0000245274.69292.ad. URL `http://www.ncbi.nlm.nih.gov/pubmed/16960481`.

R M Harris and A E Hendrickson. Local circuit neurons in the rat ventrobasal thalamus–a GABA immunocytochemical study. *Neuroscience*, 21(1):229–236, 1987. ISSN 03064522. doi: 10.1016/0306-4522(87)90335-6.

Y M Hart and S D Shorvon. The nature of epilepsy in the general population. I. Characteristics of patients receiving medication for epilepsy. *Epilepsy research*, 21(1):43–9, May 1995. ISSN 0920-1211. URL `http://www.ncbi.nlm.nih.gov/pubmed/7641675`.

I Hashimoto, T Mashiko, and T Imada. Somatic evoked high-frequency magnetic oscillations reflect activity of inhibitory interneurons in the human somatosensory cortex. *Electroencephalography and clinical neurophysiology*, 100(3):189–203, May 1996. ISSN 0013-4694. URL `http://www.ncbi.nlm.nih.gov/pubmed/8681860`.

Christina Hassler, Tim Boretius, and Thomas Stieglitz. Polymers for neural implants. *Journal of Polymer Science Part B: Polymer Physics*, 49(1): 18–33, January 2011. ISSN 08876266. doi: 10.1002/polb.22169. URL `http://doi.wiley.com/10.1002/polb.22169`.

W. Allen Hauser, John F. Annegers, and Walter A. Rocca. Descriptive Epidemiology of Epilepsy: Contributions of Population-Based Studies From Rochester, Minnesota. *Mayo Clinic Proceedings*, 71(6):576–586, June 1996. ISSN 00256196. doi: 10.4065/71.6.576. URL `http://www.sciencedirect.com/science/article/pii/S0025619611641153`.

S M Hayton, a Kriss, and D P Muller. Comparison of the effects of four anaesthetic agents on somatosensory evoked potentials in the rat. *Laboratory animals*, 33(3):243–51, July 1999. ISSN 0023-6772. URL `http://www.ncbi.nlm.nih.gov/pubmed/10780843`.

SH Hendry and HD Schwark. Numbers and proportions of GABA-immunoreactive neurons in different areas of monkey cerebral cortex. *The Journal of . . .*, 7(May): 1503–1519, 1987. URL `http://www.jneurosci.org/content/7/5/1503.short`.

M Herkenham. Laminar organization of thalamic projections to the rat neocortex. *Science (New York, N.Y.)*, 207(4430):532–535, 1980. ISSN 0036-8075. doi: 10.1126/science.7352263.

Shaul Hestrin. Neuroscience. The strength of electrical synapses. *Science (New York, N.Y.)*, 334(6054):315–6, October 2011. ISSN 1095-9203. doi: 10.1126/science.1213894. URL http://www.ncbi.nlm.nih.gov/pubmed/22021844.

E M C Hillman. Optical brain imaging in vivo: techniques and applications from animal to man. *J Biomed Opt.*, 12(5):1–49, 2007. doi: 10.1016/j.neuroimage.2011.02.058.Focused.

AL Hodgkin and AF Huxley. A quantitative description of membrane current and its application to conduction and excitation in nerve. *The Journal of physiology*, 117:500–544, 1952. URL http://www.ncbi.nlm.nih.gov/pmc/articles/pmc1392413/.

AL L Hodgkin and B Katz. The effect of sodium ions on the electrical activity of the giant axon of the squid. *The Journal of physiology*, 108:37–77, 1949. URL http://www.ncbi.nlm.nih.gov/pmc/articles/PMC1392331/.

D S Holder. Feasibility of developing a method of imaging neural activity in the human brain: a theoretical review. *Medical & Biological Engineering*, (January): 2–11, 1987.

D S Holder. *Electrical impedance tomography: methods, history, and applications*. Institute of Physics Pub., 2005. ISBN 0750309520. URL http://books.google.com/books?id=cjcRd4m_jUQC&pgis=1.

D S Holder and a Khan. Use of polyacrylamide gels in a saline-filled tank to determine the linearity of the Sheffield Mark 1 electrical impedance tomography (EIT) system in measuring impedance disturbances. *Physiological measurement*, 15 Suppl 2:A45–50, May 1994. ISSN 0967-3334. URL http://www.ncbi.nlm.nih.gov/pubmed/8087049.

M W Hollmann, H T Liu, C W Hoenemann, W H Liu, and M E Durieux. Modulation of NMDA receptor function by ketamine and magnesium. Part II: interactions with volatile anesthetics. *Anesthesia and analgesia*, 92(5):1182–91, May 2001. ISSN 0003-2999. URL http://www.ncbi.nlm.nih.gov/pubmed/11323344.

K Holthoff and OW Witte. Intrinsic optical signals in rat neocortical slices measured with near-infrared dark-field microscopy reveal changes in extracellular space. *The Journal of neuroscience*, 76(8):2740–2749, 1996. URL http://www.jneurosci.org/content/16/8/2740.short.

J B Hopfinger, C Büchel, a P Holmes, and K J Friston. A study of analysis parameters that influence the sensitivity of event-related fMRI analyses. *NeuroImage*, 11(4):326–33, April 2000. ISSN 1053-8119. doi: 10.1006/nimg.2000.0549. URL http://www.ncbi.nlm.nih.gov/pubmed/10725188.

M Hunfeld, K J Pope, S P Fitzgibbon, J O Willoughby, and M Broberg. Effects of anesthetic agents on seizure-induction with intra-cortical injection of convulsants. *Epilepsy research*, 105(1-2):52–61, July 2013. ISSN 1872-6844. doi: 10.1016/j.eplepsyres.2012.12.009. URL http://www.ncbi.nlm.nih.gov/pubmed/23357722.

JB B Hursh. Conduction velocity and diameter of nerve fibers. *American Journal of Physiology*, 127(1):131–139, 1939. URL http://psycnet.apa.org/psycinfo/1940-01714-001.

Bruce Hutcheon and Yosef Yarom. Resonance, oscillation and the intrinsic frequency preferences of neurons. *Trends in neurosciences*, 23(5):216–222, 2000. URL http://www.sciencedirect.com/science/article/pii/S0166223600015472.

Hiroaki Ikeda, Leonard Leyba, and Anton Bartolo. Synchronized spikes of thalamocortical axonal terminals and cortical neurons are detectable outside the pig brain with MEG. *Journal of Neurophysiology*, 87:626–630, 2002. URL http://jn.physiology.org/content/87/1/626.short.

K F Jensen and H P Killackey. Terminal arbors of axons projecting to the somatosensory cortex of the adult rat. I. The normal morphology of specific thalamocortical afferents. *The Journal of neuroscience : the official journal of the Society for Neuroscience*, 7(11):3529–3543, 1987. ISSN 0270-6474.

M S Jones and D S Barth. Spatiotemporal organization of fast (>200 Hz) electrical oscillations in rat Vibrissa/Barrel cortex. *Journal of neurophysiology*, 82(3):1599–609, September 1999. ISSN 0022-3077. URL http://www.ncbi.nlm.nih.gov/pubmed/10482773.

V Jousmäki. Tracking functions of cortical networks on a millisecond timescale. *Neural networks : the official journal of the International Neural Network Society*, 13(8-9):883–9, 2000. ISSN 0893-6080. URL http://www.ncbi.nlm.nih.gov/pubmed/11156199.

Rachel Jurd, Margarete Arras, Sachar Lambert, Berthold Drexler, Roberta Siegwart, Florence Crestani, Michael Zaugg, Kaspar E Vogt, Birgit Ledermann, Bernd Antkowiak, U W E Rudolph, and Specific Aim. General anesthetic actions in vivo strongly attenuated by a point mutation in the GABA A receptor. *The FASEB Journal*, 17:250–252, 2003. doi: 10.1096/fj.02.

Eric R. Kandel, James Harris Schwartz, and Thomas M. Jessell. *Principles of neural science*. McGraw-Hill, Health Professions Division, 2000. ISBN 0838577016. URL http://books.google.com/books?id=yMtpAAAAMAAJ&pgis=1.

S. Kastl. Simplification of rat intubation on inclined metal plate. *AJP: Advances in Physiology Education*, 28(1):29–32, March

2004. ISSN 1043-4046. doi: 10.1152/advan.00008.2003. URL http://ajpadvan.physiology.org/cgi/doi/10.1152/advan.00008.2003.

Bertram G. Katzung and Anthony J. Trevor. *Basic and Clinical Pharmacology, 11th Edition*. McGraw-Hill Medical; 11 edition, 2009. ISBN 0071604057.

A. E. Kennely. AMERICAN INSTITUTE OF ELECTRICAL Engineers: -76th meeting. In *Impedance*, 1893.

V N Kharazia and R J Weinberg. Glutamate in thalamic fibers terminating in layer IV of primary sensory cortex. *The Journal of neuroscience : the official journal of the Society for Neuroscience*, 14(10):6021–6032, 1994. ISSN 0270-6474.

E T Kim, C Kim, S W Lee, J-M Seo, H Chung, and S J Kim. Feasibility of microelectrode array (MEA) based on silicone-polyimide hybrid for retina prosthesis. *Investigative ophthalmology & visual science*, 50(9):4337–41, September 2009. ISSN 1552-5783. URL http://www.ncbi.nlm.nih.gov/pubmed/19264890.

Rainer Klinke and Stefan Silbernagel. *Lehrbuch der Physiologie*. Thieme, 4. edition, 2003. ISBN 3137960045. URL http://books.google.com/books?id=1k2YAQAACAAJ&pgis=1.

K a Klivington and R Galambos. Rapid resistance shifts in cat cortex during click-evoked responses. *Journal of neurophysiology*, 31(4):565–73, July 1968. ISSN 0022-3077. URL http://www.ncbi.nlm.nih.gov/pubmed/5709872.

R Klivington, K Galambos. Resistance Shifts Accompanying the Evoked Cortical Response in the Cat. *Science*, 157(3785):211–213, 1967.

Irene a W Kotsopoulos, Tiny van Merode, Fons G H Kessels, Marc C T F M de Krom, and J André Knottnerus. Systematic review and meta-analysis of incidence studies of epilepsy and unprovoked seizures. *Epilepsia*, 43(11):1402–9, November 2002. ISSN 0013-9580. URL http://www.ncbi.nlm.nih.gov/pubmed/12423392.

Hans-Joachim Kretschmann and Wolfgang Weinrich. *Cranial Neuroimaging and Clinical Neuroanatomy: Magnetic Resonance Imaging and Computed Tomography*. Thieme, 2004. ISBN 1588901459. URL http://books.google.com/books?hl=en&lr=&id=9c3W5Cy6-R4C&pgis=1.

T Kurita, M Doi, T Katoh, H Sano, S Sato, H Mantzaridis, and G N Kenny. Auditory evoked potential index predicts the depth of sedation and movement in response to skin incision during sevoflurane anesthesia. *Anesthesiology*, 95(2):364–70, August 2001. ISSN 0003-3022. URL http://www.ncbi.nlm.nih.gov/pubmed/11506107.

K K Lauer, L a Connolly, and W T Schmeling. Opioid sedation does not alter intracranial pressure in head injured patients. *Canadian journal of anaesthesia = Journal canadien d'anesthésie*, 44(9):929–33, September 1997. ISSN 0832-610X. doi: 10.1007/BF03011963. URL http://www.ncbi.nlm.nih.gov/pubmed/9305555.

R D Linden, C B Shields, Y P Zhang, H L Edmonds, and M a Hunt. A laryngoscope designed for intubation of the rat. *Contemporary topics in laboratory animal science / American Association for Laboratory Animal Science*, 39(2):40–2, March 2000. ISSN 1060-0558. URL http://www.ncbi.nlm.nih.gov/pubmed/11487239.

Adam Liston, Richard Bayford, and David Holder. A cable theory based biophysical model of resistance change in crab peripheral nerve and human cerebral cortex during neuronal depolarisation: implications for electrical impedance tomography of fast neural activity in the brain. *Medical & biological engineering & computing*, 50(5):425–37, May 2012. ISSN 1741-0444. doi: 10.1007/s11517-012-0901-0. URL http://www.ncbi.nlm.nih.gov/pubmed/22484662.

Nikos K Logothetis. What we can do and what we cannot do with fMRI. *Nature*, 453(7197):869–78, June 2008. ISSN 1476-4687. doi: 10.1038/nature06976. URL http://www.ncbi.nlm.nih.gov/pubmed/18548064.

Nikos K Logothetis, Christoph Kayser, and Axel Oeltermann. In vivo measurement of cortical impedance spectrum in monkeys: implications for signal propagation. *Neuron*, 55(5):809–23, September 2007. ISSN 0896-6273. doi: 10.1016/j.neuron.2007.07.027. URL http://www.ncbi.nlm.nih.gov/pubmed/17785187.

S M Lu and R C Lin. Thalamic afferents of the rat barrel cortex: a light- and electron-microscopic study using Phaseolus vulgaris leucoagglutinin as an anterograde tracer. *Somatosensory & motor research*, 10(1):1–16, 1993. ISSN 0899-0220. doi: 10.3109/08990229309028819.

H Lullies. Über die Polarisation in Geweben. *Pflugers Archiv fur die gesamte Physiologie des Menschen und der Thiere*, 296(1928):69–86, 1930.

Hongtao Ma, Mingrui Zhao, and Theodore H Schwartz. Dynamic neurovascular coupling and uncoupling during ictal onset, propagation, and termination revealed by simultaneous in vivo optical imaging of neural activity and local blood volume. *Cerebral cortex (New York, N.Y. : 1991)*, 23(4):885–99, April 2013. ISSN 1460-2199. doi: 10.1093/cercor/bhs079.

Emilie Macé, Gabriel Montaldo, Ivan Cohen, Michel Baulac, Mathias Fink, and Mickael Tanter. Functional ultrasound imaging of the brain. *Nature methods*, 8(8):662–4, August 2011. ISSN 1548-7105. doi: 10.1038/nmeth.1641. URL http://www.ncbi.nlm.nih.gov/pubmed/21725300.

H Mantzaridis and G N Kenny. Auditory evoked potential index: a quantitative measure of changes in auditory evoked potentials during general anaesthesia. *Anaesthesia*, 52(11):1030–6, November 1997. ISSN 0003-2409.

Henry Markram, Maria Toledo-Rodriguez, Yun Wang, Anirudh Gupta, Gilad Silberberg, and Caizhi Wu. Interneurons of the neocortical inhibitory system. *Nature reviews. Neuroscience*, 5(10):793–807, October 2004. ISSN 1471-003X. doi: 10.1038/nrn1519. URL `http://www.ncbi.nlm.nih.gov/pubmed/15378039`.

M Martina, J H Schultz, H Ehmke, H Monyer, and P Jonas. Functional and molecular differences between voltage-gated K+ channels of fast-spiking interneurons and pyramidal neurons of rat hippocampus. *The Journal of neuroscience : the official journal of the Society for Neuroscience*, 18(20):8111–25, October 1998. ISSN 0270-6474. URL `http://www.ncbi.nlm.nih.gov/pubmed/9763458`.

K McAlonan. Thalamic reticular nucleus activation reflects attentional gating during classical conditioning. *The Journal of ...*, 20(23):8897–8901, 2000. URL `http://www.jneurosci.org/content/20/23/8897.short`.

H Meinardi, R a Scott, R Reis, and J W Sander. The treatment gap in epilepsy: the current situation and ways forward. *Epilepsia*, 42(1):136–49, January 2001. ISSN 0013-9580. URL `http://www.ncbi.nlm.nih.gov/pubmed/11207798`.

S Mense. Group III and IV receptors in skeletal muscle: are they specific or polymodal? *Progress in brain research*, 113:83–100, January 1996. ISSN 0079-6123. URL `http://www.ncbi.nlm.nih.gov/pubmed/9009729`.

Robert C Molthen. A simple, inexpensive, and effective light- carrying laryngoscopic blade for orotracheal intubation of rats. *Journal of the American Association for Laboratory Animal Science : JAALAS*, 45(1):88–93, January 2006. ISSN 1559-6109. URL `http://www.ncbi.nlm.nih.gov/pubmed/16539342`.

RR R MONROE and WA A MICKLE. Alpha chloralose-activated electroencephalograms in psychiatric patients. *The Journal of Nervous and Mental Disease*, pages 59–68, 1967.

RR R Monroe, RG G Heath, William Miller, and C Fontana. EEG activation with chloralosane. *Electroencephalography and clinical neurophysiology*, 8(2):279–287, 1956. URL `http://www.sciencedirect.com/science/article/pii/0013469456901195`.

V N Murthy and E E Fetz. Synchronization of neurons during local field potential oscillations in sensorimotor cortex of awake monkeys. *Journal of neurophysiology*, 76(6):3968–82, December 1996. ISSN 0022-3077. URL `http://www.ncbi.nlm.nih.gov/pubmed/8985893`.

a C Ngai, M A Jolley, R D'Ambrosio, J R Meno, and H R Winn. Frequency-dependent changes in cerebral blood flow and evoked potentials during somatosensory stimulation in the rat. *Brain research*, 837(1-2):221–8, August 1999. ISSN 0006-8993.

Anthony K Ngugi, Christian Bottomley, Immo Kleinschmidt, Josemir W Sander, and Charles R Newton. Estimation of the burden of active and life-time epilepsy: a meta-analytic approach. *Epilepsia*, 51(5):883–90, May 2010. ISSN 1528-1167. doi: 10.1111/j.1528-1167.2009.02481.x. URL http://www.pubmedcentral.nih.gov/articlerender.fcgi?artid=3410521&tool=pmcentrez&ren

Dolores B Njoku, Robert S Greenberg, Mohammed Bourdi, Craig B Borkowf, Elizabeth M Dake, Jackie L Martin, Lance R Pohl, and D Pharm. Autoantibodies associated with volatile anesthetic hepatitis found in the sera of a large cohort of pediatric anesthesiologists. *Anesthesia and analgesia*, 94 (2):243–9, table of contents, February 2002. ISSN 0003-2999. URL http://www.ncbi.nlm.nih.gov/pubmed/20124980.

Ivar Ø stby, Leiv Ø yehaug, Gaute T Einevoll, Erlend a Nagelhus, Erik Plahte, Thomas Zeuthen, Catherine M Lloyd, Ole P Ottersen, and Stig W Omholt. Astrocytic mechanisms explaining neural-activity-induced shrinkage of extraneuronal space. *PLoS computational biology*, 5(1):e1000272, January 2009. ISSN 1553-7358. doi: 10.1371/journal.pcbi.1000272. URL http://www.pubmedcentral.nih.gov/articlerender.fcgi?artid=2613522&tool=pmcentrez&ren

T Oh, O Gilad, a Ghosh, M Schuettler, and D S Holder. A novel method for recording neuronal depolarization with recording at 125-825Â Hz: implications for imaging fast neural activity in the brain with electrical impedance tomography. *Medical & biological engineering & computing*, 49(5):593–604, May 2011a. ISSN 1741-0444. doi: 10.1007/s11517-011-0761-z. URL http://www.ncbi.nlm.nih.gov/pubmed/21448692.

T Oh, O Gilad, A Ghosh, M Schuettler, and D S Holder. A novel method for recording neuronal depolarization with recording at 125-825 Hz: implications for imaging fast neural activity in the brain with electrical impedance tomography. *Medical & biological engineering & computing*, 49(5):593–604, May 2011b. ISSN 1741-0444. doi: 10.1007/s11517-011-0761-z. URL http://www.ncbi.nlm.nih.gov/pubmed/21448692.

T Olsson, M Broberg, K J Pope, a Wallace, L Mackenzie, F Blomstrand, M Nilsson, and J O Willoughby. Cell swelling, seizures and spreading depression: an impedance study. *Neuroscience*, 140(2):505–15, June 2006. ISSN 0306-4522. doi: 10.1016/j.neuroscience.2006.02.034. URL http://www.ncbi.nlm.nih.gov/pubmed/16580141.

Brett C Packham. *Imaging Fast Neural Activity in the Brain with Electrical Impedance Tomography*. PhD thesis, University College London, 2013.

Changlin Pang, Jorge Cham, Zoran Nenadic, Sam Musallam, Yu-Chong Tai, Joel Burdick, and R Andersen. A new multi-site probe array with monolithically integrated parylene flexible cable for neural prostheses. *Conference proceedings : ... Annual International Conference of the IEEE Engineering in Medicine and Biology Society. IEEE Engineering in Medicine and Biology Society. Conference*, 7:7114–7, January 2005. ISSN 1557-170X. URL `http://www.ncbi.nlm.nih.gov/pubmed/17281915`.

George Paxinos. *The Rat Nervous System*. Academic Press, third edit edition, 2004. ISBN 0080542611. URL `http://books.google.com/books?id=F5xkDtDL4AUC&pgis=1`.

George Paxinos and Charles Watson. *The Rat Brain in Stereotaxic Coordinates: Hard Cover EditionÂ (Google eBook)*. Academic Press, 2007. ISBN 0080475132. URL `http://books.google.com/books?id=4OBQ8wpK0usC&pgis=1`.

Carl C H Petersen. The functional organization of the barrel cortex. *Neuron*, 56(2): 339–55, October 2007. ISSN 0896-6273. doi: 10.1016/j.neuron.2007.09.017. URL `http://www.ncbi.nlm.nih.gov/pubmed/17964250`.

D Peterson, Drummon JC, and M Todd. Effects of Halothane, Enflurane, Isoflurane and Nitrous Oxide on Somatosensory Evoked Potentials in Humans. *Anesthsiology*, 65:35–40, 1986.

D. Pinault, J. Bourassa, and M. Deschenes. The axonal arborization of single thalamic reticular neurons in the somatosensory thalamus of the rat. *European Journal of Neuroscience*, 7(1):31–40, 1995.

A Pitkaenen, P A Schwartzkroin, and S L Moshe. *Models of Seizures and Epilepsy (Google eBook)*. Academic Press, 2005. ISBN 0080457029. URL `http://books.google.com/books?id=Qw6KqLjwtZQC&pgis=1`.

Martin Pospischil, Maria Toledo-Rodriguez, Cyril Monier, Zuzanna Piwkowska, Thierry Bal, Yves Frégnac, Henry Markram, and Alain Destexhe. Minimal Hodgkin-Huxley type models for different classes of cortical and thalamic neurons. *Biological cybernetics*, 99(4-5):427–41, November 2008. ISSN 1432-0770. doi: 10.1007/s00422-008-0263-8. URL `http://www.ncbi.nlm.nih.gov/pubmed/19011929`.

E Proctor and A R Fernando. Oro-endotracheal Intubation in the Rat. *British journal of anaesthesia*, 45:139–142, 1973.

E Puil, H Meiri, and Y Yarom. Resonant behavior and frequency preferences of thalamic neurons. *Journal of neurophysiology*, 71(2):575–82, February 1994. ISSN 0022-3077. URL `http://www.ncbi.nlm.nih.gov/pubmed/8176426`.

J B Ranck. Specific impedance of rabbit cerebral cortex. *Experimental neurology*, 7:144–52, February 1963. ISSN 0014-4886. URL http://www.ncbi.nlm.nih.gov/pubmed/13990734.

Anling Rao. *Electrical Impedance Tomography of Brain Activity: Studies into its accuracy and physiological mechanisms*. PhD thesis, 2000.

J E Rash, W a Staines, T Yasumura, D Patel, C S Furman, G L Stelmack, and J I Nagy. Immunogold evidence that neuronal gap junctions in adult rat brain and spinal cord contain connexin-36 but not connexin-32 or connexin-43. *Proceedings of the National Academy of Sciences of the United States of America*, 97(13): 7573–8, June 2000. ISSN 0027-8424.

G Regesta and P Tanganelli. Clinical aspects and biological bases of drug-resistant epilepsies. *Epilepsy research*, 34(2-3):109–22, April 1999. ISSN 0920-1211. URL http://www.ncbi.nlm.nih.gov/pubmed/10210025.

R Remie, A Bertens, JJ Van Dongen, JW Rensema, and GHJ Van Wunnick. *Anaesthesia of the laboratory rat - Manual of microsurgery on the rat*. Elsevier, 1990.

W E Renehan and B L Munger. Degeneration and regeneration of peripheral nerve in the rat trigeminal system. I. Identification and characterization of the multiple afferent innervation of the mystacial vibrissae. *The Journal of comparative neurology*, 246(1):129–145, 1986. ISSN 0021-9967. doi: 10.1002/cne.902460109.

Domenico Restuccia, Ivana Del Piero, Lucia Martucci, and Sergio Zanini. High-frequency oscillations after median-nerve stimulation do not undergo habituation: a new insight on their functional meaning? *Clinical neurophysiology : official journal of the International Federation of Clinical Neurophysiology*, 122(1):148–52, January 2011. ISSN 1872-8952. doi: 10.1016/j.clinph.2010.06.008. URL http://www.ncbi.nlm.nih.gov/pubmed/20619726.

FL Rice and BT Fundin. Comprehensive immunofluorescence and lectin binding analysis of vibrissal follicle sinus complex innervation in the mystacial pad of the rat. *Journal of . . .*, 184(June 1994):149–184, 1997.

Petra Ritter, Frank Freyer, Gabriel Curio, and Arno Villringer. NeuroImage High-frequency (600 Hz) population spikes in human EEG delineate thalamic and cortical fMRI activation sites. *NeuroImage*, 42(2):483–490, August 2008. ISSN 1095-9572. doi: 10.1016/j.neuroimage.2008.05.026. URL http://www.ncbi.nlm.nih.gov/pubmed/18586526.

Jim E. Riviere and Mark G. Papich. *Veterinary pharmacology and therapeutics*. John Wiley and Sons, 2009. ISBN 0813820618. URL http://books.google.com/books?id=ievLulSqwBAC&pgis=1.

D Rodger, a Fong, W Li, H Ameri, a Ahuja, C Gutierrez, I Lavrov, H Zhong, P Menon, and E Meng. Flexible parylene-based multielectrode array technology for high-density neural stimulation and recording. *Sensors and Actuators B: Chemical*, 132(2):449–460, June 2008. ISSN 09254005. URL `http://linkinghub.elsevier.com/retrieve/pii/S0925400507009070`.

E Roggendorf. The biostability of silicone rubbers, a polyamide, and a polyester. *Journal of biomedical materials research*, 10(1):123–43, January 1976. ISSN 0021-9304. doi: 10.1002/jbm.820100112. URL `http://www.ncbi.nlm.nih.gov/pubmed/1249086`.

A Rosenblueth and WB Cannon. Cortical responses to electrical stimulation. *American journal of physiology.*, 135(1941):690–739, 1941.

B Rudy and C J McBain. Kv3 channels: voltage-gated K+ channels designed for high-frequency repetitive firing. *Trends in neurosciences*, 24(9):517–26, September 2001. ISSN 0166-2236.

Bernardo Rudy, Gordon Fishell, SooHyun Lee, and Jens Hjerling-Leffler. Three groups of interneurons account for nearly 100% of neocortical GABAergic neurons. *Developmental neurobiology*, 71(1):45–61, January 2011. ISSN 1932-846X. doi: 10.1002/dneu.20853.

K. J. Sanderson, W. Welker, and G. M. Shambes. Reevaluation of motor cortex and of sensorimotor overlap in cerebral cortex of albino rats. *Brain Research*, 292 (2):251–260, 1984.

S Sapienza, B Talbi, J Jacquemin, and D Albe-Fessard. Relationship between input and output of cells in motor and somatosensory cortices of the chronic awake rat. A study using glass micropipettes. *Experimental brain research. Experimentelle Hirnforschung. Experimentation cerebrale*, 43(1):47–56, 1981. ISSN 0014-4819. doi: 10.1007/BF00238808.

S Saporta and L Kruger. The organization of thalamocortical relay neurons in the rat ventrobasal complex studied by the retrograde transport of horseradish peroxidase. *The Journal of comparative neurology*, 174(2):187–208, July 1977. ISSN 0021-9967. doi: 10.1002/cne.901740202. URL `http://www.ncbi.nlm.nih.gov/pubmed/68039`.

C F Schaefer, D J Brackett, P Downs, P Tompkins, M F Wilson, F Wilson, Paul Tompkins, and Michael F Wilson Laryngoscopic. Laryngoscopic endotracheal intubation of rats for inhalation anesthesia Laryngoscopic endotracheal intubation of rats for inhalation anesthesia. *Journal of applied physiology*, 56:533–535, 1984.

Donald L. Schomer. *Niedermeyer's Electroencephalography: Basic Principles, Clinical Applications, and Related Fields.* Lippincott Williams and Wilkins, 2011. ISBN 0781789427.

Stephan U Schuele and Hans O Lüders. Intractable epilepsy: management and therapeutic alternatives. *Lancet neurology*, 7(6):514–24, June 2008. ISSN 1474-4422. doi: 10.1016/S1474-4422(08)70108-X. URL http://www.ncbi.nlm.nih.gov/pubmed/18485315.

M Schuettler, J S Ordonez, C Henle, D Oh, O Gilad, and D S Holder. A Flexible 29 Channel Epicortical Electrode Array. *Biomed Technol*, 53(suppl.:232–235, 2008.

Martin Schuettler, Christian Henle, Juan Ordonez, Gregg J Suaning, Nigel H Lovell, Thomas Stieglitz, and Senior Student Senior Student Member. Patterning of Silicone Rubber for Micro-Electrode Array Fabrication. *2007 3rd International IEEE/EMBS Conference on Neural Engineering*, pages 53–56, May 2007. doi: 10.1109/CNE.2007.369610. URL http://ieeexplore.ieee.org/lpdocs/epic03/wrapper.htm?arnumber=4227215.

Martin Schuettler, Damir Pfau, Juan S Ordonez, Christian Henle, Peter Woias, and Thomas Stieglitz. Stretchable tracks for laser-machined neural electrode arrays. *Conference proceedings : ... Annual International Conference of the IEEE Engineering in Medicine and Biology Society. IEEE Engineering in Medicine and Biology Society. Conference*, 2009:1612–5, January 2009. ISSN 1557-170X. doi: 10.1109/IEMBS.2009.5333224. URL http://www.ncbi.nlm.nih.gov/pubmed/19964006.

Jürgen Schüttler and Helmut Schwilden. *Modern anesthetics*. Springer, 2008. ISBN 3540728139. URL http://books.google.com/books?id=JpkkWhPbh2QC&pgis=1.

Per B Sederberg, Andreas Schulze-Bonhage, Joseph R Madsen, Edward B Bromfield, David C McCarthy, Armin Brandt, Michele S Tully, and Michael J Kahana. Hippocampal and neocortical gamma oscillations predict memory formation in humans. *Cerebral cortex (New York, N.Y. : 1991)*, 17(5): 1190–6, May 2007. ISSN 1047-3211. doi: 10.1093/cercor/bhl030. URL http://www.ncbi.nlm.nih.gov/pubmed/16831858.

C Sekirnjak, M E Martone, M Weiser, T Deerinck, E Bueno, B Rudy, and M Ellisman. Subcellular localization of the K+ channel subunit Kv3.1b in selected rat CNS neurons. *Brain research*, 766(1-2):173–87, August 1997. ISSN 0006-8993. URL http://www.ncbi.nlm.nih.gov/pubmed/9359601.

Fernando Seoane, Kaj Lindecrantz, Torsten Olsson, Ingemar Kjellmer, Anders Flisberg, and Ralph Bå genholm. Spectroscopy study of the dynamics of the transencephalic electrical impedance in the perinatal brain during hypoxia. *Physiological measurement*, 26(5):849–63, October 2005. ISSN 0967-3334. doi: 10.1088/0967-3334/26/5/021. URL http://www.ncbi.nlm.nih.gov/pubmed/16088073.

Wolf Singer and CM Gray. Visual feature integration and the temporal correlation hypothesis. *Annual review of neuroscience*, 18:555–86, 1995. URL http://www.annualreviews.org/doi/pdf/10.1146/annurev.ne.18.030195.003011.

Tod B. Sloan. Anesthetic Effects on Electrophysiologic Recordings. *Journal of Clinical Neurophysiology*, 15(3):217–226, May 1998. ISSN 0736-0258. doi: 10.1097/00004691-199805000-00005.

Tod B Sloan and Eric J Heyer. Anesthesia for intraoperative neurophysiologic monitoring of the spinal cord. *Journal of clinical neurophysiology : official publication of the American Electroencephalographic Society*, 19(5):430–43, October 2002. ISSN 0736-0258. URL `http://www.ncbi.nlm.nih.gov/pubmed/12477988`.

T G Smith, R B Wuerker, and K Frank. Membrane impedance changes during synaptic transmission in cat spinal motoneurons. *Journal of neurophysiology*, 30(5):1072–96, September 1967. ISSN 0022-3077. URL `http://www.ncbi.nlm.nih.gov/pubmed/4293409`.

Aleksander Sobolewski, Ewa Kublik, Daniel Swiejkowski, Szymon Leski, Jan Kaminski, and Andrzej Wrobel. Cross-trial correlation analysis of evoked potentials reveals arousal-related attenuation of thalamo-cortical coupling. *Journal of computational neuroscience*, 29(3):485–93, December 2010. ISSN 1573-6873. doi: 10.1007/s10827-010-0220-0. URL `http://www.ncbi.nlm.nih.gov/pubmed/20177762`.

VS Sohal, F Zhang, O Yizhar, and K Deisseroth. Parvalbumin neurons and gamma rhythms enhance cortical circuit performance. *Nature*, 459(7247):698–702, 2009. doi: 10.1038/nature07991.Parvalbumin. URL `http://www.nature.com/nature/journal/v459/n7247/abs/nature07991.html`.

P Somogyi, T F Freund, and a Cowey. The axo-axonic interneuron in the cerebral cortex of the rat, cat and monkey. *Neuroscience*, 7(11):2577–607, January 1982. ISSN 0306-4522. URL `http://www.ncbi.nlm.nih.gov/pubmed/7155343`.

S S Spencer, P D Williamson, D D Spencer, and R H Mattson. Human hippocampal seizure spread studied by depth and subdural recording: the hippocampal commissure. *Epilepsia*, 28(5):479–89, 1987. ISSN 0013-9580. URL `http://www.ncbi.nlm.nih.gov/pubmed/3653050`.

R Spreafico, P Barbaresi, R J Weinberg, and A Rustioni. SII-projecting neurons in the rat thalamus: a single- and double-retrograde-tracing study. *Somatosensory research*, 4(4):359–375, 1987. ISSN 0899-0220. doi: 10.3109/07367228709144614.

R A Stark, M L Nahrwold, and P J Cohen. Blind oral tracheal intubation of rats. *Journal of Applied Physiology*, 51(5):1355–1356, 1981.

S S Stensaas and L J Stensaas. Histopathological evaluation of materials implanted in the cerebral cortex. *Acta neuropathologica*, 41(2):145–55, February 1978. ISSN 0001-6322. URL `http://www.ncbi.nlm.nih.gov/pubmed/636844`.

T Stieglitz, H Beutel, M Schuettler, and J U Meyer. Micromachined , Polyimide-Based Devices for Flexible Neural Interfaces. *Biomedical Microdevices*, 2(4):283–294, 2000.

T Stieglitz, M Schuettler, J Badia, and X Navarro. Evaluation of Polyimide As Substrate Material for Electrodes to Interface the Peripheral Nervous System. In *5th International IEEE EMBS Conference on Neural Engineering*, pages 529–533, 2011.

Peter J Stienen, Zainal L Haberham, Walter E Van Den Brom, Harry N M De Groot, Anjop J Venker-van Haagen, and Ludo J Hellebrekers. Evaluation of methods for eliciting somatosensory-evoked potentials in the awake, freely moving rat. *Journal of Neuroscience Methods*, 126(1):79–90, June 2003. ISSN 01650270. doi: 10.1016/S0165-0270(03)00070-0. URL `http://linkinghub.elsevier.com/retrieve/pii/S0165027003000700`.

R J Storer, P Butler, K L Hoskin, and P J Goadsby. A simple method, using 2-hydroxypropyl-beta-cyclodextrin, of administering alpha-chloralose at room temperature. *Journal of neuroscience methods*, 77(1):49–53, November 1997. ISSN 0165-0270. URL `http://www.ncbi.nlm.nih.gov/pubmed/9402556`.

M Sugitani, J Yano, T Sugai, and H Ooyama. Somatotopic organization and columnar structure of vibrissae representation in the rat ventrobasal complex. *Experimental brain research. Experimentelle Hirnforschung. Experimentation cerebrale*, 81(2):346–352, 1990. ISSN 0014-4819. doi: 10.1007/BF00228125.

Minah Suh, Sonya Bahar, Ashesh D Mehta, and Theodore H Schwartz. Temporal dependence in uncoupling of blood volume and oxygenation during interictal epileptiform events in rat neocortex. *The Journal of neuroscience : the official journal of the Society for Neuroscience*, 25(1):68–77, January 2005. ISSN 1529-2401. doi: 10.1523/JNEUROSCI.2823-04.2005. URL `http://www.ncbi.nlm.nih.gov/pubmed/15634768`.

H a Swadlow. Efferent neurons and suspected interneurons in S-1 vibrissa cortex of the awake rabbit: receptive fields and axonal properties. *Journal of neurophysiology*, 62(1):288–308, July 1989. ISSN 0022-3077. URL `http://www.ncbi.nlm.nih.gov/pubmed/2754479`.

Simona Temereanca and Daniel J Simons. Local field potentials and the encoding of whisker deflections by population firing synchrony in thalamic barreloids. *Journal of neurophysiology*, 89(4):2137–45, April 2003. ISSN 0022-3077. doi: 10.1152/jn.00582.2002. URL `http://www.ncbi.nlm.nih.gov/pubmed/12612019`.

Texas Instruments. AN-1515 A Comprehensive Study of the Howland Current Pump. Technical report, 2013.

AM Thomson and Jim Deuchars. Temporal and spatial properties of local circuits in neocortex. *Trends in neurosciences*, 2:119–126, 1994. URL http://www.sciencedirect.com/science/article/pii/016622369490121X.

a T Tidswell, a Gibson, R H Bayford, and D S Holder. Electrical impedance tomography of human brain activity with a two-dimensional ring of scalp electrodes. *Physiological measurement*, 22(1):167–75, February 2001a. ISSN 0967-3334. URL http://www.ncbi.nlm.nih.gov/pubmed/11236877.

T Tidswell, a Gibson, R H Bayford, and D S Holder. Three-dimensional electrical impedance tomography of human brain activity. *NeuroImage*, 13(2): 283–94, March 2001b. ISSN 1053-8119. doi: 10.1006/nimg.2000.0698. URL http://www.ncbi.nlm.nih.gov/pubmed/11162269.

J Travis. Anesthetics are slowly giving up the secrets of how they work. *Science News*, 166(1):8–9, 2004.

S F Traynelis and R Dingledine. Role of extracellular space in hyperosmotic suppression of potassium-induced electrographic seizures Role of Extracellular Space in Hyperosmotic Suppression of Potassium-Induced Electrographic Seizures. *Journal of neurophysiology*, 61:927–938, 1989.

N Tsukahara and D R Fuller. Conductance changes during pyramidally induced postsynaptic potentials in red nucleus neurons. *Journal of neurophysiology*, 32(1):35–42, January 1969. ISSN 0022-3077. URL http://www.ncbi.nlm.nih.gov/pubmed/4303836.

M Ueki, G Mies, and K a Hossmann. Effect of alpha-chloralose, halothane, pentobarbital and nitrous oxide anesthesia on metabolic coupling in somatosensory cortex of rat. *Acta anaesthesiologica Scandinavica*, 36(4):318–22, May 1992. ISSN 0001-5172. URL http://www.ncbi.nlm.nih.gov/pubmed/1595336.

H Van Der Loos. Barreloids in mouse somatosensory thalamus. *Neuroscience letters*, 2(1):1–6, 1976. ISSN 03043940. doi: 10.1016/0304-3940(76)90036-7.

Martijn E van Raaij, Liis Lindvere, Adrienne Dorr, Jianfei He, Bhupinder Sahota, F Stuart Foster, and Bojana Stefanovic. Functional micro-ultrasound imaging of rodent cerebral hemodynamics. *NeuroImage*, 58(1):100–8, September 2011. ISSN 1095-9572. doi: 10.1016/j.neuroimage.2011.05.088. URL http://www.ncbi.nlm.nih.gov/pubmed/21704715.

Martijn E van Raaij, Liis Lindvere, Adrienne Dorr, Jianfei He, Bhupinder Sahota, F Stuart Foster, and Bojana Stefanovic. Quantification of blood flow and volume in arterioles and venules of the rat cerebral cortex using functional micro-ultrasound. *NeuroImage*, 63(3):1030–1037, July 2012. ISSN 1095-9572. doi: 10.1016/j.neuroimage.2012.07.054. URL http://www.ncbi.nlm.nih.gov/pubmed/22871388.

Pierre Veinante, Mark F. Jacquin, and Martin Desch??nes. Thalamic projections from the whisker-sensitive regions of the spinal trigeminal complex in the rat. *Journal of Comparative Neurology*, 420(2):233–243, 2000.

Ricardo Velluti, Kenneth Klivington, and Robert Galambos. Evoked Resistance Shift in subcortical Nuclei. *Currents in Modern Biology*, 2:78–80, 1968.

KR Visser, R Lamberts, HHM Korsten, and WG Zijlstra. Observations on blood flow related electrical impedance changes in rigid tubes. *Pflügers Archiv: European Journal of Physiology*, 291:289–291, 1976.

Anna Vongerichten, Kirill Aristovich, Gustavo Sato Dos Santos, Andrew W McEvoy, and David S Holder. Design for a three-dimensional printed laryngoscope blade for the intubation of rats. *Lab animal*, 43(4):140–2, March 2014. ISSN 1548-4475. doi: 10.1038/laban.463. URL `http://www.ncbi.nlm.nih.gov/pubmed/24651789`.

Serge Vulliemoz, Louis Lemieux, Jean Daunizeau, Christoph M Michel, and John S Duncan. The combination of EEG source imaging and EEG-correlated functional MRI to map epileptic networks. *Epilepsia*, 51(4):491–505, April 2010. ISSN 1528-1167. doi: 10.1111/j.1528-1167.2009.02342.x.

T Waelbers, K Peremans, I Gielen, S Vermeire, I Polis, and Small Animal Orthopedics. Brain perfusion part 2 : anesthesia and brain perfusion in small animals. *Vlaams Diergeneeskundig Tijdschrift*, pages 179–189, 2010.

P M Waite. Somatotopic organization of vibrissal responses in the ventro-basal complex of the rat thalamus. *The Journal of physiology*, 228(2):527–540, 1973.

Kui Wang, Chao Zheng, Chen Wu, Ming Gao, Qiang Liu, Kechun Yang, Kevin Ellsworth, Lin Xu, and Jie Wu. alpha-Chloralose diminishes gamma oscillations in rat hippocampal slices. *Neuroscience letters*, 441(1):66–71, August 2008. ISSN 0304-3940. doi: 10.1016/j.neulet.2008.06.014. URL `http://www.ncbi.nlm.nih.gov/pubmed/18597935`.

J G Webster and J W Clark. *Medical instrumentation: application and design*. Wiley, 1995. ISBN 0471124931. URL `http://books.google.com/books?id=fUlRAAAAMAAJ&pgis=1`.

M Weiser, E Bueno, C Sekirnjak, M E Martone, H Baker, D Hillman, S Chen, W Thornhill, M Ellisman, and B Rudy. The potassium channel subunit KV3.1b is localized to somatic and axonal membranes of specific populations of CNS neurons. *The Journal of neuroscience : the official journal of the Society for Neuroscience*, 15(6):4298–314, June 1995. ISSN 0270-6474. URL `http://www.ncbi.nlm.nih.gov/pubmed/7790912`.

H R Weiss. Measurement of cerebral capillary perfusion with a fluorescent label. *Microvascular research*, 36(2):172–80, September 1988. ISSN 0026-2862. URL `http://www.ncbi.nlm.nih.gov/pubmed/3141746`.

B Weksler, B Ng, J Lenert, and M Burt. A simplified method for endotracheal intubation in the rat. *Journal of applied physiology*, 76:1823–1825, 1994.

C Welker. Microelectrode delineation of fine grain somatotopic organization of (SmI) cerebral neocortex in albino rat. *Brain research*, 26(2):259–275, 1971. ISSN 00068993. doi: 10.1016/S0006-8993(71)80004-5.

PF F White, RR R Johnston, and CR R Pudwill. Interaction of Ketamine and Halothane in Rats. *Anesthesiology*, 42(2):179–186, 1973.

T Whittem, K S Pasloske, M C Heit, and M G Ranasinghe. The pharmacokinetics and pharmacodynamics of alfaxalone in cats after single and multiple intravenous administration of Alfaxan at clinical and supraclinical doses. *Jounal of vetenary pharmacological Therapy*, 31:571–579, 2008. doi: 10.1111/j.1365-2885.2008.00998.x.The.

H Wieler, H Herzog, D D Patton, A Schmid, E Rota, and L E Feinendegen. Functional studies in brain and heart with positron emission tomography. *Medical Progress Through Technology*, 11(2):73–106, 1986.

M N Williams and R L Faull. The distribution and morphology of identified thalamocortical projection neurons and glial cells with reference to the question of interneurons in the ventrolateral nucleus of the rat thalamus. *Neuroscience*, 21 (3):767–780, 1987. ISSN 03064522. doi: 10.1016/0306-4522(87)90036-4.

Sarah Wolfensohn and Maggie Lloyd. *Handbook of laboratory animal management and welfare*. Blackwell, 2010. ISBN 1405111593. URL `http://books.google.com/books?id=fXjKjwEACAAJ&pgis=1`.

N Wu, C F Hsiao, and S H Chandler. Membrane resonance and subthreshold membrane oscillations in mesencephalic V neurons: participants in burst generation. *The Journal of neuroscience : the official journal of the Society for Neuroscience*, 21(11):3729–39, June 2001. ISSN 1529-2401. URL `http://www.ncbi.nlm.nih.gov/pubmed/11356860`.

S Yasaki and P J Dyck. A simple method for rat endotracheal intubation. *Laboratory animal science*, 41(6):620–2, December 1991. ISSN 0023-6764. URL `http://www.ncbi.nlm.nih.gov/pubmed/1667210`.

R J Yerworth, R H Bayford, G Cusick, M Conway, and D S Holder. Design and performance of the UCLH mark 1b 64 channel electrical impedance tomography (EIT) system, optimized for imaging brain function. *Physiological measurement*, 23(1):149–58, March 2002. ISSN 0967-3334. URL `http://www.ncbi.nlm.nih.gov/pubmed/11876228`.

A Yoshida, J O Dostrovsky, and C Y Chiang. The afferent and efferent connections of the nucleus submedius in the rat. *The Journal of comparative neurology*, 324 (1):115–133, 1992. ISSN 0021-9967. doi: 10.1002/cne.903240109.

Mingrui Zhao, Minah Suh, Hongtao Ma, Challon Perry, Andrew Geneslaw, and Theodore H Schwartz. Focal increases in perfusion and decreases in hemoglobin oxygenation precede seizure onset in spontaneous human epilepsy. *Epilepsia*, 48(11):2059–67, November 2007. ISSN 0013-9580. doi: 10.1111/j.1528-1167.2007.01229.x. URL `http://www.ncbi.nlm.nih.gov/pubmed/17666071`.